Mudstone porosity and clay fraction in overpressured basins

Ecclestone-Brown, Paul

Mudstone Porosity and Clay Fraction in Overpressured Basins

Paul Ecclestone-Brown

Department of Geological Sciences

University of Durham

A thesis submitted to the University of Durham in partial fulfilment of the degree of Doctor of Philosophy

DECLARATION

No part of this thesis has been submitted previously for a degree in this or any other university. The work described in this thesis is entirely that of the author, except where reference is made to previously published or unpublished work.

Paul Ecclestone-Brown

Department of Geological Sciences

University of Durham

May 2002

ABSTRACT

This thesis demonstrates the use of a mixture of standard and novel petrophysical techniques to estimate physical parameters of mudstone and explores the use of a generic, clay fraction-dependent compaction model in the context of pore pressure evaluation.

Mudstones are often highly heterogeneous, yet many authors use a single compaction trend to describe their behaviour. Previous work has shown that the rate of a mudstone's compaction with vertical effective stress is a function of its clay fraction, the proportion of the sediment matrix with a particle diameter of less than 2μm. This observation forms the basis of the generic mudstone compaction model used in this thesis.

The use of the generic compaction model is explored in two case studies using characterised mudstone samples and wireline log data from the Gulf of Thailand and Gulf of Mexico. Further mudstone samples from the Central North Sea were characterised.

An error analysis showed that the compaction model can provide estimates of pressure to within ±1.8MPa at a burial depth of 3km (equivalent to ±0.5ppg mudweight) when the input parameters are constrained to an attainable level. In both cases studied, standard methods of analysis could not provide reasonable estimates of pressure in mudstone using wireline resistivity and porosity log data compared to pressure measurements in associated sand bodies. The deep sediments of the two wells studied from the Gulf of Thailand are overconsolidated with respect to their current stress state. The generic compaction model was used to determine that the overconsolidated sediments were uplifted by 1,300m and have been reburied beneath 900m of sediment that now overlies a regional unconformity. The generic compaction model was used in conjunction with an artificial neural network technique for the characterisation of mudstones from wireline data to determine pressure estimates in the mudstones of three deepwater wells in the Gulf of Mexico. A pressure transition zone in one well was shown to be associated with a 10% increase of mudstone clay fraction within the zone compared to surrounding rocks. In both case studies disequilibrium compaction was identified as the key overpressure generation mechanism.

ACKNOWLEDGEMENTS

This project was set up and supervised by Dick Swarbrick of Durham and Andy Aplin of Newcastle University. They have supported my development from open-mouthed undergraduate to cynical postgraduate student admirably. I wish to thank them both for helping me through the project, for all their advice and help. I hope that they had as much fun and felt as challenged as I did throughout the project.

I must thank Yunlai Yang for my access to his research, and especially for use of *ShaleQuant*. His input to the project and, indeed, to the understanding of mudstone compaction has been very valuable.

A big thank you to the all the people that I have been able to talk pressure with, to Dave Darby, James Iliffe, Stephan Düppenbecker, Tim Dodd, Andy Pepper, Phil Heppard, Chris Hawkes, Dan Moos, Martin Traugott, Bill Kilsdonk, T K Kan, Anthony Mallon, Fred Gyllenhammar and to all the others with whom I have had the opportunity to discuss the complexities of mudstone behaviour.

Thank you to all the technical staff that have eased my way through the PhD woes; Rob Hunter & Dave Scorer who put up with my ineptitude in the lab, to Carole Blair, Claire Whitehill, Dave Asbery, Karen Atkinson, Ron Hardy, Gary Wilkinson and Dave Schofield for every bit of help that you gave me.

But most of all, thank you to Kate, who I have relied on over the last few years to keep me motivated and to keep my feet on the ground.

CONTENTS

FIGURES

1 INTRODUCTION

1.1 General introduction

1.1.1 Thesis outline

The work described in this dissertation is a study of the use of generic compaction curves compared to the use of locally derived compaction curves in the assessment of pore fluid pressure in young (<65Myr), cool (<70°C), siliciclastic basins.

The key drivers for the research are twofold, academic and industrial. The academic challenge lies in the fact that mudstones are the most voluminous part of the sedimentary record, yet they are possibly the least well understood. The oil industry takes an interest as mudstones frequently act as pressure seals. Unexpected overpressure in exploration wells causes 90% of rig down time, so any further understanding of the causes or detection of overpressure will ultimately reduce drilling costs and increase safety.

Chapters 1 and 2 provide an outline of the concepts involved in the estimation of pore fluid pressure, the processes involved in estimation of physical properties of rocks from wireline log data and the computational processes employed throughout the pressure estimation process. The methodology used throughout the following chapters is presented in Chapter 2.

Chapter 3 describes a study of the errors involved in the analysis of pressure using generic compaction curves. This work involved a sensitivity analysis of the compaction models to errors in all their input parameters and full error analysis using Monte Carlo techniques.

Chapters 4 and 5 are case studies in which several techniques were used to provide an estimate of pore fluid pressure and ascertain geological histories of the case study areas. The data are taken from the Gulf of Thailand and the Gulf of Mexico, two contrasting basins in which high pressure caused difficulties during drilling. The pressure evaluation and physical property evaluation techniques involved are assessed in each chapter together with the petrophysical and geological conclusions associated with each study.

Chapter 6 consists of a short description of the characterisation of some mudstone samples from the UK sector of the Central North Sea.

Chapter 7 summarises the overall conclusions and provides a short review of how this study could be extended beyond the scope of the thesis.

1.1.2 Chapter summary

This chapter describes the fundamental concepts of pressure, defining pressure terms and ancillary rock properties where necessary. The compaction behaviour of siliciclastic sediments is discussed together with the effects of abnormal pressure on that behaviour. The estimation of porosity and mudstone lithology from wireline log data is

also described. Finally, the concepts underlying the numerical and computational techniques involved in the artificial neural network (ANN) analysis of the wireline log data selected for the studies are explained.

1.2 Pressure concepts and measurement

1.2.1 Pressure definitions

> *'The ability to consistently and correctly predict pressures is critically dependent upon including all parameters relevant to pressure in a model, and providing accurate values of those critical parameters.'* - Waples (1998)

The pore fluid pressure is commonly compared to two fundamental pressures, hydrostatic pressure and lithostatic pressure (the vertical component of the confining stress). The hydrostatic pressure, p_{hyd}, at any depth below the water surface, z, is equal to that produced by a column of water of average fluid density, $\overline{\rho}_{fl}$, thus:

$$p_{hyd} = \overline{\rho}_{fl} g z \tag{1.1}$$

and lithostatic pressure, s_v, is equivalent to that of a column of rock with an average bulk density, $\overline{\rho}_b$, thus:

$$s_v = \overline{\rho}_b g z \tag{1.2}$$

Any pore fluid pressure that is not equal to the hydrostatic pressure for that depth is deemed to be abnormal, with pore fluid pressures in excess of hydrostatic pressure being described as overpressures and those below hydrostatic described as underpressures (e.g. Mouchet & Mitchell, 1989).

The difference between the pore fluid pressure and lithostatic pressure is the vertical effective stress. Other forms of effective stress exist, such as the mean effective stress which is defined as the difference between the mean of all three principal stresses and the pore fluid pressure. The hydrostatic effective stress is the difference between the confining stress (mean or vertical) and hydrostatic pressure, i.e. the effective stress associated with normally pressured regimes.

The vertical confining stress is the easiest to estimate, since an estimate of mean confining stress requires the ability to estimate or measure the horizontal confining stress, which is difficult (Breckels & van Eekelen, 1982; Mouchet and Mitchell, 1989; Goulty, 1998; Harrold *et al.* 1999).

Throughout the rest of the dissertation reference to effective stress means the vertical effective stress unless it is referred to as mean effective stress explicitly.

1.2.2 Drivers for accurate pressure prediction

The drivers for the accurate evaluation of pressure in mudstones fall into two major categories: academic and industrial. The academic challenge lies in the poor understanding of the geological and petrophysical behaviour of

the most voluminous and arguably the most variable sedimentary lithology. The industrial drivers for the research are drilling safety and economics.

During drilling, mud is pumped down the drill bit and circulates up through the hole back up to the surface. This mud supports the hole, acts as a lubricant for the drilling process and removes the rock chips from the drill bit. During drilling the density of the drilling mud is varied so as to match the prognosed pore fluid pressure. This estimate of pressure must be accurate as both under- and overestimates of pressure cause problems during drilling.

If pressure is underestimated fluid will flow from the formation into the drill hole in highly permeable lithologies, such as sandstones. In extreme cases the flow will cause a well kick, or at worst a blowout, in which the pressure-containment valves on the drilling rig are unable to contain the fluid flow from the wellbore and the well-head assembly explodes. These explosions are potentially lethal, hazardous to the environment since large amounts of pollution can be produced and can destroy drilling rigs.

If pressures are overestimated and the mud pressure exceeds the minimum component of confining stress of the formation, the drilling fluid will induce hydraulic fractures in the formation. These fractures will enable drilling fluid loss into the formation. In serious cases of fluid loss, the drill string can become stuck and even snap. This is dangerous for workers on the drilling rig or ship and is expensive as equipment is destroyed and sidetracks to wells may have to be drilled.

The pressure profile of a well is essential in the designing of the casing strategy of the well, since if there are any significant increases of pressure in wells, mud weight has to be increased to control the well. This increase in mudweight could induce fractures in shallower, uncased intervals if the minimum component of confining stress is exceeded in that interval. If significant, unexpected overpressure is encountered whilst drilling, the hole may have to be shut down temporarily and cased. The early casing may mean that the target depth cannot be reached, so the sum spent on drilling the well, up to $100 million for a deep water Gulf of Mexico well, (Duppenbecker, pers. com., 2000), could be wasted.

1.2.3 Derivation of vertical stress

Most of the pressure calculation procedures presented rely on the calculation of lithostatic pressure, or overburden. This is a non-trivial calculation as it involves the evaluation of

$$s_v = \int_0^h g\rho \, \mathrm{d}z = \int_0^h g\left[\rho_{ma} + \phi\left(\rho_{fl} - \rho_{ma}\right)\right] \mathrm{d}z \tag{1.3}$$

where ρ_{ma} and ρ_{fl} are the matrix and fluid densities, respectively, and ϕ is the porosity at any burial depth, z. Since all the constituents of the integral vary with depth, a unique overburden curve exists for each well drilled. The simplest approximation of this would be to assume an overburden pressure gradient of ~22.6MPa km^{-1} (1psi ft^{-1}) (Mouchet and Mitchell, 1989). This is obviously flawed. The best empirical solution would be to measure formation bulk density throughout the drilled interval. This is time consuming and expensive, so it is not done frequently. Other wireline 'porosity' logs (i.e. sonic and resistivity logs) are more commonly acquired over a larger portion of the drilled interval, so these can be used, together with assumptions of matrix and fluid density, to derive

a pseudo density log. Apart from very rare exceptions, the very top of the drilled interval, the first ~400m, drilled using 36" and 26" bits, are not logged (Rider, 1996). This shallow section is typically where the rate of compaction is highest (Rieke and Chilingarian, 1974) and thus the rate of change of overburden is highest. In this depth range, an assumption of 22.6MPa km^{-1} overburden gradient cannot be used at all as Fertl (1976) has shown that the gradients can be as low as 15MPa km^{-1}. In these cases local or regional scale overburden curves such as those developed for the shallow water Gulf of Mexico and North Sea by Fertl and Timko (1972) should be used.

1.2.4 Generation of abnormal pressure

Abnormal pressure can be generated in several ways. Swarbrick & Osborne (1998) have summarised the mechanisms of abnormal pressure generation as follows:

- Disequilibrium compaction
- Tectonic stress
- Temperature increase
- Water release due to mineral transformation
- Hydrocarbon generation
- Cracking of oil to gas
- Osmosis
- Hydraulic head
- Buoyancy due to density contrasts

Disequilibrium compaction During compaction the permeability of mudstones becomes so low that fluid flow through the rock's pore network is retarded over geological time periods. On further loading, since sufficient fluid cannot be expelled from the pores, the fluid begins to bear some of the weight of the rock overburden and pore fluid pressure rises above expected hydrostatic levels. This mechanism is thought to dominate in young, (<65Myr), cool (<70°C) basins and deltas experiencing rapid sedimentation, e.g. Nile Delta (Mazzoni *et al.*, 1997; Nashaat, 1998), Mississippi Delta (Burrus, 1998), Tertiary Section of the North Sea (Darby *et al.*, 1998, Holm, 1998), Mahakam Delta (Burrus, 1998; Goulty, 1998), Caspian Sea (Bredehoeft *et al.*, 1988), Malay Basin (Yusof & Swarbrick, 1994) and the Beaufort-Mackenzie Basin (Tang & Lerche, 1993). It has been successfully modelled by many workers (e.g. Mann & MacKenzie, 1990; Audet & McConnell, 1992; Tang & Lerche, 1993; Schneider *et al.*, 1993). Disequilibrium compaction is typically the most important mechanism in the creation of overpressure (Swarbrick & Osborne, 1998).

Tectonic The same principles of compaction and disequilibrium compaction apply if lateral stresses are applied to a sediment column. Overpressure in and around fault zones has been reported by Byerlee (1993).

Temperature increase Water expands when heated above 4°C. If water is heated in a sealed vessel, the pressure increases rapidly. Barker (1972) suggested that this could be a contributory factor in the development of overpressure because, as sediments are buried, their temperature rises, and the thermal expansion coefficient of brine is much greater than that of the matrix. Swarbrick & Osborne (1998) state for this to happen the environment must be almost completely isolated, with virtually zero permeability. Luo & Vasseur (1992) have shown through modelling that these conditions are highly unlikely, with negligible amounts of overpressure being produced in mudstones, even with unrealistically low permeabilities as low as than 10^{-7}nD. Hunt (1990) has suggested that diagenetic seals with permeabilities close to zero may be feasible.

Water release due to mineral transformation Several mineral reactions involve the release of water including smectite dehydration, the dehydration of gypsum to anhydrite and the transformation of smectite to illite. The details of both reactions involving smectite are still the subject of debate, with the kinetics and thermodynamics of smectite dehydration still poorly understood (Colton-Bradley, 1987; Hall, 1993), and the bulk volume difference created in the smectite-illite transition ranging from a volume decrease of 23% (Hower *et al.*, 1976) to a 25% increase (Boles & Franks, 1979).

Hydrocarbon generation and cracking of oil to gas These both involve changes in the fluid composition and total volume of the combined rock and fluid. There are several mechanisms involving various amounts of potential volume change, including oil generation from kerogen (e.g. Meissner 1978a; Meissner, 1978b, Sweeney, 1995), gas generation from kerogen (e.g. Meissner 1978a; Meissner, 1978b; Law, 1984) and the cracking of oil or bitumen to gas (MacKenzie & Quigley, 1988; Barker, 1990). The reactions involving kerogen result in the increase in pore fluid from the decomposition of some of the solid phase of the rock. Pressure must be high in these cases, since petroleum fluids regularly migrate from typically low permeability source rocks, although the exact mechanism for primary migration remains poorly understood.

Osmosis Large contrasts in the salinity of pore fluids across a semi permeable membrane will induce fluid flow from the region of low salinity to the region of high salinity across the membrane. Marine & Fritz (1981) suggested that this process could cause the initiation of some overpressure. Swarbrick & Osborne (1998) refute this suggestion, stating that the presence of any fractures in the membrane would make osmosis impossible.

Hydraulic head The hydraulic (potentiometric) head resulting from the elevation of the water table results in the exertion of pressure in the subsurface if the aquifer is overlain by a seal (e.g. Neuzil, 1995). Lateral continuity of aquifers and elevation of the aquifers above the hydrostatic datum are required.

Hydrocarbon buoyancy Since most hydrocarbons are less dense than water, they have lower associated pressure gradients than water. This means that small amounts of overpressure will be associated locally with all hydrocarbon accumulations, but present only in the hydrocarbon phase.

1.2.5 Pressure transference

In the subsurface fluid flows, if abnormally pressured, from areas of high pressure to areas of low pressure so long as there is permeability to facilitate flow. This effect is most apparent in rocks with high permeability, but fluid flow also occurs in low permeability mudstones (e.g. Bjørlykke, 1993) over geological time periods. Pressure

profiles in tilted, overpressured, sand bodies typically exhibit hydrostatic gradients, with pressure enhancement with respect to the pressure in surrounding lower permeability formations at the top of the sand body and pressure depletion at the base. Swarbrick & Osborne (1998) describe this phenomenon in greater detail. Transference of pressure can also take place vertically, typically associated with active faulting (Burley *et al.*, 1989).

There are several examples of lateral transfer of pressure (Yardley & Swarbrick, 2000), including cases in the Mahakam Delta (Burrus *et al.*, 1992), and the Palaeocene sands of the North Sea (Cayley, 1987). Vertical leakage of pressure is documented in a Southeast Asian basin by Grauls & Cassignol (1993).

1.2.6 Pressure measurement

The principal methods for quantitative pressure measurement are repeat formation tests (RFT) and drill stem tests (DST). These methods are described below. They are used to determine the pore fluid pressure of permeable units such as sandstones and the measurements are obtained after drilling. Methods for pressure estimation after drilling using wireline log data are also possible and are discussed in Section 1.5. Other pressure estimation techniques are commonly based on drilling parameters, such as drilling rate and bit torque are beyond the scope of this study.

The repeat formation test (RFT) is the generic name used here for pressure measurements using a wireline tool. The tool is several metres long, samples reservoir fluids and measures formation pressure buildup versus time. It can test many depths in a single run. At the zone to be tested, a backup shoe is pressed against the well wall to force a rubber pad with a valve against the opposite wall. The valve is opened and formation fluids can flow into the tool as the pressures are measured. The pressure records can also be used to calculate formation permeability. Two large sample chambers, each holding several litres, are used to obtain a sample of formation fluids. Modern tools allow multiple sampling.

The drill stem test (DST) is used primarily to determine the fluids present in a particular formation and the rate at which they can be produced. The test is run in an uncased hole filled with drilling mud. Pressure exerted by the drilling mud in the well prevents fluids from flowing out of the formation into the well. A hollow pipe called a drill stem is lowered down the well. The drill stem has two expandable devices, called packers, around it. The drill stem is lowered into the well until one packer is just above the formation to be tested and the other below. The packers are then expanded to close the well above and below the formation. Sealing the well around the formation eliminates the pressure exerted by drilling mud on the formation. The test usually (ideally) involves flow to the surface of oil and/or gas or water. The flow is maintained for a period, generally measured in hours, to permit an assessment of reservoir performance. The pressures are measured downhole, near the packers, as well as at the well head. From the point of view of estimation of formation pressure, it is determined from analysis of the pressure build up when flow has halted and the well has been shut in. The best estimates come from a long shut in period after a short flowing period.

1.2.7 Industrial approach to pressure evaluation

Pressure evaluation is an ongoing process throughout the well planning process, during drilling and through post-drill analysis. Pre-drill analysis comprises pressure evaluation from seismic, where seismic velocities are analysed to produce a pressure profile by comparing observed seismic velocities with expected values using methods similar

to the method described by Rubey & Hubbert (1959). The depth migrated seismic data may be used to define grids for a set of forward basin models which can be used for pressure analysis. Also during this period, offset well data, if available, should be reanalysed to produce profiles and to calibrate the pressure from seismic and basin modelling analysis.

During drilling all possible data, including and wireline data obtained while drilling, trip and connection gas, D-exponent, cutting density and pressure measurements of permeable layers are used to obtain a reliable pressure profile as described by Mouchet & Mitchell (1989).

After the well has been completed any wireline data that has been obtained is used to provide insight into discrepancies between pre drill pressure predictions, estimates whilst drilling and direct pressure measurements. This post-drill analysis of all available data provides information that is useful for pre-drill prediction of pressure for any further wells to be drilled in the locality and possibly further afield.

1.3 Porosity-depth and porosity-effective stress relationships

1.3.1 Compaction fundamentals

> *'There is a definite need to constrain porosity vs. depth (or effective stress) relationships. This has long been recognised for reservoir rocks. A knowledge of shale porosity is at least equally important in basin modelling, because shales dominate most sequences volumetrically, and because hydrocarbon generation and expulsion takes place in shales.'* - Hermanrud (1993)

Porosity, ϕ, is defined as the ratio of the volume of pores to the total volume of a porous medium. Void ratio, e, is the ratio is defined as the ratio of pore volume to the volume of the solid phases of the porous medium, thus:

$$e = \frac{\phi}{1-\phi} \tag{1.4}$$

The compaction behaviour of argillaceous sediments is a function of several variables, including effective stress, age of sediments, lithology, mineralogy, tectonic stress, deposition rate, formation thickness, sorting, fabric, cementation and chemistry of pore and bound fluids (Dzevanshir *et al.*, 1986).

As the loading of sediment increases, the overall volume of the sediment decreases. This decrease is caused by the reduction of the porosity of the sediment, i.e. compaction. There are three fundamental phenomena which contribute to the compaction of sediments (Schneider *et al.*, 1994): mechanical rearrangement of grains, mechanical deformation and chemical deformation of grains.

Mechanical rearrangement of grains is firstly associated with the expulsion of pore water, followed by the expulsion of bound water. Mechanical deformation is associated with the deformation of the framework of the grains. This deformation is a combination of elastic, plastic, viscous and brittle deformation (Schneider *et al.*, 1994). Chemical deformation includes pressure dissolution phenomena, dissolution-reprecipitation and mineral reactions.

The microscopic effects of loading and unloading of sediments have been investigated uniaxially and triaxially in several studies, including those of Karig & Hou (1992), Vasseur *et al.* (1995) and Djéran-Maigre *et al.* (1998). The studies of Vasseur *et al.* (1995) and Djéran-Maigre *et al.* (1998) include analysis of transmission electron micrographs of clay samples that have undergone progressively increasing loads of up to 50MPa, an equivalent burial depth of 2.5km. These experiments are performed over laboratory timescales, so time dependent phenomena such as chemical reactions and viscous creep are not observed (Karig & Hou, 1992).

1.3.2 Macroscopic description of compaction

Many attempts at producing mathematical models to describe macroscopically the porosity reduction process have been published and have been reviewed by Giles *et al.* (1998) and Brown *et al.* (1999). The first attempt was made by Athy (1930), in which he described an exponential relationship between porosity and depth:

$$\phi = \phi_0 \exp(-cz) \tag{1.5}$$

where c is the compaction coefficient. This equation has been commonly used. The formulation was improved by Hubbert and Rubey (1959) to use effective stress instead of depth and has been used by several authors (e.g. Smith, 1971; Sclater & Christie, 1980; Shi & Wang, 1986; Bethke & Corbett, 1988; Luo & Vasseur, 1992), thus:

$$\phi = \phi_0 \exp(-d\sigma) \tag{1.6}$$

This approach to compaction description was extended empirically further by Schneider *et al.* (1996) to produce a compaction curve of the form:

$$\phi = \phi_0 + \phi_a \exp(-c_a\sigma) + \phi_b \exp(-c_b\sigma) \tag{1.7}$$

where the constants ϕ_0, ϕ_a, ϕ_b, c_a and c_b are all determined locally. This formulation was created in order to calibrate shale compaction trends that generally have a high curvature at low effective stresses.

Baldwin & Butler (1985) suggested a power law relationship, relating solidity $(1-\phi)$ to depth. The relationship is based on curve fitting exercises with an extended public compaction database for worldwide mudrocks. Written in terms of porosity their relationship is

$$\phi = 1 - \left(\frac{z}{6020}\right)^{\frac{1}{6.35}} \tag{1.8}$$

where depth, z, is measured in metres.

All the above approaches are empirical, and so underlying compaction mechanisms need not be understood to use these models; however, it would be useful to have a more complete understanding of the processes involved to assess each model's validity.

The soil mechanics approach to compaction is based on the observations by Skempton (1970) on the compression of natural clays. He concluded that the relationship between void ratio, *e*, and the logarithm of vertical effective stress is essentially linear for any particular clay, and that the compactional behaviour of the clay is dependent upon the nature and amount of clay minerals present, thus:

$$e = e_\gamma - \beta \ln\left(\frac{\sigma_v}{\sigma_\gamma}\right) \tag{1.9}$$

where e_γ is the void ratio at a given vertical effective stress, σ_γ, typically 100kPa, and β is termed the compression coefficient (Aplin *et al.*, 1995) which is a description of the intrinsic strength of the sediment (Audet & McConnell, 1992).

Many workers have based their work upon these soil mechanics observations including Burland (1990), Mann & MacKenzie (1990), Audet & McConnell (1992) and Aplin *et al.* (1995). Of these, only Burland (1990) and Aplin *et al.* (1995) consider mudstone variability. Both suggest that lithology exerts a major control on mudstone compactional behaviour. Burland (1990) also suggests that initial depositional conditions exert an influence on compactional behaviour. Aplin *et al.* (1995) in a simplifying assumption neglect that effect, use vertical effective stress as a proxy for degree of loading, and link variations in compactional behaviour to variations of clay fraction, v_{cf}, the proportion of the sediment matrix with a grain diameter less than 2μm. Throughout this dissertation, clay fraction is used solely to describe grain-size based descriptions of lithology whereas clay content is used for any other description of clay lithology. Aplin *et al.* (1995) define the relationship between clay fraction and compression coefficient as

$$\beta = 0.0789 + 0.677 v_{cf} \tag{1.10}$$

The void ratio at 100kPa was defined in two ways, using linear and quadratic functions of the compression coefficient:

$$e_{100} = 0.208 + 5.271\beta \tag{1.11}$$

or

$$e_{100} = 0.3417 + 3.745\beta + 3.224\beta^2 \tag{1.12}$$

This approach has been developed, using significantly more calibration data, by Yang & Aplin (2000). They did not publish the actual numerical relationships between clay fraction and the compaction parameters; however, the calibration data were shown together with graphical representations of the relationships. The relationships are given below (Yang, pers. com., 1999):

$$\beta = 0.0407 + 0.2479 v_{cf} + 0.3684 v_{cf}^2 \tag{1.13}$$

and

$$e_{100} = 0.3024 + 1.6867 v_{cf} + 1.9505 v_{cf}^2 \tag{1.14}$$

The calibration data used to produce these relationships are shown in Figure 1.1 in terms of measured versus modelled void ratio taken from the model. There are 3,847 points on this plot and the correlation coefficient between the two types of void ratio is 0.92. Equations 1.13 and 1.14 form the basis of research for the majority of this study. The disadvantage of these equations is that they need lithological calibration to provide an estimate of the normal compaction trend. A method for derivation of this information has been developed by Aplin *et al.* (1999) and will be discussed in Section 1.6.4.

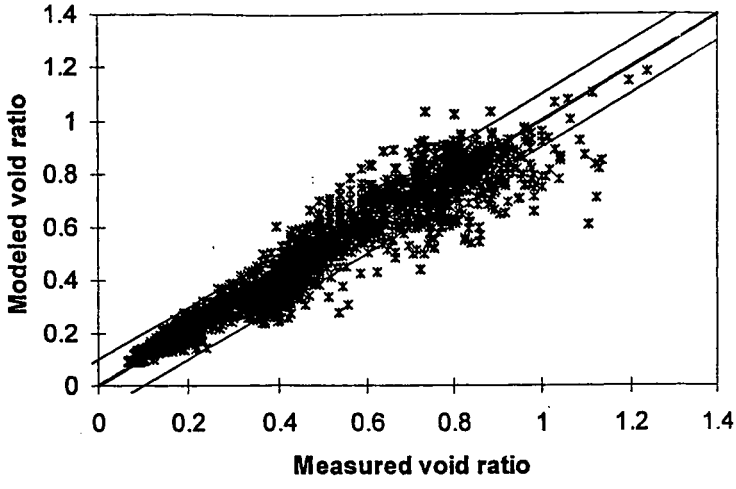

Figure 1.1 - Measured versus modelled void ratio after Yang & Aplin (2000).

Other workers have included other factors in their compaction algorithms. Schmoker & Gaultier (1989) suggest a compaction relationship that is entirely dependent upon temperature and time thus:

$$\phi = 0.3 I_{tt}^{-0.33} \tag{1.15}$$

where I_{tt} is the time-temperature index of thermal maturity described by Lopatin (1971), thus:

$$I_{tt} = \sum_{i=0}^{t} 2^{[(T_i/10)-10.5]} \tag{1.16}$$

where t is time measured in million-year periods and T_i is the formation temperature (°C) in the i^{th} time period. Schmoker & Gaultier (1989) state that their model applies mainly to sandstones and limestones, but they suggest that it may be appropriate for shallowly buried mudstones. They note that porosity depth curves are a static description of the sedimentary section and do not incorporate the idea that porosity reducing processes operate more or less continuously in sedimentary basins. They admit that the influence upon porosity of factors such as grain size, mineralogy, cementation and pressure solution on porosity is empirically combined in the regression coefficients (set at 0.3 and -0.33 in Equation 1.15). They suggest that their model, like traditional porosity-depth relationships, does not provide much insight into the mechanical and chemical processes affecting porosity.

Dzevanshir *et al.* (1986) suggest a compaction relationship which is dependent on depth of burial in metres, z, geologic age in millions of years, A, and shale content , R, thus:

$$\phi = \phi_0 \exp\left[-0.014(13.3\ln A - 83.25\ln R + 2.79)\times 10^{-3} z\right] \tag{1.17}$$

They do not provide any rigorous physical basis for their algorithm apart from stating that compaction must be related to age and lithology. They then provide two empirically obtained relationships relating a single parameter to lithology and age. The two relationships are combined in a way that they do not justify to produce their final relationship. They use their relationship stated in Equation 1.17 in an attempt to explain the porosity trends observed in three wells. They combine overpressure and unloading phenomena within their relationship, so it is not a normal compaction relationship. One area of concern is that even though the paper was published in 1986 all the cited references data from before 1977 apart from one reference to a paper written by Buryakovskiy *et al.* (1983), but that paper is only cited to confirm that expulsion of fluids is impeded in low permeability porous media.

Schneider *et al.* (1996) suggest a model that is dependent upon lithology, effective stress, temperature and time, of the form

$$\frac{\mathrm{d}\phi}{\mathrm{d}t} = -\beta(\phi,\sigma)\frac{\mathrm{d}\sigma}{\mathrm{d}t} - \alpha(\phi,\mu_s)\sigma \tag{1.18}$$

where the mechanical component of compaction, β, is

$$\beta(\phi,\sigma) = c_a\phi_a \exp(-c_a\sigma) + c_b\phi_b \exp(-c_b\sigma) \tag{1.19}$$

and the time dependent, chemical component, α, is described by

$$\begin{cases} \alpha(\phi,\mu_s) = (1-\phi)\dfrac{1}{\mu_s} & \sigma > 0 \text{ and } \phi > \phi_{\min} \\ \alpha(\phi,\mu_s) = 0 & \sigma \le 0 \text{ or } \phi \le \phi_{\min} \end{cases} \tag{1.20}$$

where the sediment viscosity, μ_s, is defined as

$$\mu_s = \mu_0 \exp\frac{E_\mu}{R}\left(\frac{1}{T} - \frac{1}{T_0}\right) \tag{1.21}$$

where μ_0 is the sediment viscosity at a reference temperature, T_0 (here T_0=15°C) and E_μ is an activation energy for the set of reactions. This formulation is only useful for the forward modelling of porosity during basin modelling, the numerical simulation of hydrocarbon generation and fluid flow in basins over geological time periods. The mechanical component of this algorithm is based on work by Smith (1971) in that it used the adaptation of Athy's (1930) relationship cast in terms of effective stress. They use this relationship as they state that the soil mechanics based relationship described by Equation 1.9 yields negative values of porosity at high levels of effective stress. The derivation of all required constants is empirical. The non-mechanical component in the

algorithm is based on the modelling of grain scale pressure solution interactions. They consider the sediment to be a viscous fluid whose viscous deformation is irreversible and they assume that solid volume is conserved during the pressure solution process. The rate of reaction is assumed to be temperature dependent. The pressure solution model is similar to those proposed by Rutter (1983) and Tada *et al.* (1987).

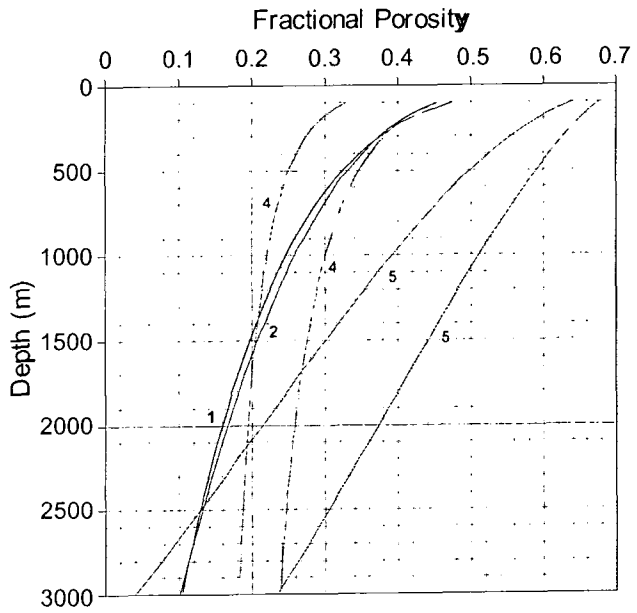

Figure 1.2 - Published shale compaction curves.

1 - Mann & Mackenzie (1990), 2 - Baldwin and Butler (1985), 3 - Dickinson (1953), 4 - Burland (1990) and 5 - Aplin *et al.* (1995).

Some selected mudstone compaction trends are shown in Figure 1.2. This diagram shows a mudstone compaction envelope broadly similar to that shown by Rieke & Chilingarian (1974). The curves shown in Figure 1.1 were derived by using data taken from different locations and depth regions. As discussed above, different assumptions have been used in their derivations. Only the curves derived by Aplin *et al.* (1995) and Burland (1990) suggest that changes in lithology influence the compactional behaviour of the mudstones. The other three curves shown were presented as generic compaction curves for mudstones. Baldwin and Butler (1985) showed their compaction curve in relationship to the solidity-depth data used to derive it. The data showed a significant amount of scatter about the trend, suggesting that a range of curves should have been used to derive the curves.

Burland (1990) suggests that lithological variation exerts a control upon the compaction coefficients he used to populate the soil mechanics-based void ratio effective stress relationship described by Skempton (1944), however he does not try to quantify the effects of the lithological variation, showing the compactional behaviour of various individual clay samples as distinct compaction trends. This is only useful as a starting point for a generic set of mudstone compaction curves. Two individual approaches have been used to further this research, both using an individual parameter as a proxy for lithology. Aplin *et al.* (1995) and Yang & Aplin (2000), as discussed above, used clay fraction as the lithological descriptor. Harrold (2000) used wireline gamma ray as a proxy for lithology. Both methods were data driven techniques for the definition of compation curves. Harrold's (2000) method is simpler to implement than the clay fraction based method, as gamma ray data are simpler to obtain than clay

fraction; however, he did not use any data taken from laboratory measurements to calibrate the wireline data to porosity transforms used in his compaction curve derivation. He stated that local derivation of the curves was necessary. The basis of Yang & Aplin's (2000) compaction curves is rigorous laboratory measurement of mudstone properties, such as matrix density, that can be used in conjunction with wireline data to produce reliable estimates of porosity. This, in conjunction with the laboratory measurement of clay fraction and sourcing of sample material from many wells from geographically diverse locations, means that the clay fraction-based method is more generic than the gamma ray based method, so one must make a balance between the pragmatism of the gamma ray-based method and the complexities of clay fraction estimation or measurement.

Goulty (1998) has suggested that the degree of compaction is controlled by mean effective stress, the difference between the mean of the three principal stresses and the pore fluid pressure, rather than the vertical effective stress. This method requires detailed knowledge of the variation of all three components of confining stress with depth. The easiest of the three to constrain is the vertical stress (Mouchet & Mitchell, 1989). The minimum horizontal stress is next easiest, as it is often assumed to approximate the leak off pressure in Leak Off Tests (Mouchet & Mitchell, 1989), except in extreme compressional tectonic regimes where the minimum principal stress is vertical. The relationship between the minimum horizontal stress and pore pressure and depth has been modelled in several regional settings by Breckels & Van Eekelen (1982). The magnitude of the maximum horizontal confining stress is the most difficult to constrain, so estimates have to be made. This was done by Harrold *et al.* (1999) in a study involving pressure estimation in Southeast Asia. They assumed that the horizontal pressures were isotropic and the horizontal confining stresses were calculated using an algorithm based on the relationship given by Breckels & Van Eekelen (1982). Goulty (1998) suggests that there is a general agreement that in shallow, hydrostatically pressured sections of passive margins and deltaic environments the ratio of minimum horizontal stress to vertical stress is approximately 0.7, rising to reach values of ~0.9 in deeper overpressured sections (Breckels & Van Eekelen, 1982; Gaarenstroom *et al.*, 1993; Yassir & Bell, 1994).

If a simplifying assumption is made that the ratio of vertical effective stress to horizontal effective stress is constant throughout any studied intervals, it follows that the use of vertical and mean effective stress in compaction studies are comparable (Goulty, pers. com., 2001). In the set of studies described in this dissertation, the principal compaction algorithm used is the soil mechanics based relationship between vertical effective stress and void ratio.

1.3.3 Conversion of porosity-effective stress to porosity-depth relationships

Although the concept of effective stress is useful for the mathematical description of compaction, it is less satisfactory for the geological visualisation of compaction trends since the relationship between effective stress and depth, even in normally pressured, monolithological successions, is not linear (Aplin *et al.*, 1995).

The soil mechanics relationship defining void ratio, and hence porosity, as a function of effective stress in units of pascals is

$$\sigma_v = 10^5 \exp\left(\frac{e_{100} - e}{\beta}\right) \tag{1.22}$$

where e_{100} is the void ratio at a vertical effective stress of 100kPa. The definition of vertical effective stress (e.g. Atkinson, 1993) states that

$$\sigma_v = s_v - P_p \tag{1.23}$$

If pore pressure is hydrostatic throughout the formation,

$$P_p = \int_0^h g\rho_{fl}\,\mathrm{d}z \tag{1.24}$$

where all quantities in this analysis are in the base SI units of metres, kilograms and seconds.

Vertical confining stress is

$$s_v = \int_0^h g\rho_b\,\mathrm{d}z = \int_0^h g\left[\rho_{fl}\phi + \rho_{ma}(1-\phi)\right]\mathrm{d}z \tag{1.25}$$

Substituting Equations 1.24 and 1.25 in 1.23 yields

$$\sigma_v = \int_0^h g\left(\rho_{ma} - \rho_{fl}\right)(1-\phi)\mathrm{d}z \tag{1.26}$$

or, in terms of void ratio

$$\sigma_v = \int_0^h \frac{g}{1+e}\left(\rho_{ma} - \rho_{fl}\right)\mathrm{d}z \tag{1.27}$$

Therefore the solution of the following integral equation yields a soil mechanics-based void ratio-depth relationship

$$10^5 \exp\left(\frac{e_{100} - e}{\beta}\right) - \int_0^h \frac{g}{1+e}\left(\rho_{ma} - \rho_{fl}\right)\mathrm{d}z = 0 \tag{1.28}$$

Several attempts have been made to solve this equation analytically (e.g. Parasnis, 1960; Aplin *et al.*, 1995). The latter attempt involved the consideration of lithology-dependent compaction trends. The solution approach taken in the studies described in this dissertation is simpler, creating approximate numerical solutions as outlined in Chapter 4 and Appendix D.

1.4 Lithological evaluation using wireline logs

1.4.1 Introduction to wireline log data

'The geological hammer is past: it isn't necessary to hit things any more to understand them.' - Rider (1996)

The standard wireline logs can be separated into three broad groups, lithology logs, porosity logs, and electrical logs. The lithology logs include gamma ray and spectral gamma ray logs. Porosity logs include sonic transit time logs, formation density logs and neutron logs. Electrical logs include resistivity logs and spontaneous potential logs.

A full description of the acquisition and standard use of wireline logs is widely documented (e.g. Rider, 1996; Schlumberger, 1989; Asquith & Gibson, 1982). The following descriptions of the properties measured by the various wireline tools are provided as a summary.

Natural minerals contain three principal radioactive elements: uranium, thorium and potassium. All three elements emit gamma rays of characteristic energy, and hence frequency, on decay. A natural gamma ray log uses a scintillation counter to measure the natural radioactivity of rocks in the well. The spectral gamma ray tool uses a more sensitive scintillation chamber to measure the energy of the gamma rays entering as well as counting them. The absolute abundance of the three elements is estimated by analysing the energy spectrum of the gamma rays observed in the scintillation chamber. Clay minerals and potassium feldspars are the only mineral sedimentary rock components that typically exhibit high radioactivity, due to high concentrations of potassium (Rider, 1996). Hence high gamma ray signatures in sedimentary sequences potentially indicate clay mineral-rich rocks - mudstones, or feldspathic sandstones.

The sonic or acoustic transit time log measures the time taken for sound to pass through each rock layer in the well. A typical sonic logging tool has a set of ultrasonic transducers and receivers spaced along the tool. Pulses of ultrasound is emitted by the transducers and are recorded by the receivers. The standard tool measures the first arrival time of the compressional waves. The travel time difference is dependent upon many factors, including rock matrix type, porosity and connectivity of pores (Rider, 1996). The effects of the sound waves travelling through the drilling mud can be removed by comparing first arrival times of the signal to two receivers, the difference between the two is the sonic travel time between the two receivers. Movement of the tool during measurement is compensated for by recording two sets of times: one set for a transducer at the top of the tool and receivers lower down, and the other set with a transducer at the bottom of the tool and receivers higher up. Through the use of local calibration, sonic transit time-porosity transforms have been produced for many lithologies. These transforms will be discussed in Section 1.4.2.

The formation density log or gamma-gamma is another type of porosity log. Essentially the tool measures electron density of the rock. A radioactive source bombards the rocks with medium-high energy (0.2-2.0MeV), collimated gamma rays. The denser and less porous a rock, the more gamma ray energy will be absorbed by the electron cloud due to Compton scattering (for an explanation see Rider, 1996) and fewer scattered gamma rays will return to the detector in the logging tool. This log allows the electron density in the formation to be measured, and hence density of the subsurface rock to be estimated. Porosity can be calculated using the bulk density estimate provided values of fluid density and matrix density can be estimated. The rocks are calibrated using limestone saturated in fresh water. The ratio of electron density to bulk density depends on the ratio of atomic number to atomic weight, and so will be different for other pore fluids and matrix mineralogies.

The neutron logging tool has a radioactive source that bombards the rocks with fast neutrons with a typical energy of 4MeV (Rider, 1996). If a fast neutron collides with particles heavier than itself, it is scattered elastically, losing

only a small amount of their energy. If the fast neutron collides with a particle of similar mass, i.e. a hydrogen nucleus, the neutron is scattered, losing significant amounts of its energy to the hydrogen nucleus. The neutrons are reduced to thermal and epithermal states in consequent collisions, but collisions of neutrons with hydrogen nuclei are always associated with greater levels of energy loss. Eventually an epithermal neutron will be absorbed into the nucleus of a larger element, releasing a gamma ray of capture. Thus the higher the concentration of hydrogen, the higher the rate of neutron retardation. The neutron tool may detect thermal or epithermal neutrons or the gamma rays of capture. The log essentially measures the hydrogen index of the formation, from which the porosity can be calculated. This measurement measures both free and bound water within the mineralogic structure. The logs are calculated in terms of limestone porosity units assuming that the rocks are saturated in fresh water.

1.4.2 Porosity estimation using the sonic log

Wyllie *et al.* (1956) produced a simple algorithm for the estimation of porosity from the sonic transit time:

$$\phi = \frac{\Delta t - \Delta t_{ma}}{\Delta t_{fl} - \Delta t_{ma}} \tag{1.29}$$

where Δt is the measured sonic transit time, and Δt_{ma} and Δt_{fl} are the matrix and fluid transit times, respectively. This equation was built based on the assumption that all sediments are formed of closely packed spherical grains. Wyllie *et al.* (1956) stated that this transform should be used with care and in the knowledge that the assumptions on which the equation was based were unreasonable. The equation was modified to include a factor termed the correction factor, C_p, (Schlumberger, 1989):

$$\phi = \frac{1}{C_p}\frac{\Delta t - \Delta t_{ma}}{\Delta t_{fl} - \Delta t_{ma}} \tag{1.30}$$

Raymer *et al.* (1980) produced two transforms following the interpretation of sonic log and density log trends in sandstones. The first included terms describing the bulk and matrix densities, ρ and ρ_{ma}, respectively, of the formation and the sonic transit times

$$\phi = 1 - \left(\frac{\Delta t_{ma}}{\Delta t}\sqrt{\frac{\rho}{\rho_{ma}}}\right)^{\frac{1}{1.9}} \tag{1.31}$$

and the second describes the porosity solely in terms of sonic transit times

$$\frac{1}{\Delta t_{ma}}\phi^2 + \left(\frac{1}{\Delta t_{fl}} - \frac{2}{\Delta t_{ma}}\right)\phi - \frac{1}{\Delta t} = 0 \tag{1.32}$$

These transforms have limited use as they were solely calibrated using data from sandstones. There is no physical model underlying these equations since they have been created empirically (Raiga-Clemenceau *et al.*, 1988).

Raiga-Clemenceau *et al.* (1988) suggested that first arrival acoustic waves are transmitted solely through the grains of a rock, avoiding pore spaces. This lead to the formulation of a sonic-porosity transform similar to the inverse of equations describing the transmission of electric currents through porous media (Chapman, 1981):

$$\phi = 1 - \left(\frac{\Delta t_{ma}}{\Delta t} \right)^{\frac{1}{x}} \tag{1.33}$$

This equation does not apply to gas-filled sediments (Hansen, 1996a). It is important to note that this relationship was originally calibrated empirically using data from sandstones and limestones (Raiga-Clemenceau *et al.*, 1988).

Other equations relate porosity with sonic transit time or velocity together with many other factors. Eberhardt-Phillips *et al.* (1989) suggested that effective stress and clay content of sandstones, as well as porosity, controlled seismic velocity. However, Raiga-Clemenceau *et al.* (1988) concede that much disappointment has arisen regarding the accuracy of porosity determinations made from sonic transit time measurements. They suggest that this disappointment may be due to the lack of adequate interpretive models and relevant transform models.

It is important to note that all the above transforms have been defined for sandstones. The use of these equations for the estimation of mudstone porosity is based on the assumption that sound is propagated through mudstones in an identical way to the way it is propagated through sandstones. This may not be the case (Rider, 1996). Vernik & Liu (1997) show that the sonic velocity of mudstones is highly anisotropic; therefore the overall sonic velocity of mudstones will depend upon the dip of their beds as well as porosity, effective stress, mineralogy and clay fraction.

Several attempts have been made to calibrate Equations 1.29 to 1.33 for mudstones. Some of these are generic in approach, (e.g. Rider, 1996; Ellis *et al.*, 1988). Others have been locally based (e.g. Hansen, 1996a; Issler, 1992; Brigaud *et al.*, 1992). Hansen (1996a) used mudstone porosity estimated from density logs, calibrated by samples from the wells in the Norwegian Shelf (see next section), to calibrate Equations 1.30 and 1.33, yielding

$$\phi = \frac{\Delta t - 59.0}{204.1} \tag{1.34}$$

and

$$\phi = 1 - \left(\frac{76.5}{\Delta t} \right)^{\frac{1}{1.17}} \tag{1.35}$$

Brigaud *et al.* (1992) suggested, after analysis of data from the North Viking Graben, North Sea, that the form of Wyllie *et al.'s* (1956) transform should be:

$$\phi = \frac{\Delta t - 71}{118} \tag{1.36}$$

Issler (1992) measured the sonic velocity of core plug samples of mudstone from the Beaufort-MacKenzie Basin and the MacKenzie Corridor. He calibrated Raiga-Clemenceau *et al.'s* (1988) relationship to yield

$$\phi = 1 - \left(\frac{67.1}{\Delta t}\right)^{\frac{1}{2.19}} \tag{1.37}$$

In all these cases, sonic transit time is stated in oilfield units, μs ft^{-1}.

These sonic transit time-to-porosity transforms are shown in Figure 1.3, together with indications of Raymer *et al.'s* (1980) sonic-porosity relationship calibrated using estimates of matrix and fluid transit times of 71μs ft^{-1} and 189μs ft^{-1}, respectively.

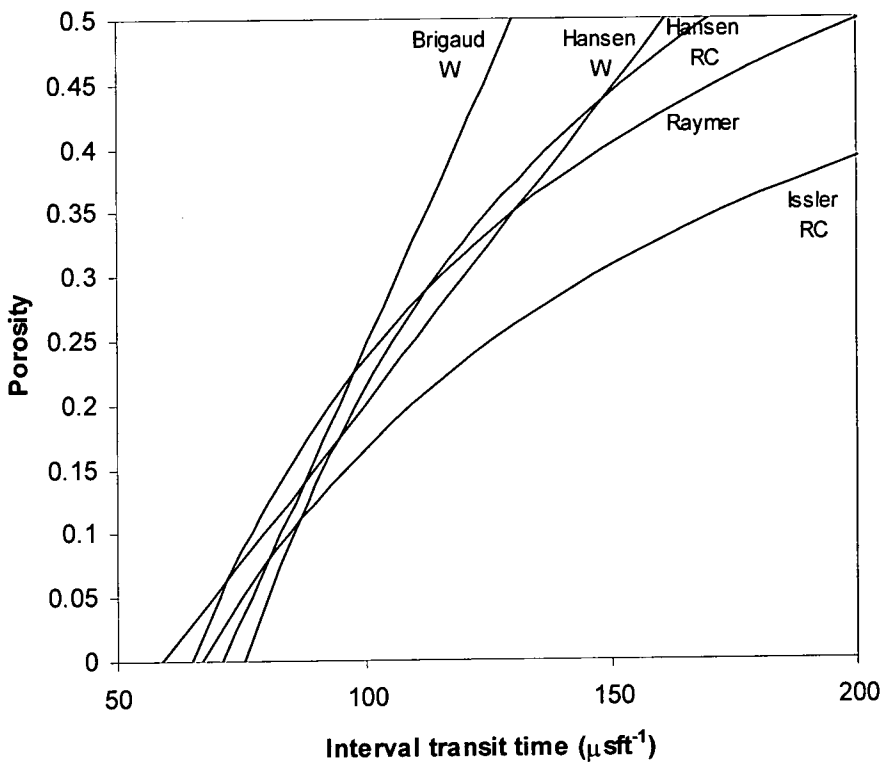

Figure 1.3 - Variation in sonic transit time-porosity transforms (W - Wyllie et al. (1956), RC - Raiga-Clemenceau et al. (1988) and Raymer (1980) transforms, Calibrated by Brigaud et al. (1992), Issler (1992) and Hansen (1996a)).

The variation in transforms reflects the different porosity ranges used during calibration, the different methods of calibration and the wide range of lithologies classified as shales or mudstones. Clearly, local calibration is necessary when the sonic log is used to provide porosity data.

1.4.3 Porosity from the density and neutron logs

The density-porosity transform algorithm is less controversially defined than the sonic transforms:

$$\phi = \frac{\rho - \rho_{ma}}{\rho_{fl} - \rho_{ma}} \tag{1.38}$$

where the density of the fluid, ρ_{fl}, is taken to be from 1.005g cm^{-3} (Rider, 1996) to 1.05g cm^{-3} (Hansen, 1996a) for brine and the matrix density, ρ_{ma}, is measured from core and cuttings samples or is estimated. Frequently the porosity estimated from the density log is cast in terms of limestone porosity units, using a matrix density of 2.71g cm^{-3} (Rider, 1996).

The neutron porosity log is measured in limestone porosity units (e.g. Schlumberger, 1989). The neutron porosity measurements of mudstones are up to 30% higher than the estimates derived from the density log or the sonic log. This is due to the neutron log measuring bound water as well as free water (Rider, 1996). Since the amount of bound water varies from mineral to mineral (Rider, 1996), it is difficult to use this log for porosity estimates in mudstones.

1.4.4 Lithology from wireline logs

The gamma ray log has frequently been used as a proxy for clay content (Rider, 1996), with the assumption that high gamma ray measurements are indicative of high concentrations of clay minerals. This is not strictly true, as high potassium and thorium estimates from a spectral gamma ray log are more indicative of high clay mineral concentrations (Quirein *et al.*, 1982). The ratio of potassium to thorium measured in a rock is thought to be indicative of the rock's mineralogy (Quirein *et al.*, 1982). Uranium behaves as an independent geochemical constituent in sedimentary rocks (Rider, 1996). It has been connected to depositional setting (Adams & Weaver, 1958). All these methods of lithological analysis are highly empirical, often based on local normalisation (Rider, 1996).

If both neutron and density logs are available, the difference between porosity estimates, when both are produced in limestone porosity units, will give a measure of the bound water content of the rock. This gives a measure of the clay content of the rock (Asquith & Gibson, 1982).

1.5 Deviation of porosity trends from normal compaction curves

1.5.1 Introduction to pressure estimation

There are three major methods for relating wireline log data to pore fluid pressure (Traugott *et al.*, 1999): empirical, deterministic and numerical models. Empirical models include that of Eaton (1972) and the Equivalent Depth Method (Rubey & Hubbert, 1959). Deterministic methods include the use of the clay fraction dependent compaction curves defined by Aplin *et al.* (1995) and Yang & Aplin (2000) described in this set of case studies. The numerical approaches combine the estimation techniques from wireline logs together with basin modelling techniques (Heppard *et al.*, 1998; Traugott *et al.*, 1999).

All of these models for the estimation of pore fluid pressure assume that if porosity ceases to decrease with increasing depth, it is associated with the onset of overpressure. This is only true if lithology remains constant over the depth interval of interest (Aplin *et al.*, 1995) and disequilibrium compaction is the sole mechanism responsible for overpressure generation (Bowers, 1994).

1.5.2 The empirical methods

Rubey and Hubbert (1959) observed that the onset of overpressure was frequently matched with a change in trend of the sonic velocity and density logs within mudstone sections. The procedure is outlined in Figure 1.4.

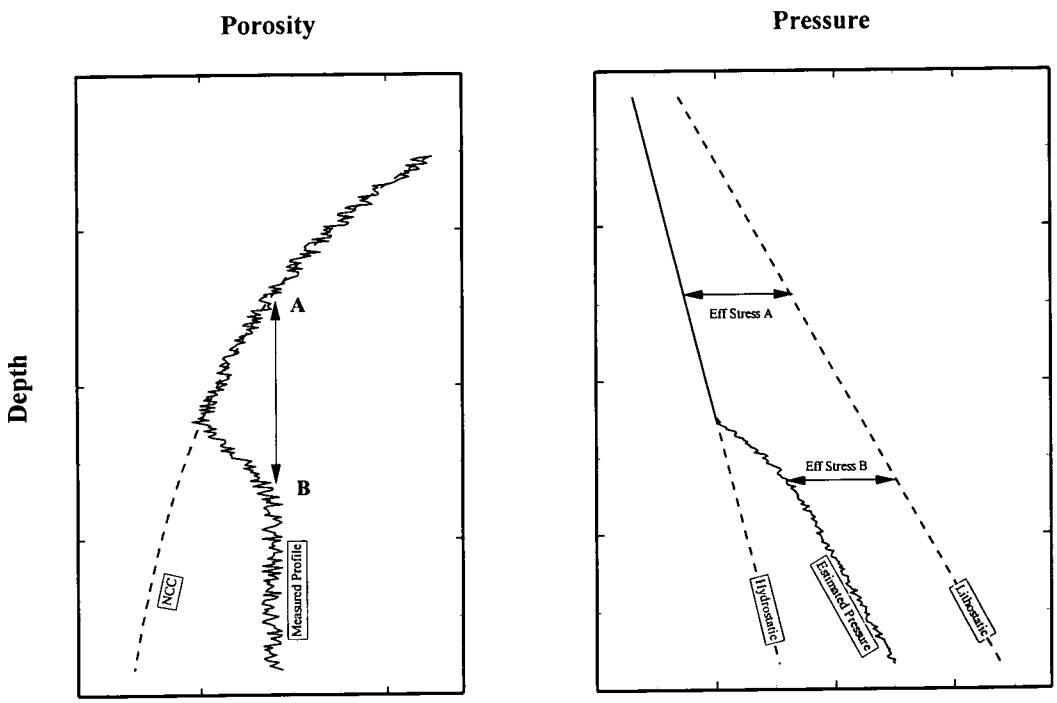

Figure 1.4 - Cartoon showing the principle of the equivalent depth method.
Porosity is an indication of any proxy for porosity, such as bulk density or sonic transit time.

Compaction trends are defined in the upper sections of wells, where the pressure is assumed to be hydrostatic. Pressure is assumed to be abnormal where the proxy for porosity deviates from this trend. Points in the well with equal porosity, such as A and B in Figure 1.4, are assumed to be at equal effective stress levels. Subtracting the estimate of effective stress from the overburden produces a pressure estimate.

Eaton (1975) formulated a direct pressure estimation algorithm from locally defined compaction curves using resistivity and sonic logs.

$$P' = s'_v - \left(s'_v - P'_{hyd}\right)\left(\frac{R_{obs}}{R_n}\right)^{1.2} \tag{1.39}$$

for resistivity and

$$P' = s'_v - \left(s'_v - P'_{hyd}\right)\left(\frac{\Delta t_{obs}}{\Delta t_n}\right)^{3.0} \tag{1.40}$$

for sonic transit time, where P' is pore fluid pressure, s'_v is lithostatic pressure, P'_{hyd} is hydrostatic pressure, R_{obs} and Δt_{obs} are observed resistivity and sonic transit time, and R_n and Δt_n are the expected values of resistivity and transit time taken from locally defined trends.

Provided the overburden and normal compaction trends are locally known, these pressure estimation methods are potentially robust and, indeed, they are used commonly as methods for pressure estimation (Mouchet & Mitchell, 1989). They are not applicable for use in areas where little is known about the normal compaction trend of sediments, for example in deep water areas, where overpressure frequently occurs at depths below 500m below the seafloor (Traugott *et al.*, 1999).

1.5.3 Deterministic models

The clay fraction dependent compaction curves derived by Aplin *et al.* (1995) and Yang & Aplin (2000) allow for direct estimates of pressure from wireline log data provided accurate estimates of lithology, porosity and overburden are available. This is done by producing an estimate of effective stress using Equation 1.9 calibrated with Equations 1.10 and 1.11 or Equations 1.12 and 1.13. This effective stress estimate is subtracted from overburden to provide an estimate of pressure. These methods are reliant upon accurate estimates of porosity and the selection of the correct compaction relationships.

1.5.4 Failure of pressure estimation from wireline logs

The models described above rely upon porosity solely affecting response of the density, resistivity and sonic logs. This is not the case (Rider, 1996; Eberhardt-Phillips *et al.*, 1989). Hermanrud *et al.* (1998) have observed that porosity estimates from the density and neutron logs taken in mudstones of the Jurassic Not Formation in the Haltenbanken region differ significantly from those estimated using the sonic and resistivity logs. They suggest that this deviation is due to the resistivity and sonic logs responding to overpressure as they discount the effect of mineralogical change. The rocks that they studied are also old (Jurassic in age) and deeply buried (>4.4km), and hence are at a correspondingly high temperature (in excess of 130°C assuming a thermal gradient of 30°C m^{-1}). At these temperatures and ages, it is likely that chemical compaction processes will have taken place (Schneider *et al.*, 1996). Goulty (1998) suggests that the mismatch between pressure estimates measurements is due to an unloading mechanism such as pressure transference.

Bowers (1994) observed that in some cases, the traditional methods of pressure estimation underestimated the actual pore fluid pressure in a formation. He ascribed this to fluid expansion phenomena such as aquathermal pressuring (Barker, 1972), hydrocarbon maturation (Spencer, 1987) and fluid expulsion and expansion during clay mineral diagenesis (Powers, 1967; Bruce, 1984). He produced an empirically modified version of Eaton's (1975) relationship between sonic velocity and effective stress accounting for these fluid expansion phenomena. Burrus (1998) continued with this work in terms of basin modelling, suggesting that some of the mismatch between traditional mechanical basin modelling is due to unloading effects brought on by fluid expansion.

Burrus (1998) also suggested the use of a 'Biot' (1941) coefficient in the Terzaghi (1923) effective stress law, thus:

$$\sigma = s_v - \alpha P \tag{1.41}$$

where α is termed as the 'Biot' coefficient which was determined empirically. Goulty (1998) stated that the use of a 'Biot' coefficient was physically questionable and suggested the use of mean effective stress as the control on the compaction of porous media. This suggestion was carried out by Harrold *et al.* (1999) in studying some sonic velocity data from S E Asia where it seemed that it was impossible to match measured sandstone pressures and mudstone pressures estimated using sonic derived porosity and vertical effective stress based compaction relationships. The use of mean effective stress based compaction relationships indicated that the mudstones and sandstones pressures were in equilibrium.

1.5.5 Estimation of exhumation associated with major unconformities

Major unconformities are typically associated with abrupt reductions in apparent porosity. This abrupt change in wireline characteristics may be due to lithologic change, (Aplin *et al.,* 1995), but it also may be due to over consolidation due to deep burial followed by exhumation and incomplete reburial (e.g. Bulat & Stoker, 1987).

Sediment compaction is primarily an irreversible process (Karig & Hou, 1992). If load is removed from a body of sediment, porosity will increase elastically, but this increase is very small in comparison to the porosity reduction during loading (Karig & Hou, 1992). Thus provided, for example, that fracturing does not affect the acoustic properties of the rock, the wireline properties of the formations will remain largely unaffected by exhumation (Bulat & Stoker, 1987). Assuming that the elastic dilatation is zero, the sediments normally pressured and well drained, and the compactional behaviour of the sediment is understood, the amount of apparent exhumation can be calculated simply by comparing expected wireline log response with observed response. This process is shown in the upper part of Figure 1.5. The total amount of erosion is the apparent exhumation, E_A, added to the depth of the observed unconformity.

On reburial, the exhumed section's compaction trend approaches the normal compaction trend. When the load on the sediment equals the original load, the exhumed sediments start to compact along the normal compaction trend, and wireline log evidence for exhumation may be lost, unless there is a marked facies change across the unconformity.

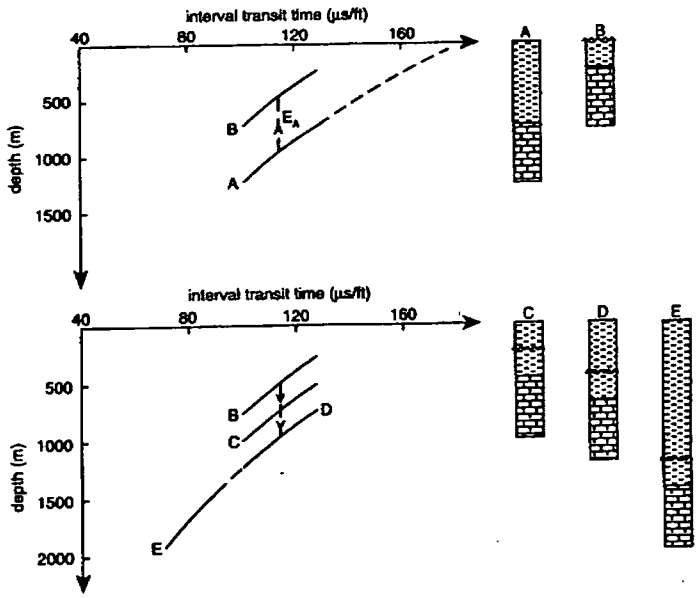

Figure 1.5 - Cartoon indicating compaction processes involved in exhumation and subsequent burial (from Hillis, 1995).

The situation in overpressured or closed systems, where overall permeability of the rocks is low enough to inhibit fluid flow, is more complicated. Luo & Vasseur (1995) suggest that if the rocks are perfect seals, effective stress remains constant, and so underpressure can result if there is enough exhumation. However, others suggest that pore pressure remains constant through exhumation (Iliffe, 1999). This seems unlikely. There are suggestions that the fluid composition of the exhumed rocks will affect the pressure history of the formation during the exhumation process (Katahara & Corrigan, 1998).

1.6 Artificial neural networks

1.6.1 Introduction

> *'What does the reader do when he wishes to see in what the precise likeness or difference of two objects lies? He transfers his attention as rapidly as possible, backwards and forwards, from one to the other. The rapid alteration of consciousness shakes out, as it were, the points of difference or agreement, which would have slumbered forever unnoticed if the consciousness of the objects compared had occurred at widely distant periods of time. What does the scientific man do when he searches for the reason or law embedded in a phenomenon? He deliberately accumulates all the instances he can find which have any analogy to that phenomenon; and by simultaneously filling his mind with them all, he frequently succeeds in detaching from the collection the peculiarity which he was unable to formulate in the one alone; even though that one had been preceded in his former experience by all those with which he now at once confronts it.'* - James (1890)

Artificial neural networks are collections of simple processing units interconnected in a similar fashion to the way nerve cells are connected in organic brain tissue (Beale & Jackson, 1990). These networks are commonly thought of as methods for pattern recognition (Kohonen, 1988). There are several algorithms that can be used including multi-

layer perceptrons (McClelland & Rumelhart, 1986), self organising networks, (Kohonen, 1990) and adaptive resonance networks (Carpenter & Grossberg, 1988). The first of these algorithms is described below and full descriptions of the latter two, and other, algorithms are given by Beale & Jackson, (1990) and Dowla & Rogers (1995).

ANN's are objective data analysis tools which enable data driven models to be developed completely without bias from the operator. Since no *a priori* choice of underlying mathematical model is required, they can be thought of as initial model-free multiple non-linear regression tools (Huang *et al.*, 1996). In this sense ANN's are very useful for handling complicated problems with very many inputs and highly complicated inter-relationships between input and output data. Dowla & Rogers (1995) claimed that ANN's are very good at making generalisations and that they are robust when faced with noisy data.

The basic processing units of a neural network, called neurons or nodes, accept many numeric inputs, and calculate a single numeric output based on a selected transfer function of the inputs and a selection of typically multiplicative weights, outlined in Figure 1.6.

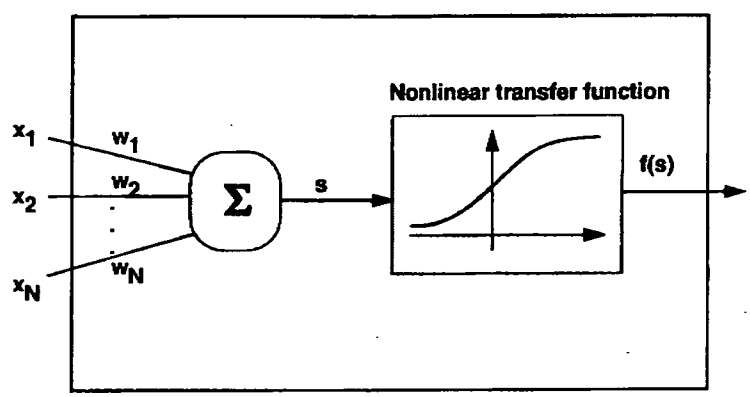

Figure 1.6 - Functional representation of a single neuron (from Dowla & Rogers, 1995).

A typical transfer function used in the neuron is the sigmoid function

$$f(s)=\frac{1}{1+e^{-s}} \tag{1.42}$$

where s is the weighted sum of the n inputs to the neuron

$$s=\sum_{i=1}^{n} w_i x_i \tag{1.43}$$

where x and w are the inputs and weights, respectively. In order to make these neurons useful, training data are presented to the neuron, the neuron's output is compared to the desired output and the weights are adjusted in order to reduce the error in neuron output.

Single neurons can only handle very simple processes, such as logical AND and logical OR operations (Beale & Jackson, 1990). Combinations of neurons are able to tackle more complicated problems. The combination used in

this set of case studies is the multi-layer perceptron (Rumelhart *et al.*, 1986), in which the neurons are arranged in layers, with the n^{th} layer providing its outputs as the inputs to the $n+1^{th}$ layer, shown in Figure 1.7.

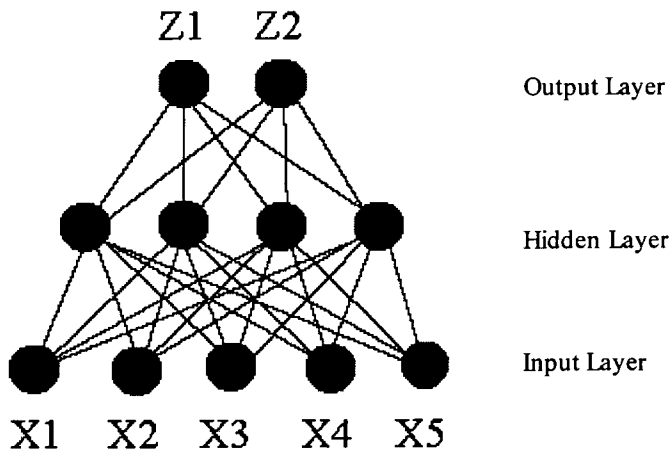

Figure 1.7 - The multilayer perceptron.

The hidden and output layers are calculative layers. A network with a single hidden layer of two neurons and a single output neuron is capable to perform the logical exclusive OR operation (Beale & Jackson, 1990). The inclusion of further hidden layers and/or further neurons will enable the network to complete more complicated tasks.

1.6.2 The backpropagation of errors training algorithm

The method to determine the optimum values of each weight in a network is not trivial. A full derivation of the algorithm is shown in Appendix A. The training process is iterative. Initially the input weights are set to random values. Each training example data vector is presented to the network and the network's output is compared to the desired value. All the weights are systematically modified so as to minimize the network output error. Once the network can solve a problem with a very large set of examples, the assumption is that the network can generalise from these examples to previously unseen data, or test data.

A key problem that must be avoided during the training of a network is referred to as overtraining. Overtraining occurs when it is assumed that the examples used are noise free and the network is forced, by continued exercise of error minimisation, to make the output error very small. Overtraining of the network can be avoided by using a large, well distributed set of examples and by comparing the performance of the training and testing events. When the test results are as good as the training set results, the network is assumed to have reached an optimum training state.

1.6.3 Geological, geophysical and petrophysical uses of artificial neural networks

The multi-layer perceptron model, coupled with a backpropagation learning algorithm similar to that discussed in section 1.6.2, has been used frequently in geoscientific research (Dowla & Rogers, 1995).

Rogers *et al.* (1992) used a simple 2-layer ANN to estimate lithology from standard wireline logs. This lithological variation was between dolomite, limestone, sandstone and shale. They used a limited number of training data taken from the expected wireline log values of the lithologies stated by Asquith & Gibson (1982). The output from the neural network was successfully validated by cuttings data from the well.

Huang & Williamson (1996) used ANN modelling to characterise source rocks using wireline log data. They produced an ANN derived estimate of total organic carbon content. Their results, although noisy, were very close to measured values of TOC. They then used the trends of the output to produce geological histories based on organic carbon preservation.

Huang *et al.* (1996) produced an ANN based method for the determination of sandstone permeability from wireline log data. They highlighted the need for comprehensive training datasets over the entire ranges of input and required output values, but they produced a very good first order estimate of permeability very quickly.

Luthi & Bryant (1997) used ANN's to provide assistance in well log correlation. This work highlighted the applicability of the technique to analysis of time (or depth) series. Benaouda *et al.* (1999) inferred the lithology of downhole rock by using ANN's presented with wireline log data. They compared their results with results from traditional lithology inference techniques such as cluster analysis and principal component analysis.

FitzGerald *et al.* (1999) trained ANN's using wireline data together with fracture density measured from borehole televiewer data to estimate fracture density from standard wireline log data. They observed that the ANN's performed well distinguishing between noise (drilling induced fractures) and true phenomena (natural fractures).

1.6.4 Application of the backpropagation algorithm to lithological identification

The use of artificial neural networks in this study is based upon the work of Aplin *et al.* (1999). They have created a set of neural networks that are able to estimate mudstone clay fraction, total organic carbon and grain density using standard wireline log data including density, sonic, resistivity, caliper and gamma ray logs. The method is described in Chapter 2 These grain density estimates are used to calibrate density logs to provide an accurate estimate of porosity and hence void ratio. The clay fraction estimate is used to select which compaction curve to use in the pressure analysis. This analysis enables the use of Yang & Aplin's (2000) and Aplin *et al.'s* (1995) compaction curves to their best effect.

1.7 The thesis

The aim of the thesis was to test the validity of generic compaction models in the context of pore pressure estimation.

The approach taken to meet this aim was as follows:

- Standard pressure estimation and lithological evaluation techniques, discussed in the remainder of this chapter were applied to wireline data. The resulting lithological evaluation and pressure estimates were

compared to measurements made downhole. It was noted if the methods failed to produce acceptable results. These performance failures of standard techniques formed the basis of the continuing research.

- Generic compaction models were selected and tested in order to find the one most suitable for the situation.
- Measurements of the physical characteristics of mudstones were collected to support the use of, and calibrate, the chosen generic model(s).
- Where possible, the generic compaction models were used to provide geological explanations of the observed porosity and pressure profiles in each well studied.
- The generic models were tested with data from different, geographically diverse basins to test their performance when presented with data taken from mudstones of variable lithology and mineralogy, age, depth and temperature.
- Throughout the analytical process the analysis toolkit available for the processing of wireline data was evaluated and new tools were developed where necessary.

Data from three areas were provided. These comprised data from the Gulf of Thailand, the Gulf of Mexico and the Everest and Lomond fields of the UK sector of the Central North Sea. The challenges that were met when using these data sets were diverse:

Gulf of Thailand

- There are no published pressure and mudstone data derived from the area.

Gulf of Mexico

- No porosity logs were run in the shallow, hydrostatically pressure section of any wells so local calibration of porosity log-based pressure algorithms was not possible.
- Sharp transition zones were observed in the overpressured sections of two wells so detailed pressure and lithology profiles were required for analysis.

Central North Sea

- It is uncertain whether overpressure is present in the Tertiary section of the wells studied. Porosity changes in the section may be due to changes in effective stress or lithology.

The key findings of the research were:

Error analysis

- The generic compaction model used in the thesis can provide estimates of pressure direct from wireline bulk density measurements within a required tolerance of up to an equivalent pressure gradient of ±0.5 pounds per US gallon (up to ±1.77MPa at a depth of 3km).

- Significant errors are likely to occur if an unsuitable compaction or overburden model is employed during pressure analysis.

Wireline log data visualisation

- *ColourLog*, an original software package for Microsoft Windows was created. This software enables the visualisation of three sets of time series data by combining them into a single strip of colour.

Gulf of Thailand

- The origin of overpressure in the area is disequilibrium compaction.

- A set of 25 mudstone samples was fully characterised.

- The sediments in the lower section of both wells examined were overconsolidated.

- This overconsolidation suggests that the wells have undergone uplift and reburial.

Gulf of Mexico

- Locally calibrated resistivity-based methods did not give reliable pressure estimates at depth.

- Generic compaction models produced estimates of pressure in mudstone that were in accord with pressure measurements in associated sandstones when provided with lithological information using neural networks.

- One of the pressure transition zones could be explained by an apparent reduction in grain size on the mudstones within the transition zones.

Central North Sea

- The quality of the wireline data is suspect due to the influence of a gas cloud on the sonic log data taken from the post-Palaeocene sediments in the Lomond area. Thus the original aims of the case study have not been met, and no conclusions can be made about the nature of the pressure profile in the Tertiary section of the area.

- Twenty-six mudstone samples were characterised, yielding a range of matrix density values from 2.64g cm^{-3} to 2.92 g cm^{-3} and a range of clay fraction measurements from 40% to 65%.

2 GENERIC METHODS

2.1 Introduction

2.1.1 Chapter summary

This chapter describes the generic methods used in initial analysis of the wireline logs during sample selection, initial pressure analysis, laboratory analysis of samples and further data analysis techniques used throughout the case studies. The initial wireline analysis was performed using standard petrophysical techniques. Laboratory analysis of the shale samples comprised a mixture of standard soil mechanics-based tests, automated methods calibrated to standard methods and some techniques developed by Yang and Aplin (1997). Several data analysis techniques were used to produce a range of lithological information from all available wireline and sample data: notably multivariate linear regression and artificial neural network techniques.

2.1.2 Aims

The aims of this chapter are to outline the general petrophysical, geological, laboratory and numerical techniques used to perform the lithological analysis on wireline log data and rock samples required for the detailed pressure analyses presented throughout this work.

2.2 Initial wireline analysis

2.2.1 Pre-processing data

The wireline data used in the study were provided in digital form and, in some cases, paper composite log form. The paper format was useful for quick look checks for data availability and quality. Checks were made that different sized tools from different logging runs were producing comparable measurements of the data required; also it could be ensured that no obvious unwanted logging effects such as cycle skipping of the sonic log as described by Rider (1996) were present. The depth range over which each tool was run was noted either from the paper logs or the accompanying drilling reports.

Histograms of the gamma ray logs from each well were produced in order to estimate a 'shale line' (Rider, 1996) over various intervals. These were then used to ascertain an approximate indication of shale-rich strata, termed wireline shales, assuming that each region examined contains a reasonably constant clay mineralogy. This assumption is necessary as gamma ray readings are functions of thorium, potassium and uranium concentration in the surrounding formation. Many clay minerals are rich in potassium and thorium is very often associated with them as well (Rider, 1996); however, potassium feldspars are also associated with high gamma ray measurements, so it is important to use locally calibrated shale lines, derived at least from detailed examination of the logs and at best from laboratory examination of material taken from the well to make a first order distinction between wireline sands and shales.

Sections of the wells were identified where log characteristics remained constant for at least 10m and where the gamma ray was sufficiently high to indicate the presence of shale. The constant wireline response in these regions is assumed to be due to a single lithology. Shale samples were taken in core, sidewall core and cutting form, whichever was available, from these sections of the wells.

Where a full wireline dataset was available, including neutron and density logs, a matrix inversion method similar to that suggested by Doveton (1992) was used to identify the lithology at each depth point using multiple log characteristics. This method assumes that the entire lithologic section sampled by the wireline log measurements consists of mixtures of only a few lithologies and that wireline response is due to the mixing of lithologies. Thus, for a three phase system of sand, shale and water, measured by gamma ray and density tools:

$$\gamma = \gamma_{sand} v_{sand} + \gamma_{shale} v_{shale} + \gamma_{water} \phi \tag{2.1}$$

$$\rho = \rho_{sand} v_{sand} + \rho_{shale} v_{shale} + \rho_{water} \phi \tag{2.2}$$

$$1 = v_{sand} + v_{shale} + \phi \tag{2.3}$$

where γ, γ_{sand}, γ_{shale} and γ_{water} are the gamma ray readings of the whole rock, sand matrix and shale matrix and water, respectively, ρ, ρ_{sand}, ρ_{shale} and ρ_{water} are the bulk density, matrix densities and fluid densities, and v_{sand}, v_{shale} and ϕ are volume fractions of sand, shale and porosity. The gamma ray and density properties of the various phases can be taken from standard assumed values or determined empirically from the logs. Equations 2.1-2.3 can be written in matrix form as

$$\begin{pmatrix} \gamma \\ \rho \\ 1 \end{pmatrix} = \begin{pmatrix} \gamma_{sand} & \gamma_{shale} & \gamma_{water} \\ \rho_{sand} & \rho_{shale} & \rho_{water} \\ 1 & 1 & 1 \end{pmatrix} \begin{pmatrix} v_{sand} \\ v_{shale} \\ \phi \end{pmatrix} \tag{2.4}$$

and thus

$$\begin{pmatrix} v_{sand} \\ v_{shale} \\ \phi \end{pmatrix} = \begin{pmatrix} \gamma_{sand} & \gamma_{shale} & \gamma_{water} \\ \rho_{sand} & \rho_{shale} & \rho_{water} \\ 1 & 1 & 1 \end{pmatrix}^{-1} \begin{pmatrix} \gamma \\ \rho \\ 1 \end{pmatrix} \tag{2.5}$$

and, provided the inverse of the rock property matrix can be calculated, an estimate of the rock proportions can quickly be made direct from the wireline readings. This method is an extension of the crossplot methods suggested by Asquith & Gibson (1982) and has the advantage that several logs can be used together to produce estimates of many more than two solid phases. A caveat is that many log responses are not linear in nature, so these calculations are merely estimates of lithology.

2.2.2 Determination of overburden

Since the overburden pressure gradient is controlled by grain and fluid density and the volume fractions of each constituent, several overburden curves were calculated for each well. In sections where the density log was available, this was used to derive the overburden. Where the density log was unavailable, several techniques were used:

- Local curves derived from density logs from local offset wells.
- Regional compaction curves, where available, such as those derived by Fertl & Timko (1972).
- Pseudo density logs derived using other logs.
- Basin modelling techniques.

2.2.3 Preliminary pressure analysis

Several pressure estimation techniques were used, some quick look using the entire wireline data for wireline shales, others using picked data from the wireline logs. Most of these techniques involved the estimation of porosity from wireline, others (e.g. Eaton, 1975) used raw wireline data to produce direct pressure estimates. The porosity methods involved the definition of a normal compaction curve or set of normal compaction curves and the use of an equivalent depth or equivalent effective stress method to estimate effective stress and hence pore pressure. Comparison with direct pressure measurement was made where possible.

Initial estimates of porosity were made from all available porosity logs. Those estimates using the density log required the assumption of a variable mudstone grain density ranging from 2.5g cm^{-3} to 2.9g cm^{-3} and a water density of 1.01g cm^{-3} (Rider, 1996). Porosity estimates using the sonic log were performed using Hansen's (1996a) calibration of the time average equation suggested by Wyllie *et al.* (1956), which was further adjusted by Schlumberger (1989), and both Issler's (1992) and Hansen's (1996a) calibrations of the acoustic formation factor relationship proposed by Raiga-Clemenceau *et al.* (1988). Several estimates of porosity were made in each well, as the porosity estimates were not calibrated, so the provision of a range of possible porosity estimates was advisable.

Two whole-log porosity-effective stress methods were used. The first relied on the assumption that the upper section of the sediment in each well was normally pressured. This section was used to define a normal compaction curve for the well. The second involved the use of the clay fraction dependent compaction curves established by Yang & Aplin (2000). These compaction curves were compared to the upper, assumed normally pressured section of the porosity curves, and the best fitting curve was used as the compaction curve for the entire logged interval. As discussed in Chapter 1, the use of monolithological compaction curves is not the most accurate method for pressure estimation, since there may be major lithological change with depth within an overpressured section. Furthermore, the shallow section of a well may not be normally pressured (Traugott *et al.*, 1999). Harrold's (2000) picking strategy was used to produce a set of wireline shales with known gamma ray value and porosity throughout studied wells. The gamma ray log was used as a lithological discriminant and the dataset was used to produce separate compaction curves for various gamma ray ranges both by the mathematical curve fitting algorithm and by

comparison with the soil mechanics compaction curves. In all cases, deviation away from these compaction curves could be used to infer abnormal pore fluid pressure. They could then be used together with an equivalent depth algorithm to infer *in situ* effective stress and pore pressure.

Eaton's (1972) method was used to derive pressure from the resistivity and sonic logs independently. Again, this depended upon the assumption that the upper section of the logged interval was normally pressured and that there was no vertical lithological variation. The calculation of pore pressure using this technique consists of a direct transform from wireline log response to pore pressure.

Wherever possible multiple methods for estimating any property of the mudstones were used in order to gain an insight into the uncertainty of the estimate.

2.3 Laboratory sample analysis

2.3.1 Pre-processing

The first major stage in pre-processing of rock samples was the selection and cleaning of mudstone samples from each depth range. In the cases of sidewall core and normal core samples, approximately 10g of the sample was taken and brushed to remove drilling mud and stored in a glass vial. The bags containing dry cuttings samples were taken and their contents were sieved using a 1mm gauge sieve and brushed gently to separate the fines from larger cuttings. The fines were discarded as they were most likely to be dominated by drilling mud and non-shale particles. The larger cuttings were taken individually, examined under a binocular microscope to check that the sample was a mudstone, brushed clean and stored in glass vials.

2.3.2 Total carbon and organic carbon content

Approximately 0.4-0.5g of each sample was ground to a powder using a mortar and pestle. 0.1g of the sample was added to a weighed ceramic crucible to be used for total carbon measurements. Another 0.1g was added to a weighed porous ceramic crucible to be used for organic carbon analysis. The remaining sample could be used to perform replicate analyses. Both crucibles containing sediment were weighed. Approximately 5ml of concentrated (5Mol) hydrochloric acid was added to the sediment in the porous crucible to remove all carbonate from the sample. This was left for an hour. The acid was then removed by washing it away using de-ionised water and the sediment was dried in an oven. Both sets of samples were then analysed for carbon content using a Leco induction furnace connected to a Leco carbon and sulphur analyser.

2.3.3 Disaggregation

Yang and Aplin's (1997) freeze-thaw method for the gentle disaggregation of shales was used, to minimise the breakage of the sediment particles. Approximately 6g of each sample was put into metal trays, having been gently crushed so that the size of the constituent particles were less than 3mm in diameter. This sediment was covered in distilled, de-ionised water. The samples were placed into a vacuum for at least an hour to force water into as many of the pores as possible. The samples were frozen in a domestic freezer for at least 2 hours, thawed, and this process was repeated up to 10 times, until the samples disaggregated. Disaggregation could be checked by examining some

of the sample under a binocular microscope. Finally, the samples were frozen and freeze-dried. The samples were then placed in an oven to ensure that all water had been driven off.

2.3.4 Matrix density measurements

Grain density of the samples was measured using the small pycnometer method (Yang & Aplin, 1997). Approximately 3g of the sample was taken and placed into a clean, dry, weighed (m_b), 50ml density bottle. The bottle and sediment were dried at 105°C for at least 12 hours and then weighed (m_{b+s}). Some de-ionised (18MΩ) water was de-aired under a vacuum for 1-2 hours and then poured gently into the density bottle until it was full. The density bottle was put under a vacuum for a further hour to ensure that no air was dissolved in the vessel and sediment. The apparatus was then put into a water bath at a temperature of 25°C for an hour. The outside of the bottle was then dried and the bottle, water and sediment were weighed (m_{b+w+s}). The bottle was emptied, cleaned and filled with de-aired, de-ionised water, placed under a vacuum for an hour, placed in the 25°C water bath and finally weighed (m_{b+w}). The density of the sediment is given by:

$$\rho_{ma} = \rho_{w25} \frac{m_{b+s} - m_b}{m_{b+w} + m_{b+s} - m_{b+w+s} - m_b} \tag{2.6}$$

Again, if there was enough sample available, replicate analyses were performed to ascertain the accuracy of the analysis. The precision of the method was tested by measuring the density of standard samples of mudstone and quartz.

2.3.5 Grain size distribution

A gravitational settling method was used to determine grain size distribution of the sediment sample. Stokes' law (e.g. Micromeritics, 1982) states that the settling velocity of a particle in a viscous fluid is proportional to the equivalent spherical diameter of the sediment particle and the difference between the grain density of the particle and the fluid density of the viscous medium. Thus if it is assumed that all the particles in a sediment sample have the same density and that the sediment suspension is sufficiently diffuse so that interparticular interaction is minimal, it is possible to calculate those velocities. This is the basis of the sedimentation pipette method which is a standard laboratory technique for the analysis of grain size distributions of fine grained powders (British Standards, 1377, part 6, 1990). The method involves adding a known mass of sediment to an aqueous dispersant solution of sodium metaphosphate and sodium carbonate and shaking thoroughly to ensure that the suspension is as homogeneous as possible. This suspension is added to a known volume of distilled water that is held at 25°C by a large water bath. The suspension is left to equilibrate thermally so that no convection occurs and then shaken again create a homogeneous suspension of sediment. As soon as the column of sediment is returned to the vertical, a stopwatch is started. The times taken for particles of a set of diameters to fall 10cm are calculated using Stokes' law. At these times a 10ml pipette is introduced carefully into the fluid column and 10ml of the sediment suspension is removed. These samples are dried in an oven and then weighed. From these masses, the proportion of sediment with an equivalent spherical diameter less than the set diameters can be calculated. The fraction of sediment with a diameter greater than 63μm was established by sieving.

The sedimentation pipette method has several experimental drawbacks. The experiment time is long, commonly over 26 hours. It is necessary for the apparatus to be still for the entirety of the experiment so that there are no induced fluid movements. The measurement technique is invasive, as the introduction of the pipette and the removal of a significant volume of fluid will create turbulence within the fluid column.

Another gravitational sedimentation method using a Micromeritics Sedigraph 5000ET was employed. This method is far quicker than the pipette method, taking 40 minutes per sample. The fraction of the sediment with an equivalent spherical diameter less than a set amount is measured by the attenuation of X-rays, so the technique is not invasive. The sedimentation cell is ~2cm in height and its temperature is controlled so that turbulence and convection are minimised. The X-ray source and detector move relative to the sedimentation cell using precision gears and so the data acquisition can be performed speedily. The analysis provides a continuous grain size curve, rather than the discrete distribution provided by the pipette method.

Approximately 3g of sediment sample was weighed and added to 30ml of de-ionised water in a thick centrifuge tube. An ultrasonic probe was used for 30 minutes to ensure that the sample was completely disaggregated. 5ml of dispersant solution (33g sodium metaphospate and 7g sodium carbonate per litre of distilled water) was added and the sediment was transferred to a 100ml beaker. The suspension volume was made up to 50ml by adding more de-ionised water. A magnetic stirring bead was added and the beaker was placed within the Sedigraph on a magnetic stirrer to equilibrate thermally with the Sedigraph apparatus. The maximum intensity of X-rays, occurring when water and dispersant solution alone were passed through the Sedigraph cell, was measured and taken as a base line for all measurements. The cell was emptied. After 30 minutes the suspension was introduced into the Sedigraph sedimentation cell by means of a peristaltic pump. At this point the minimum intensity of the X-rays was measured and taken as the 100% level for the analysis. The pump was stopped and sedimentation was allowed to start. The variation in intensity was measured with respect to time, which was directly converted to equivalent spherical diameter by the machine. Full details of this analysis technique are available in the Sedigraph manual (Micromeritics, 1982). After the analysis, the sediment was sieved using a 63μm sieve and the >63μm fraction was weighed.

Possible sources of error in this technique are edge effects, as the sedimentation cell is narrow, less than 1cm. However, these effects are minimal under controlled conditions (Micromeritics, 1982). The major drawback is that the Sedigraph technique does not measure the same property as the pipette method. The pipette method is a mass-based method whereas the Sedigraph measures the attenuation of X-rays, which is influenced by mineralogy and density of particles. Thus the grain size distribution produced by the Sedigraph has been calibrated with data derived by the pipette method (Yang, pers. com., 2000).

2.4 Further wireline log analysis

2.4.1 Visual technique of cluster analysis of wireline log data using colour

The lithological information contained in wireline logs is often very subtle and contained in several logs at a time. The pattern recognition required to describe detailed stratigraphic variation utilises multiple log traces or cross plots of log data. If the changes in lithological character are abrupt, it is easy to visualise change using multiple logs;

however, in complex zones the subtle changes in one or more logs may be overlooked. In crossplots of data the pattern buried within the complexity of the log responses can be visualised, but the depth at which lithological change occurs is lost. One way to combine the information of the crossplot and the multiple log traces is by the use of colour.

Briggs (1985) suggested the use of the colour cube, renamed the Briggs cube by Collins and Doveton (1986), as a reference point for the representation of three logs simultaneously. This system uses normalised values of logs that are associated to the intensities of the three primary colours. The red, green and blue components are then mixed together using the same additive scheme that a computer monitor uses to produce a colour dependent upon the three input logs. Figure 2.1 shows the interaction and colour mixing within the cube. Rocks possessing similar petrophysical characteristics will therefore exhibit similar hues in the Briggs colour cube.

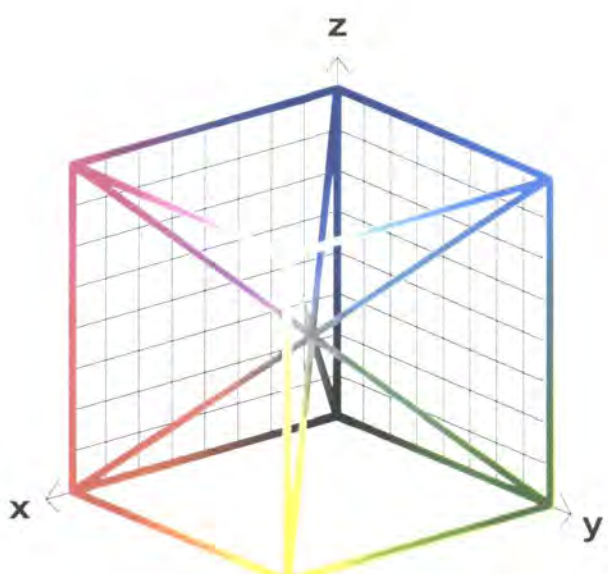

Figure 2.1 - The Briggs colour cube. The x axis coincides with the intensity of red, the y axis with green and the z axis with blue.

Doveton (1992) and Collins *et al.* (1992) provide many examples of the use of the colour cube concept including stratigraphic correlation between wells and lithological discrimination.

The program *ColourLog*, available on the accompanying CD ROM, was written by the author based on these ideas. The major difference between the algorithm by Briggs and the algorithm used in *ColourLog* is that it is possible to assign variable, non-linear colour ranges to the values of the input logs. This allowed more flexibility in the colour analysis. The program was used throughout the studies to produce pictorial representations of not only raw wireline data, but also transformed logs used in the neural network analysis described below.

2.4.2 Lithology information from artificial neural network analysis

The primary use of ANN analysis of data in this work was carried out using the program *ShaleQuant* (Yang , 1999) which is based upon work presented by Aplin *et al.* (1999). This program accepts several combinations of standard wireline logs. The data used were taken from the gamma ray, sonic transit time, caliper, medium resistivity, density and neutron logs. Where available, the density log was used to estimate porosity, assuming that the pore fluid was a saturated brine with density 1.05g cm^{-3}, where

$$\phi_\rho = \frac{2.71 - \rho}{1.66} \tag{2.7}$$

Also the resistivity, R, at T°F was transformed to calculate the resistivity of the formation at 75°F (23.89°C), R_{75}, by using by using the Arps equation (Schlumberger, 1989)

$$R_{75} = R\frac{T+7}{82} \tag{2.8}$$

The wireline data were then transformed, using the density-derived porosity, as outlined below, to calculate wireline-based parameters that are reasonably unaffected by compaction. The parameters, together with their derivations, where applicable, are shown in Table 2.1, where $C, B_s,$ and z_{SM} represent the caliper measurement, bit size and depth below the seabed in metres, respectively.

Input parameter	Derivation	Reference
Gamma Ray (γ)	-	-
Bulk density (ρ)	-	-
Matrix transit time (Δt_{ma})	$\Delta t_{ma} = \frac{\Delta t - 200\phi_\rho}{1-\phi_\rho}$	Wyllie *et al.* (1956)
Archie cementation factor (m)	$m = -\frac{\ln(10R_{75})}{\ln(\phi_\rho)}$	Rider (1996)
D log	$D = -6.906 + 3.186\log_{10}(\Delta t) + 0.487\log_{10}(R_{75})$	Meyer & Nederlof (1984)
Pseudo-bound water (BW)	$BW = \frac{\phi_N - \phi_\rho}{1-\phi_N}$	Rider (1996)
Differential caliper (ΔC)	$\Delta C = C - B_s$	-
Logarithm of depth ($z_{\log}$)	$z_{\log} = \log_{10}(z_{SM})$	-

Table 2.1 - Wireline log transformations performed within *ShaleQuant*.

These transformed logs, or those that were available, were then used as the input parameters to a set of artificial neural networks trained to estimate grain density of mudstones. The estimated grain density of the sediment was then used to estimate porosity from the density log more precisely using the following equation:

$$\phi_\rho = \frac{\rho - \rho_{ma}}{1.05 - \rho_{ma}} \tag{2.9}$$

The input parameters were recalculated using the new value for porosity. These parameters were then presented to two sets of neural networks making estimates of TOC and clay fraction.

The output from *ShaleQuant* comprises estimates of clay fraction, total organic carbon content and matrix density.

2.4.3 Synthetic wireline logs using artificial neural network analysis

The ShaleQuant technique for lithological description of mudstones relies upon the availability of a comprehensive suite of standard wireline log data. These data are not always available over the entire logging interval, since the neutron and density tools are typically only run over the prognosed reservoir intervals to the target depth of the well. Since the density log is useful for the creation of overburden curves, an attempt at creating a synthetic density log over the entire logged interval is appropriate.

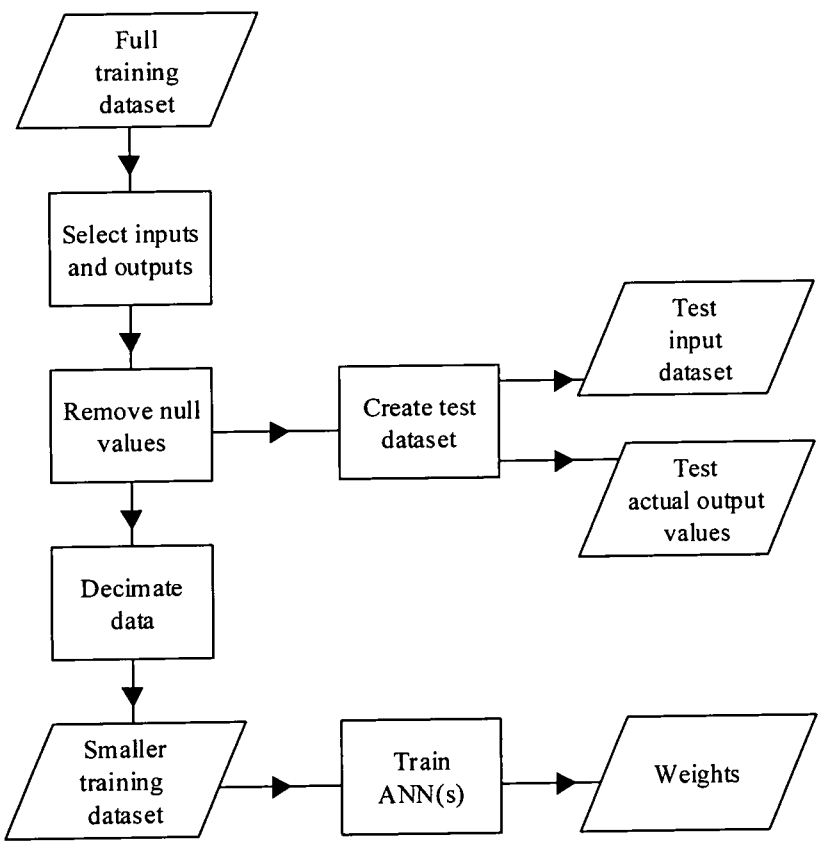

Figure 2.2 - Creation of training and test data files from a wireline log dataset and subsequent training of neural networks.

The data made available from the Gulf of Thailand comprised full log coverage including density and neutron logs from ~420m TVD sub seabed. By comparison, in North Sea drilling programmes only the gamma ray, sonic and resistivity logs are typically acquired over the majority of the drilled interval below the 20" casing shoe. In the rare cases where the density log is available over the same interval, the data from that well can be used to train a set of artificial neural networks to provide an estimate of the density log data in other wells. The process is outlined in Figure 2.2. For these analyses the input data are taken to be the gamma ray, sonic and resistivity logs. Ten multi-layer perceptron neural networks were created for each collection of data, thus a measure of precision of the ANN output was available. Each of these ten networks had the same architecture with one hidden layer containing five nodes. Since at the start of training all the weights applied to nodes are randomised, each network followed a unique training path As Figure 2.2 shows, the training dataset was a subset of the dataset from the entire logged interval. The selection of this subset was performed by random selection. These are attempts to remove any bias from the input dataset since, provided the number of training examples is large enough, examples of the majority of lithologies encountered downhole in various compaction states will be provided for training. The relative proportions of the lithologies encountered downhole and by the ANN are preserved. Appendix B provides more information on the training of the neural networks and the software employed. Multiple linear regression and polynomial models were created for comparison with the neural network approach. Several regression models were created and compared with each other, and a single regression model was created using the entire composite training dataset.

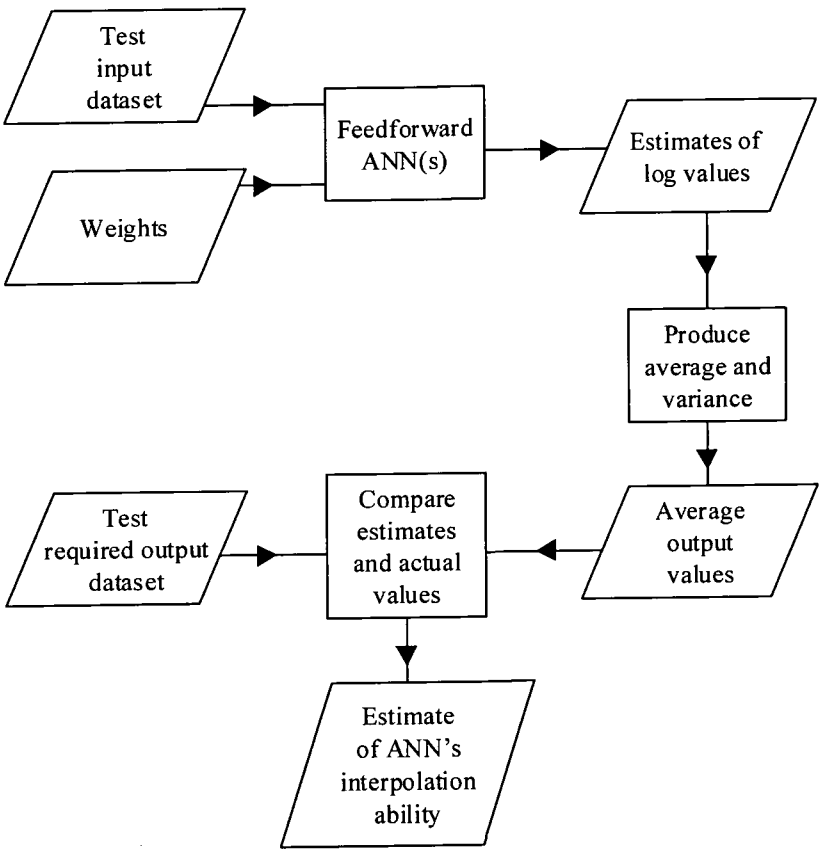

Figure 2.3 - The feed forward testing (and use) stage of the ANN models.

The models created using the subsets, however obtained, were then tested using the entire dataset from the training well, as shown in the flow diagram in Figure 2.3. The validity of the models were further tested by applying the sets of ANN weights and regression formulae derived from data from one well to input data from a neighbouring well. The models were then tested using data taken from wells in other regions and finally globally as shown in the flow diagram, Figure 2.4. In each case, the estimates from the ten separate neural networks were compiled and average estimates were calculated together with a measure of estimate variability at each depth point. The estimated variability could be used as an indication of the model calibration quality at each depth interval.

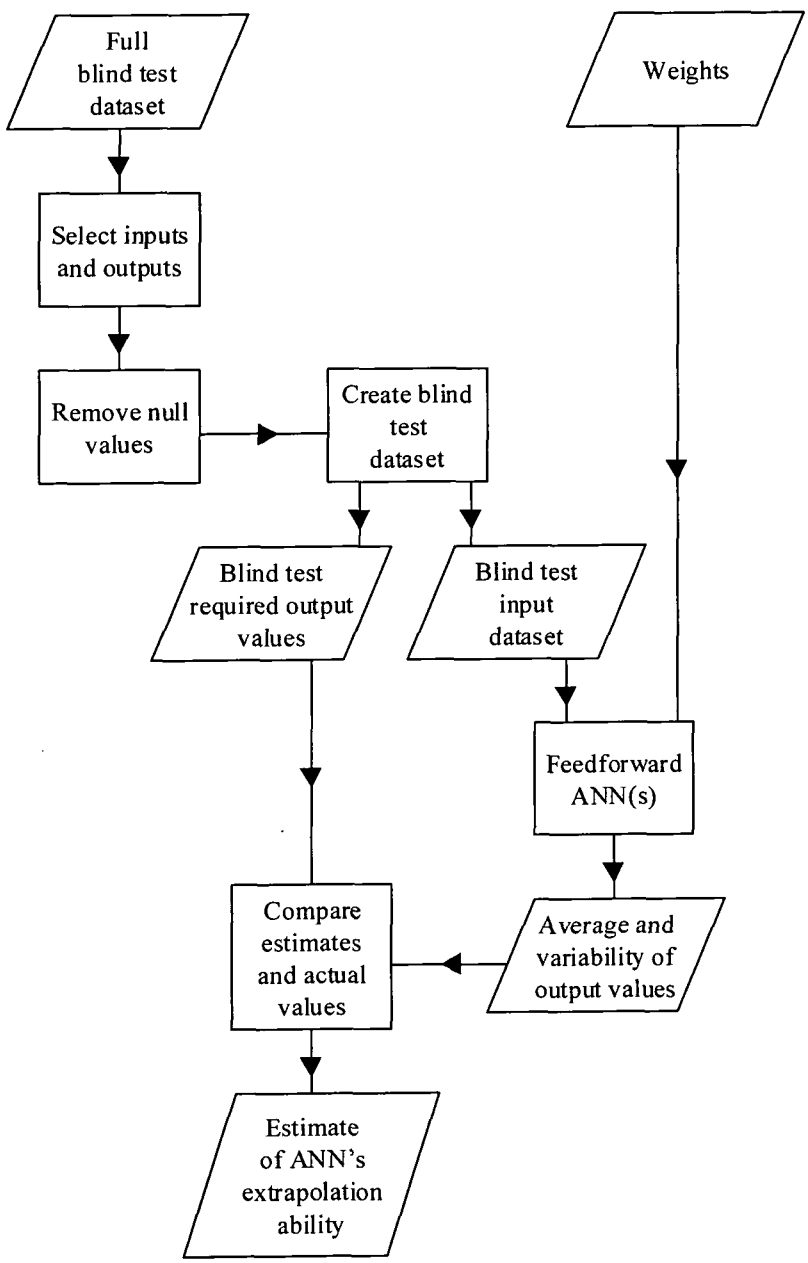

Figure 2.4 - Procedure for ANN blind testing (and use).

The logs provided for the Gulf of Mexico case study are typical for the area in that they consist of only gamma ray and resistivity from near the sediment surface. All the other logs were only run over intervals deeper in the well. Since no local calibration of the technique was available in the shallow region in the Gulf of Mexico, no log reconstruction was performed.

If the quality of the models was deemed to be high enough, the models could be used within their areas of calibration to produce a guide to the values of missing density logs using a similar scheme to that shown in Figure 2.4, omitting the comparison with known values. The quality standard required for production of synthetic wireline data will be discussed in Chapters 3 and 4. In cases where there are significant mismatches between synthetic and actual values of wireline data there may be an indication of unfamiliar lithologies or poor wireline data quality. This will be developed in Chapter 4.

2.5 Discussion and conclusions

2.5.1 Summary of techniques

A flow diagram showing the major stages of the work done in the three case studies comprising Chapters 4 to 6 is shown in Figure 2.5.

Throughout this work many graphical techniques, including compatible and incompatible log crossplots, three-dimensional plots and ColourLogs were used to visualise variation and trends within complex polyvariate datasets. If the dimensionality of the data set was too great, principal component analysis was used to reduce the number of constituent variables so that they could be visualised readily.

The results of the error analysis performed and described in the next chapter were used throughout the work as a benchmark for the suitability of the data used in any pressure calculation. The degree of quality control is discussed in each case study summary.

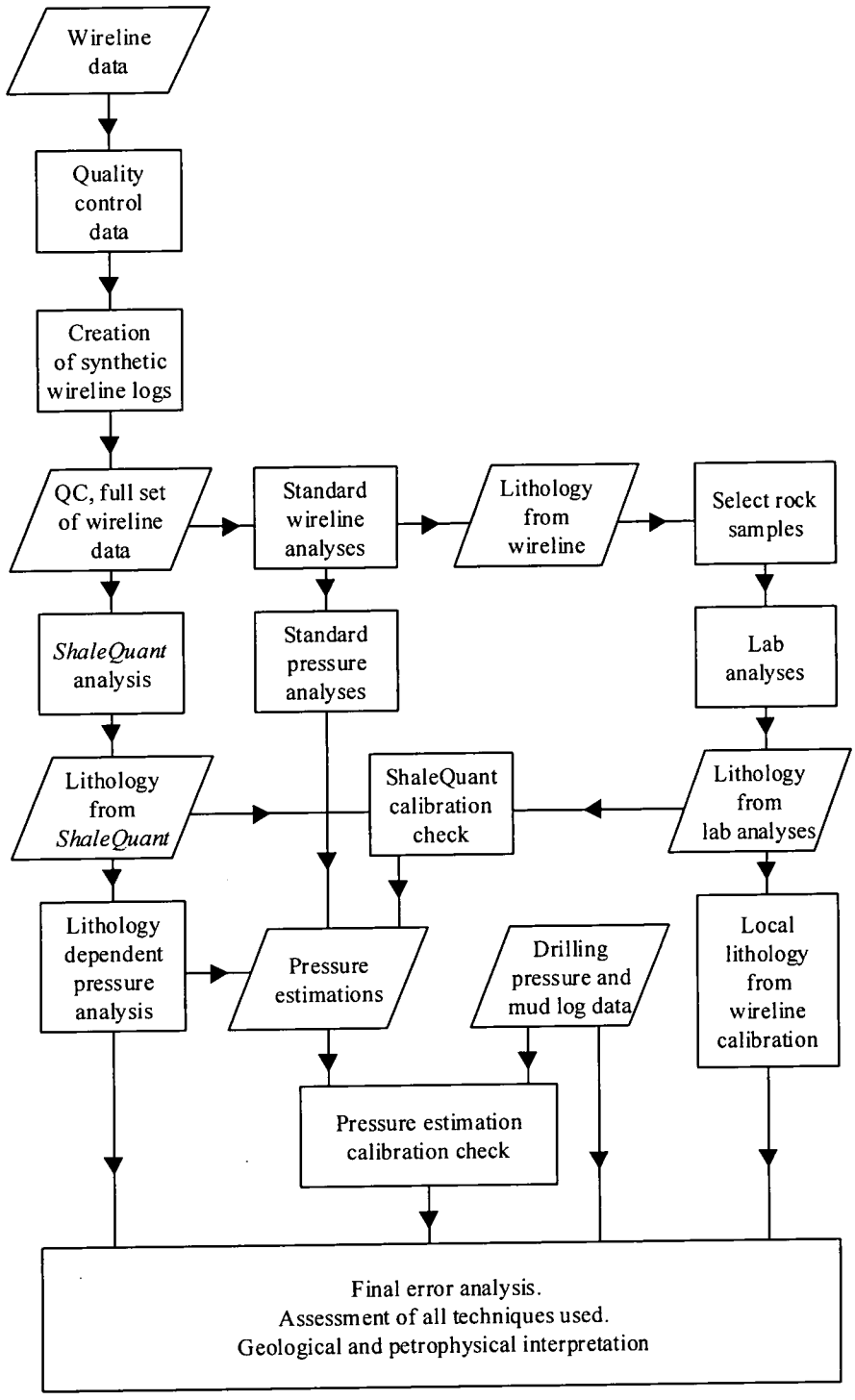

Figure 2.5 - Simplified work flow for pressure case studies throughout this work.

3 ERROR AND SENSITIVITY ANALYSIS

3.1 Introduction

3.1.1 Chapter summary

The determination of pore fluid pressure and, indeed, any petrophysical properties of rocks direct from wireline data is subject to errors arising from uncertainties in all the parameters used in the calculation. This chapter describes a study of how the errors in model parameter estimates can propagate through the set of equations used in the pore pressure model introduced in Chapter 2.

Two methods were used to investigate the interaction between the parameter errors, a deterministic study and a stochastic analysis involving Monte Carlo simulation. The deterministic error modelling was used to gain an understanding of the relative magnitude of errors arising from the various parameters used whilst the stochastic techniques were employed to gain an estimate of the total expected error due to various known levels of parameter uncertainty.

It was assumed during error modelling that porosity was derived using the density log. The sensitivity of effective stress estimates from the clay fraction dependent compaction models derived by Yang & Aplin (2000) to errors in bulk density and matrix density was shown to be particularly high; however, estimates of pressure to within ±1.8MPa at 3km burial (equivalent to a mudweight of 0.5 pounds per US gallon) were shown to be possible at easily attainable levels of input parameter uncertainty. The Monte Carlo error analysis suggested that on average the model was prone to overestimate effective stress and hence underestimate pore fluid pressure.

Major errors in the estimation of pressure were shown to be possible if unsuitable compaction trends or lithostatic gradients were during the evaluation. This study highlights the necessity of detailed local calibration of compaction trends where possible for accurate pressure evaluation.

3.1.2 Aims

This chapter contains a description of three theoretical error analyses of the clay fraction dependent, soil mechanics based compaction model derived by Yang & Aplin (2000). The aims of the analyses were:

- To identify the sensitivity of the model to errors in its individual input parameters.
- To determine the accuracy of measurement of the input parameters to produce a reasonable estimate of pressure.
- To gain an understanding of the combination and propagation of errors through the model.
- To show the importance of selecting the correct compaction model and lithostatic gradient during pressure evaluation.

A key driver for this research was to show the need for full calibration of the generic compaction model with accurate estimates or measurements of clay fraction and porosity.

3.1.3 Underlying assumptions

The soil mechanics-based oedometric experimental results (e.g. Atkinson, 1993) relating void ratio to effective stress are assumed to be correct, thus:

$$\sigma' = 100 \exp\left(\frac{e_{100} - e}{\beta}\right) \tag{3.1}$$

where β is the compression coefficient, e is void ratio, σ' is vertical effective stress in kPa and e_{100} is the void ratio at 100kPa vertical effective stress. Yang & Aplin's (2000) calibration of this model was used so that β and e_{100} were related to clay fraction, v_{cf}, by the following expressions:

$$\beta = 0.0407 + 0.2479 v_{cf} + 0.3684 v_{cf}^2 \tag{3.2}$$

and

$$e_{100} = 0.3024 + 1.6867 v_{cf} + 1.9505 v_{cf}^2 \tag{3.3}$$

These relationships were determined empirically by regression where the correlation coefficient, r^2, for the regression line was 0.92. The quality of fit between the observed void ratio data and model estimates of void ratio is displayed in Figure 1.1. The resultant normal compaction curves for 40%, 60% and 80% clay fraction are shown in Figure 3.1.

It is assumed in the models that the density log is available and so void ratio can be derived from density data. Matrix density measurements of the sediment are required during this process. These matrix density data can be obtained by measurement or assumption. Measurement at every depth interval would be highly labour intensive and is impractical. Assumption of grain density values can be made by the use of a single grain density value for all wells, or by use of Aplin *et al.*'s (1999) artificial neural network technique for the estimation of matrix density from wireline data. This neural network model is used to supply estimates of clay fraction as well as matrix density, so the correct compaction curve can be selected to describe the normal compaction behaviour of any sample of sediment.

All the input parameters to the model are subject to errors in estimation and measurement. The following study shows the sensitivity of the model to errors in each of the input parameters.

The major assumption in the following sensitivity and stochastic analyses is that the soil mechanics model used to describe the compaction behaviour of mudrocks is correct. The model is not always correct, as Yang & Aplin (2000) show that at least 90% of the estimates of void ratio using the soil mechanics based model calibrated using

clay fraction obtained from the neural network model lie within ±0.1 of the actual measured value in a dataset derived from North Sea and Gulf of Mexico sediments.

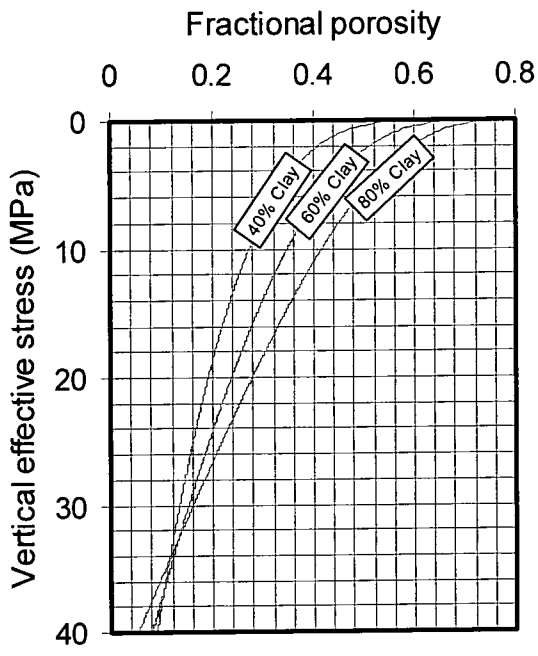

Figure 3.1 - Sample of the compaction curves used in the error analysis.

At the end of the chapter, the errors incurred by the use of the incorrect compaction model are demonstrated by comparing pressure estimates derived from Aplin *et al.*'s (1995) and Yang & Aplin's (2000) calibrations of the soil mechanics relationships.

3.1.4 Sources of error - wireline logs

The model parameters are all subject to errors. These are all assumed to be purely random in nature, with the effect of any systematic errors removed. The raw wireline data are subject to measurement errors due to uncertainties in hole quality, tool reliability, and the fact that many of the tools (particularly the gamma ray, neutron and density tools) use radiation produced from the natural decay of radionuclides, which is a semi-random process (Rider, 1996).

Very few data exist concerning the accuracy of wireline tools in the public domain. The main source of data is that of repeat sections in each logging run. The repeat data provided by the operators for the two cases studies outlined in Chapters 4 and 5 showed that the majority of the repeat data were within 1% of the original data. In many other cases, however, many logs are affected by poor hole quality. The data from these should be analysed carefully as the difference between hole width and bit size increases, the wireline data become poorer in quality and accuracy.

3.1.5 Sources of error - clay fraction and matrix density

Aplin *et al.*'s (1999) artificial neural network (ANN) determination of bulk density, grain density and clay fraction are all statistical models based on noisy input data and so have their own inherent uncertainty. Also, one of the

difficulties of using simple ANN techniques is that one cannot be certain of the uncertainty in the model's output other than knowing that the network was originally trained to within a defined tolerance. This can be avoided by training several neural networks using the same training data. This process is described fully in Chapter 4. The networks' initial weights are set randomly (Dowla & Rogers, 1995) and so each network, when trained, will produce slightly different outputs in response to a particular set of input parameters. The uncertainty in outputs will grow in cases when the model complexity increases or when constraint decreases due to paucity of calibration data. Thus, estimates of the variance in a set of ANN outputs, whilst not being true error estimates, will yield a measure of the quality of model constraint that can be used to provide an idea of the expected range of resultant effective stress and pressure estimates.

3.2 Sensitivity analysis

3.2.1 Outline

Estimation of vertical effective stress using the soil mechanics-based models for compaction essentially relies upon the measurement accuracy of compaction parameters and porosity. Estimates of effective stress using Yang & Aplin's (2000) clay fraction dependent compaction model are sensitive to errors, therefore, in the estimation of porosity and clay fraction. In turn, estimates of porosity using density data are sensitive to errors in estimates or measurements of bulk density (density log measurement), matrix density and fluid density. This study shows the sensitivity of model to errors in all the input parameters mentioned above.

Two stages of the sensitivity analysis were performed. The first was a preliminary stage in which only porosity and clay fraction were considered as the input parameters to the calibration of soil mechanics compaction models. The second stage considered all possible parameters used if the density log is used to calculate porosity. In all cases, the porosity for a given clay fraction and effective stress was calculated. Each parameter to be considered was adjusted by a known proportion whilst all other parameters were kept constant. The adjusted parameter and all others were then used to calculate an effective stress. The error in this effective stress estimate was calculated. The procedure was repeated for different imposed errors on parameters and a range of effective stresses.

It was found that pressure analysis using the compaction curves and density log derived porosity is critically dependent upon the accuracy of bulk density and matrix density. Errors in the measurement and estimation of other input parameters to the model are far less influential upon the eventual error in pressure estimate.

3.2.2 Errors in porosity and clay fraction

The sensitivity of the generic mudstone compaction model to errors in clay fraction estimate is demonstrated in Figure 3.2. Both porosity-effective stress plots show three compaction curves of which the central curve is the expected curve (50% or 70% clay fraction). The other two curves represent the compaction curves of lithologies with clay fractions with absolute differences of ±5% from the expected value, with the lower clay fraction showing a lower porosity for a given effective stress below 30MPa. The errors in estimation of vertical effective stress for two given porosities are represented in the diagrams by the horizontal shaded bands. Since the curves are convergent below 30MPa, the expected error in effective stress estimate associated with an error in clay fraction evaluation

reduces with increasing effective stress. The distribution of the errors is not symmetrical about the expected value with the magnitude of error associated with underestimating clay fraction being larger than that of overestimating clay fraction for effective stresses below 30MPa. The magnitude of error exhibited in the 70% expected curve is lower than that of the 50% clay fraction case.

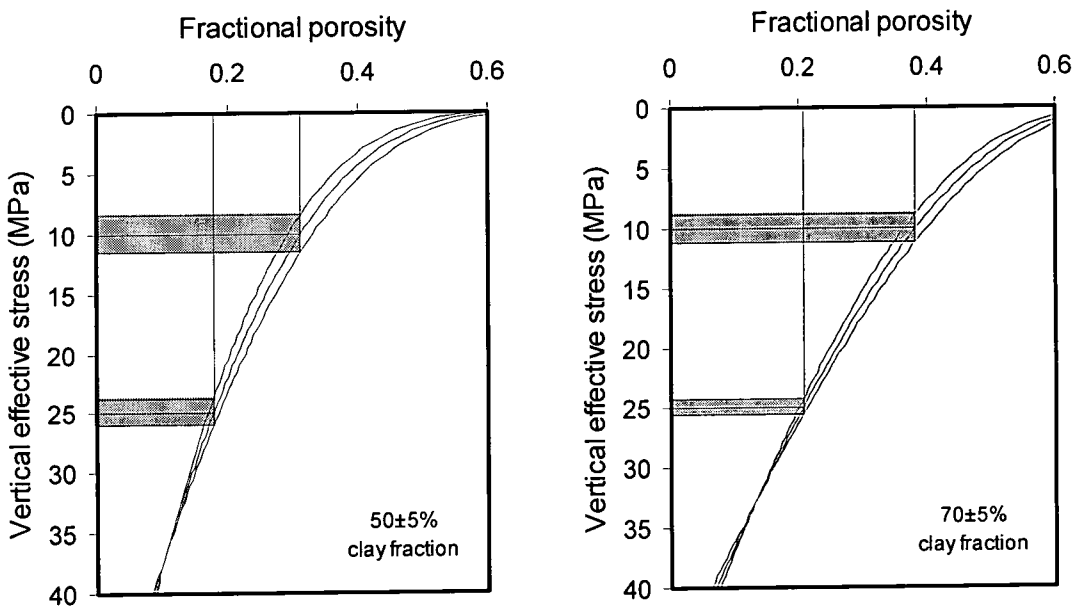

Figure 3.2 - A demonstration of the influence of compaction curve geometry on errors in effective stress estimation when clay fraction is incorrectly estimated by an absolute value of ±5%.

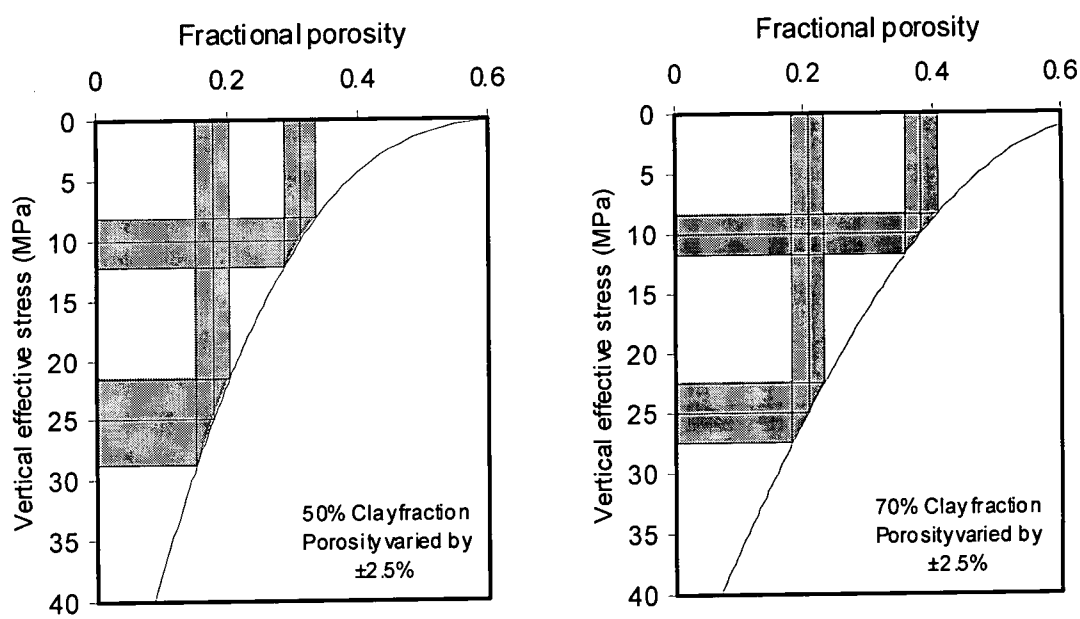

Figure 3.3 - A demonstration of the influence of compaction curve geometry on errors in effective stress estimation when porosity is incorrectly estimated by an absolute value of ±2.5%.

If, for a given clay fraction, the porosity is incorrectly estimated the error in effective stress estimate associated with the incorrect evaluation of porosity increases with effective stress. This effect is demonstrated in Figure 3.3 for two separate compaction curves, one representing a 50% clay fraction lithology, the other 70% clay fraction.

These effects are further shown in two sets of spider diagrams (Figures 3.4 and 3.5). Each plot in the set is associated with an individual effective stress, namely 10, 20, 30 or 40MPa. The diagrams show the magnitude of error associated with relative errors in measurements of input parameters. The first set of spider diagrams (Figure 3.4) are concerned with the 40% clay fraction compaction curve. Similar relative errors in porosity estimates of the 10-30MPa cases yield similar absolute errors in effective stress estimate, however the relative error reduces significantly. In all cases an underestimate in porosity yields an overestimate in effective stress, and hence a pressure underestimate.

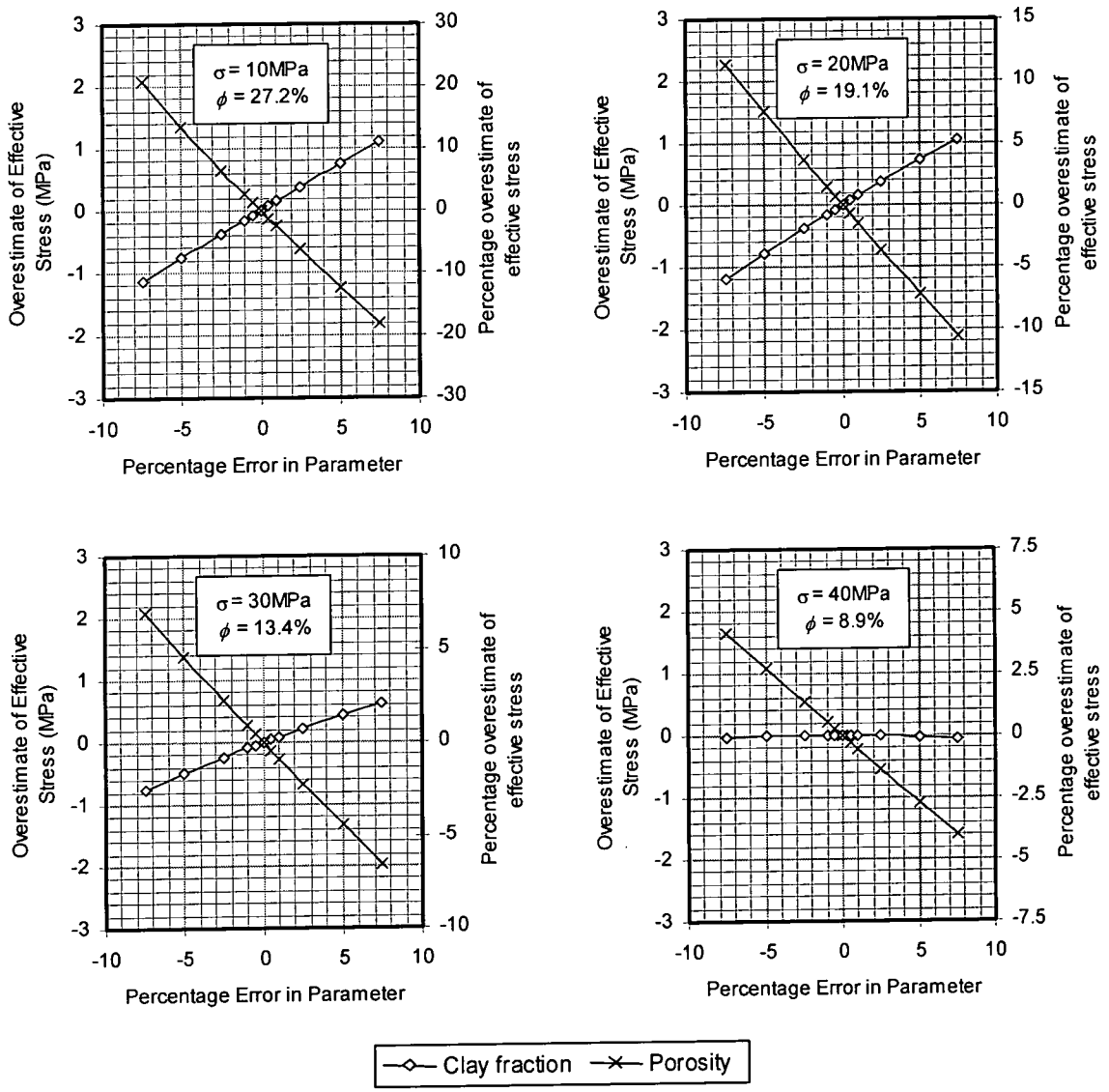

Figure 3.4 - Spider diagrams showing sensitivity of Yang and Aplin's (2000) compaction curve for a mudstone with a clay fraction of 40% to errors in estimates of clay fraction and porosity at given effective stresses.

The varying sensitivity of the 40% clay compaction model to errors in clay fraction estimate is also shown in Figure 3.4. In the 10-30MPa cases an underestimate of clay fraction causes an underestimate of clay fraction; however, the sensitivity of the model to errors in clay fraction measurement decreases with increasing effective stress. The model is virtually insensitive to errors in clay fraction measurement at 40MPa. The non-linearity of the model's sensitivity to error in clay fraction estimate is visible as both large underestimates and overestimates of clay fraction yield very small underestimates of effective stress.

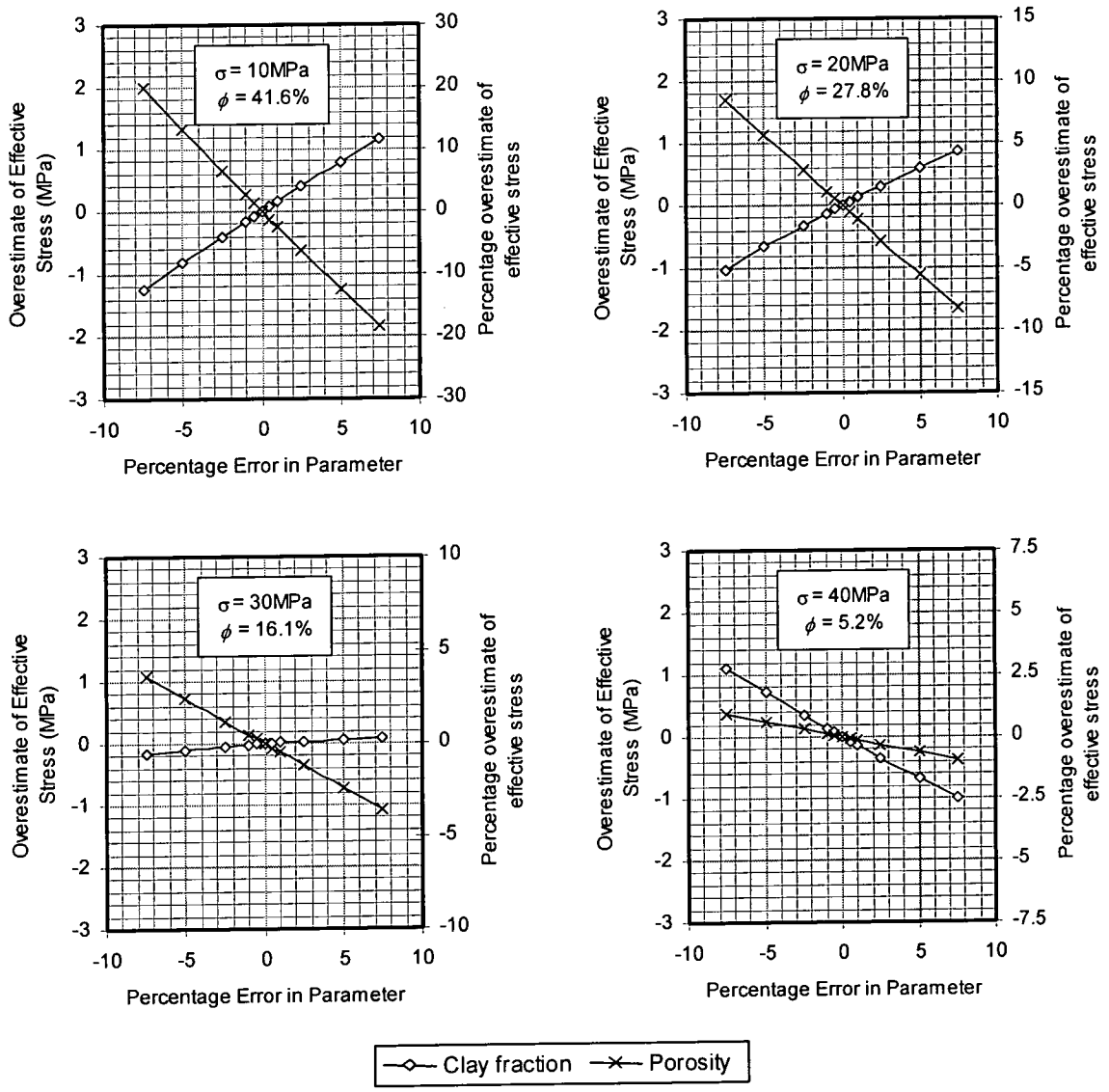

Figure 3.5 - Spider diagrams showing sensitivity of Yang and Aplin's (2000) compaction curve for a mudstone with a clay fraction of 80% to errors in estimates of clay fraction and porosity at given effective stresses

The sensitivity of Yang & Aplin's (2000) 80% clay fraction model to errors in porosity measurement is shown in Figure 3.5. The absolute error in effective stress associated with the relative errors in porosity decreases with increasing effective stress. The sensitivity of the model output to errors in clay fraction show some of the characteristics of the 40% clay fraction model, but the effective stress at which the model becomes insensitive to

errors in clay fraction lies somewhere between 30 and 40MPa and an underestimate of clay fraction at 40MPa yields an overestimate of effective stress.

3.2.3 Errors in density measurements

The sensitivity analysis was repeated assuming that the density log was used to derive porosity so the sensitivity of Yang and Aplin's (2000) compaction model to errors in bulk, matrix and fluid density was assessed together with clay fraction and overall porosity.

The results from this study are presented in Figures 3.6-3.8. The models are most sensitive to relative errors in matrix density and bulk density estimates. The sensitivity of the models to errors in both density parameters increases with decreasing effective stress. The sensitivity curves are not linear. An underestimate of the bulk density of sediment yields a smaller magnitude underestimate in effective stress than the magnitude of an overestimate in effective stress caused by an overestimation of matrix density of the same magnitude. The sensitivity of the models to errors in both forms of density estimations grows in an absolute sense, but falls as a proportion of actual effective stress, with increasing effective stress.

If bulk density were known to ±0.01g cm^{-3} at an effective stress of 20MPa, the error in effective stress estimates would range from ±0.5MPa to ±1.2MPa depending upon clay fraction and grain density. If matrix density is known to an accuracy of ±0.05g cm^{-3} at an effective stress of 20MPa, the error in effective stress estimates would range from ±1.8MPa to ±4.1MPa depending on lithology. If the clay fraction estimate is known to be accurate to within ±2.5% (absolute), the error in calculated effective stress due to the uncertainty in that estimate at 20MPa is ±0.4MPa for the 80% clay fraction case and ±0.9MPa for the 40% clay fraction case.

3.2.4 Summary

The sensitivity of Yang and Aplin's (2000) lithology-dependent compaction curves to uncertainty in input parameters, namely porosity and clay fraction, are highly variable according to the actual effective stress at which the readings are taken and the actual clay fraction of the lithology being assessed. The absolute magnitude of errors in effective stress estimates due to errors in clay fraction measurement decreases with respect to increasing actual effective stress up to approximately 30-40MPa whereas the errors in effective stress estimate due to poor porosity estimation increase monotonically with increasing actual effective stress. Errors in effective stress are not symmetrical about the actual value, that is to say an underestimate of porosity does not yield an error of effective stress estimate of the same magnitude as a porosity overestimate of the same magnitude.

When the density log is used to evaluate porosity, effective stress estimates using the model are particularly sensitive to errors in matrix and bulk density measurements. Table 3.1 summarises the sensitivities of both models to errors in input parameters by showing the absolute accuracy within which each input parameter is required to be estimated if all other parameters are totally accurate so that the error of effective stress is accurate to ±1MPa at an actual pressure of 20MPa. All these accuracies are attainable provided models are well calibrated.

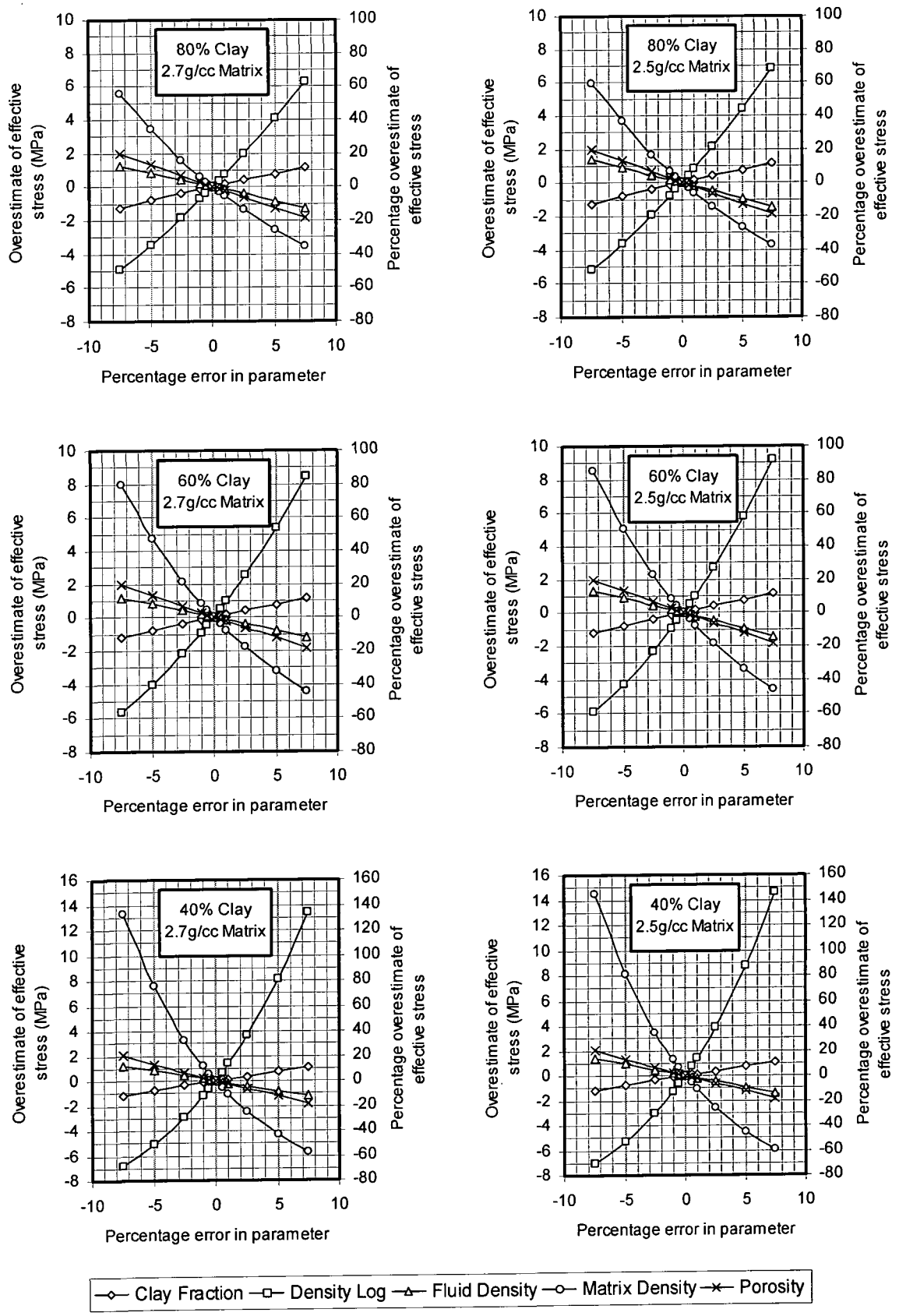

Figure 3.6 - Spider diagrams showing the sensitivity of the generic compaction model for a variety of grain densities and clay fractions at 10MPa effective stress.

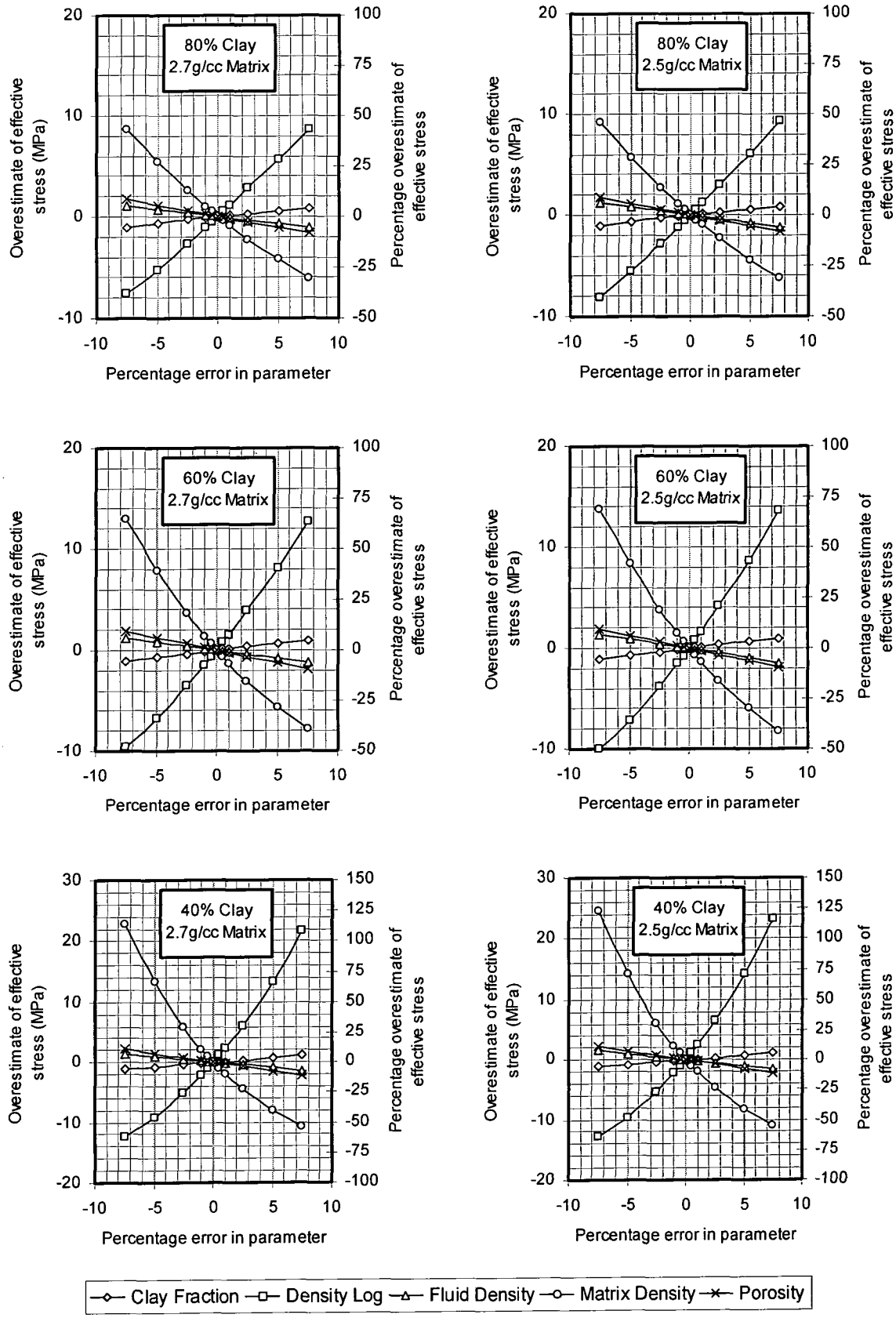

Figure 3.7 - Spider diagrams showing the sensitivity of the generic compaction model compaction curves for a variety of grain densities and clay fractions at 20MPa effective stress.

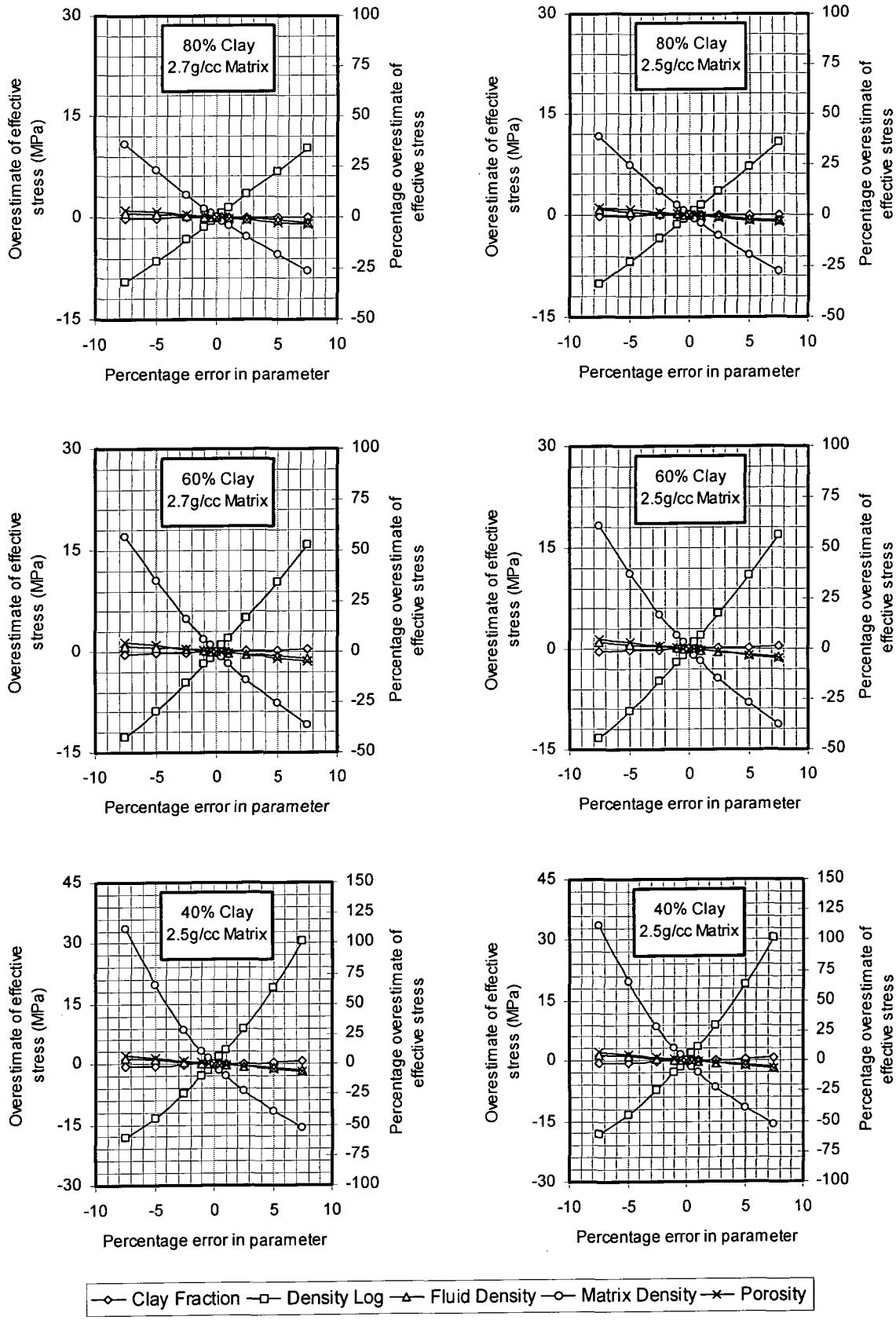

Figure 3.8 - Spider diagrams showing the sensitivity of the generic compaction model compaction curves for a variety of grain densities and clay fractions at 30MPa effective stress.

When using density-derived porosity, care must be used to obtain error bounds for the bulk density measurements from density log readings from repeat runs over the same interval if available. The repeat readings made available in the two following case studies are typically within 1% of each other. The major source of uncertainty is therefore the estimate of matrix density, so substantial local calibration should be performed, ideally using laboratory measurement or using other estimation techniques such as Aplin *et al.*'s (1999) artificial neural network techniques discussed in Chapter 2.

Parameter	Clay fraction (%)	Grain density (g cm^{-3})	Input parameter accuracy required
Clay Fraction (±%)	80	-	6.8
	40	-	2.8
Porosity (±%)	80	-	1.3
	40	-	0.65
Matrix density (±g cm^{-3})	80	2.7	0.059
		2.5	0.050
	40	2.7	0.020
		2.5	0.017
Bulk Density (±g cm^{-3})	80	2.7	0.037
		2.5	0.032
	40	2.7	0.013
		2.4	0.010

Table 3.1 - Accuracy required in input parameters to produce an effective stress estimate of 20±1MPa using Yang and Aplin's (2000) compaction model.

This study shows that accurate measurement of bulk density and estimation of matrix density are critical for accurate evaluation of pore pressure. If a typical error estimate of bulk density readings was taken to be ±0.01g cm^{-3}, which is typical for a density tool which is working well (Traugott, pers. com., 2000), this would result in an error in effective stress of approximately ±0.4-1MPa at 20MPa actual effective stress. If the estimation of matrix density was deemed to be accurate to ±0.05g cm^{-3}, then at an effective stress of 20MPa, the errors in the estimation effective stress would range from ±1MPa to ±2.3MPa depending upon the actual grain density and clay fraction of the rock.

This sensitivity analysis is limited as it shows only the effect of errors in one input parameter at a time. Further error analysis showing how errors in several input parameters combine is shown in the following section.

3.3 Random errors

3.3.1 Outline of study

A stochastic error analysis was performed to indicate how errors in all the input parameters combine to produce errors in effective stress estimates. The analysis was separated into two sections. The initial analysis was performed

to determine the optimum number of calculation passes required to produce reasonable distribution in the shortest time possible. The second analysis was used to evaluate expected output distributions a variety of simulated lithologies with varying levels of input parameter quality.

A large number of passes, 20,000 per depth point, were required to produce reliable results. Any further passes yielded progressively less information in the definition of the output distributions.

Symmetrical distributions were supplied to the model but the output distribution was skewed. All measures of central tendency of the distribution were overestimates of the actual effective stress. If the errors in input parameters were well constrained, the output was also reasonably well constrained and the apparent overestimate of effective stress was less than 1MPa even at actual effective stresses of over 30-35MPa.

3.3.2 The Monte Carlo method

In the Monte Carlo simulations, all model parameters are assumed to be normally distributed about a mean, μ, with a standard deviation, σ. Each distribution is assumed to be independent of all the others. Several thousand values of effective stress can then be calculated for each depth value using values of each parameter taken at random from their respective distributions. The resulting model distribution can then be analysed at each depth. Several descriptive statistics can be calculated such as the interquartile range, median, kurtosis, average and standard deviation. The latter two values assume that the resulting distribution is approximately normal in nature. As will be seen later, this is not always the case and so care must be used when using these statistics.

Initially, the Monte Carlo simulations were run several times with different input parameters using the program *mc2000* listed in the accompanying CD ROM. This was done to find an optimum number of calculations per depth step required to produce a consistent distribution to which it is easy to assign an approximate continuous distribution using curve fitting routines and to find the effects of varying the nature of each of the parameters. This scope analysis was required as the simulations are reasonably computationally intensive, with 1,000 depth steps each with 50,000 model passes taking over 20 minutes to perform on a 'fast' personal computer.

The full analysis was then started. Several base data sets were used, each case assuming a normally pressured, monolithological column. The lithology and the level of input parameter uncertainty was varied between each case. Table 3.2 outlines the size of errors that were used to describe the various error levels simulated within the models. These errors are expressed in absolute terms. To simplify calculations, the error distributions were regarded as normal and each error quoted in Table 3.2 is taken to be one standard deviation. In reality many of the input parameter distributions are not normal, many will have a Poisson distribution (Christie, pers. com., 2001). The magnitudes of the errors were assumed to represent best-, worst- and an intermediate-case scenarios. The best-case scenario is an ideal situation when all model parameters are well constrained: all the wireline tools were working well within a good quality hole and the ANN models were working well within a well-defined area of the parameter n-space. The worst-case scenario represents a situation where no calibration data are available at all, and so major assumptions have to be made about the physical properties of the mudstones and their composition. The assumptions are that the matrix density varies between 2.5g cm^{-3} and 2.9g cm^{-3} and that clay fraction of the sediment ranges from 40% to over 80%. The distribution parameters are therefore set so that the distribution encompasses all

possible property values: μ and σ are set so that ranges shown above lie within $\pm 2\sigma$ from the mean. The intermediate-case scenarios represent more realistic situations in which the parameters are of variable quality, due to poor quality wireline logs or poorly defined values of clay fraction and grain density. In each case, the clay fraction and grain density values were set either high (H) or low (L) values. These values are summarised in Table 3.3.

Error level	Absolute errors imposed		
	Grain density ($g\ cm^{-3}$)	Clay fraction (%)	Bulk density ($g\ cm^{-3}$)
Low	0.025	2.5	0.01
Medium	0.05	5	0.025
High	0.1	10	0.05

Table 3.2 - Sizes of error imposed on parameters during error modelling.

Value description	Parameter values used	
	Grain density ($g\ cm^{-3}$)	Clay fraction (%)
L	2.65	55
H	2.75	75

Table 3.3 - Actual input parameter values used during the Monte Carlo simulation.

3.3.3 Initial analysis

Four cases were modelled to create example histograms of expected distributions produced by the Monte Carlo simulation of effective stress estimation using Yang & Aplin's (2000) clay fraction dependent compaction model. Extremes of porosity and imposed error were considered at two burial depths. Yang & Aplin's (2000) model indicates that mudstones with low grain density and high clay fraction have higher porosities than those with high grain density and low clay fraction at burial depths of less than 3.5km. Thus, high porosity scenarios are ascribed low grain density and high clay fraction and low porosity scenarios were ascribed a high grain density and low clay fraction as described in Table 3.3. Each case was modelled twice, one with high input parameter uncertainty and the other with low uncertainty imposed on the input parameters as described in Table 3.2. Each experiment was run using 50,000 calculation passes. Each experiment is referred to by two figures representing the depth at which the effective stress of the model was evaluated divided by 100, then two letters representing the high (H) or low (L) value of porosity and error used in the model.

The resultant distributions from the experiments are shown in Figure 3.9 with an indication of the population averages for each experiment. All the frequency axes are plotted to the same scale and experiments using the same physical parameters are plotted together for easy comparison of results. Three of the four distributions resulting from well constrained input parameters are visibly log-normal. The distribution from experiment 32SL with well constrained input parameters (3,200m depth, 2.7g cm^{-3} matrix density, 55% clay fraction with well constrained input parameters) is not obviously log-normal, as histogram sampling was at too low a resolution, but if the resolution is

increased, the distribution becomes more recognisably log-normal in shape. The distributions from the poorly constrained experiments (in red) all are particularly skewed to low values of effective stress. Experiments 03HL and 03LH both produced very highly skewed distributions when their input parameters were poorly constrained. If the resolution of the histograms is increased, the frequency of effective stress estimates tends to zero as effective stress approaches zero and rises to a maximum around 5-10kPa. These distributions are again log-normal but with a very large width compared to the results of the well constrained experiments.

In each experiment, the arithmetic mean of all the effective stress estimates exceeds the actual value of effective stress used in the soil mechanics model to define the experiment. The median value of each population corresponds far more closely to the actual value, but also exceeds it.

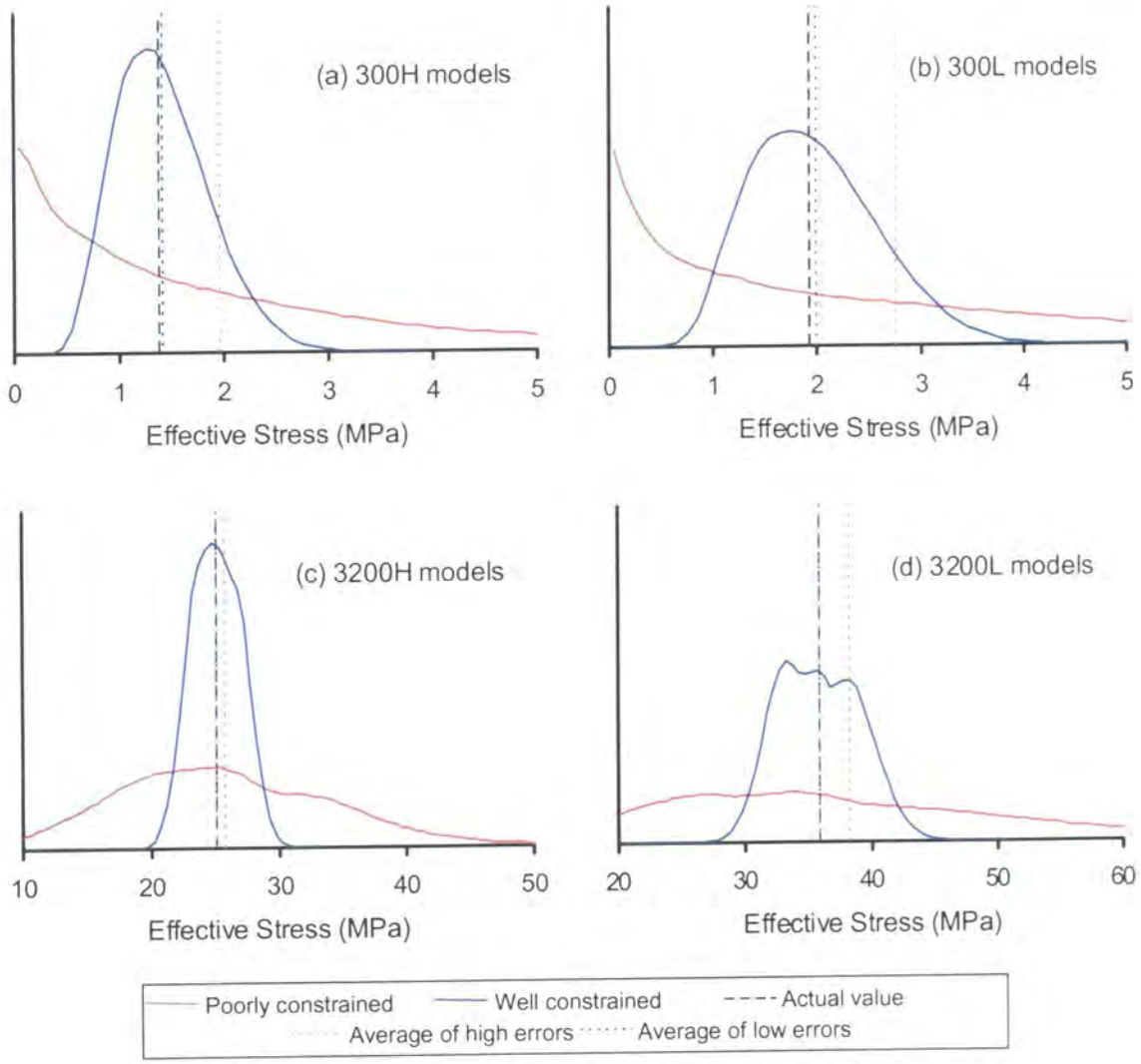

Figure 3.9 - Histograms resulting from the initial Monte Carlo experiments.

Accuracy and precision analyses were performed on four of the experiments, 03HH, 03LL, 32HH and 32LL. These were performed in order to evaluate the optimum number of passes for each depth point during full Monte Carlo analysis. A base distribution was obtained for each case by running simulations with 10,000,000 passes. For each

case 20 simulations were run using from 100 to 50,000 passes. The accuracy of each experiment was determined by calculating the Spearman's rank correlation coefficient between each experiment and the 10 million pass base distribution. The precision of the numerical experiments was estimated by calculating the Spearman's rank correlation coefficient between each run using the same number of passes.

The results of the accuracy and precision analyses are shown in Figure 3.10. All of the analyses showed that the distributions provided by more than 1,000 iterations were statistically more that 99% significant. Also the Spearman Rank Correlation Coefficient estimate of accuracy and precision of all experiments, apart from 03LL, tended to a maximum value of over 0.995 between 10,000 and 20,000 iterations. Model 03LL was less accurate and precise due to the large width of the distributions created in this experiment. The interquartile range of the distributions resulting from experiment 03LL is 5.05MPa, 14.1% of the actual effective stress used in the experiment. This is similar to the proportion of the interquartile range and effective stress produced by experiment 32HL (12%). Therefore, to ensure highly accurate definition of the estimate, it may be necessary to use a number of iterations proportional to the initial estimate of effective stress. This may not be the case, as it must be noted that Yang and Aplin's (2000) model is less well constrained at high effective stresses exceeding 35MPa. This is because many porosity reducing processes other than mechanical compaction are common at the burial depths required for such large effective stresses.

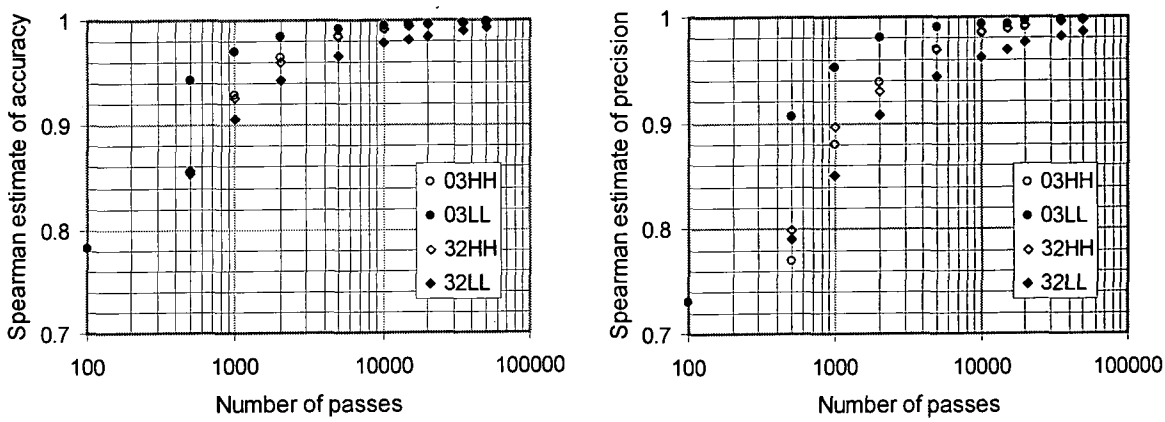

Figure 3.10 - Accuracy and precision results from the preliminary Monte Carlo experiments.

Taking all the analysis into consideration it was decided that 20,000 would be the optimum number of passes used in further Monte Carlo simulations for the error analyses using Yang and Aplin's (2000) compaction models.

3.3.4 Full analysis

Four experiments were set up using the lithology assumptions described in Section 3.3.2. The experiments were referred to using the values of clay fraction and matrix density to describe the lithology; for example, the lithology described in experiment SHL had a low matrix density, but high clay fraction. The Monte Carlo experiments were run, and calculations of pressure based on vertical stress and effective stress were calculated. Since it has been shown that the distributions of effective stress estimates are log-normal in nature, it is not appropriate to use standard deviation as a measure of distribution width, so the interquartile range of each resultant pressure distribution was calculated.

Figures 3.11-3.14 show pressure plots of the actual hydrostatic pressure surrounded by the quartile values of pressure, plots of the interquartile ranges with respect to depth and a calculation of the overestimate of effective stress, and hence underestimate of pore pressure, produced in each experiment. Since Monte Carlo Simulation is a random selection methodology, plots of data resulting from the technique were not smooth. This is exhibited particularly in the plots of the overestimation of effective stress using the arithmetic average of the distribution. The results of this set of analyses show a definite trend, but individual points deviate from the trend within a maximum range of ±50kPa.

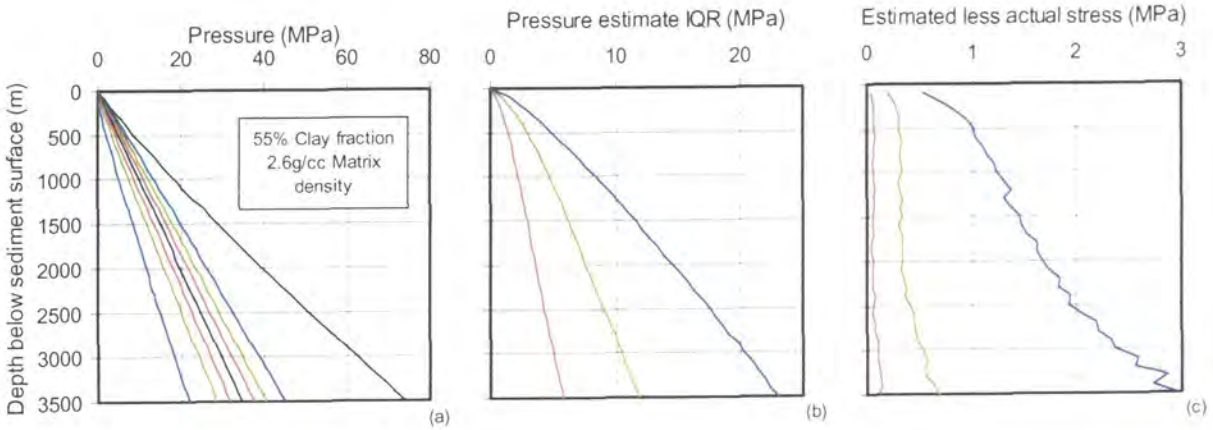

Figure 3.11 - Error analysis results from experiment SLL.

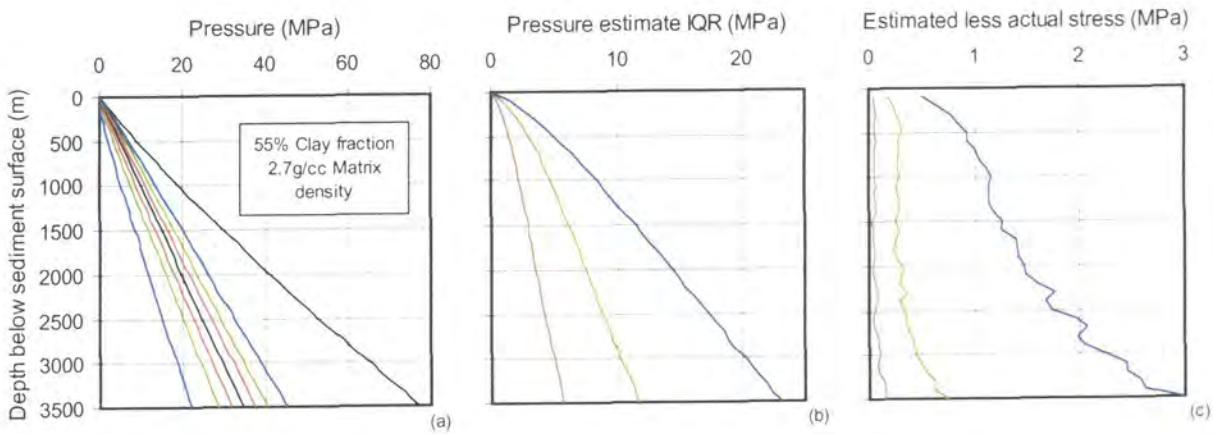

Figure 3.12 - Error analysis results from experiment SLH.

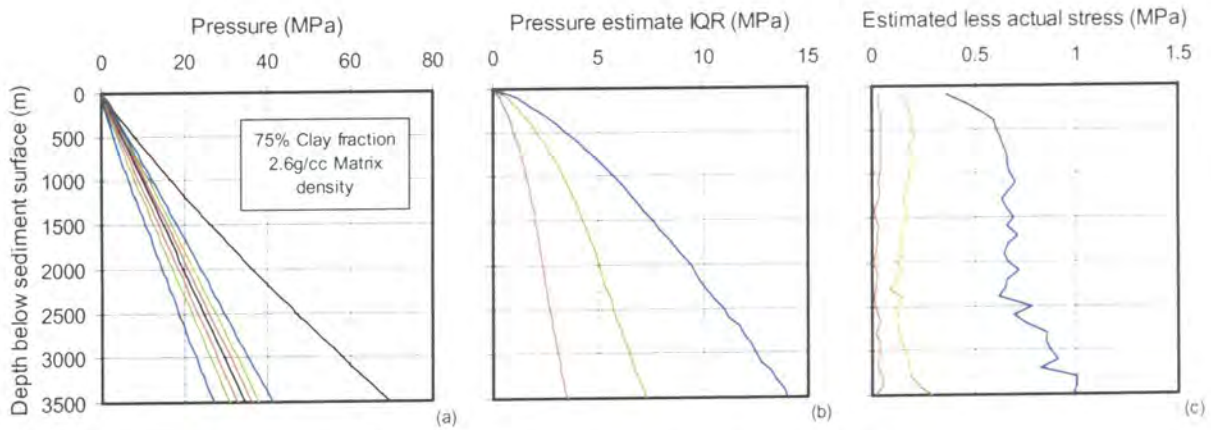

Figure 3.13 - Error analysis results from experiment SHL.

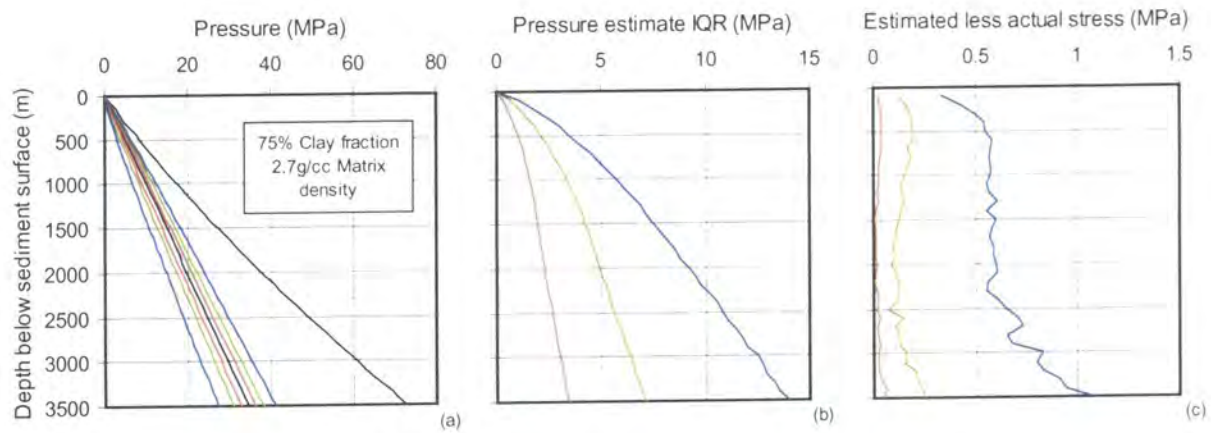

Figure 3.14 - Error analysis results from experiment SHH.

As indicated in the initial study, as effective stress in the models increases, the width of the distributions of effective stresses and pressures increases. The rate of increase of distribution width with respect to depth is affected more by change in the clay fraction than grain density used in the separate experiments. The lower clay fraction experiments exhibited a broader distribution width for a given matrix density, effective stress and error level. This change of distribution width is significant. The interquartile ranges of the high error experiments rises by approximately 9.1MPa from 14.0MPa (75% clay fraction) to 23.1MPa (55% clay fraction) at a burial depth of 3500m. The similar increases in width in the medium and low error experiments are 4.6MPa and 2.2MPa, respectively.

The use of the arithmetic average of the distribution to produce an estimate of effective stress will yield an overestimate. This overestimate is quantifiable, being relatively insensitive to matrix density used and moderately sensitive to clay fraction at low to medium levels of error. In all experiments, the apparent overestimate of pressure rises from zero at the sediment surface to a local maximum at approximately 500m burial depth. The overestimate remains approximately constant to a burial depth of 2500m and then rises with increasing depth.

3.3.5 Summary

The objectives of this analysis were to assess how random errors in all input parameters affected the vertical effective stress and hence pressure estimate when using Yang & Aplin's (2000) mudstone compaction model combined with estimates of porosity derived from bulk density data.

In all cases, the width of the distributions of pressure estimates were dependent on the value of clay fraction used in the experiments, with higher clay fraction values yielding smaller distribution widths at any given vertical effective stress; whereas the distribution of pressure estimates were relatively insensitive to matrix density values at any given clay fraction.

The magnitude of the errors exhibited by the low error experiments were within the tolerances required for drilling as suggested by Mouchet and Mitchell (1989) at most depths, with pressure estimates at 3,500m TVDSS possible to within ±2MPa. Since overpressure is highly likely at this depth, effective stress will be lower and hence the expected error will lower. The medium error experiments yielded understandably wider pressure estimate distributions, however at lower effective stresses these distributions were still within the required tolerances.

If Yang & Aplin's (2000) compaction model is used to estimate pressure without any knowledge of rock properties, one should apply significant error bars on the analysis or provide a envelope of potential pressure estimates.

3.4 Systematic errors

3.4.1 Outline

The discussion of errors so far in this chapter has been mainly concerned with random errors and their propagation through the soil mechanics algorithm for vertical effective stress calculation. There are many potential sources of systematic errors in the direct calculation of pore pressure from wireline logs. These include selection of incorrect compaction curves, incorrect overburden models and poor quality wireline data. An attempt at compensation for the effects of poor quality wireline data may be made using the results of the sensitivity analysis presented in the previous sections of this chapter. If this cannot be done, poor quality data may be filtered out. Since the pressure estimation methodology being investigated in this work relies on reliable estimation of effective and confining stress, reliable models for both quantities are essential.

This study shows the outcome of using unsuitable compaction models and overburden calculation procedures. It shows in particular the invalidity of using an assumed 1psi ft^{-1} overburden gradient even in first look analyses.

3.4.2 Overburden calculation

A lithostatic pressure gradient of 22.6MPa km^{-1} (1psi ft^{-1}) is commonly taken as the basis a reasonable first-guess estimate of overburden pressure (Mouchet & Mitchell, 1989). This is entirely empirical and does not take lithological variation and compaction into account. It implies, unreasonably, that sediments have a constant bulk density of 2.31g cm^{-3}. As has been seen in Chapter 2 overburden pressure at a depth z' can be written as:

$$s_v = \int_0^z g\left[\rho_{fl}\phi + \rho_{ma}(1-\phi)\right]\mathrm{d}z \tag{3.4}$$

where g is the gravitational acceleration and ρ_{fl} and ρ_{ma} are the fluid density and grain density, respectively. All the parameters vary with depth, so the evaluation of overburden is non-trivial and is location dependent. Figure 3.15 shows a variety of overburden curves as a pressure-depth plot (Figure 3.15a) and as a difference between the calculated overburden and that calculated using a constant lithostatic pressure gradient of 22.6MPa km^{-1}. These curves are taken from the literature and derived from both Yang and Aplin's (2000) and Aplin *et al.*'s (1995) soil mechanics-based compaction models. There are four soil mechanics-based overburden curves shown: two from each model, a high porosity (using low grain density and high clay fraction) and a low porosity case. All of the models assume hydrostatic pore fluid pressures at all depths. The two overburden curves presented are taken from work by Fertl (1972). They are generic overburden curves for the North Sea and shallow water Gulf of Mexico. At shallow depths, the overburden predicted by all the non-constant gradient models is significantly less than that estimated by using the 22.6MPa km^{-1} model. This is logical since shallow sediment bulk densities are typically far less than 2.31g cm^{-3}. The two low porosity soil mechanics-based overburden curves start to converge with the 22.6MPa km^{-1} model below 2,000m burial depth. This is because the bulk density of the sediments exceeds 2.31g cm^{-3}.

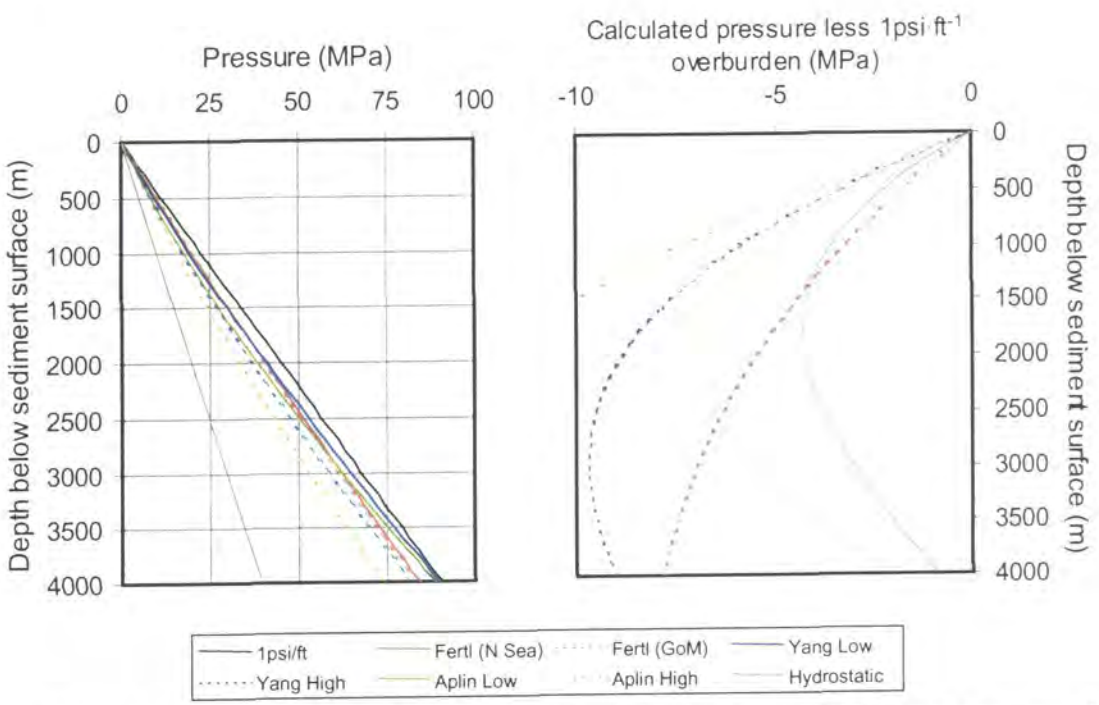

Figure 3.15 - An indication of the variation in lithostatic gradients available: (a) shown as a pressure-depth plot and (b) shown as the difference between the selected model and a 1psi ft^{-1} (22.6MPa km^{-1}) lithostatic gradient.

Since overpressure caused by disequilibrium compaction and porosity are intrinsically linked, since onset of overpressure is frequently marked by the cessation of compaction, overpressure has an effect on the overburden stress. This is demonstrated in Figure 3.16. The two low porosity soil-mechanics based models were used with hydrostatic pore pressure imposed from the surface to 1,500m burial depth. Below this depth perfect disequilibrium

compaction is assumed to occur, with constant porosity with respect to depth. Figure 3.16a shows the difference between the overburden estimated using these models and the 22.6MPa km^{-1} model. Figure 3.16b shows the overburden gradients of the models. In both diagrams, Fertl's (1972) overburden model and the hydrostatic examples of the soil mechanics-based overburden models are shown for comparison. At the onset of overpressure, bulk porosity and hence bulk density remains constant in these models since there is no lithological variation.

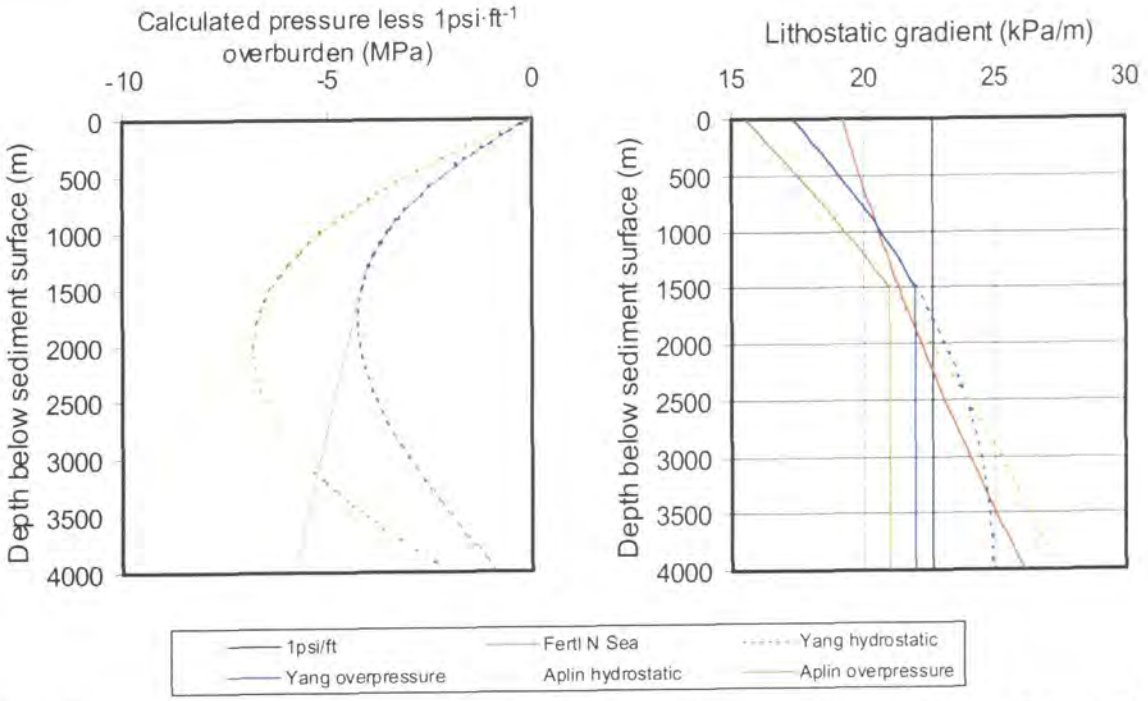

Figure 3.16 - The effect of overpressure on lithostatic gradients: (a) plotted as the difference between the calculated value and pressure corresponding to a 1psi ft^{-1} (22.62MPa km^{-1}) pressure gradient and (b) plotted as pressure gradients. In both cases the fluid retention depth is set at 1,500m.

3.4.3 Selection of incorrect compaction model

When evaluating pressure care must be take to select the correct compaction models. This may be straightforward when a shale section of known hydrostatic pressure and good wireline coverage is available. In other cases, where the onset of overpressure is very shallow, for example, selection of the correct models is made far more difficult.

Throughout the early part of this chapter, Yang and Aplin's (2000) soil mechanics-based compaction model has been used in all the error analysis. This compaction model was based on calibration techniques similar to those used in the derivation of Aplin *et al.*'s (1995) model which was calibrated using data solely from the Norwegian sector of the Northern North Sea. Yang and Aplin's (2000) model calibration dataset is geographically more diverse, coming from a larger area of the North Sea and using data from a selection of deep water wells in the Gulf of Mexico. Also, this model was calibrated using more data from a wider range of effective stresses.

The possible errors in effective stress estimation if unsuitable compaction models are used are shown in Figure 3.17. The red lines represent situations where Aplin *et al.*'s (1995) compaction models have been used to define compaction trends for 70% clay fraction (solid line) and 50% clay fraction (dotted line) lithologies. The resultant porosity values were taken and Yang and Aplin's (2000) models were used to calculate an effective stress using the

known clay fraction and porosity and the difference between the known and calculated effective stresses. The blue lines represent the opposite case where the later compaction model is used to define the correct porosity-effective stress relationship and the earlier model was used to estimate the effective stress. As can be seen, significant errors in effective stress and pressure estimation can occur if the incorrect model is used.

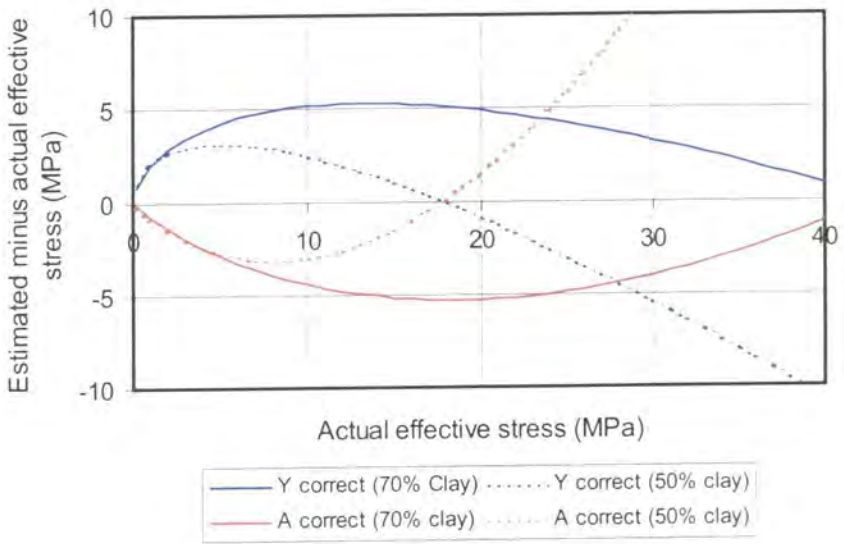

Figure 3.17 - The effects of selecting an incorrect compaction model on pressure estimations.

3.5 Discussion and conclusions

3.5.1 Random errors

The sensitivity of Yang & Aplin's (2000) lithology-dependent compaction curves to errors in input parameters, namely porosity and clay fraction, are highly variable according to the actual effective stress at which the readings are taken and the actual clay fraction of the lithology being assessed. When the density log is used to evaluate porosity, effective stress estimates using the model are particularly sensitive to errors in matrix and bulk density measurements.

The major source of uncertainty in estimating pressure direct from the density log using the soil mechanics based mudstone compaction model lies in the selection of the correct matrix density and clay fraction. If these data are not available, a set of compaction curves should be used to produce a range of possible pressure estimates. A possible source of the required lithological data is using Aplin *et al.*'s (1999) neural network method for rapid assessment of lithological characteristics direct from wireline data.

3.5.2 Systematic errors

Good quality local calibration of all models is required, especially for the overburden and compaction models. However, it must be remembered that the soil mechanics models described and tested above enable the calculation of only the component of overpressure that is due to disequilibrium compaction. They also require the assumption that no non-mechanical compaction has occurred and that the sediments are at their maximum burial depth.

Goulty (1998) has suggested that mechanical compaction is dependent upon mean effective stress and not vertical effective stress as commonly used in soil mechanics studies. Thus, if his assertion is correct, there will be a model misfit error between any vertical effective stress and mean effective stress model. The current soil mechanics models would have to be recalibrated in terms of mean effective stress. This would add further uncertainty to any pressure evaluation, as it is very difficult to estimate the mean confining stress.

3.5.3 Conclusions

On average, Yang & Aplin's (2000) compaction model tends to underestimate pore pressure as the Monte Carlo distributions of effective stress are skewed to high effective stress. Thus, any random selection from these distributions is more likely to overestimate effective stress and hence underestimate pore pressure.

Any pressure evaluation not using detailed lithological information requires the understanding that the methodology could be subject to very large errors that cannot be quantified accurately.

This work has shown that using relatively simple techniques, the errors involved in shale pressure evaluation can be calculated quickly.

4 GULF OF THAILAND CASE STUDY

4.1 Introduction

4.1.1 Chapter summary

This chapter details the use of wireline compaction analysis to evaluate the quantity of uplift that has occurred in an area. It concentrates on the data from two wells, Wells A and B drilled in the Gulf of Thailand. The area was formed by tectonic extrusion during the Cenozoic. The resulting basins were very rapidly deposited up to the Mid-Late Miocene during which time there was a significant regional inversion event associated with widespread uplift. After the late Miocene the area has reverted to undergo major deposition.

Work on the log data was centred on understanding the porosity log characteristics throughout the logged interval, especially around the Mid Miocene Unconformity situated at 1,010m TVDSS and 770m TVDSS in wells A and B, respectively. Comparison of log data between wells showed that both wells had broadly similar log characteristics below 1,500m TVDSS. The log characteristics between this depth and the unconformity are different in either well. The abrupt change in porosity over the unconformity is ascribed to an apparent maximum uplift of 450m in Well A and 360m in Well B. This corresponds to 1.3km exhumation and subsequent 1km reburial of Well A and 1km exhumation and 0.8km reburial of Well B.

4.1.2 Aims

This chapter describes a compaction study performed on wireline log data taken from two wildcat exploration wells A and B drilled in the Gulf of Thailand. The wells are separated by less than 50km, but they are from separate sub-basins. They were spudded within two months of each other in the same drilling campaign, Well A being drilled first. The company providing the data has requested that the exact location of the wells is kept confidential. The aim of the study was to use wireline data to constrain the geological history of the drilling area during the Cenozoic by:

- Using standard wireline data analysis to provide lithological characterisation of the Cenozoic rocks in the areas of both wells.
- Using methods including artificial neural networks and multiple linear regression to compare the wireline log characteristics of the two wells to show the validity of using artificial neural networks in the analysis of wireline log data.
- Performing an equivalent depth-type pressure analysis on the porosity estimates derived from the wireline log data from both wells.
- Quantification of the exhumation associated with an unconformity, which is pervasive in the area, using methods after Bulat & Stoker (1987) and Hillis (1995) and the generic mudstone compaction model developed by Yang & Aplin (2000).

The chapter is concluded by a geological evaluation of the local validity of the methods mentioned above.

4.1.3 Structure of the Gulf of Thailand and its surrounds

The major structural elements of the area at the present day are shown in Figure 4.1. The wells studied are in basins to the southwest of the Three Pagodas Fault. The Mae Ping and Three Pagodas faults are thought to continue southeastward offshore, terminating in the Mekong basin (Tapponier *et al.*, 1982) and the West Natuna Basin (Daly *et al.*, 1991) respectively.

The basins in the Gulf of Thailand are predominantly north-south trending grabens and half grabens formed in the Late Oligocene as a consequence of the convergence of India with Southern Asia. The Pattani and Malay basins are very deep, containing up to 8km of Oligocene and younger sediments. Basins to the east and west of these major basins are shallower, typically containing up to 4km of Mid to Late Cenozoic sediments.

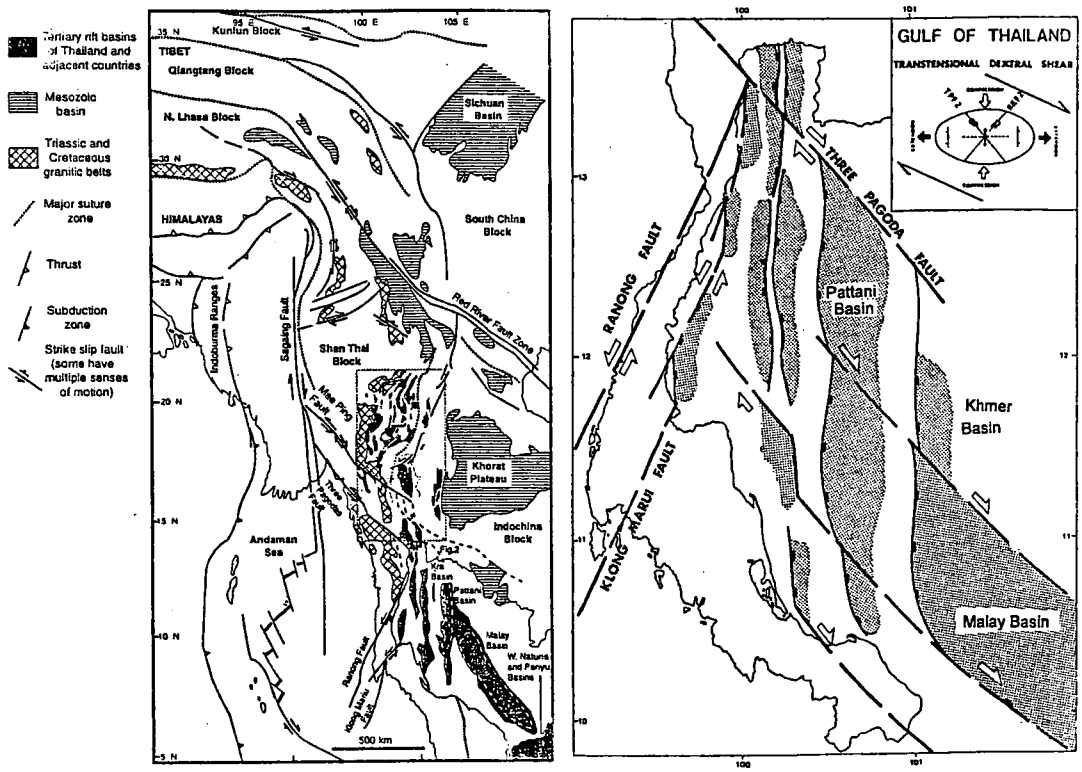

Figure 4.1 - Map showing the major structural elements of the Gulf of Thailand area, from Polachan *et al.* (1991) and Morley *et al.* (2001).

4.1.4 Cenozoic tectonic evolution of the Gulf of Thailand area

The main sources of data on the tectonics of the area are from mineral, petroleum and associated exploration onshore and offshore Thailand and regional palaeomagnetic work. Malay, Cambodian and Vietnamese exploration has been slower to materialise, so publicly available data are less common. Large scale plate tectonic models of Southeast Asia have been described by Daly *et al.* (1991), Lee and Lawver (1994) and Hall (1996). They ascribe

varying relative importance to the collision of the Indian and Eurasian plates and the influence of the clockwise movement of the Philippine Sea Plate (Rangin *et al.*, 1990; Hall, 1996).

Polachan *et al.'s* (1991) summary of Gulf of Thailand tectonics simplifies the area as consisting of two continental blocks, the Shan-Thai and Indochina. Since the collision of India with Eurasia staring in the Eocene, these blocks have been heavily tectonised (e.g. Tapponnier *et al.*, 1982; Polachan *et al.*, 1991; Hall, 1996). Tapponnier *et al.* (1982) suggested that movement of India relative to Eurasia has caused Shan-Thai and Indochina to be extruded during the collision with large scale movement of up to 1000km along NW-SE trending strike-slip faults such as the Red River, the Mae Ping (also known as the Wang Chao) and Three Pagodas faults. The sense of the movement along the fault zones is debated (Polochan *et al.*, 1991). Evidence for dextral movement includes dextral offset of Quaternary beds by the Red River faults in Yunnan Province, China, (Allen *et al.*, 1984) and Vietnam (Tapponnier *et al.*, 1986), palaeomagnetic comparisons of sediments on the Khorat Plateau and Yunnan and Szechuan Provinces, China across the Red River Fault (Maranate & Vella, 1986) and fault plane solutions of earthquakes in the Red River and Mae Ping fault zones (Le Dain *et al.*, 1984). Evidence for sinistral movement includes the offset of Permo-Triassic strata (Tapponnier *et al.*, 1982), Palaeozoic strata (Le Dain *et al.*, 1984) and a Late Triassic ophiolite suite in east Thailand (Bunopas, 1981) by the Mae Ping and Three Pagodas Faults. Further evidence includes $^{40}Ar/^{39}Ar$ dating of sinistral macroscopic and microscopic shear sense indicators in the Red River (Schärer *et al.*, 1990), Mae Ping and Three Pagodas Fault zones (Lacassin *et al.*, 1997).

Lacassin *et al.* (1997) account for most of the observations listed above in a model in which there is intense left lateral shear on the Three Pagodas Fault between 36Ma and 33Ma, on the Mae Ping Fault between 33Ma and 29Ma and on the Red River Fault between 26Ma and 17Ma. This is based on $^{40}Ar/^{39}Ar$ dating of fault movements in central Thailand. The $^{40}Ar/^{39}Ar$ measurements indicate that there was a period of uplift in central Thailand between 29Ma and 23Ma. The model then states that these NW-SE faults were reactivated in a dextral sense, eventually leading to the present day tectonic regime. During the development of this model, Harder *et al.* (1994) suggested that the reason for the reversal in shear sense was the relative position of the compressional front between the Indian indenter and Eurasia and Indochina, the collision causing a compressional wave of extrusion followed by relaxation.

The movement along the NW-SE trending faults is responsible for the formation of the sedimentary basins in the area (e.g. Hutchinson, 1989; Polachan *et al.*, 1991; Lacassin *et al.*, 1997). Tapponnier *et al.* (1986) claim that the rifting of the parts of the Pattani Trough, Khmer basin and Malay basins was initiated by transtension due to the left lateral shear at the termination of the Mae Ping and Three Pagodas fault zones. Sedimentation continued in these basins after rifting due to thermal subsidence (Pigott & Sattayarak, 1991). The rifting episode that created the smaller basins in the area is connected to E-W extension (Polachan *et al.*, 1991; Packham, 1993; Lacassin *et al.*, 1997) which required dextral movement of the strike-slip fault systems. Extension continued in these areas until the Late Miocene (Pigott & Sattayarak, 1991). At this time, regional inversion and unconformity took place. Polachan *et al.* (1991) suggest that the unconformity represents a major episode of uplift at the end of the main extensional phase of most of the basins. This unconformity has been dated in the Pattani Basin as Mid-Late Miocene by Wollands and Haw (1976) using age deterministic flora. Morley *et al.* (2001) suggest that the inversion associated with the unconformity was more intense in the southern basins such as the Pattani and Malay Basins.

The area has continued to subside thermally from the Latest Miocene to the present day (Pigott & Sattayarak, 1991) with the period marked in the Pattani and Malay basins by substantial subsidence (Polachan *et al.,* 1991).

4.1.5 Stratigraphy of basins in the Gulf of Thailand

Very few wells have been drilled into the pre-Tertiary section in the Gulf of Thailand. The section is thought to consist of the same sequence of rocks as described by Vysotsky *et al.* (1994) onshore Cambodia and in Thailand by Pradidtan & Dook (1982) and Lian & Bradley (1986), namely Mesozoic to Carboniferous intrusives, carbonates and siliciclastic sequences. The Tertiary sections throughout the area are subdivided into the syn-rift and post-rift sequences (Leo, 1997). This section has been further subdivided by Wollands & Haw (1976) and by Lian & Bradley (1986). Wollands & Haw (1976) divided the Tertiary into three separate cycles based on palynomorph data. Cycle I consists of the syn-rift sediments and some of the post-rift in the Pattani and Malay Basins until the appearance of *Florschuetza levipoli* during the Early Miocene. Cycle II sediments age from the Early- to the end of the Mid-Miocene: the extinction of *F. trilobata* and the base of the unconformity mentioned in the previous section which is within the *F. meridionalis* zone. Cycle III consists of all the sediments from the removal of *F. trilobata* to the present day. This system may be viable for dating sediments, but it is not useful structurally or sedimentologically, since Cycle I contains both syn- and post-rift sediments. Lian & Bradley (1986) suggested a division of the Tertiary into four sections based on well log and seismic analysis of the Pattani Basin. In their description, Cycle I consists of the syn-rift sediments. Cycles II and III represent two different facies of post-rift sediments deposited before the uplift event associated with the Late Miocene unconformity. Cycle IV consists of all the sediments deposited between the Latest Miocene and the present day. The units described by Lian & Bradley (1986) can also be identified in the Western Graben area of the Gulf of Thailand (Polachan *et al.,* 1991) and so in the rest of the discussion of the stratigraphy of the region the four unit description shall be used.

The Oligocene – Miocene Cycle I syn-rift sequences were deposited in isolated grabens (Leo, 1997). In the Pattani Trough and the north-western basins sediments were deposited in alluvial/fluvial and lacustrine environments (Polachan *et al.,* 1991). Lacustrine sedimentation rates can be particularly high, up to1-5mm yr^{-1} (Sladen, 1997), so very thick sequences of non-marine sediments can accumulate in short period of time. The Malay basin was more open to marine influence and deposition occurred in a fluvio-deltaic environment (Leo, 1997). The surrounding mountain ranges were uplifted during this period, and the climate was warm and humid (Sladen, 1997) so sediment supply was ample.

During the Early Miocene (Cycle II) Polachan *et al.* (1991) suggest that widespread lacustrine conditions were well developed over the Western Graben area whilst floodplain and fluvio-deltaic to brackish and limited marine conditions were established in the Pattani Trough and the Malay Basins. The Middle Miocene (Cycle III) is characterised by the occurrence of a regional regression with alluvial/fluvial influences throughout the Gulf.

The Late Miocene unconformity is represented in the rock record of the western grabens by change in facies from the flood plain and local delta plain facies to the deposition of coarse clastic sediments. In the more distal Pattani trough and Malay Basin fine grained sediment deposition took place in paralic and paludal swamps (Polachan *et al.,* 1991). The rock record in all areas of the Gulf of Thailand is completed by a transgressive succession. The shallow

marine state in the Gulf at the present day is a continuation of this latest transgression. (Chonchawalit & Bustin, 1994).

4.1.6 Drilling histories of Wells A and B

Both wells were deviated to be parallel with major faults. Well A is situated on the east of its basin, Basin A, and was drilled parallel to an antithetic fault. Well B is situated on the east margin of the structural high separating Basin A and the next basin to the east, Basin B. It was drilled on the footwall block parallel to the western boundary fault of Basin B. The schematic structural relationship between the two wells is shown in Figure 4.2.

In the pre-drill seismic analysis reports, the operator comments that the Mid Miocene Unconformity is a pervasive feature across all the surveyed volume and continued to suggest that the unconformity is associated with a significant amount of uplift. The amount of uplift is not quantified.

The facies encountered, taken from the confidential final well reports, in each well are summarised in Table 4.1 together with interpreted seismic boundaries. The pressure data measured in sands using the MDT tool for both wells together with the drilling mud pressure used while drilling are outlined in Appendix C. Pressure estimation whilst drilling was done using a selection of d-exponent, shale density and connection and trip gas techniques.

Well A was drilled over-balanced throughout the 12¼" and through most of the 16" hole section. D-exponent analysis suggested that the top of overpressure was at around 2,100m TVDSS; hence mudweight was increased to maintain mudweight overbalance. After MDT measurements were made in the 12¼" hole and showed that drilling mud pressure exceeded pore fluid pressure in the sands by over 4MPa, the mudweight was correspondingly reduced.

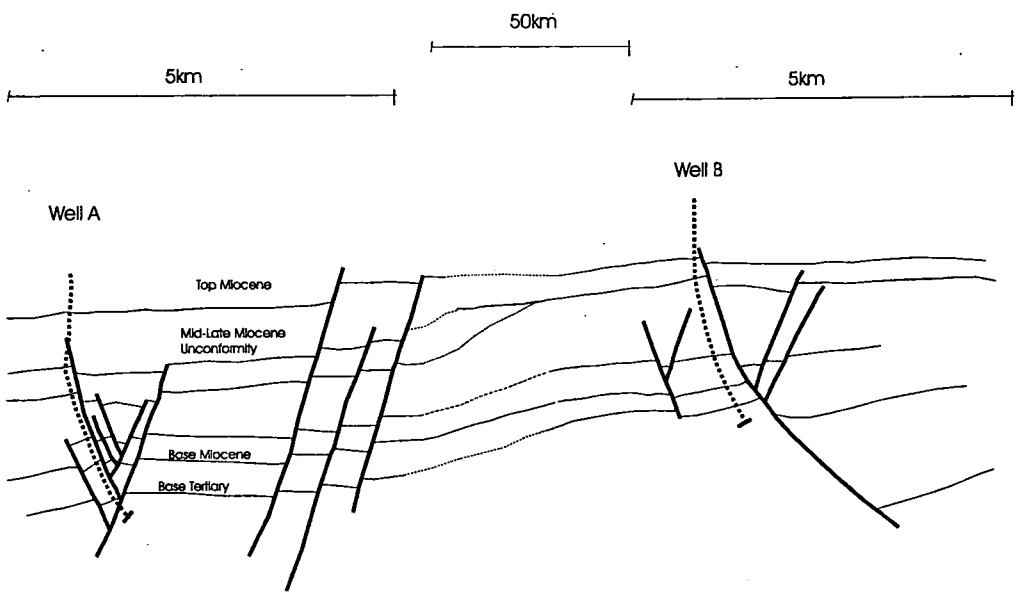

Figure 4.2 - Schematic diagram showing the structures investigated by both wells.

Interval	Lithological/Facies Description	Formation tops (MD/TVDSS m)	
		Well A	Well B
Pre-Tertiary	Ferruginous sandstones (wells A & B), Basalt (Well B)	3,890/3411	3,007/2490
Syn-rift	Lacustrine/fluvial/alluvial – thinly bedded sands, silts and mudstones together with occasional thicker (up to 15m) channel sands	3,684/3,235	2,678/2,238
Latest Oligocene	Lacustrine – thin interbedded sands, silts and mudstones	3,027/2,678	
Early Miocene	Lacustrine/fluvial – thin interbedded sandstones, mudstones with occasional coals. Sporadic Marine incursions – foraminiferal and glauconitic sands and thin bands of carbonate	2,276/2,064	1,725/1,505
Lower Mid Miocene	Fluvial/flood plain – thin sandstones, mudstones and coals Sporadic Marine incursions – foraminiferal and glauconitic sands and thin bands of carbonate	1,578/1,530	
Upper Mid Miocene	Thick red mudstones and channel sands, no coals	1,038/1,002	812/790
Latest Miocene-Recent	Basal silty sand overlain by thick mudstones and occasional lignites. Quaternary sediments are fully marine.	86/73.5	80/67.5

Table 4.1 - Lithological and facies description of rocks encountered during the drilling of wells A and B.

A mudweight of 11.5ppg was maintained until a depth of 3,230m (TVDSS), since no connection or trip gases were received at the surface, although the d-exponent indicated that the pressure was increasing. At 3,230m a large gas bubble forced mud over the rotary table on the drill-ship. Mudweight had to be increased by 2ppg (equivalent pressure increase of ~10MPa) to contain the pressure. In the final well report, the operator suggests that there was a sudden increase in pressure that could be attributed to drilling through an unconformity or unresolved fault at about 3,000m TVD.

Well B was drilled with no major pressure problems. It was drilled overbalanced throughout, with more attention paid to estimates of pressure derived from the d-exponent technique than from drilling gas.

The temperatures encountered during drilling both wells were high; the bottom hole temperature in well A (at 3,450m TVDSS) was 176°C and the bottom hole temperature in well A (at 2,525m TVDSS) was 125°C.

4.1.7 Data supplied

The dataset used in the case study comprised wireline data from both deviated wells. The wireline data supplied comprised induction logs, sonic, gamma ray, spectral gamma ray, litho-density logs and compensated neutron logs. A seismic interpretation connecting the wells was provided together with more detailed seismic interpretations taken

from 3D seismic volumes showing the track of each well. Pre- and post-drill reports, composite wireline logs, wellsite lithologs, digital wireline data and Modular Dynamics Tester (MDT) pressure measurements for both wells were provided. Rock samples were obtained in the form of cutting and standard core samples.

4.2 Initial wireline log and sample analysis

4.2.1 Quality control of the wireline data

All wireline data were checked for self-consistency and possible sources of error. Two possible problems within the two datasets were identified: data taken from caved areas and gamma ray log scale changes between logging runs.

In Well A all log readings taken at depths where the hole was more than 2.5" out of gauge, estimated by subtracting the size of the bit from the caliper log value at each measurement depth, were rejected above the unconformity and those over 1.5" out of gauge were rejected below the unconformity. Similarly for Well B, data from depths at which the hole was over 1.5" out of gauge were rejected over the entire logged interval. It was noted that this technique might have had the effect of the preferential removal of some less well-consolidated lithologies. Therefore, checks were made for this effect by comparing the bound water estimates from the density and neutron logs, assumed to be a proxy for lithology, and the difference between the caliper log and bit size. There was no discernible relationship between these quantities in either well, hence it was concluded that no preferential removal of lithologies occurred.

The values of the spectral gamma ray, γ_{SGR}, and computed gamma ray, γ_{CGR}, logs are calculated using the measurements of uranium, thorium and potassium concentrations using the following equations:

$$\gamma_{SGR} = aC_{uranium} + bC_{thorium} + cC_{potassium} \tag{4.1}$$

and

$$\gamma_{CGR} = bC_{thorium} + cC_{potassium} \tag{4.2}$$

where C_x is the concentration of element x and a, b and c are calibration constants. These constants are 8.09, 3.93 and 16.32, respectively, when the Schlumberger NGT-A tool is used and concentrations of thorium and uranium are measured in parts per million and that of potassium in percentage by weight (Schlumberger, 1989). Multiple linear regression analyses were performed in order to estimate the constants used over each casing interval in both wells. The estimates were significantly different in each case; hence new CGR and SGR logs were recalculated using equations 4.1 and 4.2 together with the values quoted above for the NGT-A tool.

4.2.2 Lithology and porosity analysis

The filtered density and neutron logs of both wells were used to estimate lithological and fluid phase proportions using the matrix inversion technique described in Section 2.2.1, expressed in Equation 4.3 where v_{sand}, v_{shale} and ϕ are volume fractions of sand, shale and porosity and ρ_b and ϕ_N are bulk density and neutron porosity.

$$\begin{pmatrix} v_{clay} \\ v_{quartz} \\ \phi \end{pmatrix} = \begin{pmatrix} 2.75 & 2.65 & 1.01 \\ 0.4 & -0.011 & 0.95 \\ 1 & 1 & 1 \end{pmatrix}^{-1} \begin{pmatrix} \rho_b \\ \phi_N \\ 1 \end{pmatrix} \quad (4.3)$$

The constants were chosen as best fits for the wells by attempting to minimise the number of negative values of v_{clay}, v_{quartz} and ϕ produced by the procedure. Although the clay phase density values used for the estimates appear to be very high, they are borne out in laboratory density measurements of mudstone samples taken from cores and cuttings in both wells, considering that mudstones are mixtures of quartz and clay minerals, therefore any estimates of lithology should use end member values for all phases. The matrix density used for clay is similar the value used by Audet (1995), but significantly higher than that used by Magara (1976) and Sclater & Christie (1980) but it is well within the range of values quoted by Ellis *et al.* (1988) and La Vigne *et al.* (1994) summarised in Table 4.2.

Mineral	Matrix density (g cm^{-3})	
	Ellis *et al.* (1988)	La Vigne *et al.* (1994)
Muscovite	2.83	2.81
Glauconite	2.83	2.96
Kaolinite	2.64	2.52
Illite	2.77	2.78 and 2.80
Smectite	2.35 (Hydrous Saponite) to 2.91 (Anhydrous nontronite)	2.79
Chlorite	2.67 (Mg Chlorite) to 3.40 (Fe Chlorite)	2.70

Table 4.2 - Example calculated and measured clay mineral matrix density values.

An estimate of clay content of the rock was calculated by dividing the proportion of the clay phase by the total solid phase estimate.

Extracts from the quality controlled wireline CGR, sonic and density data are shown together with a composite ColourLog and clay content estimates obtained above are show for Wells A and B in Figures 4.3 and 4.4, respectively. The porosity data obtained during the matrix inversion process are shown in Figure 4.5. The log data in all plots are fragmentary due to the removal of out of gauge data during the quality control process. This fragmentation of data is particularly apparent in the top section of Well A, where little analysable data are available.

The top section of Well B (from the top of the data to 770m TVDSS) is characterised by low bulk density, low velocity and lower gamma ray lithologies. The clay content estimates in this section are characterised by an overall reduction from top to bottom. This observation is apparently contradictory to the trend observed within the gamma ray log over the same interval in which there is a reasonably constant trend. The difference in trends between the two proxies for lithology may be ascribed to problems in assuming a monolithological component for solid phase over the entire logged interval, possible non-linear relationships between log response and lithology or tool malfunction due to adverse logging conditions. The first explanation is highly likely since the top section's log

character is totally different to the remainder of the logged interval, so any calibration of simple models would be biased towards the majority of the data.

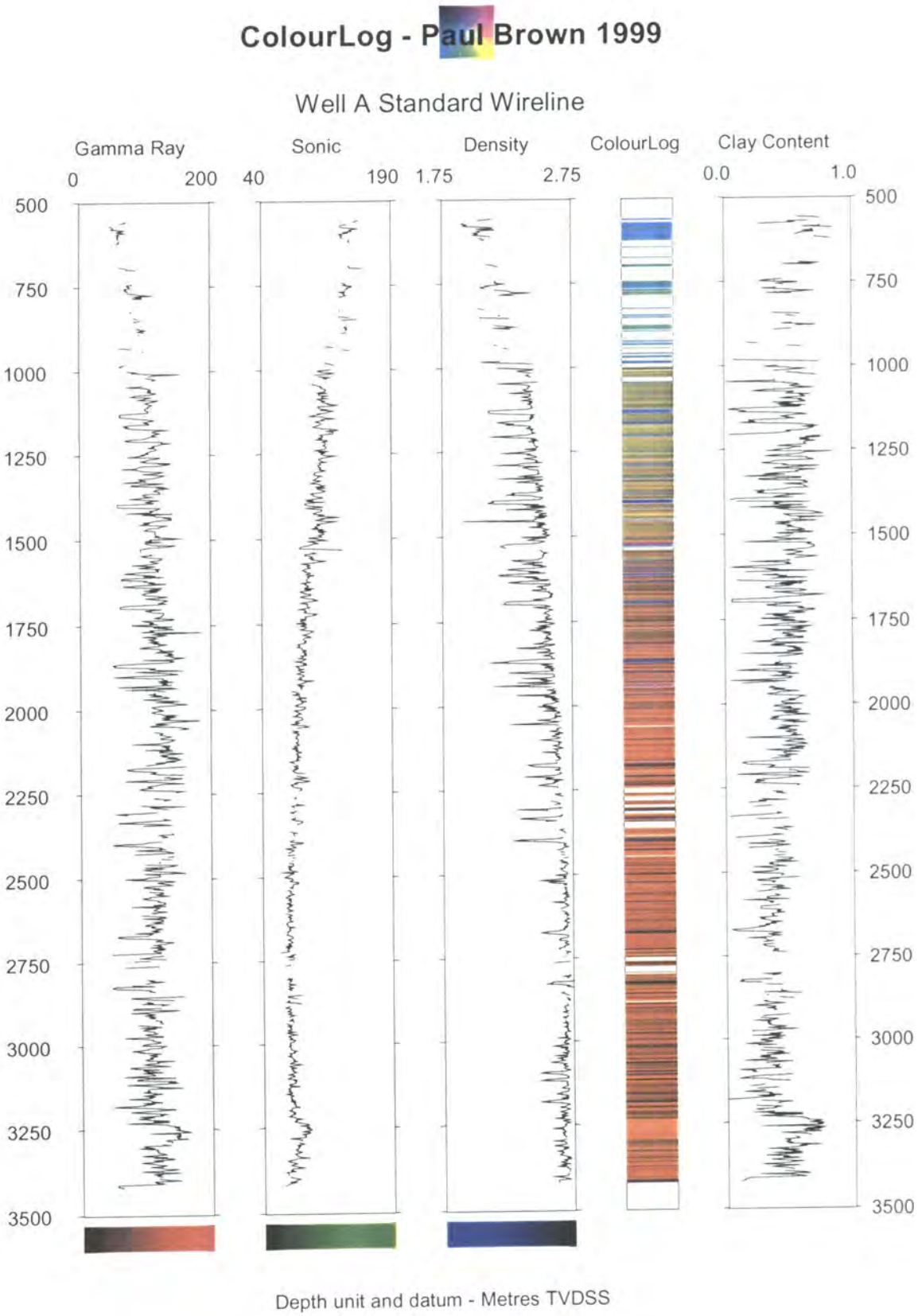

Figure 4.3 - Quality-controlled wireline data from well A.

Paul Ecclestone-Brown

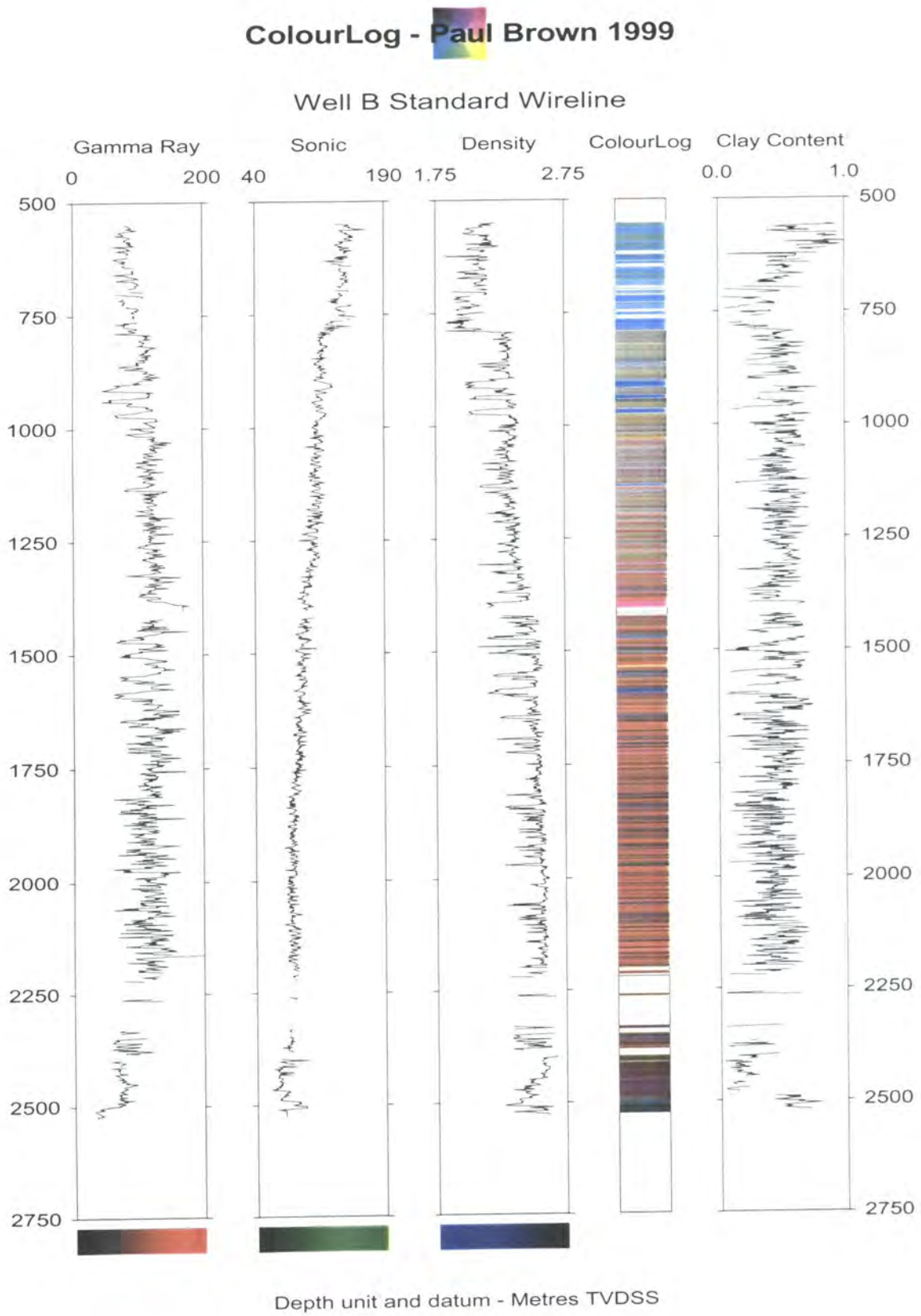

Figure 4.4 - Quality-controlled wireline data from Well B.

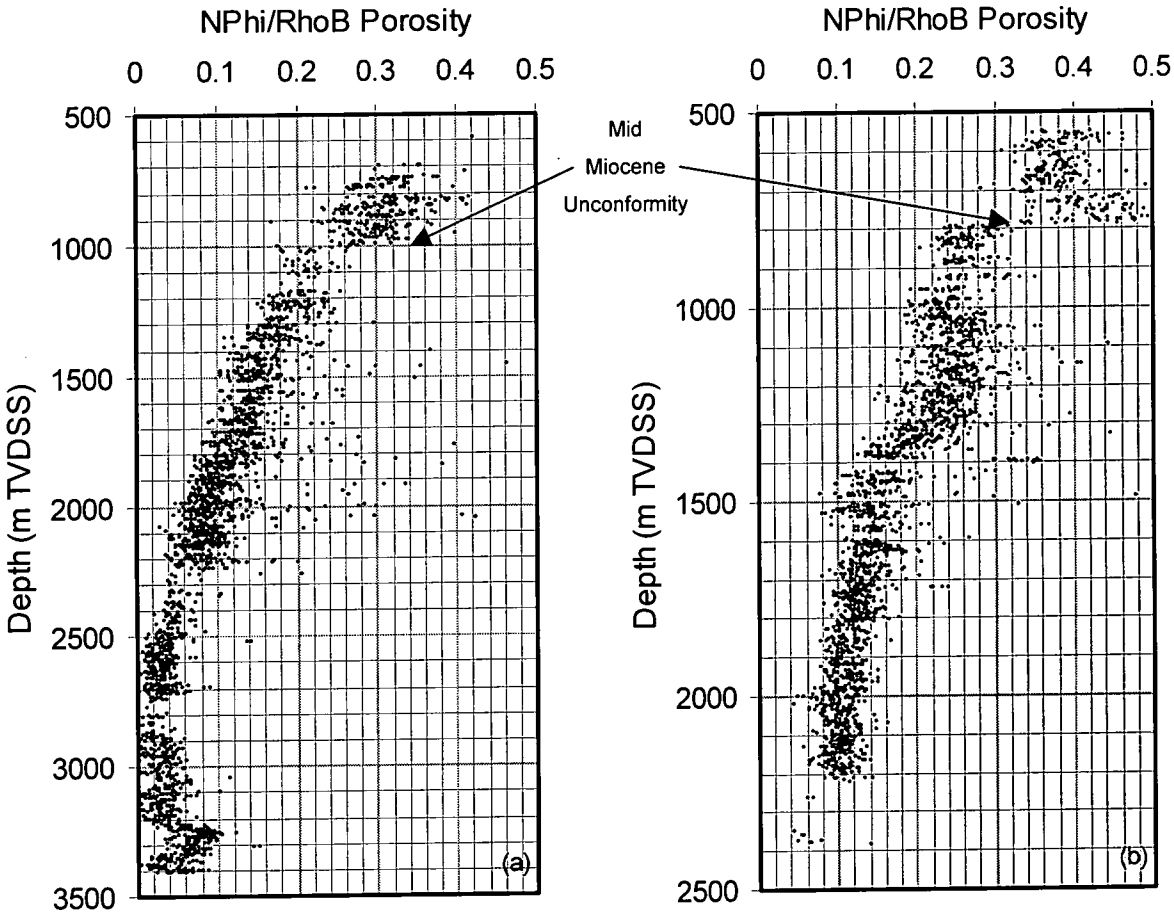

Figure 4.5 - Porosity depth plots derived from a combination of density and neutron logs for (a) Well A and (b) Well B.

The Mid Miocene Unconformity (MMU) is clearly visible in the log characteristics of both wells, at 1010m TVDSS in Well A and 770m TVDSS in Well B, indicating a abrupt apparent reduction in porosity with increasing depth and a similar change in lithology as indicated by gamma ray log signatures. Beneath this datum, lithologies are highly varied. It should be noted that the sonic log is not as heavily influenced by the lithology changes as the gamma ray and density log. The sonic and density logs suggest that compaction of mudstones stops at approximately 2000m TVDSS in both wells. This is the same depth as the onset of overpressure is noticed as measured using the MDT in the thin sandstones of both wells.

A closer examination of the trend of the density and sonic data from both wells plotted against depth under the unconformity reveals a convex-downwards shape in the upper section rather than a concave-downwards trend that would be expected if mechanical compaction of a single lithology was occurring. This convex trend is more extreme in Well B than Well A and it occurs between 1 to 1.5km TVD in both wells. It is visible in the porosity data derived from the matrix inversion technique presented in Figure 4.5 as a convex-downwards geometry within the porosity-depth plots. The data have been filtered so that lithologies with low gamma ray readings (less than

70API units above the Late Miocene Unconformity and less than 110API units below) have been removed from the analysis.

4.2.3 Further initial wireline analysis

The spectral gamma ray log data were analysed to yield information about the clay mineralogy of mudstones following methods suggested by Rider (1996) and Adams & Weaver (1958). No depth related trends in thorium-potassium and thorium-uranium ratios were found throughout the logged intervals of either wells, with indicated mudstone mineralogy remaining similar throughout both logged intervals.

4.2.4 Mudstone sample analysis

The selected mudstone samples were analysed using the techniques suggested by Yang and Aplin (1997) and described in Section 2.3 to obtain values of clay fraction and grain density. The results are tabulated in Appendix C. The analyses made at least in triplicate, enabling estimates of precision to be made. Grain density of the samples ranges from of 2.55g cm^{-3} to 2.93g cm^{-3} and clay fractions range from 49% to 74%, with values of both properties distributed evenly within these ranges.

4.3 Comparison of log trends in each well

4.3.1 Outline of study

This short study was originally performed in an attempt to show the validity of the use of Artificial Neural Networks in the analysis of wireline data to gain confidence in their use in further parts of the work. As described in Section 2.4.3 a full set of wireline logs are commonly not obtained over the full logged interval.

A method was devised to estimate density log values from density, sonic and resistivity log data using neural networks. Sets of back propagation neural networks were trained using varying training datasets from various depth intervals from single wells. Testing of these networks was then performed by comparing their estimates of bulk density with actual measurements. All work involving the application of neural networks was performed using the *BackProp* suite of programs outlined in Appendix B. The output quality of the neural network models was also compared with that of multiple linear regression models using the same training data. When the networks were presented with data from which their example dataset had been taken, their performance was high. When networks trained using data from Well B were used to estimate density log values from well A, they performed less well as those networks trained using data from Well A, with a slight (~0.05-0.1g cm^{-3}) overall underestimation of bulk density. When networks trained with data from Well A were used to recreate the density log of Well B, they produced overestimates of up to 0.2g cm^{-3} in the upper section of the well (down to 1,500m TVDSS). Below this depth, the performance of the networks vastly improved. In all situations, the ANNs outperformed the linear regression models.

The degraded performance of the models trained using data from Well A when used to estimate density logs using data from Well B compared to the opposite situation suggests that some of the lithologies encountered in Well B were not encountered in Well A possibly due to unique sediment provenances or diagenetic histories.

4.3.2 Neural network training and testing

Sets of 100 randomly selected example data, each comprising inputs of sonic, gamma ray and resistivity log values and required values of density log values from particular depth points from the entire logged interval were used to train a set of back propagation neural networks for each well. This random data selection and network training process was repeated 10 times for each well, providing 10 individually trained networks per well. Each of the networks was created using the same architecture consisting of one hidden layer of five neurons, and were trained with 5,000 training passes. The resulting numerical models were tested by comparing the desired value of density with the network estimate. Networks were rejected, reinitialised and retrained if over 5% if the estimates fell outside a 2% tolerance of the required value.

4.3.3 Use of the trained neural networks

The trained networks were used to create a set of synthetic density logs for each well. To do this, all the networks were presented with the sonic, resistivity and gamma ray data from every depth point logged. The ten synthetic logs for each well were collated and an average density estimate was calculated at each depth point together with an estimate of the standard deviation of the ten synthetic values of density. The estimate of standard deviation at each depth point was used as a measurement of uncertainty in synthetic density estimate. This process lead to the creation of four average synthetic density logs together with associated uncertainty estimates, two for each well, one where the networks were trained using data taken from the same well and the other where the networks were trained using data taken from the other well. In each case the synthetic data were compared to the expected density log values. The results of this analysis are shown in Figures 4.6 and 4.7 as crossplots.

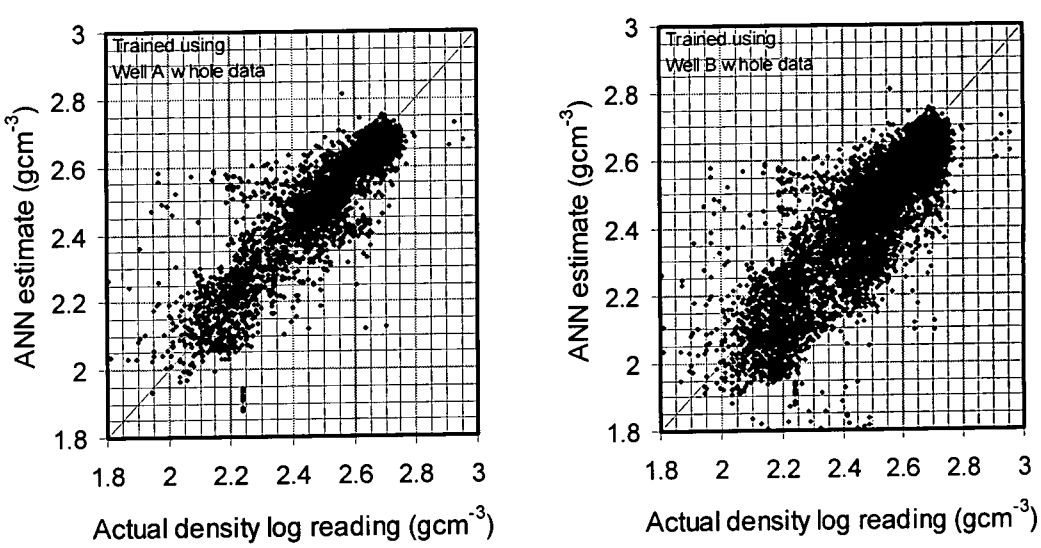

Figure 4.6 - Results of ANN creation of synthetic density log for Well A.

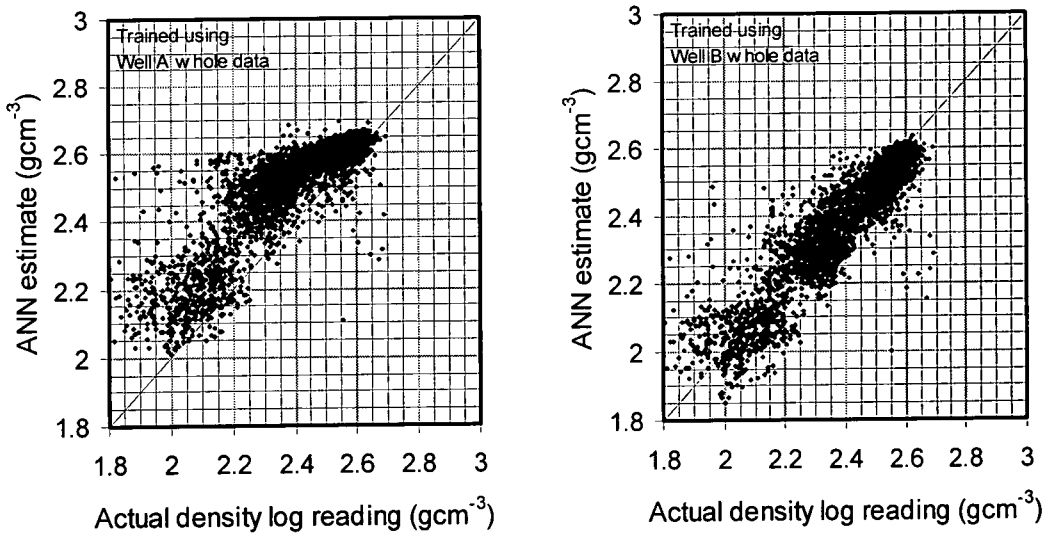

Figure 4.7 - Results of ANN Creation of synthetic density logs for Well B.

The qualitative analysis of the differences between synthetic and measured density logs are shown in Table 4.3. The misfit described when data from Well B was used to test the networks trained with data from Well B is shown in Figure 4.8. The black line in the left hand plot in this figure indicates the synthetic density log derived from the ANN modelling of the data taken from Well B and the grey line is the actual density log data. The right hand plot in the figure shows a plot of the uncertainty estimate derived from the standard deviation of density estimates at each depth. The estimate is generally too high, with the overestimate being significant in the interval just beneath the Mid Miocene Unconformity down to 1,500m sub surface.

Test data taken from:	ANNs trained using data taken from:	Quality of fit	Uncertainty Estimate
Well A	Well A	Slight underestimate in uppermost section. Good fit in mudstones (high density) beneath the Mid Miocene Unconformity (MMU) to 2,500m. There was a light underestimate of density below 2,500m.	Uncertainty was high in sands throughout the entire interval. In mudstones, the uncertainty is higher above the MMU than at any other depth. Uncertainty drops to a minimum between 1,500-2,600m, below which it rises very slightly.
Well A	Well B	Slight overestimates in mudstones predominate throughout the whole well.	Higher uncertainty than in the Well A whole ANN case.
Well B	Well A	Overestimate of density up to 2,000m. Magnitude decreases with increasing depth. Misfit is particularly pronounced over the 1,100-1,500m interval.	Variable, between 0.02-0.1g cm^{-3} with no trend apparent.
Well B	Well B	Slight underestimate throughout, especially in sandstones.	Reasonably constant error estimate in mudstones up to 2,400m depth.

Table 4.3 - Quality of synthetic density estimates using neural network models.

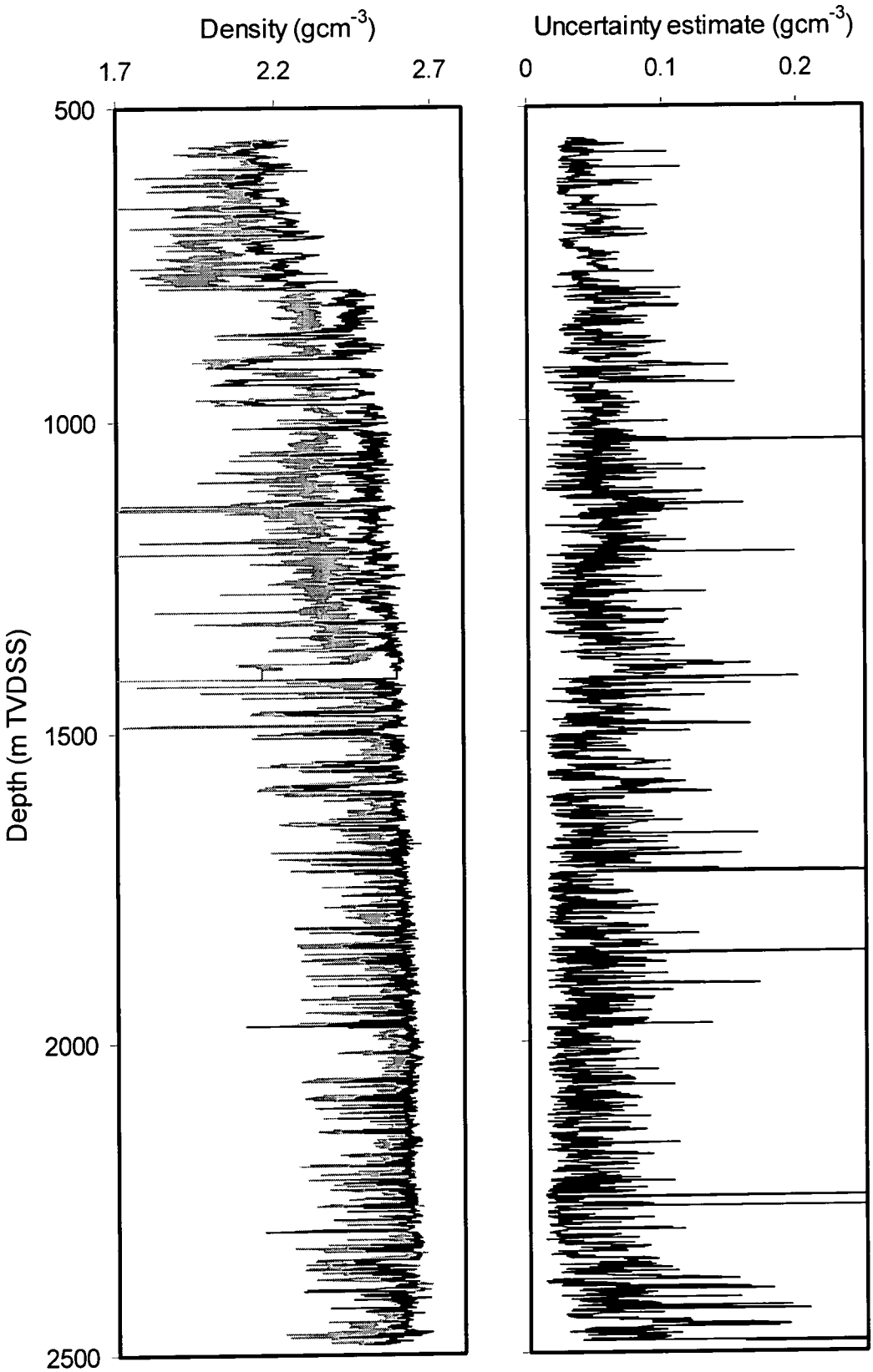

Figure 4.8 - Well B synthetic density log derived using ANNs trained using data taken from Well A.

The average uncertainty estimates over the entire logged intervals in all cases for all lithologies were 0.047-0.056g cm^{-3}. The average uncertainty for lithologies with a gamma ray reading greater than 110API was a range 0.032-0.048g cm^{-3} and that of low gamma ray lithologies was 0.054-0.073g cm^{-3}. The number of estimates that were less than 0.10g cm^{-3} and 0.05g cm^{-3} different from the actual values of density were counted in each case. The work in Chapter 3 showed that an error of 0.05g cm^{-3} would lead to an error in pressure estimate of approximately 1MPa. The accuracy of the estimates was higher when the networks were presented with data taken from the wells that were the source of training data. The accuracy of the models was higher in the high gamma ray lithologies apart from in the case where networks trained using data taken from Well A were used to estimate values of bulk density in Well A, where the accuracy was higher in low gamma ray intervals than in the high gamma ray intervals. A summary of the results of the ANN tests is shown in Table C.5 in Appendix C.

4.3.4 Multiple linear regression model creation

All the data used to train the neural networks were used to create two linear models, one for each well, describing the relationship between the values of the density, gamma ray, resistivity and sonic logs. Well A's linear model was found to be

$$\rho = 2.5539 - 0.004722\Delta T + 0.003293\gamma + 0.007431R \tag{4.4}$$

and the linear model that described the relationship between logs in Well B was found to be

$$\rho = 2.9349 - 0.007358\Delta T + 0.001809\gamma - 0.003436R \tag{4.5}$$

where density is measured in g cm^{-3}, sonic transit time in μs ft^{-1}, resistivity in Ωm and gamma ray in API units.

4.3.5 Multiple linear regression model use

Estimates of density log values in Well A made by using both linear models were plotted against actual density values and are shown in Figure 4.9. The linear model calibrated with data from Well B tends to underestimate density. The process was repeated using the entire dataset from Well B as test data, the results of which are shown in Figure 4.10. The model based on data from Well A tends to overestimate density in Well B.

The accuracy of the linear models were less accurate than their neural network counterparts. Full details regarding the accuracy statistics of the linear models and comparison with the neural network models are shown in Table C.7 in Appendix C.

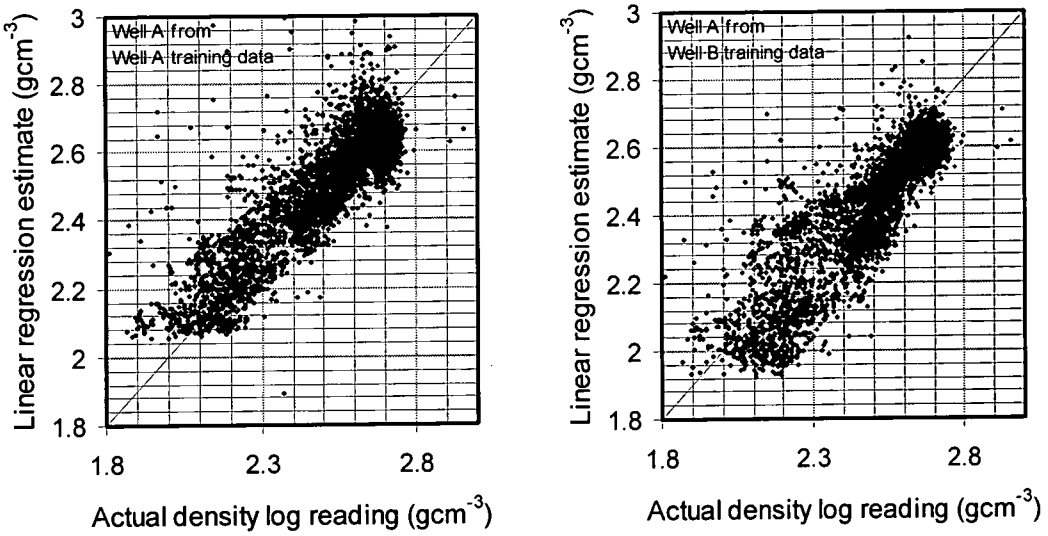

Figure 4.9 - Linear regression results from Well A.

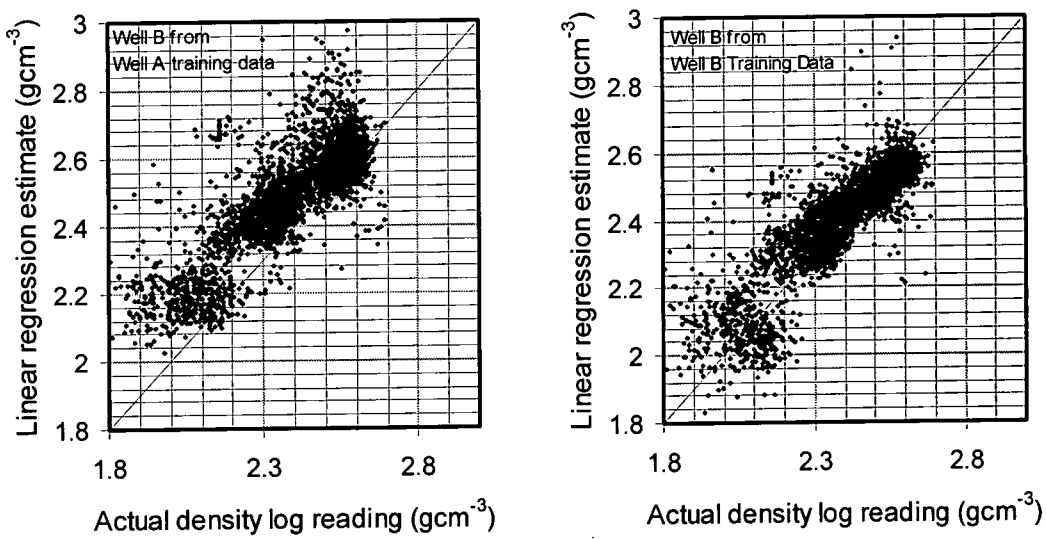

Figure 4.10 - Linear regression results for Well B.

4.3.6 Summary and discussion

The mismatch between the synthetic and actual density values in the interval of 800-1,400m TVDSS of Well B when using models calibrated with data taken from Well A suggests that there is something different in the log behaviour between the two wells. The fact that all models calibrated using data from Well B were able to produce satisfactory estimates of density in Well A, suggest that all the wireline responses encountered in Well A are also encountered in Well B. The interval between the MMU and 1,500m TVDSS in Well B contains lithologies with wireline signatures not encountered in Well A. This poor performance of the models when they were presented with

unfamiliar data highlights the need for vary careful selection of example datasets to ensure that inputs and desired outputs span the parameter space and the need for considerable amounts of model testing before their use with 'blind' datasets.

The linear regression models did not perform as well as the neural network models in all cases. This is possibly due to the fact that the neural networks can handle non-linearity in data and that they are not constrained by a pre-assumed mathematical model.

4.4 Pressure modelling

4.4.1 Outline of study

In both wells the onset of overpressure defined by MDT pressure measurements coincides with the depth at which the sediments seem to cease compacting. This may suggest that the sediments are behaving in a manner predicted by soil mechanics theory. In this study sonic-derived porosity data taken from below the Mid Miocene Unconformity in the interval that was considered normally pressured, since pressure measurements in associated sands suggested hydrostatic conditions, were used to define compaction trends for the sediments for each well. Separate compaction trends were calculated for groups of sediments of similar gamma radioactivity. These compaction trends were based on soil mechanics principles, in which sediment void ratio is related logarithmically to vertical effective stress. The compaction curves were then used to create estimates of vertical effective stress, and hence pore fluid pressure, throughout the logged intervals of both wells beneath the Mid Miocene Unconformity. The pressure estimated in mudstones agreed well with the measured pressures in neighbouring sandstones. The underlying assumption in this analysis is that the sediments are at their point of maximum burial at the time of measurement; since the Mid Miocene Unconformity is thought to represent a major uplift and erosion event, this may not be the case.

4.4.2 Creation of compaction trends

Harrold's (2000) data picking strategy was used to gather density and sonic log data grouped according to the value of the gamma ray log at the same depth. The gamma ray values were used to define a set of gamma ray lithologies, each corresponding to a distinct range of gamma ray values. The wireline data were studied and data picked where the log values were reasonably stable (within 1% tolerance) over an interval of approximately 5m. The gamma ray ranges used, together with the colour codes used in the following diagrams are shown in Table 4.4. This grouping by gamma ray was a pragmatic approach to allow for a certain amount of lithological variation throughout the logged intervals.

The density and sonic log data grouped by gamma ray value are shown in Figure 4.11. The density data do not seem to be separated with respect to the gamma ray classification. By contrast, the sonic log data of each gamma ray group can be seen to be distinct, with lower gamma ray being associated with lower sonic transit time.

Gamma ray range (API)	Colour used in diagrams
100-110	Red
110-120	Orange
120-130	Purple
130-140	Green

Table 4.4 - Values of gamma ray used for lithological grouping, and their diagram colour codes.

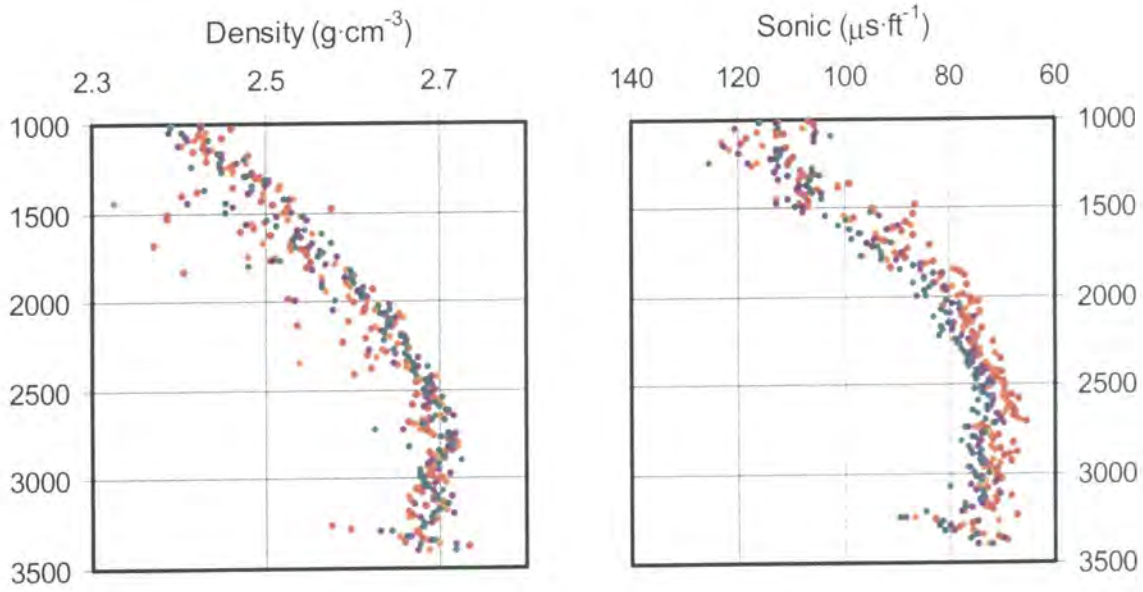

Figure 4.11 - Picked density and sonic transit time measurements from Well A grouped by gamma ray value.

Since separation in the sonic log values of different gamma ray groups at similar depths, the sonic transit time data were used to estimate void ratio for each group of data using an adaptation of Issler's (1992) calibration of Raiga-Clemenceau *et al.'s* (1988) sonic-porosity transform thus:

$$e = \left(\frac{\Delta T}{67}\right)^{\frac{1}{2.19}} - 1 \qquad (4.6)$$

where sonic transit time is measured in μs ft^{-1}. The overburden was calculated using a combination of the integrated density log, where available, and Fertl and Timko's (1972) overburden depth relationship. The hydrostatic effective stress was calculated by subtracting hydrostatic stress from the lithostatic stress at each depth point. It was assumed that the pressure regime was hydrostatic in both wells above 2,000m TVDSS since MDT measurements of pressure in adjacent sands were hydrostatic, so sonic-derived void ratio data taken from above that datum were used to obtain the compaction parameters for each group of gamma ray lithologies.

The resulting compaction trends for Well A are shown together with the data used to derive them in Figure 4.12. The compaction trends are separate over the calibration interval and are divergent at higher effective stress. At 15MPa the void ratio range suggested is 0.259 to 0.282 (20.6% to 22.0% porosity), whilst at 25MPa the range in void ratio suggested by the compaction trends has reduced to 0.123 to 0.161 (11.0% to 13.8%). The compaction parameters for each trend are shown in Table C.8 of Appendix C.

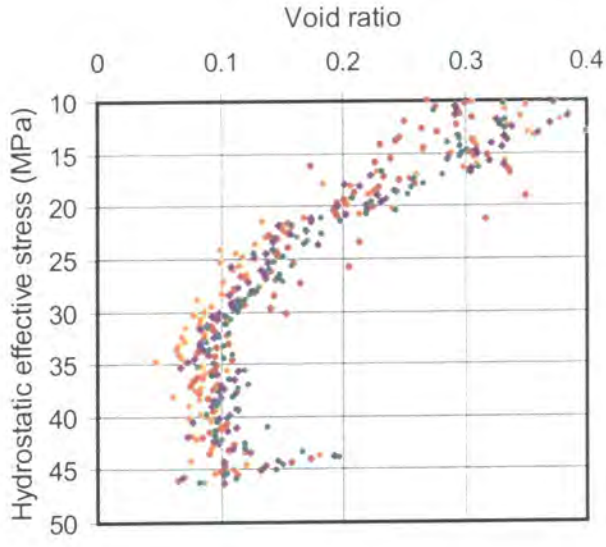

Figure 4.12 - Picked void ratio (derived from sonic log) vs hydrostatic vertical effective stress (points) and derived compaction trends (lines) associated with gamma ray for Well A.

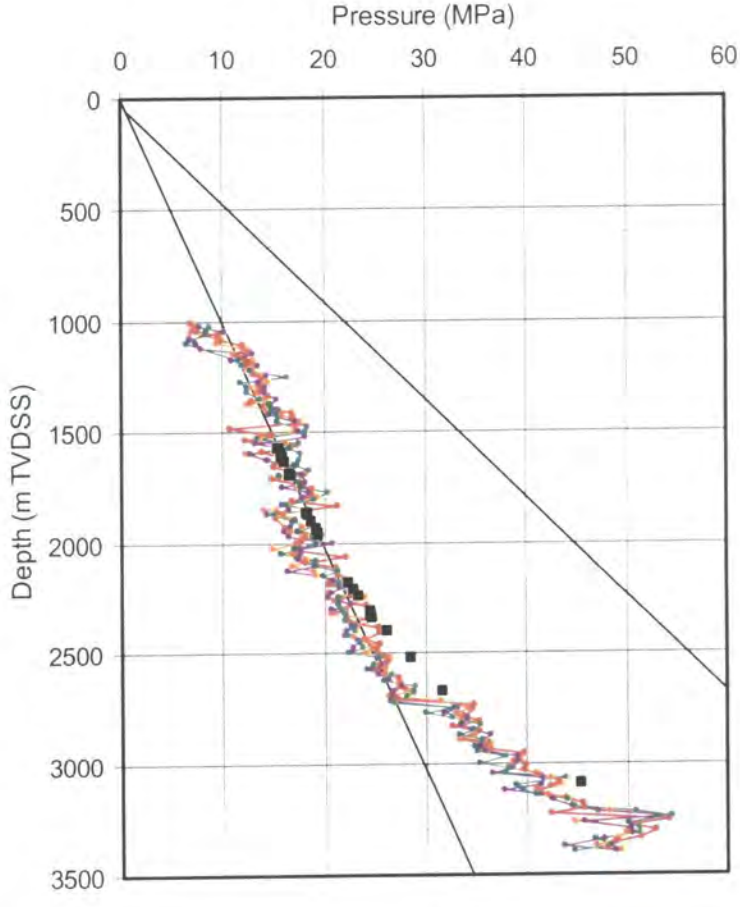

Figure 4.13 - Pressure estimation for Well A using separate, locally derived, compaction curves for lithologies grouped by gamma ray based on a void ratio-vertical effective stress method. Black squares represent MDT measurements of pressure in sand bodies.

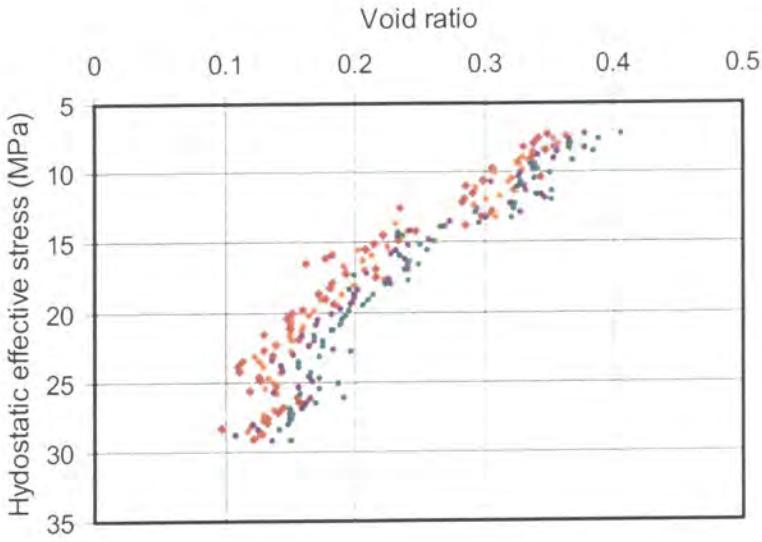

Figure 4.14 - Picked void ratio (derived from sonic log) vs hydrostatic vertical effective stress (points) and derived compaction trends (lines) associated with gamma ray for Well B.

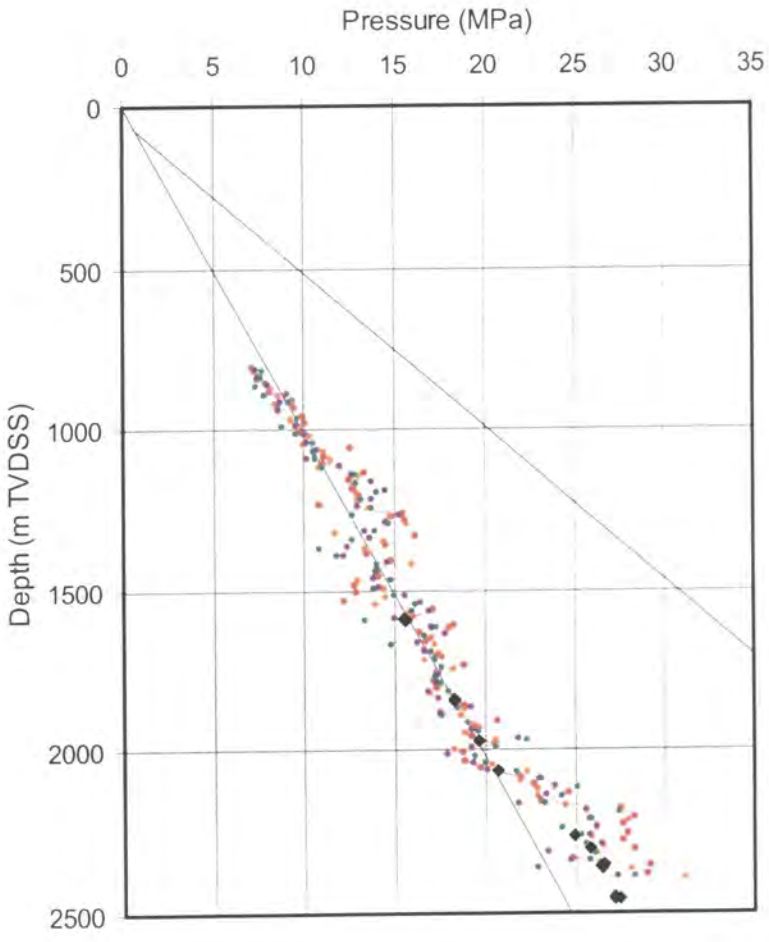

Figure 4.15 - Pressure estimation for Well B using separate, locally derived, compaction curves for lithologies grouped by gamma ray based on a void ratio-vertical effective stress method. Black squares represent MDT measurements of pressure in sand bodies.

The compaction trends derived were then used to calculate values of effective stress from the sonic-derived void ratio values throughout the logged intervals of Well A. These values of effective stress were used to calculate estimates of pressure by subtracting them from the previously calculated overburden. The resultant pressure-depth profiles are shown in Figure 4.13.

The models created suggest that the interval between 2,000 and 2,700m TVDSS is normally pressured. Beneath this depth there is a sudden 6MPa increase in estimated pressure. This corresponds to the reversal in sonic-depth trend that can be seen at 2,700m TVDSS. The process was repeated using void ratio data derived from the density log and the mismatch between estimated pressure in mudstones and the measure pressure in sands in the interval between 2,000m and 2,700m TVDSS was not present, as was the sudden pressure increase just below 2,700m. There was, however, an increase in the rate of increase of pressure with respect to depth at that depth.

The process was repeated using sonic-derived void ratio data from Well B. The sonic compaction trend in this case seems to be almost continuous, indicating lower apparent porosities with depth throughout the interval. The sonic-derived void ratio was plotted against vertical hydrostatic pressure together with compaction trends derived from the interval between 1,500m and 2,000m TVDSS and is shown in Figure 4.14. The estimation of pressure within Well B calculated using the locally derived individual lithology void ratio-vertical effective stress compaction curves and sonic derived void ratio is shown in Figure 4.15.

The compaction curves derived using data from Well B are reasonably parallel with each other over the calibration interval. The pressure estimates using data from the higher gamma ray lithologies (120-140API) shown in Figure 4.15 yield estimates of pressure in mudstones that are similar to the MDT measurements of pressure in sands throughout the entire logged interval of Well B. In both wells the lower gamma ray lithologies all produce higher estimates of pressure, typically up to 2-4MPa. As was seen in Chapter 3, this amount of error could quite easily be expected using both clay fraction-based pressure estimation techniques.

4.4.3 Summary and discussion

Mudrocks throughout the logged intervals beneath the Mid Miocene Unconformity in both wells were characterised and grouped according to their gamma ray readings at each depth point. Sonic-derived void ratio-hydrostatic vertical effective stress relationships for each gamma ray lithology were derived in what was thought to be normally pressured mudstones. These compaction trends were used to estimate pore fluid pressure in the overpressured sections in both wells. The pressure estimation attempts in Well A produced a substantial underestimate of pressure throughout the overpressured section and a significant increase in estimate of overpressure over a small interval. This increase in pressure was at the same depth as a change in logging run, so part of the discrepancy could be ascribed to poor calibration of the sonic tools used, since the density log did not show such a significant change in character over the same interval. The attempts in Well B were more successful when using high gamma ray lithologies, however the limited extent of the overpressured section in the well may have some bearing on this result: there were simply very few pressure data to match.

The fact that the sonic transit time to void ratio was calibrated using data for a single lithology from the Beaufort-MacKenzie Basin, Canada suggests that poor calibration of the sonic transform could contribute significant amounts

of error to the pressure calculation; however, this error is likely to be systematic, due to the pervasive use of the sonic transform throughout the study. During the calculation of pressure, the effects of the systematic error may be reduced since the compaction curves were defined using the void ratio data derived using the same transform as that used to estimate values of void ratio.

This analysis was performed to demonstrate what would be done to produce an initial pressure estimation. The normal compaction curves were derived using simple data beneath the Late Miocene Unconformity. The approach is entirely empirical since the possible uplift and chemical compaction of the sediments would negate the assumptions made for pure mechanical compaction of sediments at maximum effective stress at the present day.

The void ratios estimated using the derived compaction trends shown in Figure 4.12 all reach zero at vertical effective stresses of above 40MPa. This suggests that the use of these compaction models is unadvisable at high effective stress.

4.5 Estimation of uplift using generic compaction curves

4.5.1 Outline of study

Generic compaction curves suggested by Yang & Aplin (2000) were used to define possible normal compaction trends that could be used to describe the compaction behaviour of the sediments in both wells studied. The compaction of mudstones above the Mid Miocene Unconformity could be reasonably described by a single high clay fraction compaction curve; however, the similar compaction beneath the unconformity could only poorly described by unreasonably low clay fraction compaction curves.

The well operator's pre-drill reports suggest that the Mid Miocene Unconformity is associated with a significant amount of uplift. A method similar to that employed by Hillis (1995) and Hansen (1996b) was used to quantify the maximum amount of apparent uplift that is suggested by the overconsolidation of the mudstones beneath the unconformity.

The amount of uplift associated with the Mid Miocene Unconformity in each well was calculated using a numerical method. Well A exhibited evidence for 450m apparent uplift. The behaviour in well B was more complex with three apparent zones of uplift. If a monolithological model was used, the interval between 1,000 and 1,300m TVDSS was associated with an uplift value of 195m and the intervals between 800 and 1,000m, and 1,500 and 2,000m TVDSS were associated with an uplift of 360m. The values of uplift in both sections were made equal if the assumed clay fraction in the central section was increased from 60% to 70%. These values of apparent uplift are equivalent to actual uplift and erosion of 1,380m and reburial down to 930m in Well A and uplift and erosion of 1,110m and subsequent reburial of 800m in Well B.

4.5.2 Use of generic compaction curves

The neutron & density log-derived porosity trends for both wells were compared to two of the generic compaction trends defined by Yang & Aplin (2000). The porosity data were filtered so that only neutron and density data from depth points where the corresponding gamma ray reading was between 100 and 110API were selected and used in

the rest of the analysis. The generic trends selected were 60% and 30% clay fraction trends assuming a 2.75g cm^{-3} grain density and were created using the method described in Appendix D. The comparisons are shown in Figure 4.16. The plots for both wells show that the compaction of the sediments above the Mid Miocene Unconformity are reasonably well described by the 60% clay fraction compaction trend. The 30% clay fraction curve fits some of the porosity trend below the MMU in both wells, however, measured clay fractions in Well A are around 50%-60% so the 30% clay fraction curve may not be the best compaction curve to use in this situation. A more complicated geological history may have to be employed.

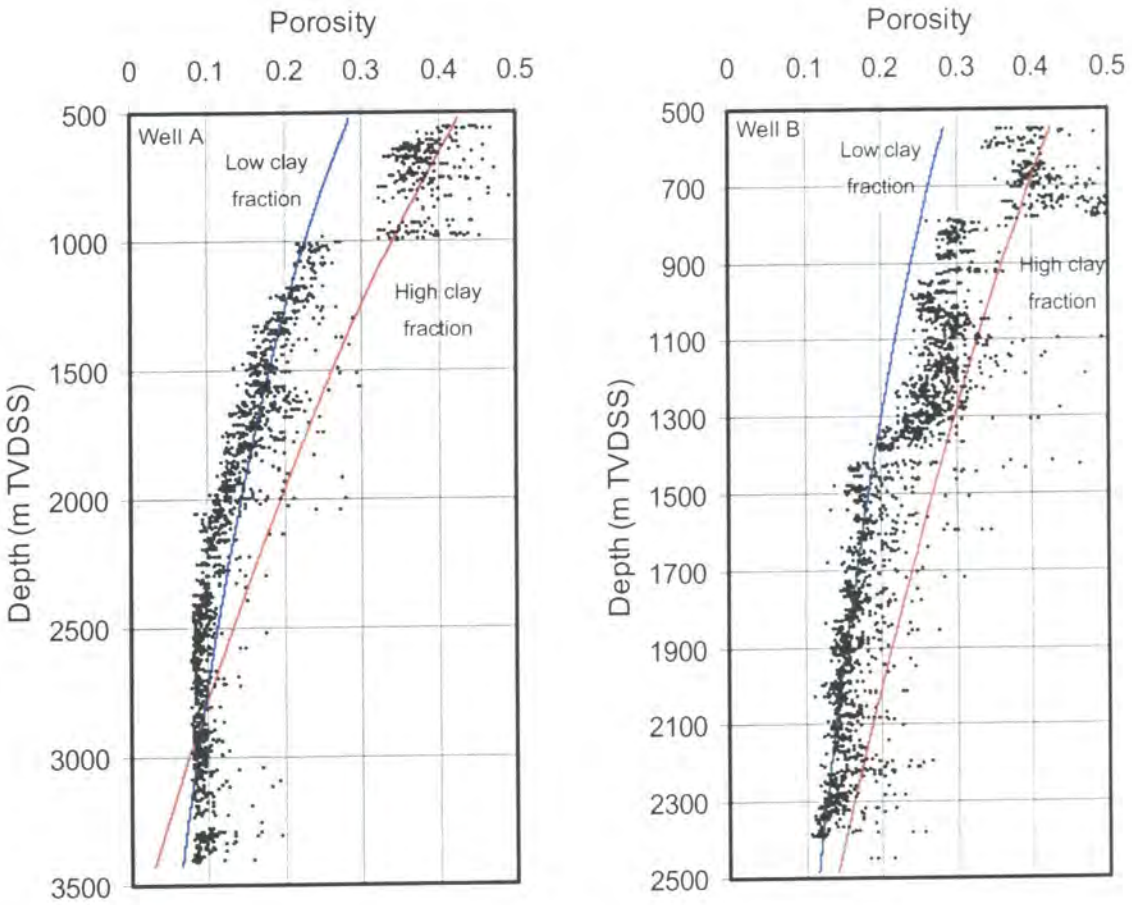

Figure 4.16 - Density-derived porosity plots compared to high and low clay fraction generic compaction curves.

4.5.3 Quantification of uplift, erosion and reburial

This portion of work is applies methods developed by Hillis (1995) for quantification of uplift in the Cretaceous and Jurassic of the British Sector of the Southern North Sea. Sonic compaction trends were used in the British Study, whereas the methodology described below involved the use of neutron and density-derived porosity trends. The sediments below the Mid Miocene Unconformity in the Gulf of Thailand were assumed to be overconsolidated. This overconsolidation was assumed to be due to uplift, erosion and subsequent partial reburial of the sediments. It was assumed that elastic expansion of the sediment on unloading was negligible and so the void ratio of the

sediments recorded the effects of the maximum stress state to which those sediments had been subjected. An initial simplification was made in that it was assumed that the compaction of all the sediment could be described by a single compaction curve. Later, this assumption was relaxed to allow the consideration of two compaction trends.

The methodology is set out as follows. In the overconsolidated section it was assumed that the present day void ratio could be used as a proxy for the maximum effective stress thus

$$\sigma_{v\text{-max}} = 100\exp\left(\frac{e_{100} - e}{\beta}\right) \tag{4.7}$$

where $\sigma_{v\text{-max}}$ is the maximum vertical effective stress encountered measured in kPa. Yang & Aplin's (2000) compaction trend for a 60% clay fraction lithology with a grain density of 2.75g cm^{-3} was used to create a porosity depth trend and a hydrostatic effective stress-depth trend for normally pressured sediments by using the procedure outlined in Appendix D. This yielded the following

$$\sigma_v = 5.95 z_{SM} + 0.002334 z_{SM}^{\ 2} - 2.212\times10^{-7} z_{SM}^{\ 3} \tag{4.8}$$

Combination of Equations 4.7 and 4.8 yields an equation that can be solved numerically, i.e. using the Newton-Raphson method (e.g. Boas, 1983), described in Appendix E, to produce an estimate of maximum burial depth from void ratio data provided by the wireline logs.

$$5.95 z_{SM} + 0.002334 z_{SM}^{\ 2} - 2.212\times10^{-7} z_{SM}^{\ 3} - 100\exp\left(\frac{e_{100} - e}{\beta}\right) = 0 \tag{4.9}$$

This relationship does not simply shift a porosity-depth trend parallel to the depth axis; it considers the effects of the changing overburden gradient with respect to depth due to compactional increase of bulk density. The amount of apparent uplift of each point was calculated by subtracting the actual burial depth from the maximum burial depth.

The base data sets for both wells were the gamma ray-filtered porosity data used in the previous section.

The average value of the apparent uplift estimate in Well A was found to be 450m. The analysis in Well B was more complex, with two separate zones of interest, one between 1,000m and 1,300m (apparent uplift of 195m) and the other 1,500-2,000m (apparent uplift 360m). A porosity-depth plot of data taken from Well A is shown in Figure 4.17 together with an indication of two 60% clay fraction compaction curves, the blue curve showing the fit between the uplifted compaction curve and the observed data. Two plots of the porosity depth data for Well B are shown in Figure 4.17; the blue curve in each case is the uplifted 60% clay fraction curve showing the effects of 195m and 360m. The amount of apparent uplift is shown in the top left hand corner of each porosity depth plot.

The sediments in the interval between 1,000 and 1,300m TVDSS in Well B appear to have been uplifted by a smaller amount than the surrounding sediments. The density log responses over the same interval were significantly different to the log responses of Well A. This difference may not be due to different amounts of uplift as the porosity of the sediments above and below the interval in question can be modelled by using a single uplift value.

Another possibility is change in lithology. The required change in lithology was calculated using the methodology described in Appendix D.2 whilst assuming that the apparent uplift was fixed at 360m. The required clay fraction was 70%.

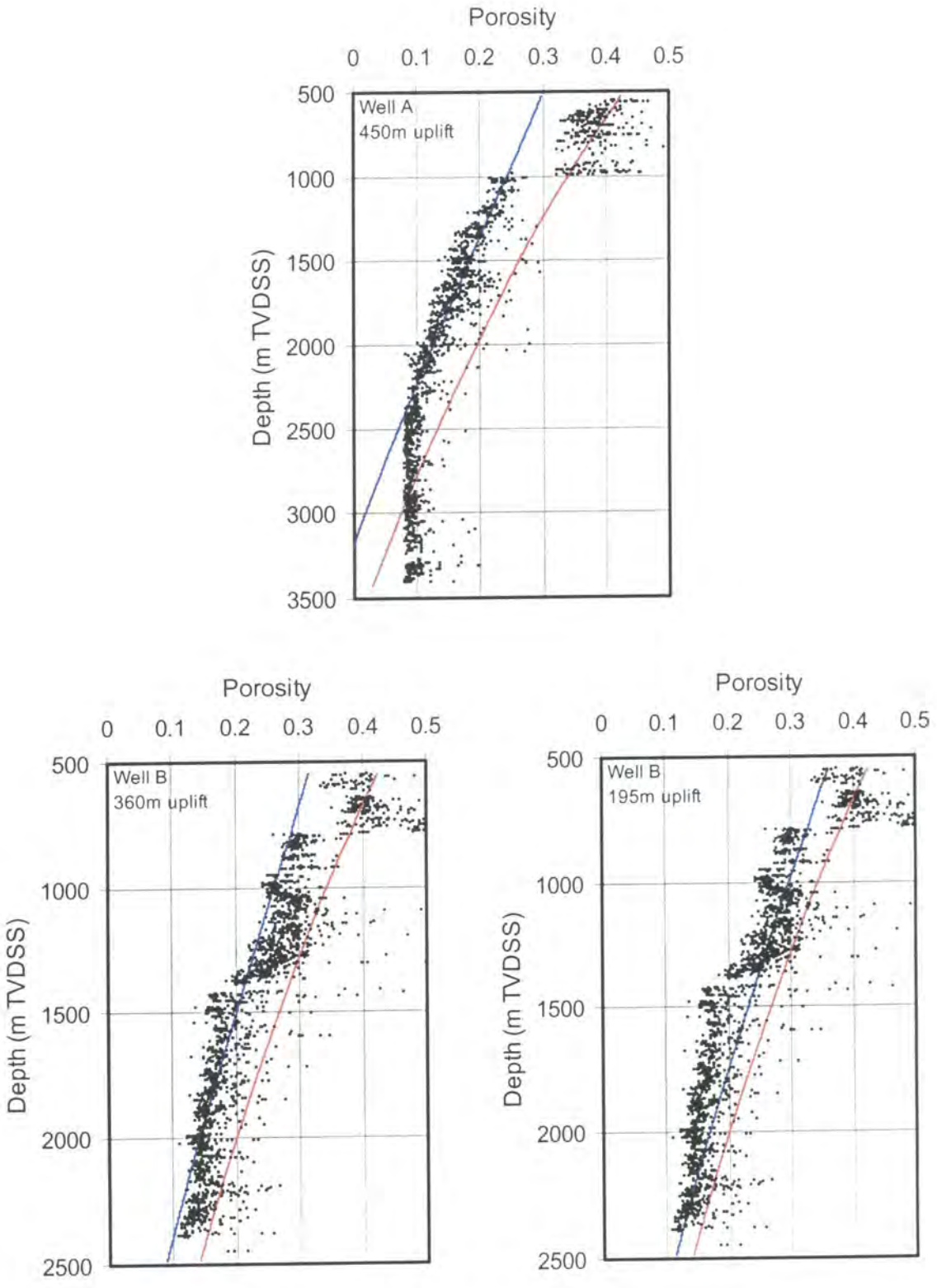

Figure 4.17 - The effect of uplift and partial on the 60% clay fraction compaction trend.

4.5.4 Summary and discussion

Generic normal compaction trends with sensible lithological parameters cannot be used to adequately describe the observed porosity-depth trends in both wells. The operator of the wells has stated that regional seismic evidence and other regional studies in neighbouring basins suggest that the Mid Miocene Unconformity is associated with a regional uplift and erosion event. Wireline analysis was used to quantify the amount of uplift experienced by the areas surrounding both wells during the inversion event. The wireline data in Well A suggest an apparent uplift of 450m, whereas the apparent uplift value of Well B is 360m.

It is important to note that an apparent uplift corresponds to erosion of the sum of the current burial depth of the erosive surface plus the apparent amount of uplift followed by reburial of the erosive surface. Thus the erosive surface in Well A was initially buried to a depth below the sea bed of 1,380m, brought back to the surface and then reburied to 930m. Similarly, the erosive surface in Well B was buried to a depth of 1,160m before being brought back to the surface by erosion and partially reburied to 830m.

The modelling of uplift in Well B requires a model using two mudstone lithologies, one being a 60% clay fraction and the other being a 70% clay fraction.

Other mechanisms could cause the overconsolidation in comparison to normal compaction trends, such as chemical compaction and lateral compression. The conversion of smectite to illite has been observed to change compaction trends significantly in the Gulf of Mexico (Lahann, 2000). The temperature required for this is 60-70°C, this temperature is achieved at quite shallow depths (950m) in Well B but since the clay mineralogy throughout the well is broadly constant, this mineral change is unlikely to contribute to any compaction.

The uplift and reburial model potentially does not account for the high overpressures encountered at the base of Well A. Modelling by Luo & Vasseur (1995) suggests it is likely that any overpressure that had developed before the inversion would have dissipated during uplift. If the overpressure dissipated during uplift, the sediments would have compacted to match the effective stress at any depth. However, if the rate of uplift was sufficiently high all the observed sediments would have been overconsolidated with respect to their depth at the end of the inversion event, therefore no compaction due to dewatering of sediments would take place during uplift. If Luo & Vasseur's (1995) model is correct any overpressure that is measured at the present day was created after the Mid Miocene. Since the porosity of the sediments in the overpressured section is very low and hence the permeability of the same is correspondingly low, it is likely that some fluid was retained during inversion so some overpressure could have been maintained. The observed overpressure at depth is due to disequilibrium compaction before and after the Mid Miocene inversion event.

4.6 Discussion and conclusions

4.6.1 Comparison of log trends

The poor output quality of the artificial neural networks trained using data from the upper section of the wells when presented with data from the lower sections shows the importance of using well calibrated models. The reason for the poor quality of the density estimates in the upper section is that the majority of the training data were taken from

below the MMU. Many authors (e.g. Beale & Jackson, 1990; Dowla & Rogers, 1995) have claimed that ANN techniques are efficient at making generalisations. This is true, but their quality can only be as high as that of the data with which they have been trained. They produce the best results when they are presented with test data taken from the same interval from which the training data were extracted and the task is as simple as possible.

The fact that the networks and linear regression models trained and calibrated using data taken entire logged interval of Well A produced poor estimates of bulk density between 800m and 1,500m in Well B suggests that the lithologies encountered in that interval were not encountered in Well A. This type of observation may be useful in the comparison of wireline data from separate wells.

It is important to note that the networks used in the study were not biased by supplying them with depth data. This biasing was attempted, but the marginal improvement in local performance with test data from the same well as the training data was negated by the degradation of performance when the networks were presented with data from other wells. Attempts at biasing the networks were rejected to maintain the objective nature of the analysis.

4.6.2 Compaction and pressure studies

A simple, monolithological compaction model is not suitable for the description of the complex porosity-depth trends encountered in both wells from the Gulf of Thailand.

It is possible to describe the majority of the porosity profiles of both wells by using several compaction curves derived by Yang and Aplin (2000). The clay fractions required to match the profile at depth (30-35%) in both wells are unreasonably low since measurements of clay fraction in mudstones yield values greater than 50%.

Assuming no non-mechanical compaction occurred, an apparent uplift of 450m was estimated in Well A. This would entail the removal of 1,380m of sediment during the inversion followed by the deposition of 930m of new sediment. This model is compatible with the observed pressure at the present day. The amount of apparent uplift in Well B is 360m. This value of apparent uplift corresponds to the removal 1,090m of sediment followed by 830m reburial. This amount of uplift lies within the estimated range of uplift described by the operator of the wells.

The analysis of data from Well B is complicated by a potential lithological change, in that sediments in the interval between 1,000-1,300m TVDSS have a different log character and porosity depth trend to the surrounding sediments. The porosity of the surrounding sediments are matched with a 60% clay fraction mudstone's compaction trend, whilst the observed porosity trend within the interval can be matched with a 70% clay fraction mudstone's compaction trend.

4.6.3 Conclusions

- The origin of overpressure in the area is disequilibrium compaction.
- Artificial neural networks outperformed multiple linear regression techniques in the estimation of bulk density from sonic, resistivity and gamma ray wireline data.

- A set of 25 mudstone samples was fully characterised. Measured matrix densities range from 2.58g cm^{-3} to 2.93g cm^{-3} and clay fractions range from 53% to 74%.
- The sediments below the Mid Miocene Unconformity of both wells examined were overconsolidated.
- This overconsolidation suggests that the unconformity surface has undergone up to 1,300m of uplift and it has been reburied by up to 900m.

5 GULF OF MEXICO CASE STUDY

5.1 Introduction

5.1.1 Chapter summary

This chapter develops the use of wireline compaction analysis to evaluate the quantity of overpressure in an area of the deepwater (1,200m water column) Gulf of Mexico. It concentrates on three wells, W, Y and Z situated in the same salt-bounded minibasin. The oldest sediments encountered in the wells are late Pliocene in age at a depth of 6,400m TVDSS. The sedimentation rate is very high, which helps to explain why only the top 600-700m of each well is normally pressured. The only wireline data that were obtained over the shallow interval were from the gamma ray and resistivity logs so no local calibration of the porosity logs could be performed in the normally pressured section. Generic compaction curves were used in conjunction with artificial neural network estimates of lithological parameters to evaluate the pressure in mudstones at depth. This method provided reasonable estimates of pressure in mudstones in comparison with RFT measurements in associated sand bodies.

Two pressure transition zones were observed in Well W. Detailed analysis of all available wireline data suggests that one of them could be caused by a layer of particularly fine grained material acting as a permeability barrier to fluid flow. This agrees with the well operator's model of the hydrodynamics of the minibasin.

5.1.2 Aims

This chapter describes a pressure study performed on wireline log data taken from three deep-water wells W, Y and Z. The company providing the data has requested that the location of the wells is kept confidential. The aims of the studies were:

- To use standard pressure evaluation techniques to ascertain the pore pressure regime in all wells.
- To use Yang and Aplin's (2000) compaction models to estimate shale pressures in two ways:
    - Uncalibrated, assuming grain density and clay fraction in each well.
    - Calibrated using clay fraction and grain density estimates derived from the *ShaleQuant* software (Aplin *et al.*, 1999).
- To compare clay fraction and porosity estimates from *ShaleQuant* software with clay mineral content and porosity estimates and gamma ray measurements derived from standard petrophysical techniques.
- To attempt to explain the pressure transition zones observed in Well W in terms of one-dimensional processes.

5.1.3 Geological setting

The three wells are situated within 14km of each other, in the Northern Deep Gulf of Mexico, under approximately 1,200m of water. They are situated within a single salt-bounded minibasin. The oldest rocks penetrated are Late Pliocene in age at a depth of 6,400m TVDSS (5,200m TVD sub sediment surface). This corresponds to an average sedimentation rate of 2-2.1km Myr^{-1} corrected for the effects of compaction.

The basin origin, depositional history and salt tectonics of the Gulf of Mexico area are described in detail by several authors (Salvador, 1991; Weimer *et al.*, 1998a; Weimer *et al.*, 1998b; Villamil *et al.*, 1998; McBride, 1998). The basin began to form in two north-south rifting episodes in the Late Triassic and the Middle Jurassic. Associated with the second period of rifting was the deposition of a thick layer of salt. Oceanic spreading occurred in the Late Jurassic. During the Cretaceous, thermal subsidence occurred, with the newly formed oceanic crust at the basin centre subsiding at a higher rate than the continental crust at the basin margins. In the early Cenozoic regionally extensive depocentres became established in continental to shallow water situations of the Northwestern Gulf Basin. During the Miocene, the deposition in the Gulf switched from west to east, so that the entire sediment production of the central portion of Northern America was deposited to the south of Louisiana. This has continued to the present day. The distal continuation of this sedimentation resulted in the deposition of thick turbidite deposits. The weight of the rapidly deposited Cenozoic sediments caused the remobilisation of the Jurassic salt that has caused the formation of many minibasins across the area. The diapirism associated with the salt remobilisation has caused complex topographic styles that have controlled local sedimentation patterns.

The very high sedimentation rate is a principal contributory factor to the onset of extensive overpressure in the entire Gulf Coast region (e.g. Mann & MacKenzie, 1990; Mello *et al.*, 1994). Thus, significant amounts of overpressure are expected in the thick mud-dominated sediments of the study area.

5.1.4 Data supplied

The wireline data supplied by the operator comprise gamma ray and resistivity from within 50m of the sediment surface in each well together with the full complement of sonic, resistivity, density, neutron and gamma ray in the 12¼" and smaller holes. The wireline log data were supplied in paper and digital form. Pressure data are made up of RFT measurements in well W and mudweight estimates of pressure in wells Y and Z. The wireline log and ancillary data made available for the study are shown in Figures F.1 to F.7 in Appendix F.

5.1.5 Pressure regime

As expected, the pressure measurements in the sandstones encountered in Well W indicate significant amounts of overpressure. There are four distinct pressure regimes indicated within the RFT data. There is a high pressure measurement of 1.48g cm^{-3} equivalent mudweight (18.5MPa) at 4,517m TVDSS. The degree of overpressure declines to 17-17.5MPa between 4,600-5,000m. There is a very narrow pressure transition zone between 5,000-5,010m, with overpressure increasing to 25MPa (1.55g cm^{-3} equivalent mudweight). This mudweight is relatively constant between 5,012m and 5,652m TVDSS. Below this, there is another narrow pressure transition zone, with pressure increasing from 28.0-32.4MPa over 80m, which corresponds to an increase in equivalent mudweight from 1.55g cm^{-3} to 1.63g cm^{-3}.

The mudweight estimates of pressure in Well Y and Well Z are far less descriptive of the actual pressure regime encountered. Therefore, they have not been interpreted as closely. They indicate overpressures of similar magnitude to those encountered in well W were expected whilst drilling the two wells.

5.2 Initial analysis

5.2.1 Quality control of wireline data

The caliper log, where available, was examined to determine hole quality. All data points where the hole was over 38mm (1.5") out of gauge were removed from the wireline dataset. This involved the removal of less than 1% of data points. The quality controlled log data are shown in Appendix F, Figures F.2-F.7

5.2.2 Wireline log description

In each well there is an overall increase in gamma ray response with depth, suggesting a possible coarsening upwards trend, between 1,500-1,700m TVDSS and the sea floor. Below this depth to 4,000m, the gamma ray ranges between 60-100API in Wells W and Z, and 80-120API in Well Y, apart from sandstone incursions indicated by large reductions in gamma ray. In the deepest parts of each well, the gamma ray shows no major trend, apart from sharp changes between possible mudstone lithologies. The sandstone bodies are mainly thinner than 25m, apart from a major sand body approximately 100-150m thick at 5,000-5,100m, 4,800-4,950m and 5,050-5,150m TVDSS in Wells W, Y and Z, respectively.

The resistivity logs for the three wells all show the same broad features. As the gamma ray increases downwards over the first 300m of the logged interval, the resistivity increases. The resistivity continues to increase with depth until 3,000-3,500m. The gradient of the overall trend reduces with respect to depth. The actual resistivity reaches a local maximum at 3,300m in Well W and 4,000m in Wells Y and Z. The resistivity is strongly influenced by lithology, with marked deviations from the mudstone trend in the sandstones as identified by the gamma ray log. In the upper section, there is a large reduction in resistivity in the sands compared to the mudstones, whereas in the lower section this relationship is reversed in Wells W and Z, indicating the presence of hydrocarbons in the pore fluid (Rider, 1996).

More complete suites of logs were acquired in the 12¼" and smaller holes. On first inspection, the data from each well show similar trends. The gamma ray shows clear differentiation between sands and mudstones, the sonic transit times of the sands are typically 20-40μs ft^{-1} greater than those of the mudstones and the density measurements in the sands are 0.2g cm^{-3} less than those in the mudstones. An increasing trend in the density log and a decreasing trend in the sonic log with depth is exhibited by the mudstones in the upper 200m fully logged section of Well Y. This could be due to some limited compaction.

On closer inspection there are very slight differences in the log characteristics of different sediment packages. In Well W there is a gradual increase in density between 5,100m and 5,200m TVDSS. Over the same interval the sonic, density, resistivity and neutron logs are all constant. This may indicate a gradual change in lithology or pore fluid composition. In Well Z there is an overall decrease in sonic value with depth in mudstones, whereas their

density log signature is relatively constant. Detailed examination of the data from Well Z reveals that there are two distinct sediment packages between 5,300m and 5,500m, separated by a sand body, in which the overall gamma ray signature is similar. However, both the density log and sonic log values of the lower package are smaller than those of the upper package. This is not to be expected from simple porosity models where an increase of porosity would be indicated by a decrease in density and an increase in sonic log value. Over this interval, more subtle changes are occurring.

5.3 Lithological assessment using wireline logs

5.3.1 Outline

This study involved mudstone lithology assessment using gamma ray, the matrix inversion technique involving neutron and density logs discussed in Section 2.2.1 and used in Section 4.2.2, and the *ShaleQuant* artificial neural network technique presented by Aplin *et al.* (1999). The lithological and porosity estimates derived using the various methods were compared and contrasted.

The comparison of the lithology estimation techniques were possible only in the 12½" interval of each well as the full suite of logs were only recorded in this interval in each well. Above this interval in each well, the resistivity and gamma ray logs were the only ones to be recorded and the gamma ray was used as the lithological discriminant.

All three methods of lithological identification yielded broadly similar results, although the neutron-density calculation seemed to suggest a more varied set of mudstone lithologies than the other two methods did. There was a broad similarity between the *ShaleQuant* model's estimates of clay fraction and the corresponding gamma ray reading, although the former output was clearly influenced by other parameters, this suggests that the *ShaleQuant* model is highly influenced by gamma ray reading.

A further examination of the lithology and porosity data derived from both the neutron-density and *ShaleQuant* models suggest that beneath 4,000m TVDSS in each well the lithology exerts a major influence on porosity. The pressure in the wells at these depths is very high and hence compaction is unlikely to be taking place.

5.3.2 Lithological analysis using gamma ray, neutron and density logs

The range of values for the gamma ray logs of each well were analysed. All gamma rays lay between 0 and 150API. A simple Vshale model was created by normalising the gamma ray log so its values lay between 0 and 100. This was achieved by dividing all values of the logs by 1.5 to provide an estimate clay content log for each well.

The neutron and density logs, where available, were used to provide the inputs to the matrix inversion technique discussed in Sections 2.2.1 and 4.2.2. The model was centred on the solution of the following equation at each depth point.

$$\begin{pmatrix} v_{clay} \\ v_{quartz} \\ \phi \end{pmatrix} = \begin{pmatrix} 2.75 & 2.65 & 1.05 \\ 0.4 & 0 & 1 \\ 1 & 1 & 1 \end{pmatrix}^{-1} \begin{pmatrix} \rho_b \\ \phi_N \\ 1 \end{pmatrix} \tag{5.1}$$

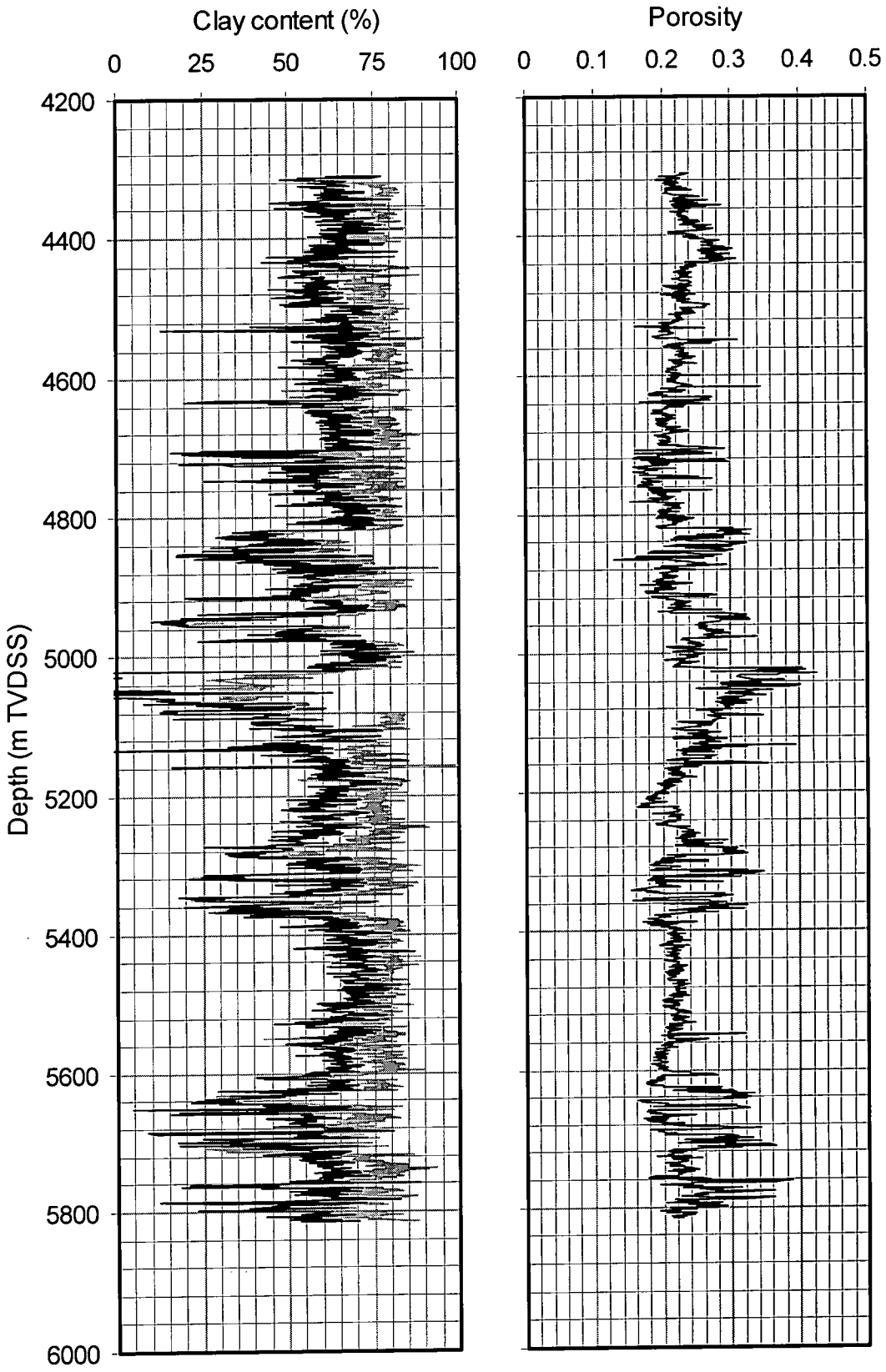

Figure 5.1 - Well W lithological and porosity information from neutron-density matrix inversion.

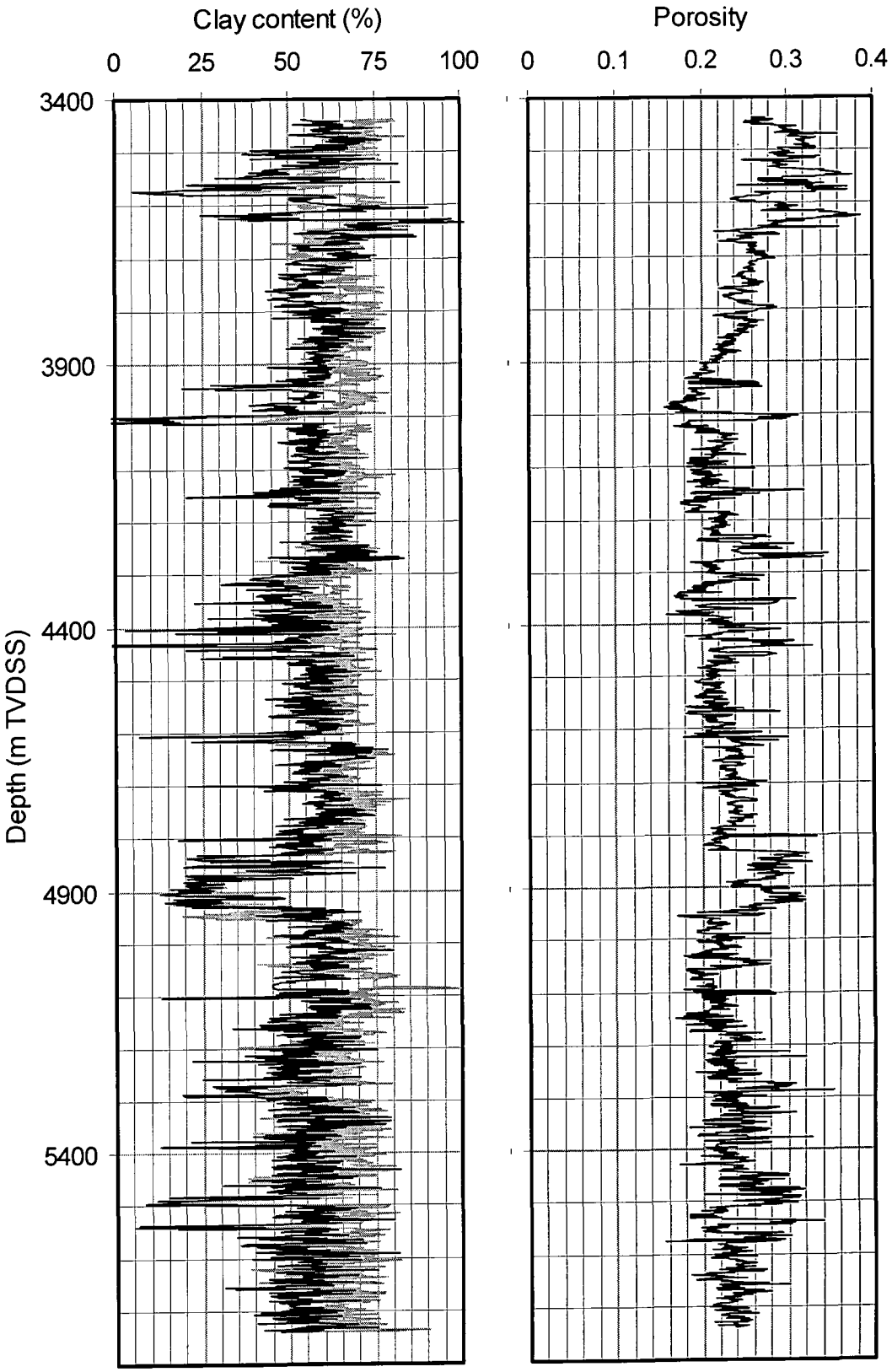

Figure 5.2 - Well Y lithological and porosity information from neutron-density matrix inversion.

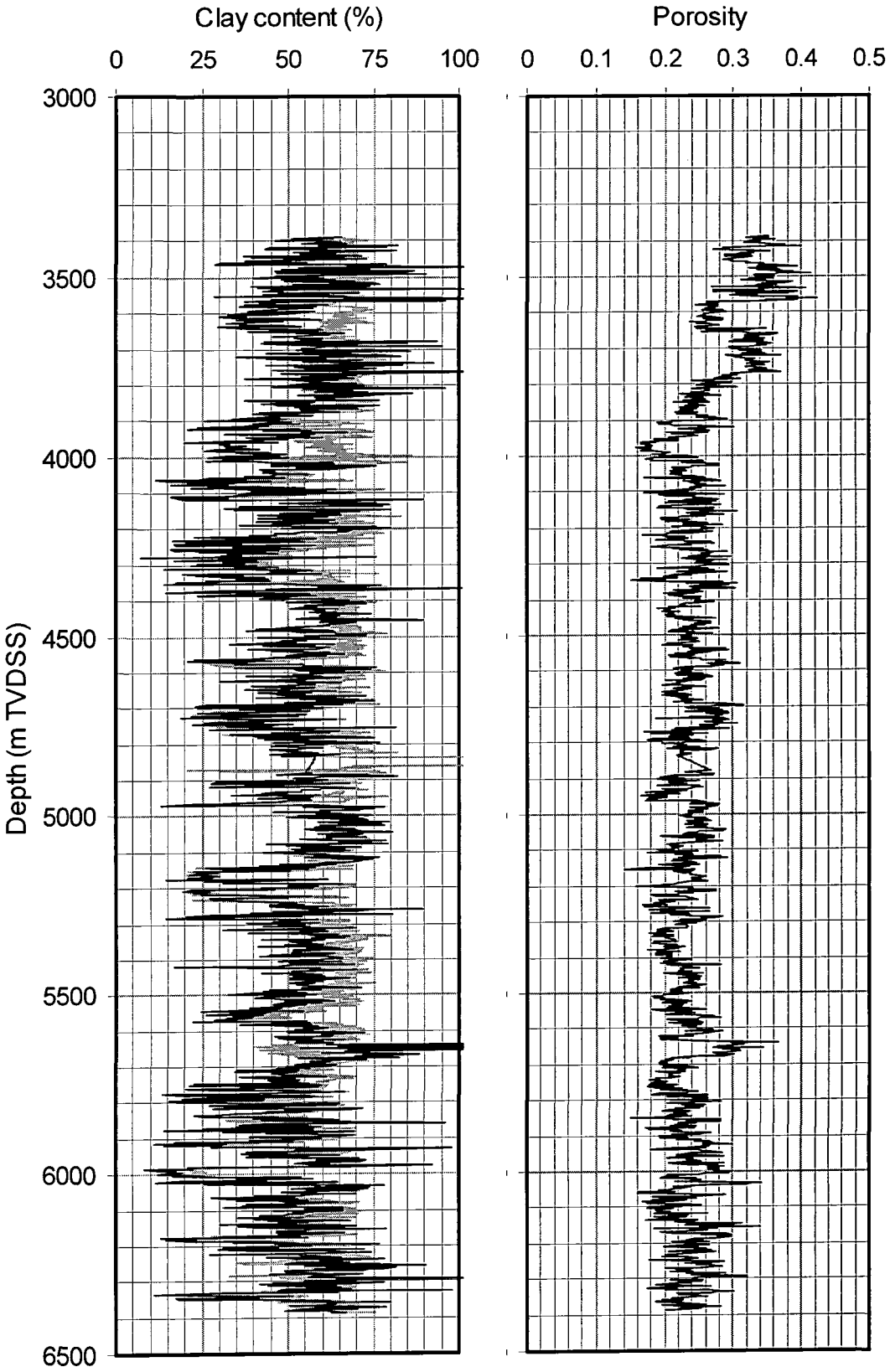

Figure 5.3 - Well Z lithological and porosity information from neutron-density matrix inversion.

where bulk density, ρ_b, was measured in g cm^{-3} and neutron porosity, ϕ_N, was measured in limestone porosity units. Neutron-density-derived clay content was calculated by

$$C_{clay} = \frac{v_{clay}}{\left(v_{clay} + v_{quartz}\right)} \times 100\% \tag{5.2}$$

The results of the analysis for each well are shown in Figures 5.1-5.3 together with the normalised gamma ray as discussed above. Both methods generally produce the same style of results, indicating the presence of sands over the same depth intervals. The indications of clay content in the mud rich intervals provided by the gamma ray and neutron/density are not parallel; there are subtle variations in trend from the neutron and density tools that are not observed by the largely constant trend of the gamma ray. The porosity trends in all three wells suggest that the major control on porosity value below 4,000m is lithology, with sandstones exhibiting higher porosities than the surrounding mudstones. This is particularly evident in Wells W and Y as can be seen in Figure 5.4. The major lithological tend is not as evident as may be due to the high proportion mudstones compared to sandstones sampled. In the upper fully logged sections of wells Y and Z the porosity in the mudstones declines from approximately 30% to 20%. This reduction is probably due to compaction of the rocks, associated with decreasing overpressure (increasing effective stress) as illustrated by the pressure reversal in Well W, and the mudweight reduction in Well Z.

In Well W (Figure 5.1), the abnormally low density log values between 5,050m and 5,200m are reflected in lower estimates of clay fraction than would be expected from analysis of the gamma ray. There is a steady decrease in porosity with depth over this interval apart from two possible sandstones at 5,130 and 5,160m.

The only major deviation of the neutron-density-derived clay mineral content away from the gamma ray trend observed in Well Y (Figure 5.2) occurs between 3,800m and 4,200m. This highlights a change in the compaction gradient observed in the density and neutron logs between 3,800m and 4,000m compared with the section directly above. This reduction in porosity is observed in the matrix inversion porosity estimate (Figure 5.2), a rapid reduction of the sonic transit time and in an increase in resistivity measurement over the interval.

The intervals between 5,300-5,400m and 5,400-5,500m in Well Z (Figure 5.3) are differentiated by a slightly smaller clay mineral content estimate (55% as compared to 58%) and an increase in porosity (20% and 24%) between the upper and lower interval. There is an overall apparent reduction of clay content and porosity over the fully logged interval. This corresponds with the overall reduction in sonic transit time observed over the same interval.

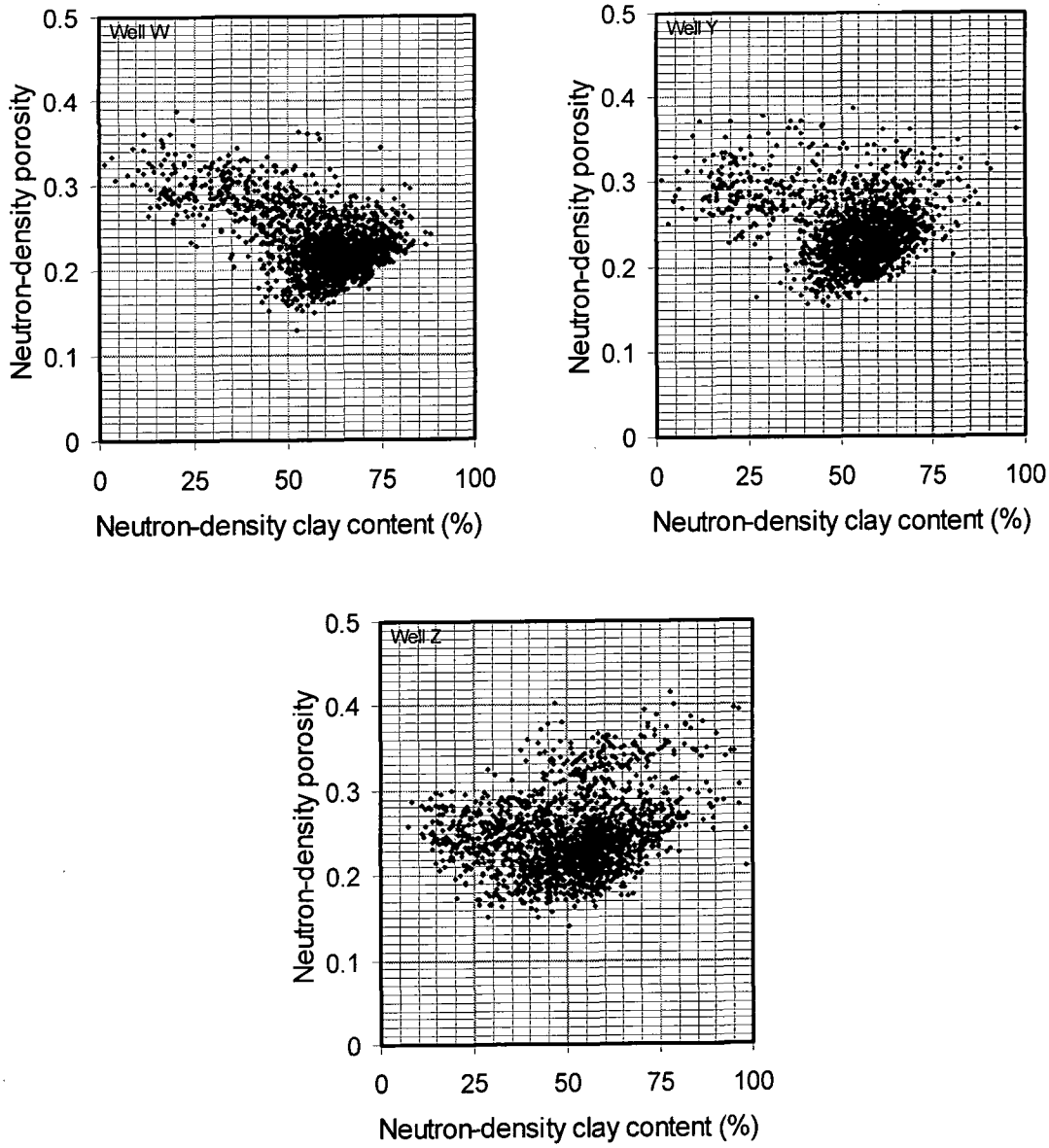

Figure 5.4 - Plots of estimated clay content against porosity derived from neutron and density logs.

5.3.3 Lithological analysis using artificial neural networks

The wireline data from the wells were analysed using *ShaleQuant* as discussed in Section 2.4.2. The program's estimates of clay fraction, total organic content and porosity are presented in Figures 5.5-5.7 together with an indication of gamma ray and neutron density-derived porosity.

The results of the analysis of data from Well W (Figure 5.5) show typically low estimates of TOC in mudstones and upper sands. The sandstone sequence between 5,010 and 5,080m and lower sands show high (~4%) TOC values. This is a consequence of the high resistivity value in these low gamma ray intervals. The mudstone interval beneath this sand, between 5,100m and 5,200m TVDSS, is marked by low TOC estimates that are comparable to those of other depths. The clay fraction estimates delineate sand-rich sections, producing estimate of clay fraction of less

than 35%. The estimated clay fraction in mudstones is in two zones. Above 5,400m, the mudstone clay fractions are approximately 60%, and below this depth, mudstone clay fractions are typically 52-55%. Porosity estimates using neutron and density data are broadly similar to the *ShaleQuant* estimates of porosity below 5,400m. The interval between 5,100m and 5,200m is marked by higher absolute estimates of porosity of up to 10% from *ShaleQuant* in comparison with sonic estimates. Above this zone the sonic log estimates are up to 4% higher than those of the *ShaleQuant* model. This difference of porosity estimate would correspond to a difference of up to 4MPa in pressure estimate.

The clay fraction estimates of the section between 4,000m and 4,800m in Well Y are broadly similar to those of well W above 4,900m. There are a few thin sandstone bodies indicated by gamma ray and clay fraction logs. The reduction in gamma ray between 3,450 m and 3,650m is mirrored by a reduction in clay fraction of 70% to 50%. The section beneath 5,000m in well Y is far more lithologically heterogeneous than in Well W, but mudstone clay fractions are comparable between wells. The TOC is typically less than 5% throughout the section, with the TOC of the sand-rich sequence around 4,900m being very low. The porosity estimates reduce from 30% at 3450m to 20% at 3,915m. The mudstone porosity remains relatively constant to 4,800m. The *ShaleQuant* estimate of porosity in mudstones beneath 4,950m is characterised by an increase from 17% to 22%. The sonic log estimates of porosity generally mirror the *ShaleQuant* estimate of porosity apart from the interval below 5,600m.

The clay fraction trend in well Z (Figure 5.7) is complicated by the heterogeneity of the rock sequence. There are far more thin sand bodies encountered throughout the fully logged section of the well in comparison to wells W and Y. Above 4,000m the clay fraction estimate seems not to be heavily influenced by the broadly constant 100API gamma ray values, varying between less than 50% to over 70%. Between 4,000m and 5,650m the mudstone clay fraction estimates are typically 60%. Beneath this datum, the clay fraction estimates in mudstones are around 50%. Total organic carbon contents are typically estimated to be low, less than 1.5%. Due to lithological variation, the porosity estimation from *ShaleQuant* is complicated. Mudstone values are typically 25% beneath 4,000m; above this datum there is evidence for compaction occurring. The lithological variation is evident in the abrupt change of porosity at 3,700m. Below 4,000m the sonic estimates of porosity are comparable to those obtained using *ShaleQuant*.

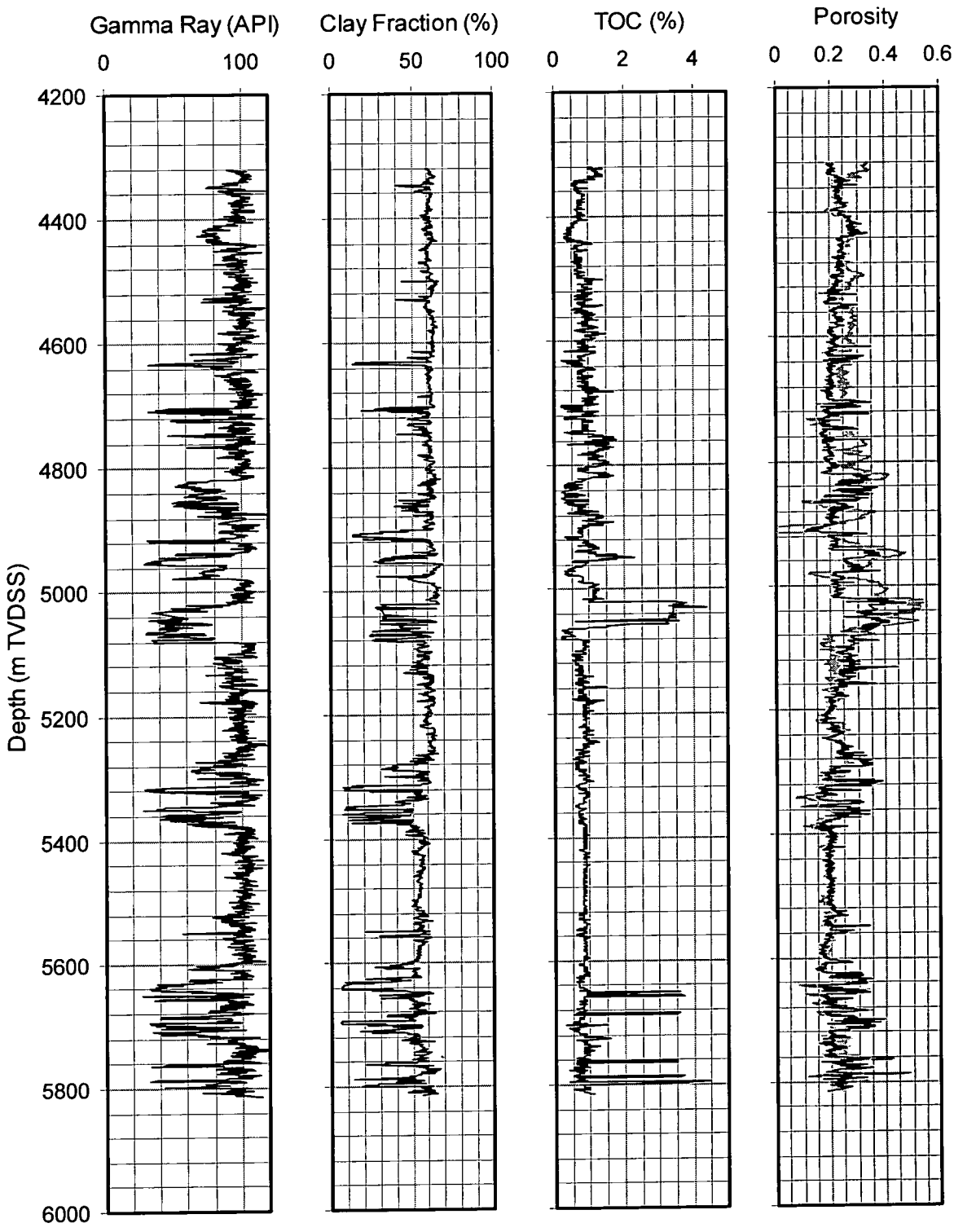

Figure 5.5 -Well W lithological and porosity information.

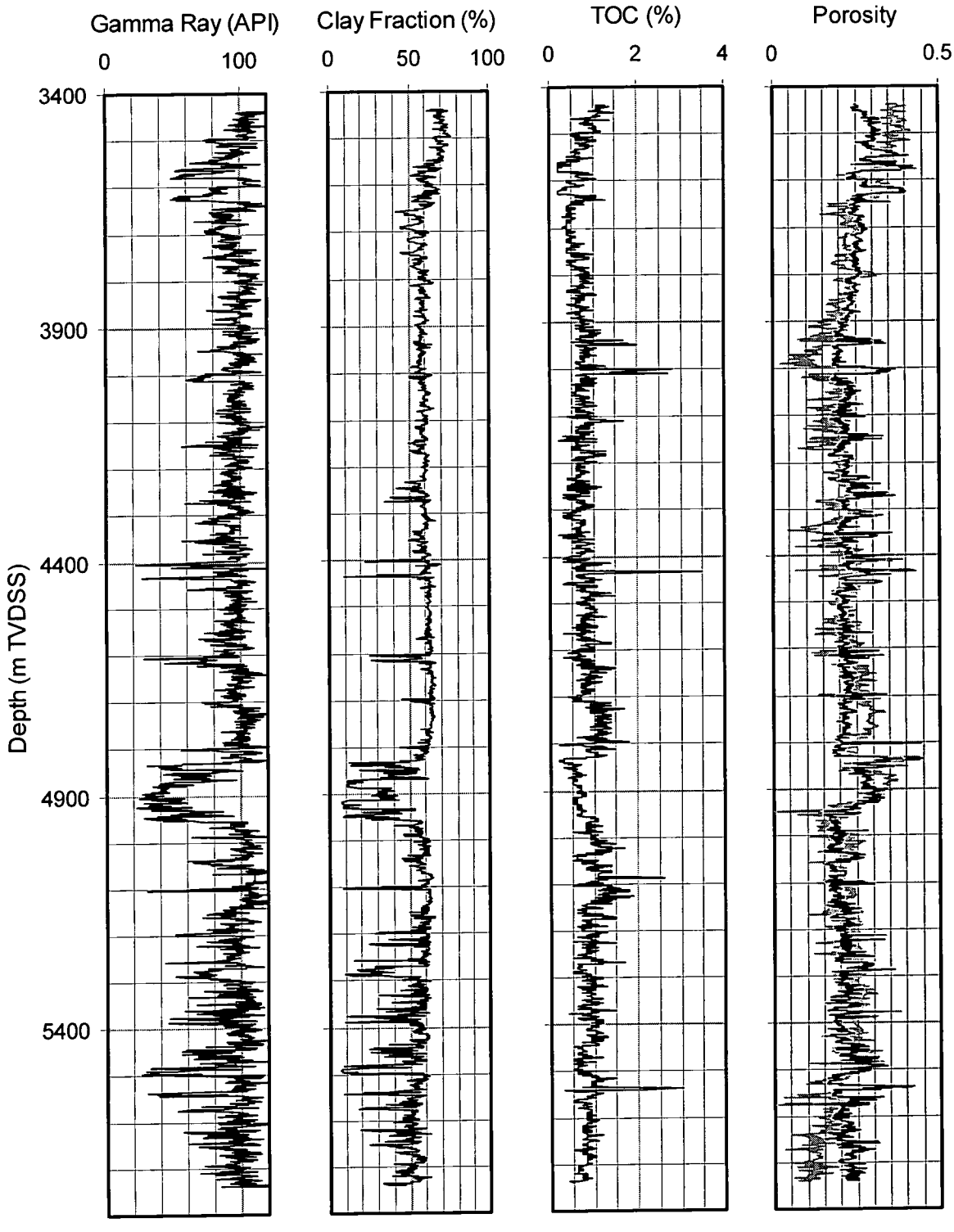

Figure 5.6 - Well Y lithological and porosity information.

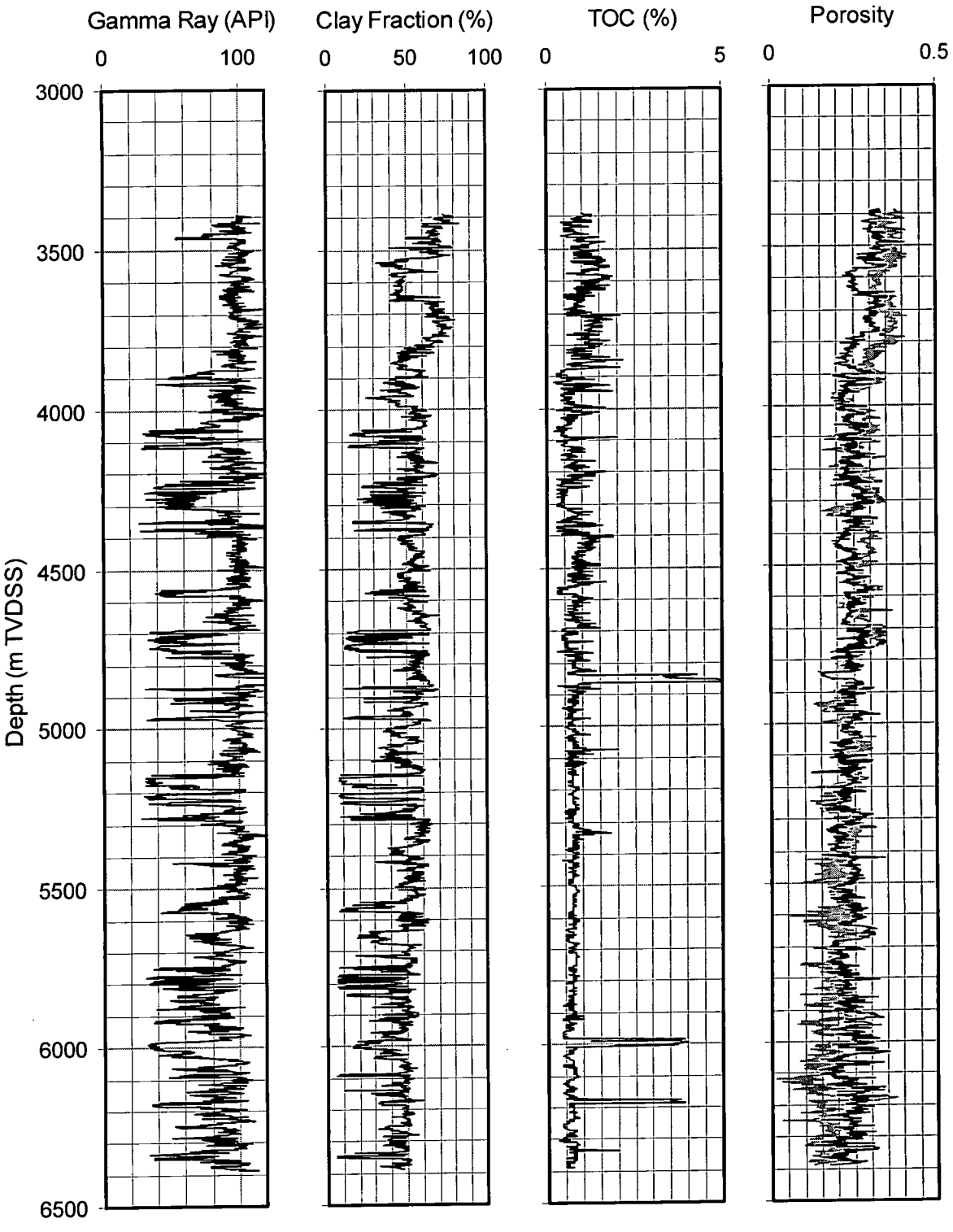

Figure 5.7 - Well Z lithological and porosity information.

As discussed in Section 2.4.2, *ShaleQuant* does not use the raw wireline log data supplied to it directly. In a pre-processing step, the data are manipulated using several petrophysical transforms in an attempt to remove the effects of variation in porosity on the log responses. A subset of the transformed data, namely the D log (Meyer & Neyderlof, 1984) derived from a resistivity log and the sonic log, sonic transit time calculated using Wyllie *et al.*'s (1956) sonic-porosity transform and the resistivity-derived cementation as defined by Archie (1942), were plotted against depth, together with corresponding *ShaleQuant*-derived clay fraction estimates, using *ColourLog* so that the inputs to the *ShaleQuant* model could be understood.

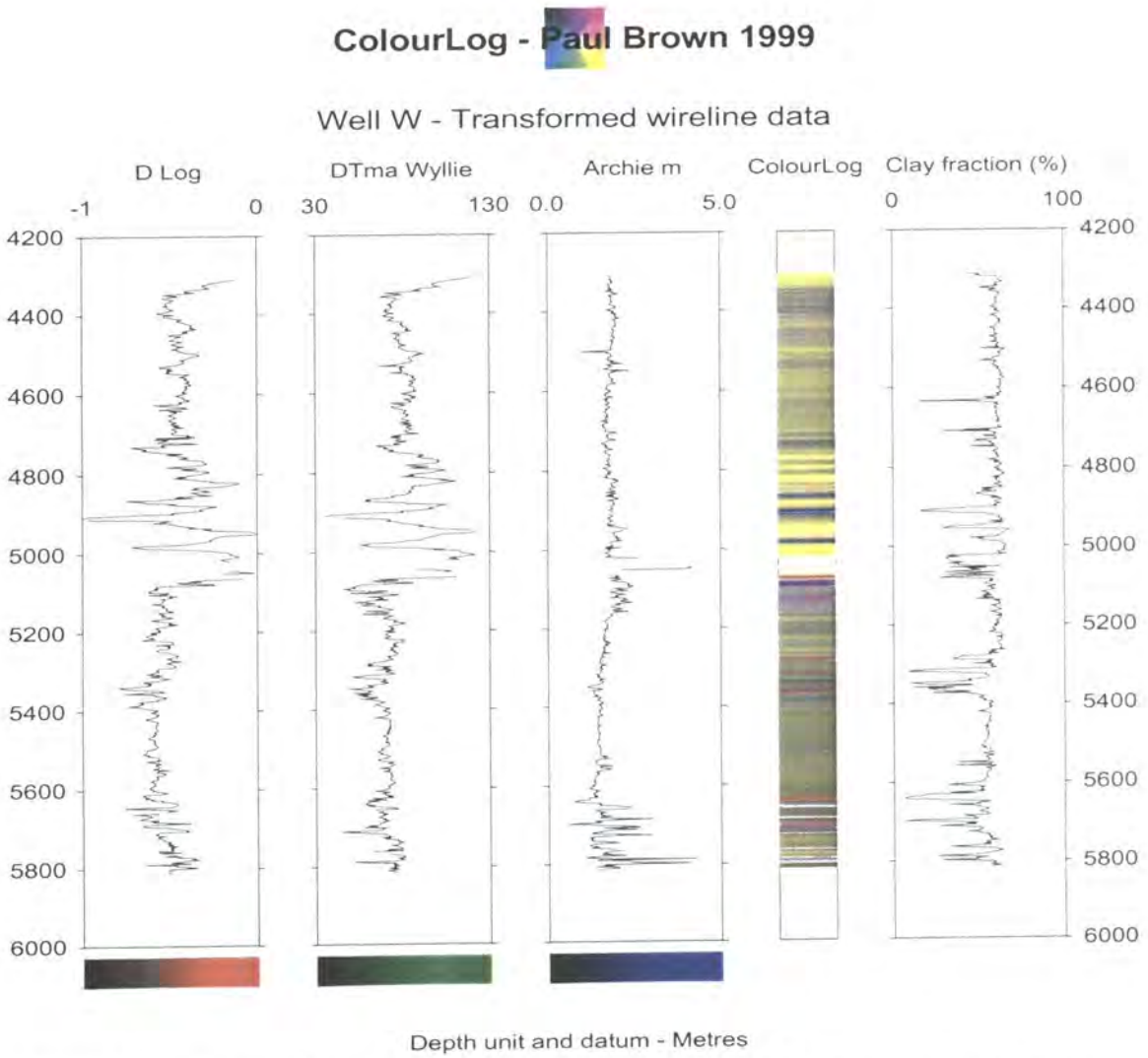

Figure 5.8 - Transformed wireline data from Well W together with a plot of calculated clay fraction.

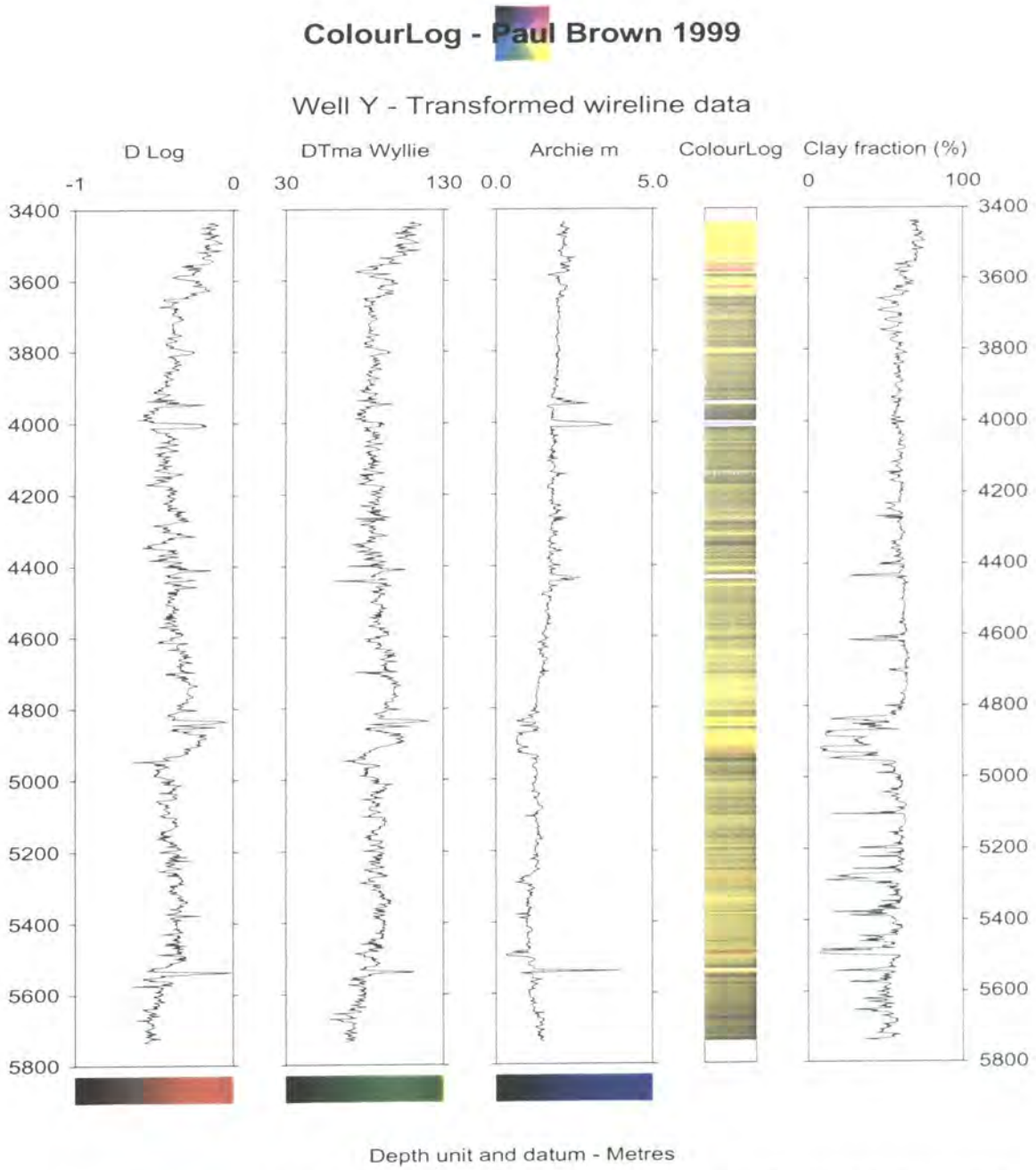

Figure 5.9 - Transformed wireline data from Well Y together with a plot of calculated clay fraction.

The density-derived porosity of the clay-rich sections is broadly constant over intervals of up to 100-200m beneath depths of 4,600m, 3,900m and 4,000m, in Wells W, Y and Z, respectively. Above these depths a reducing trend in porosity with respect to increasing depth is observable. Beneath these depths the rocks are highly overpressured and so within discrete sediment packages it was assumed that porosity variations were due mainly to lithological change.

Subtle variations in estimates of the mudstone lithology are produced by *ShaleQuant* modelling. This variation is not usually entirely due to variation in gamma ray values. The large variation in D log and sonic transit time observed in Well W between 4,800 and 5,000m TVDSS is entirely due to large variations in the sonic log trend. However, over this interval there were several oil shows reported, so the logs will have been influenced by hydrocarbons as well as lithological and pressure change. Apart from this interval, there is a general positive correlation between the values of D log, matrix transit time and cementation factor and the clay fraction value. The

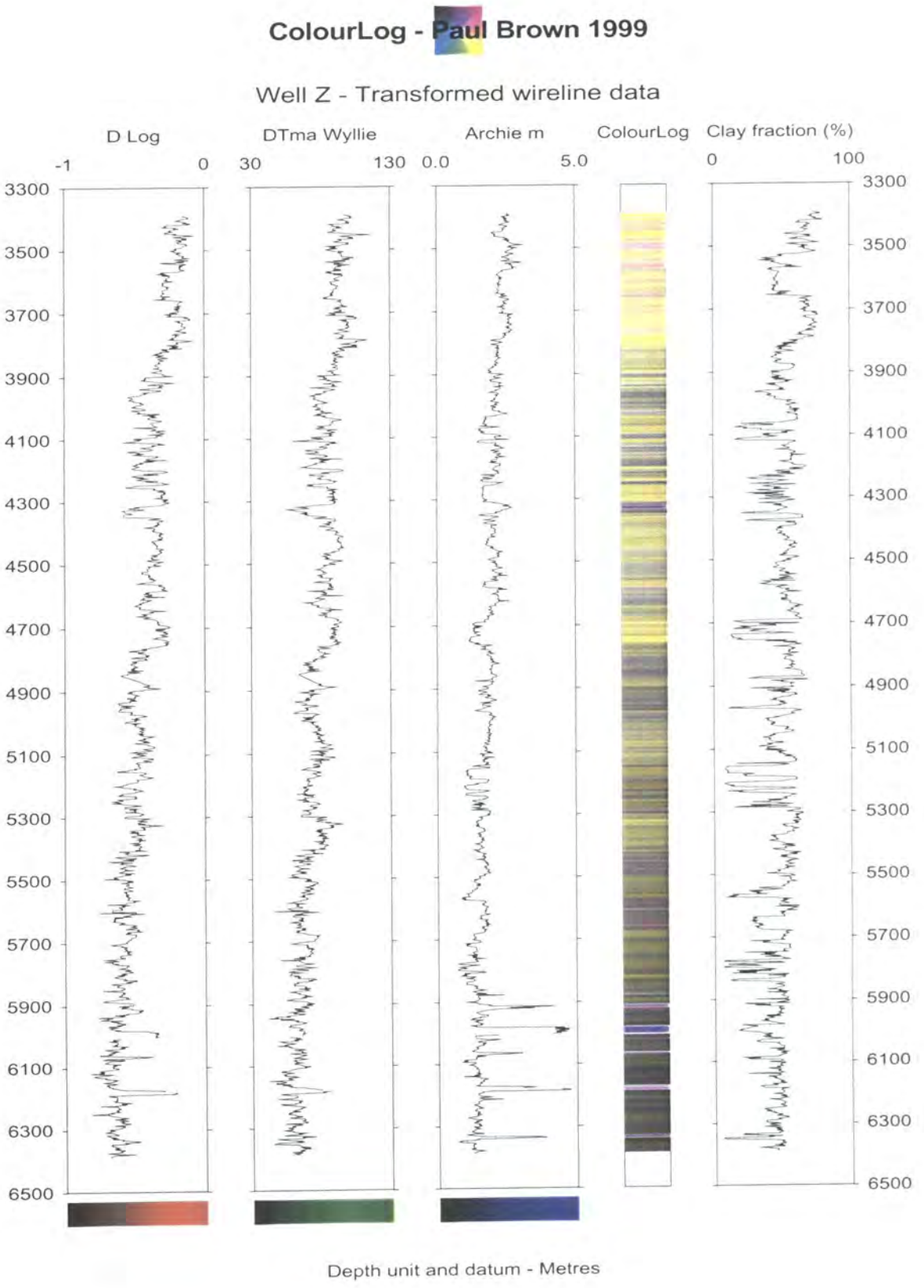

Figure 5.10 - Transformed wireline data from Well Z together with a plot of calculated clay fraction.

relationship between matrix transit time and clay fraction derived using *ShaleQuant* is in general agreement with the idea that the higher the sediment clay fraction the slower the sonic velocity through it as discussed by Rider (1996).

5.3.4 Summary - comparison of lithology models

The lithology estimates for Well W, derived from examination of the gamma ray, neutron and density logs and from use of the *ShaleQuant* model, were plotted against each other alongside a plot of porosity estimates derived from the neutron-porosity matrix inversion versus density log-derived porosity calibrated using matrix density estimated

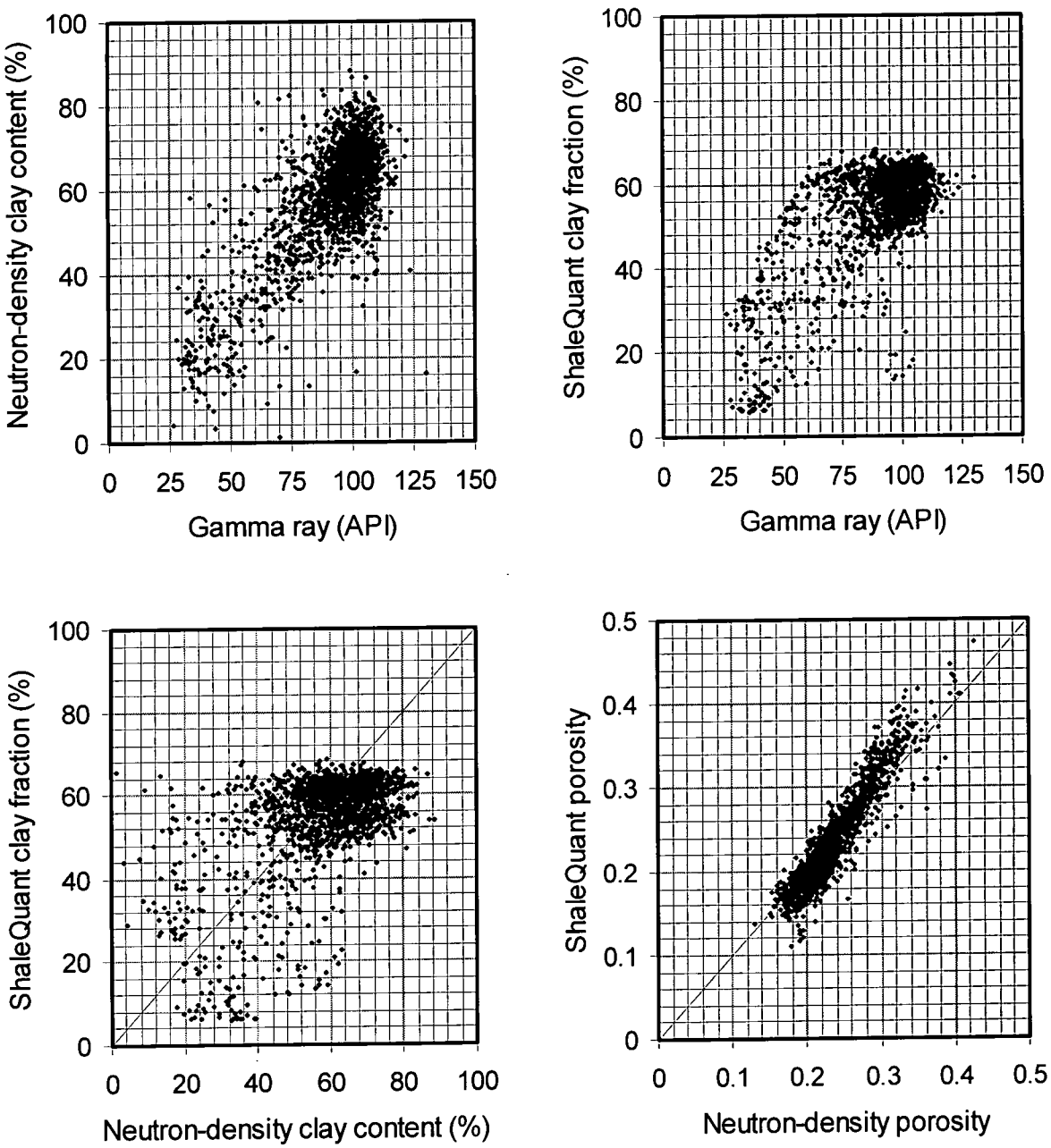

Figure 5.11 - Cross plots comparing gamma ray measurement, density/neutron-derived clay content, ShaleQuant-derived clay fraction estimate and porosities derived from ShaleQuant and density-neutron analysis using data taken from Well W.

using *ShaleQuant* as shown in Figure 5.11. At low clay content and gamma ray, there is a clear relationship between the gamma ray values and neutron-density clay content. Within the mudstone lithologies, the gamma ray ceases to increase at the same rate with increasing neutron-density clay content, essentially the gamma ray responds to mudstone lithologies in a reasonably uniform way, whereas the neutron and density logs continue to exhibit variation in response to potential lithological change. This phenomenon is not observed when a comparison is made between *ShaleQuant*-derived clay fraction and gamma ray reading. Mudstone values for these parameters tend to cluster about 60% clay fraction and 100API gamma ray reading. The clustering suggests that the *ShaleQuant* model for the Gulf of Mexico could be heavily influenced by gamma ray. This idea is supported by the lack of relationship shown between neutron-density clay content and the *ShaleQuant*-derived clay fraction for mudstone lithologies. The mudstones do not have a monotonous clay fraction with respect to gamma ray reading. This would suggest that other the other input parameters to the *ShaleQuant* model do influence its output.

The reasonable correlation between lower porosities, between 15% and 30%, derived from both methods suggest that the base assumption of material properties used in the matrix inversion technique correspond well with the estimates of those parameters provided by the *ShaleQuant* model.

The results for the other wells yielded similar relationships as exhibited by the analysis of data from Well W.

5.4 Pressure estimation

5.4.1 Outline

Three methods were used to provide pressure estimates from the wireline data provided. The resistivity data from the entire logged interval, which comprised 98% of the drilled interval in each well, were used to define a normal compaction trend and pressure estimate using Eaton's (1975) pressure determination method. Since the density and sonic logs were not created in intervals where the pressure was known to be normal, no locally derived compaction trends could be used for pressure determination and so the porosity logs were used, where available, in conjunction with Yang & Aplin's (2000) generic compaction curves. The curves were used in two ways; first they were used with assumed values of clay fraction and porosity estimates were derived from density data using an assumed value of matrix density, then the curves were used in conjunction with calibration data derived from the *ShaleQuant* model as described in Section 5.3.3.

Since the deposition rate in the area has been so high throughout the Eocene to present, the onset of overpressure is at a reasonably shallow depth; therefore resistivity data from a very limited interval extending over only 600-700m were available for creation of the local normal compaction trend. The estimates of pressure derived from the resulting compaction trend were reasonable to a depth of 4,000mTVDSS.

Yang & Aplin's (2000) generic compaction curves were used to evaluate the pressure regimes in the wells in two ways; firstly in an uncalibrated manner in which clay fraction was assumed and then using calibration data supplied from Aplin *et al.*'s (1999) artificial neural network method. Both approaches to the use of the generic compaction curves provided reasonable estimates of pressure. The latter approach revealed two intervals in Well W in which there was a significant increase in estimated overpressure. The uppermost of these pressure transition zones as

described by Swarbrick and Osborne (1996) could be explained with a one dimensional model; however, the lower one could not.

5.4.2 Pressure evaluation using the resistivity log

The resistivity and gamma ray data from the topmost 700m from each well were gathered together in one dataset, together with the depth at which each measurement was made. The data associated with gamma ray values of less that 70 API were removed from the dataset in order to remove sands and siltstones from consideration when examining the resistivity log. This topmost dataset was used to define a normal compaction trend for mudstones in the topmost section assuming that this section was normally pressured. Many authors (e.g. MacGregor, 1965; Rider, 1996) have suggested that there is an exponential relationship between conductivity, and hence resistivity, with depth. Others (e.g. Dewan, 1983; Heppard *et al.*, 1998; Traugott, 2000) suggest that the relationship is more complicated, involving temperature and cation exchange capacity of the constituent clay minerals of the sediment. Since the section over which the pressure is thought to be normal is limited, the simpler exponential relationship was used to define two normal resistivity trends for mudstones. The trend was defined using the raw resistivity data through regression and yielded a relationship thus:

$$R_N = 1.0393\exp(0.531 z_{SM}) \tag{5.3}$$

where R_N is the normal compaction trend for the resistivity log. The r^2 correlation statistic was 0.5683. The normal compaction relationship was then used to calculated pore fluid pressure using Eaton's (1975) relationship, namely

$$P = s_v - (s_v - P_N)\left(\frac{R}{R_N}\right)^{1.2} \tag{5.4}$$

where P is the estimated pore pressure, s_v, the overburden and P_N the hydrostatic pressure. All resistivity readings taken from depths with a corresponding gamma ray reading of 70 API or less were removed to ensure that mudstones comprised the sole sampled lithology group. The overburden was calculated using Fertl and Timko's (1972) overburden gradient curves for the Gulf Coast together with the integrated density log when bulk density data were available. The resistivity profile, derived normal resistivity curve and pressure profile calculated using Equations 5.3 and 5.4 for Well W are shown in Figure 5.12. The black line on the resistivity plot is the locally derived normal compaction trend, and the black line on the pressure plot is the pressure profile derived from mudweight and MDT measurements provided by the operator.

The pressure plot indicates the onset of overpressure just beneath 2,100m. The data used to derive the normal compaction trend were taken from an interval to 1,900m, well above this suggested onset of overpressure. The reduction of the amount of overpressure indicated between 3,000m and 3,500m is associated with a gamma ray maximum, potentially indicating a thick mudstone sequence. The estimate of pressure rises to be the same as that indicated by RFT measurements at 3,800-4,200m. Below 4,200m the pressure estimate derived from raw resistivity data rises 4-5MPa above measured pressure for 700m, then the pressure estimates rapidly approach lithostatic values.

The pressure evaluation was repeated for Wells Y and Z. The pressure profile derived using resistivity readings from Well Y is broadly similar in nature to that from Well W and hence is not shown. The profile produced with data from Well Z is shown in Figure 5.13 together with the original resistivity data. The lines on both depth plots are as described for Figure 5.12. The overall profile is broadly similar to that of Wells W and Y, but the reduction in the amount of overpressure at 3,800-3,900m TVDSS is not marked as the reduction in overpressure observed in the interval between 3,400m and 2,500m in Well W.

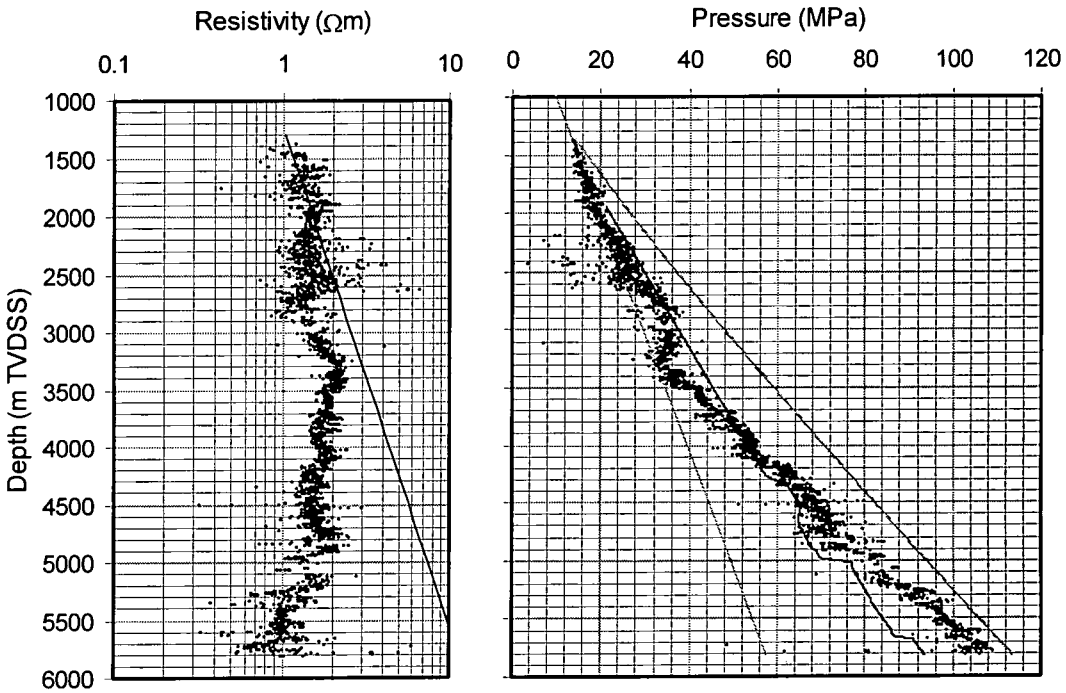

Figure 5.12 - Well W resistivity profile and pressure derived from resistivity data.

The estimates of pressure in the deeper sections of each well are highly dubious with significant disagreement of over 25MPa between RFT measurements in sands in Well W and the near lithostatic pressure of the resistivity-derived estimates of pressure. Significant differences of pressure have been observed between sands and thick shales (e.g. Luo *et al.* 1994); however, in those examples the pressure draw down into the sand units is clearly visible in the wireline signatures. This is not the case in these wells, so the assumptions used to model the pressure in the lower sections of each of the wells are likely to be incorrect. The most likely assumption to be invalid is that of the single resistivity-depth relationship. The form of the equation used to define the relationship is empirical, and not calibrated in deep, warm lithologies. The resistivity of the pore fluid may change with depth due to the proximity of major salt bodies, with significant influence over the resistivity profile in the deeper sections of the wells.

The resistivity log is the only source of data available in the upper section of each well and so the pressure information that can be derived from it must be used as much as possible due to the absence of other data. The pressure evaluation created using data in the upper section appears to yield similar estimates to that produced while drilling. The analysis has shown that overpressure develops at reasonably shallow depths and there is the possibility of significant variability of amounts of overpressure within the first 3,000m of Wells W and Y.

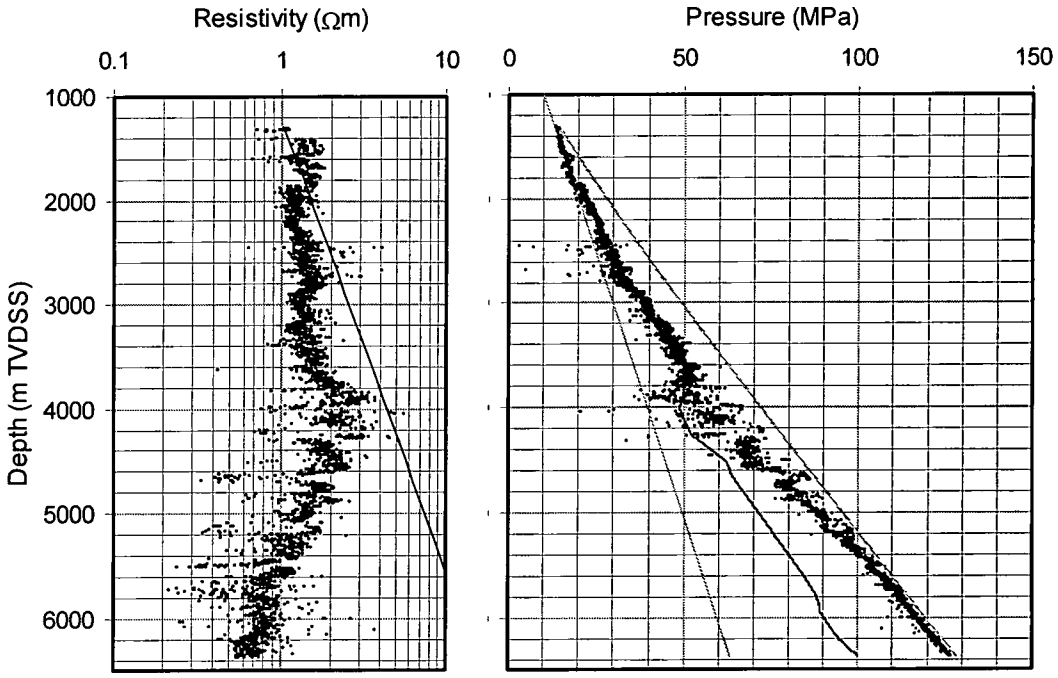

Figure 5.13 - Well Z resistivity profile and pressure derived from resistivity data.

5.4.3 Pressure evaluation using single generic compaction curves

In all three wells the porosity logs were only produced in intervals in which overpressure was already present, so it was not possible to derive locally derived normal compaction trends. Generic compaction trends were the only source of data for the calculation of effective stress and hence pore pressure using the porosity derived from the neutron, density and sonic logs.

The porosity data derived for each well using the matrix inversion of bulk density and neutron porosity data were converted to void ratio estimates after the removal of data with corresponding gamma ray values of less than 70API. These void ratio estimates were used to calculate three separate estimates of effective stress using Yang and Aplin's (2000) compaction models considering 40%, 60% and 80% clay fraction cases. The overburden derived in the previous section was used with the estimates of effective stress to calculate pressure estimates for each of these cases. The pressure estimates from this modelling are shown in Figures 5.14 and 5.15 for selected depth intervals from Well W and Well Z, respectively.

In each case the estimates of pressure using the 40% clay fraction compaction models are 8-10MPa higher than those of the 80% clay fraction models. The scatter of the estimates decreases with increasing modelled clay fraction. This latter observation is due to the geometry of the compaction curves used, as discussed in Chapter 3. The scatter associated with the estimates using the 60% clay fraction model is significantly less than the ±10MPa envelope suggested as the minimum expected uncertainty using uncalibrated wireline without lithological information in the Monte Carlo modelling of Chapter 3. This is probably due to higher quality estimates of porosity derived from two logs accounting for some lithological variation rather than the single log, monolithological model assumed in the error analysis.

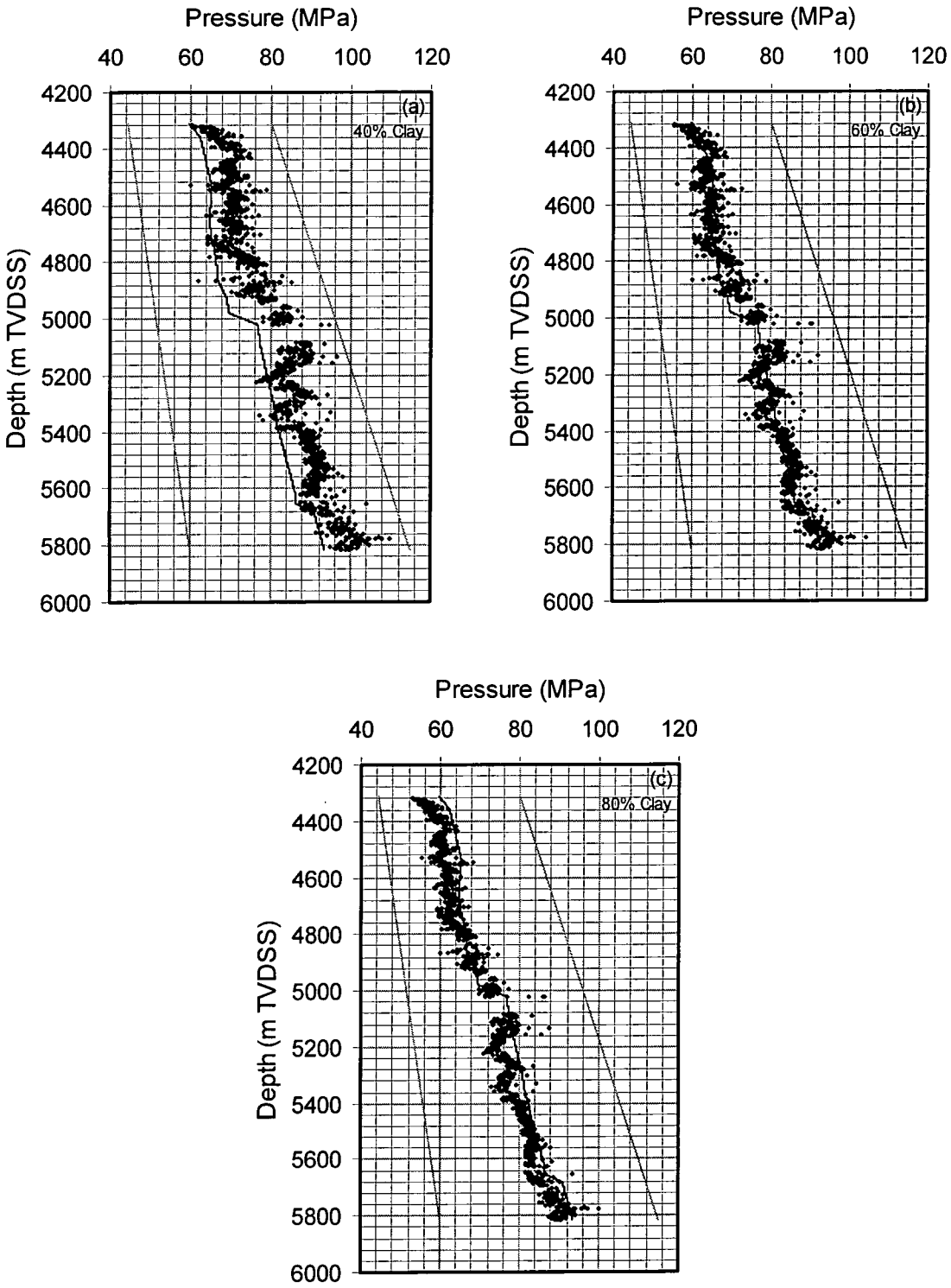

Figure 5.14 - Well W pressure estimates using generic mudstone compaction curves specifically using (a) 40%, (b) 60% and (c) 80% clay fraction compaction curves.

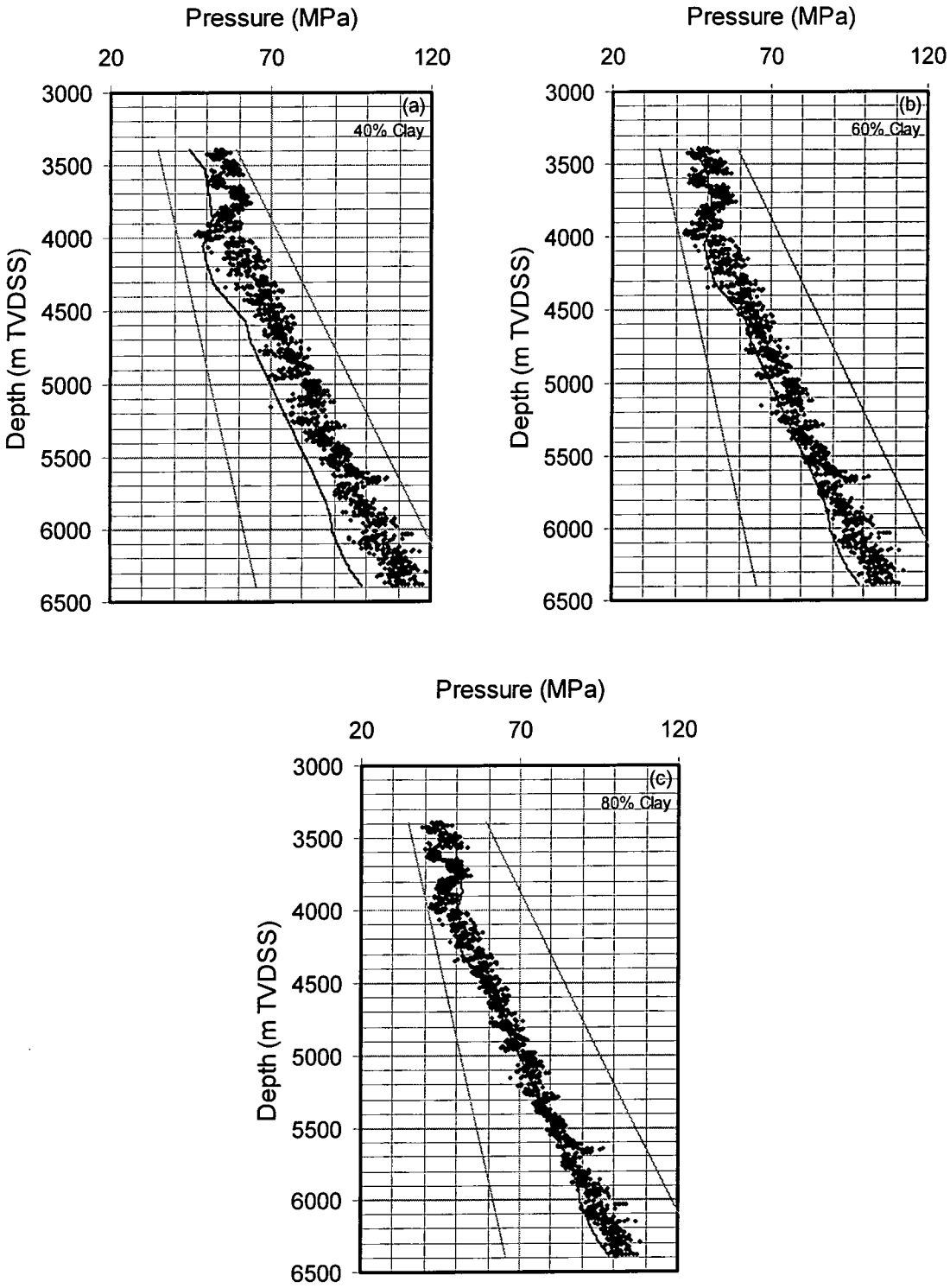

Figure 5.15 - Well Z pressure estimates using generic mudstone compaction curves specifically using (a) 40%, (b) 60% and (c) 80% clay fraction compaction curves.

In Well W, all the models produce pressure trends that run parallel to the pressure trends indicated by RFT measurements. The 60% clay fraction model appears to be the most suitable (Figure 5.14b), matching RFT pressure very well in the upper section and parts of the lower section.

The indications of clay mineral content in Well Z, derived from the matrix inversion technique (Figure 5.3) are broadly similar to those derived for the other wells, so one might initially choose to employ a 60% clay fraction model to describe the local normal compaction curve. However, the 60% clay fraction model estimate of pressure is on average 5-8MPa higher than the mudweight estimate of pressure. This suggests, provided that the mudweight estimate of pressure is accurate, that the lithology is finer grained than the 60% clay fraction assumption. The 80% clay fraction model estimate of pressure is potentially more sensible provided that an assumption is made that the mudweight estimate of pressure is accurate.

5.4.4 Pressure estimation using ANNs and generic compaction curves

The lithological data derived from wireline data using *ShaleQuant* were used to calibrate Yang and Aplin's (2000) clay fraction dependent compaction models to produce a pressure estimate for each well. These pressure estimates are presented in Figures 5.16-5.18.

The pressure estimate for Well W was produced using void ratio derived from the density log and estimates of grain density obtained using *ShaleQuant* apart from the interval between 5,080m and 5,200m where sonic-derived estimates of void ratio, calculated using Hansen's (1996a) formulation of Raiga-Clemenceau *et al*'s (1988) equation, were used. All data associated with gamma ray measurements of less than 70 API and clay fraction estimates of less than 45% were removed. The resultant pressure estimate is shown in Figure 5.16. The scatter of pressure estimates, ±2MPa, is considerably less than in the uncalibrated pressure analysis example for the same well shown in Figure 5.14. The match between estimated pressure in mudstones and measured pressure in sand bodies is excellent, with the three observed pressure regimes described by the RFT measurements clearly visible in the mudstones. The estimated pressures in the mudstones suggest that the pressure regime between ~5,000-5,650m starts just beneath the base sand of the pressure regime above.

The pressure analysis for Well Y was performed using void ratio estimates derived solely from the density log calibrated using matrix density estimates from *ShaleQuant*. The data were filtered, as in the analysis of data from Well W, removing data associated with low clay fraction and gamma ray values. The pressure estimate for Well Y is shown in Figure 5.17. There are four pressure regimes apparent in the plot. The top regime is an apparent pressure drawdown between 3,400m and 4,000m TVDSS. The other three regimes are similar to those observed in Well W and are situated in the intervals between 4,000m and 5,170m, 5,170 and 5,450m and below 5,450m. The degree of overpressure in each of the pressure regimes, apart from that below 5,450m, increases with respect to depth, but there are sharp incremental pressure transition zones between each zone. The magnitude of the pressure increase associated with each transition zone is at least 5MPa.

The pressure profile (Figure 5.18) created for Well Z using the gamma ray and clay fraction-filtered void ratio derived from the *ShaleQuant*-calibrated density log is not of the same high quality as that of the previous two wells. The scatter of the pressure estimates is high, rising from ±4MPa at 4,500m to ±8MPa at 6,400m. The upper pressure

regime described for well Y can just be observed, but other characteristics of the pressure regime in Well Z are obscured by noise. This poor model result may be due to poor wireline data quality, since the sand-mudstone ratio is substantially higher in Well Z than in the other two wells. The other possibility is poor calibration of the *ShaleQuant* lithological model. This is unlikely as data from two wells within 15km of Well Z in the same minibasin have provided reasonable results. Pressure analysis on data from this well is likely to be dubious.

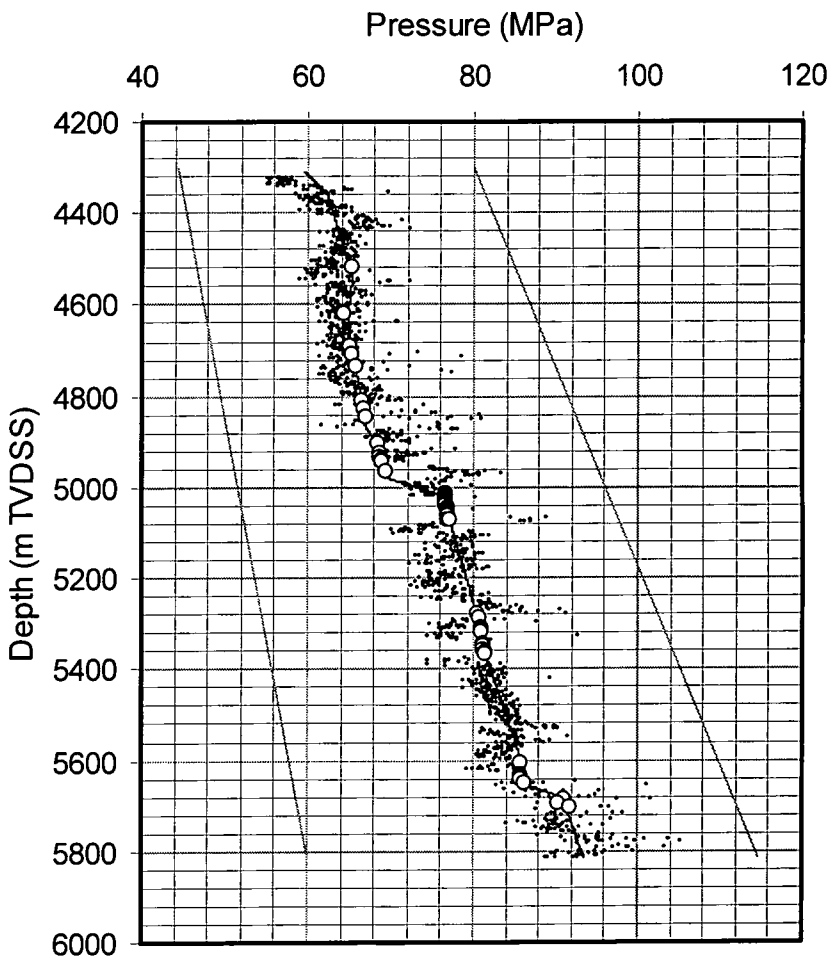

Figure 5.16 - Well W pressure estimate using generic compaction models and estimates of clay fraction and porosity from *ShaleQuant*. Open circles are RFT data from the wells.

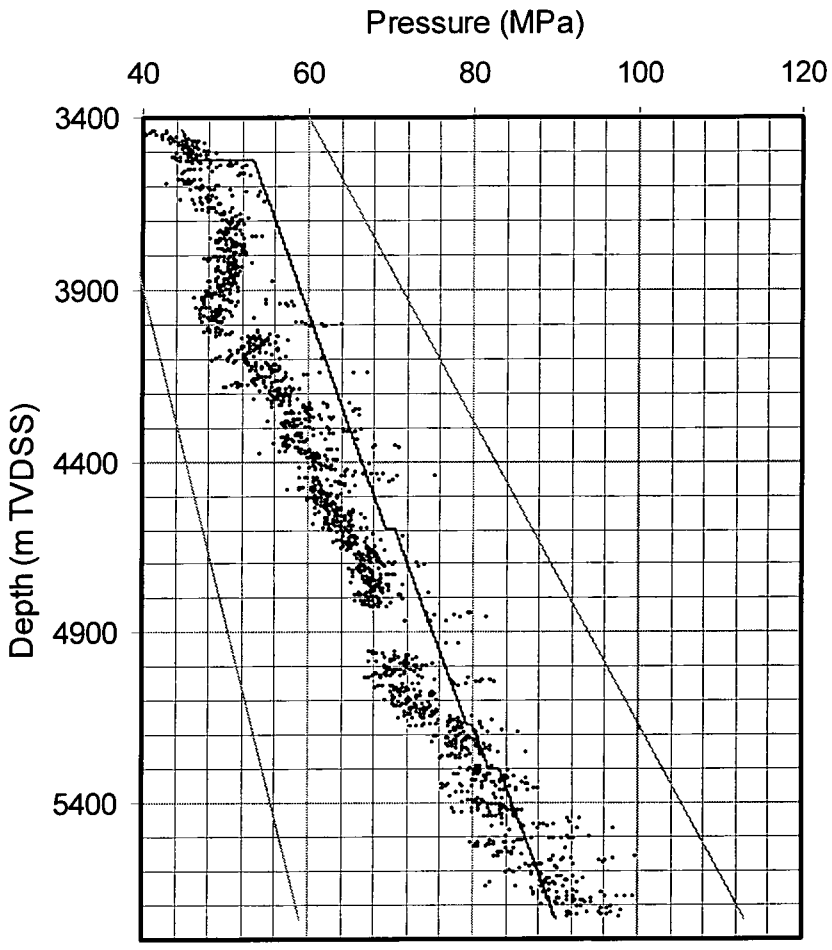

Figure 5.17 - Well Y pressure estimate using generic compaction models and estimates of clay fraction and porosity from *ShaleQuant*.

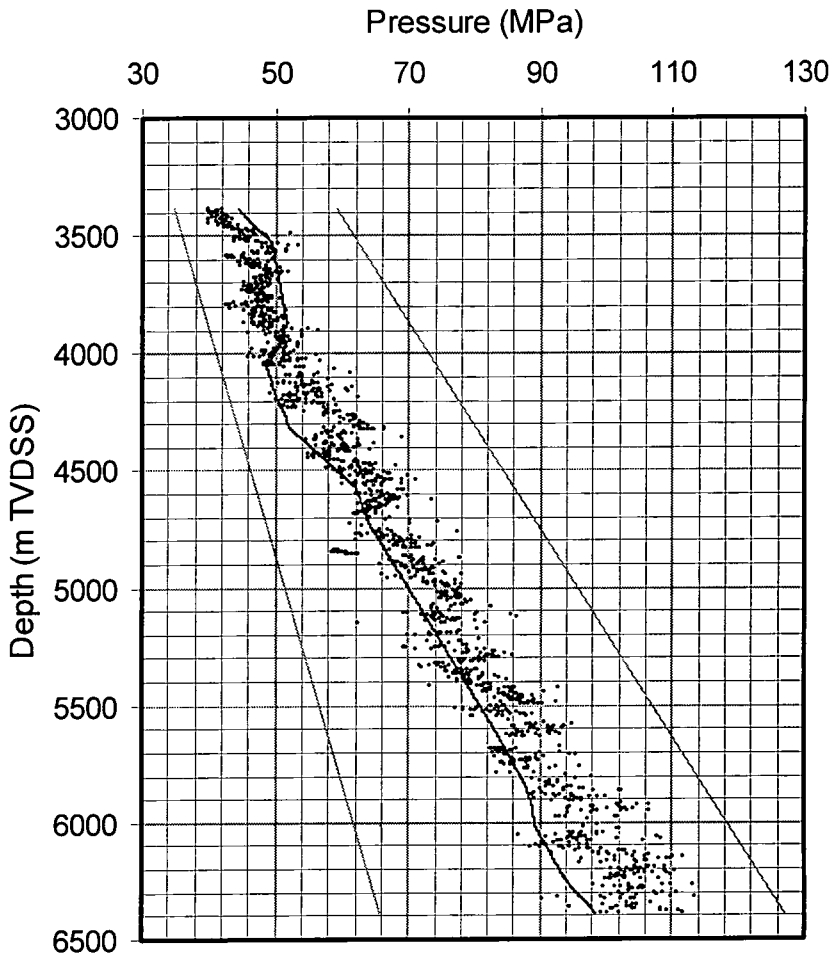

Figure 5.18 - Well Z pressure estimate using generic compaction models and estimates of clay fraction and porosity from *ShaleQuant*.

5.4.5 Investigation of pressure transition zones

The wireline log and lithological properties of the intervals surrounding the pressure transition zones in Well W were investigated. The pressure increases were over the intervals between 4,980m and 5,016m and between 5,654m and 5,696m, associated with pressure increases of 7MPa and 4.5MPa, respectively. The first pressure increase is in the same depth range as the top of the oil column in the well. Raw wireline data were plotted together with plots of transformed wireline data and *ShaleQuant*-derived clay fraction to investigate the two intervals in question.

The data from the upper interval are plotted in Figure 5.19. The transition zone interval is shaded in grey. In the section directly above the pressure transition zone there is a heterogeneous sequence with thin sand bodies up to 3m thick interbedded with mudstones. Beneath the transition zone there is a major sand body and more homogeneous mudstones. Within the transition zone interval, there are three distinct sections as delineated by the wireline data. The upper section (4,955-4,976m TVDSS) is reasonably radioactive, as indicated by the gamma ray log suggesting a silty interval. The sonic transit time is high, over 120μs ft^{-1} and the density log is low, approximately 2.3g cm^{-3}.

The middle section (4,980-4,988m TVDSS) is of high gamma ray value, over 100API, normal sonic value and density. The lower section (4,990-5,020m TVDSS) is similar to the middle section apart from a high sonic transit time of up to 140μs ft^{-1}. The calculated bound water over the lower two sections is higher than at any other point in the wells. The estimates of matrix transit time over the same sections reflect the relative constancy of the density log and the significant change in sonic transit time between the two intervals. In the lower section, the transit time estimates are the highest recorded in mudstones throughout the well. This indicates the possibility of a unique mudstone lithology in the lowest section of the transition zone. The high values of matrix transit time estimates suggest that this lithology may be fine grained. This inference is supported by the *ShaleQuant* estimates of clay fraction. The lower section comprises lithologies of very high (68%-70%) clay fraction. The surrounding mudstone lithologies are typically of 55%-60% clay fraction. The top of the upper section of the upper transition zone is associated with a high (69%) estimate of clay fraction that declines through the interval.

The approximately 10% absolute increase in clay fraction affects the permeability of the rock. Yang and Aplin (1998, p171) observed that a 73% clay fraction mudstone from similar *in situ* effective stress regimes and similar porosity as a 60% clay fraction mudstone may have a permeability one order of magnitude lower than that of the coarser grade material. This has significance as, for a certain sedimentation rate, the finer grade material of lower permeability will form an effective seal to fluid flow at a shallower burial depth than the coarser grade material.

Hydrocarbon buoyancy is unlikely to contribute 7MPa of excess pressure to the system as a hydrocarbon leg 3.5km thick would be required; however, the presence of hydrocarbons in the sediments may reduce permeability further due to relative permeability effects (Okui *et al.*, 1998). This effect still needs to be quantified in mudstone lithologies.

Another possible explanation of the pressure difference observed is that there is pressure drawdown occurring in the upper sand body. The permeability of the mudstones between the sand bodies is low enough so that the mudstones are not in pressure equilibrium with the overlying and underlying sandbodies.

The raw and transformed wireline log data around the lower transition zone, again highlighted in grey, are shown in Figure 5.20. The transition zone is marked by low sonic transit time (90μs ft^{-1}), high gamma ray (100API) and reasonably constant bulk density (~2.4g cm^{-3}). The transformed logs are also fairly constant, with low values of D log, matrix sonic transit time and bound water compared to the mudstones above. The clay fraction estimates across the transition zone are slightly lower than those of the surrounding rocks. This suggests that a purely one dimensional explanation of the second pressure regime at the base of Well W cannot be made on the basis of *ShaleQuant* estimate of clay fraction. The explanation is probably two or three dimensional, involving faulting or lateral transfer of pressure.

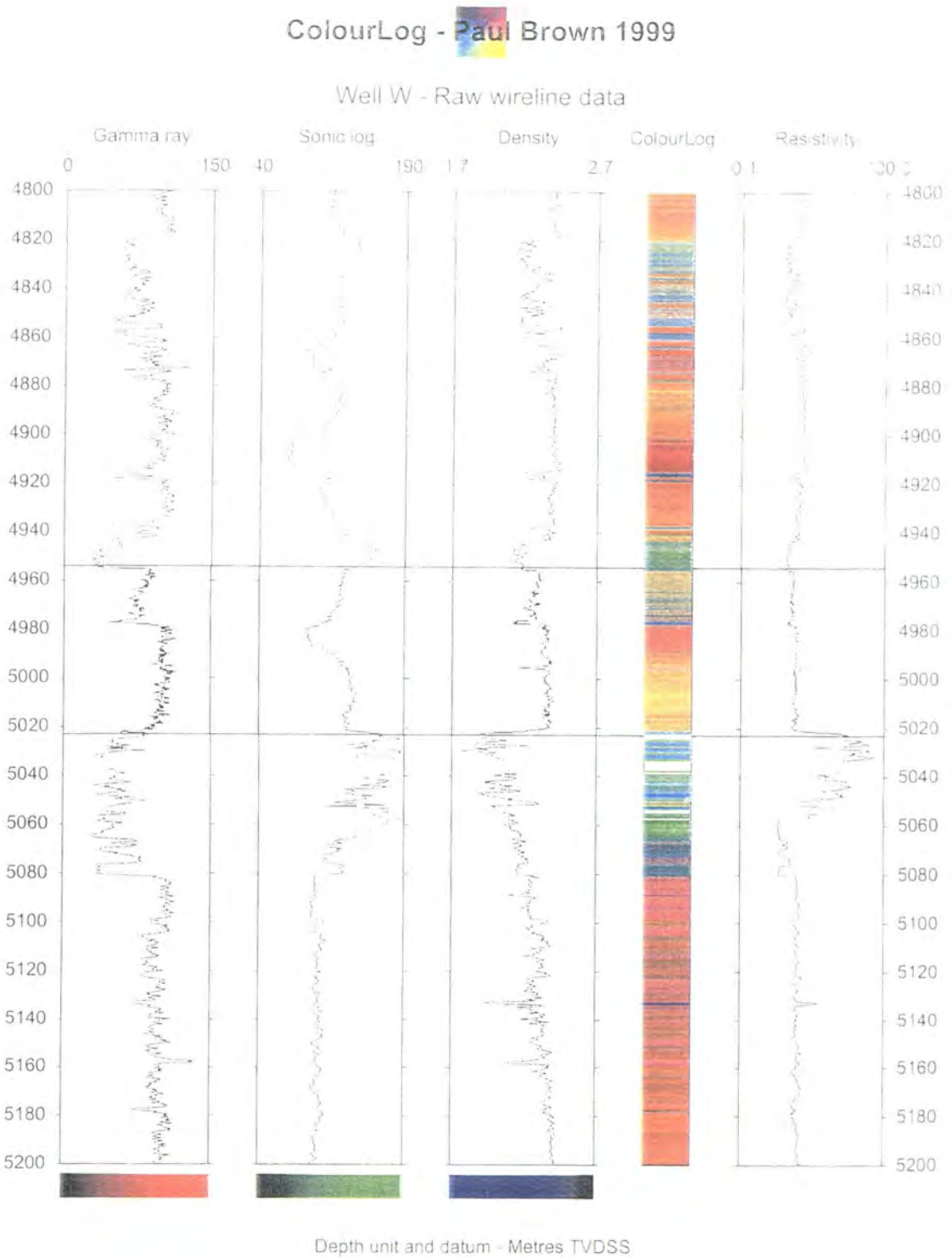

Figure 5.19 - Well W raw and transformed wireline data taken across the upper pressure transition zone.

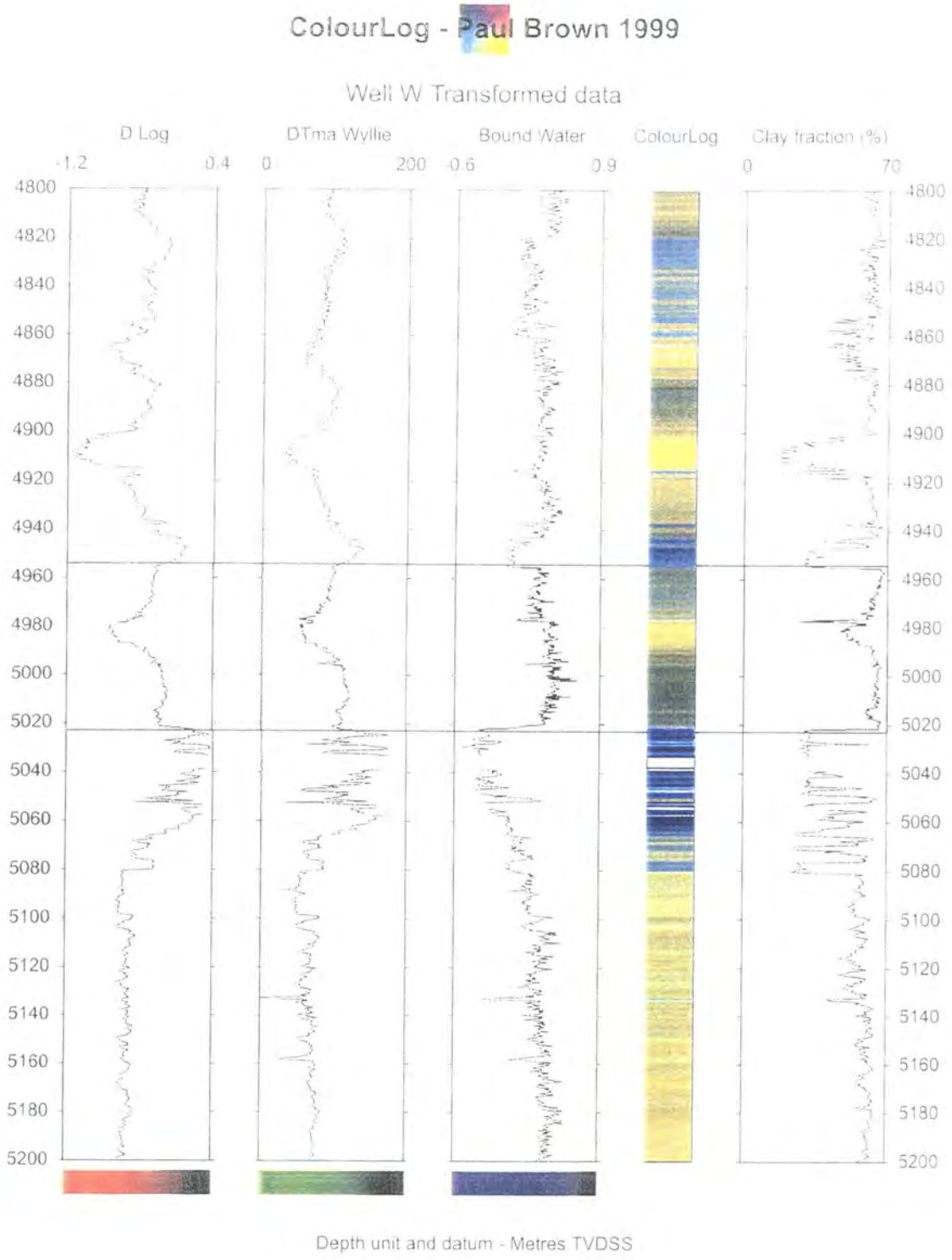

Figure 5.19 continued.

Paul Ecclestone-Brown

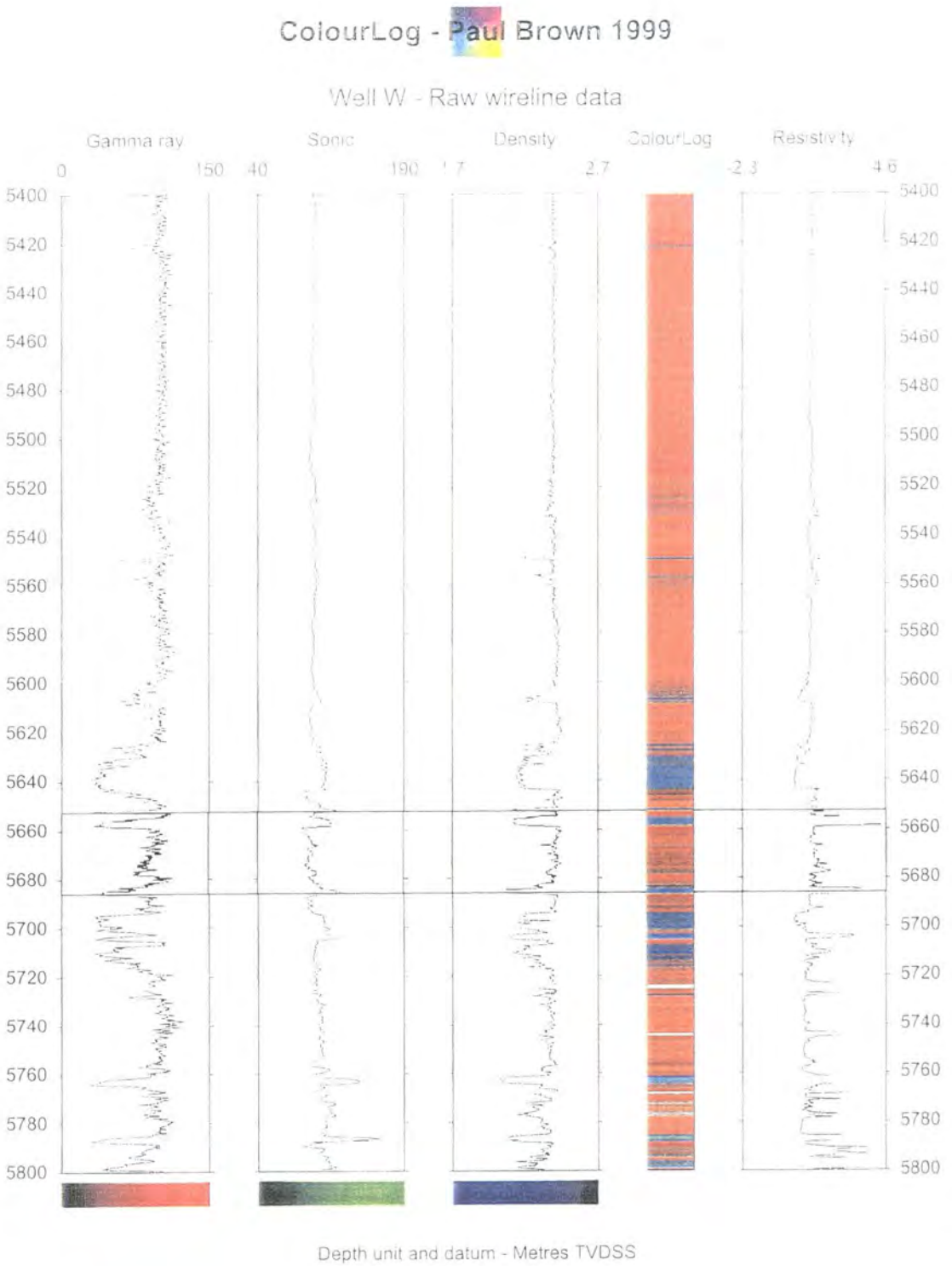

Figure 5.20 - Well W raw and transformed wireline data taken across the lower pressure transition zone.

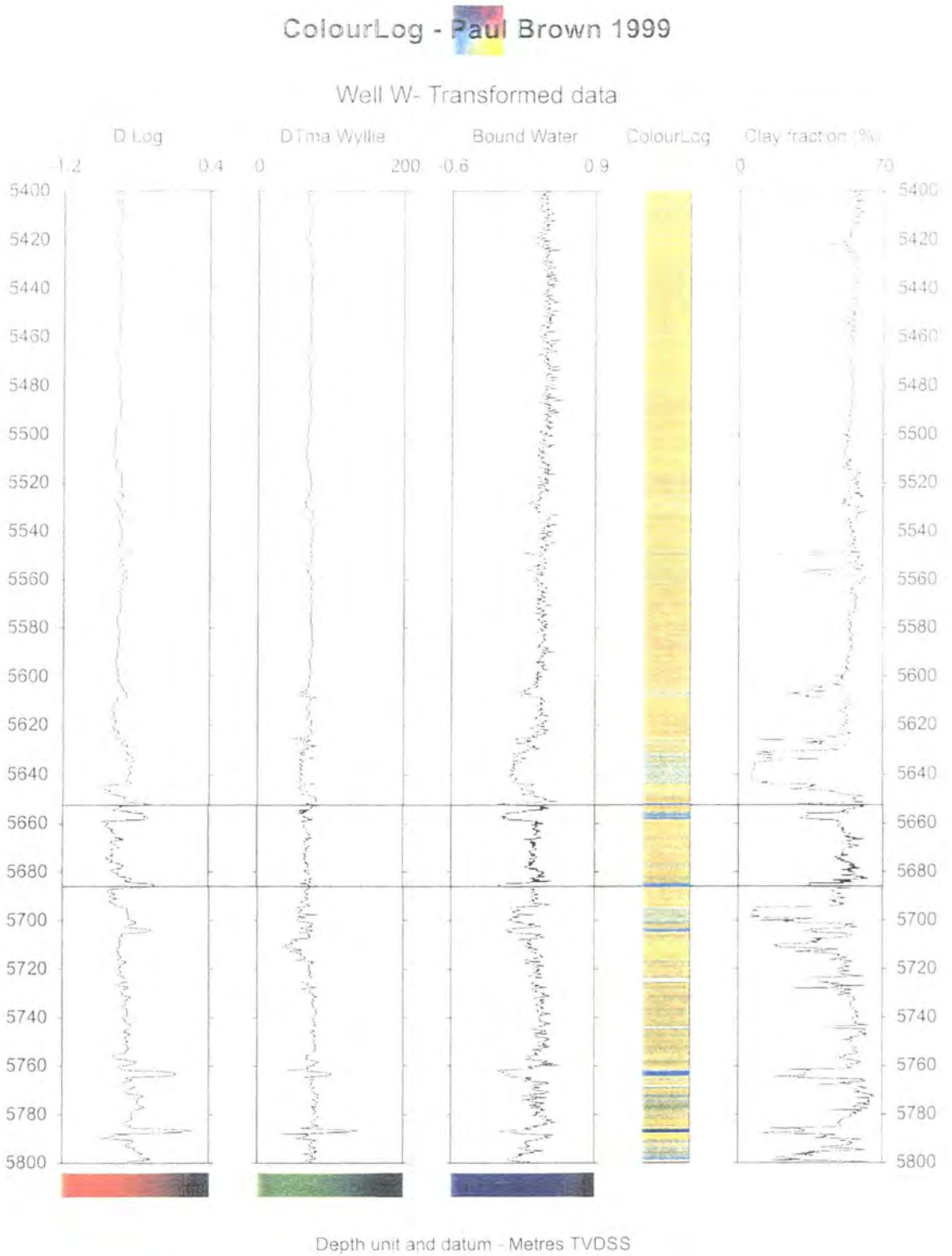

Figure 5.20 continued.

Paul Ecclestone-Brown

5.4.6 Summary - pressure evaluation techniques

The use of resistivity data in Eaton's (1975) method for pressure evaluation was only partially successful. There was only a very small interval of up to 600m from which data could be taken to calibrate a local normal compaction trend. The pressure estimates produced in the upper sections of each well matched the pressure estimates derived during drilling by the operator. The estimates in the lower section of the wells tended towards lithostatic pressure. These estimates in the lower section were unreasonable. There are several potential reasons for the failure of the model. The lithologies sampled in the shallower sections of each wells are unlikely to be the same as those encountered at depth, hence a single resistivity trend may be unlikely. There was limited amount of data available for calibration of the model, so the model may not have been ideally calibrated. The model assumes that the resistivity is solely dependent on depth, with an exponential relationship between the two variable. This simple relationship is more than likely flawed.

As there were no neutron, density or sonic data from any intervals that could be assumed to be normally pressured, no locally derived porosity-depth or porosity-effective stress trends could be defined, so Yang & Aplin's (2000) generic curves were used. The first approach to using these curves entailed using assumed values of clay fraction. This approach yielded sensible estimates of pressure in Wells W and Y, however the pressure estimates in Well Z were less conclusive. The second approach involved using calibration data derived from *ShaleQuant*. This technique provided estimates of pressure with less scatter than those provided using no calibration and enabled a more detailed examination of two specific intervals in which there were marked pressure transitions in Well W. These transition zones were different in character. The upper zone was characterised by a higher clay fraction that that estimated in mudstones from surrounding intervals, thus the mudstones in the interval could be acting as a more efficient pressure barrier than the mudstones in the surrounding sections. No such lithological variation was exhibited within the second, lower interval, so other mechanisms such as faulting must be used to explain the abrupt change in pressure. Discussions subsequent to the research with the Operator of the well have confirmed that these conclusions are viable as the path of the well did not intersect any faults around the depth of the upper transition zone, but there were several faults encountered during drilling at the depth of the second transition zone. During the post-drill basin modelling of the minibasin, the operators have employed the concept of hardgrounds to explain potential permeability barriers to fluid flow at the upper transition zone. These hardgrounds are reasonably analogous to the high clay fraction lithologies suggested by this research.

5.5 Discussion and conclusions

5.5.1 Lithological identification

It is clear from the determination of detailed mudstone lithology using three techniques, namely consideration of gamma ray value, neutron/density matrix inversion techniques and the *ShaleQuant* technique, that all yield qualitatively comparable estimates of lithology. The estimates are in many cases subtly different. One reason for this is the matter of calibration.

The first look gamma ray analysis is based on a very simple notion: the higher the gamma ray value, the higher the clay mineral content. This is typically not supported by local laboratory calibration and thus rarely yields a

comparable value of clay mineral content from field to field, or in some cases from well to well if different, poorly adjusted and calibrated gamma ray tools are used in separate drilling operations. Thus, the gamma ray-based estimation of clay mineral content, whist useful as a first look technique, should be used with great care and should be supplemented with other analyses whenever possible.

The neutron/density matrix inversion technique is based on a poorly controlled set of initial assumptions of rock properties. Use of it assumes that the rock material is purely made up of two materials, the clay mineral assemblage and quartz, and that there is a single fluid phase. A further assumption made in the modelling performed on the three wells in this study was that these three phases were constant with depth. This is not necessarily so. The choice of the constants used to describe the three phases is typically arbitrary, based on the subjective analysis of the wireline data, not on laboratory measurements.

The *ShaleQuant* software written by Yang (1999) is more objective than the other two techniques employed in the study since it was based on many laboratory analyses of mudstone samples. However, it is still possibly subject to poor calibration and the quality of input data. Simply put, if poor quality input data is presented to the neural networks in the program it is highly likely that the program will produce poor quality estimates of the mudstone physical parameters required.

5.5.2 Pressure evaluation

Pressure prediction techniques are reliant upon the definition of normal compaction trends. These trends, if used with the Eaton (1972 & 1975) method, must be valid at all depths at which pressure evaluation is required. This may be difficult when limited amounts of data of unknown quality are available for the definition of the trends, as was seen in the resistivity-based pressure analysis in which the poor quality of estimation in the deeper section was due to poor compaction trend definition.

Equivalent depth-based algorithms for the calculation of vertical effective stress require less knowledge about the compaction trend at all depths or effective stresses. If shallow porosity data are available in the well, simple checks can be made to ensure that the correct compaction trend is being used. This was not the case in the wells in this study. Thus generic compaction trends, although useful as a guide to the vertical effective stress of the sediments, must be used with extreme caution since they all need calibration to ensure their correct usage. This calibration was provided by lithological data from *ShaleQuant*, use of which provided sensible pressure estimation profiles in two of the three wells. Poor data quality may have been a contributory factor in the poor performance of the technique in the third well.

The pressure profiles produced in the upper section of each of the wells from resistivity data and in the lower section from use of generic compaction curves calibrated with data obtained from *ShaleQuant* are complicated. The pressure drawdown in the middle section of each well, between 3,500m and 4,000m cannot be explained in terms of one-dimensional phenomena. It is most likely due to lateral transfer of pressure. In Well W, the sudden increase in magnitude of overpressure around 5,000m TVDSS can probably be attributed to the increase in clay fraction of the mudstones between the sands in which the RFT measurements were made with respect to the mudstones above.

There is no evidence for similar lithological change in the mudstones at the deeper pressure transition zone, thus a purely one-dimensional explanation for the sudden increase in measured pressure at that depth is unlikely.

The *ShaleQuant* definitions of mudstone lithology clearly lend themselves to being used in conjunction with appropriate normal compaction trends in the reverse modelling of pressure from porosity. They will also probably be highly useful when used together with the compaction trends and appropriate porosity-permeability relationships within forward basin modelling simulations. This is the source of much future work.

5.5.3 Conclusions

- Locally derived, resistivity-based pressure evaluation failed to produce a reliable pressure estimate below 3,000m TVDSS in all three study wells.

- Pressure estimates in mudstones could be made to match those measured in associated sandstones reasonably well by using a single generic compaction curve.

- The pressure estimates were improved when lithological information was provided from wireline data using an artificial neural network technique to select the correct generic compaction model at each depth point.

- One of the pressure transition zones observed was associated with high clay fraction in mudstones. This fine-grained sequence acts as a permeability barrier to vertical flow of fluid and hence pressure has built up beneath it. The second transition zone requires a two-dimensional explanation.

- The clay fraction estimates provided by the ShaleQuant technique were heavily influenced by gamma ray readings at each depth point.

6 CENTRAL NORTH SEA CASE STUDY

6.1 Introduction

6.1.1 Chapter summary

This chapter contains a short description of the work performed on data provided from the Everest and Lomond Fields, Central North Sea.

The original aims of the case study were to determine whether the Tertiary section of the North Sea is overpressured and whether the log characteristics of the section were controlled by lithological change, as inferred by Hansen (1996a), or by changes in effective stress as discussed by Leonard (1993).

After completion of the study, the author discovered that the key well for the study, 23/21-2 was drilled through a gas chimney and hence the sonic log data were suspect as a gas saturation of a few percent in the pore fluid of a mudstone can decrease its sonic velocity by up to 10 percent (Rider, 1996). The majority of the analysis in the case study relied upon calibration using data from this well, so most of the study findings were suspect. However, the results of the laboratory characterisation of mudstone samples performed as part of the study are still a useful contribution to the slowly growing database of mudstone properties.

6.1.2 Summary of work performed

Work similar to that performed on the data provided from the Gulf of Mexico was performed. Due to the lack of wireline data in the upper sections of most wells, the majority of work was performed on well 23/21-2 in the Lomond Field. Mudstone cuttings and core samples taken from this well were characterised. Artificial neural networks were trained to estimate clay fraction and matrix density based on measurements on the samples. This ANN was used to provide clay fraction and matrix density estimates in all the study wells. These data were used, together with bulk density data from synthetic density logs provided by a further ANN trained to create bulk density data from sonic, gamma ray and resistivity log data from well 23/21-2, to estimate pressure in the Tertiary section of each well. The bulk density estimation was performed using a technique identical to that discussed in Section 4.3.

The operator of the Lomond Field did not mention that the field was situated under a gas cloud in the Tertiary section. The occurrence of this phenomenon was not put into publicly available literature until Probert *et al.* (2000) published their work on imaging the Lomond Reservoir through gas using four component three-dimensional seismic data.

The majority of the work detailed above was critically reliant upon the performance of the sonic log and the quality of the sonic data obtained from well 23/21-2 is questionable due to the gas cloud, so detailed discussion of this work is not included in this dissertation. A substantial amount of mudstone sample material was analysed. The results of this analysis augments the database of mudstone properties obtained by Hansen (1996a) from wells on the Norwegian Shelf.

This chapter comprised a brief geological history of the Central North Sea area together with descriptions of the geological setting of the Lomond and Everest Fields. These descriptions are followed by a presentation of the mudstone properties.

6.1.3 General geological setting

The pre-Tertiary geology of the North Sea area has been described extensively by Glennie (1990). The Central Graben is an aulacogen that trends northwest-southeast, equidistant from the Scottish and Norwegian coasts, south of the Viking Graben (Figure 6.1). The timing of rifting is debated in the literature; Fisher and Mudge (1990) claim it commenced in the Late Triassic, whereas, Cornford (1994) claims that rifting started in the Early Jurassic. Pre-rift sediments varying from Devonian aeolian sandstones, Permian fluvial sandstones and evaporates to Triassic lacustrine rocks and marine sandstones are encountered within the Central Graben (Cayley, 1987). The Permian evaporites, dominated by salt, were reactivated during the Triassic. This halokinesis has affected the deposition of sediments through to the present day (Holm, 1998). Syn-rift deposits consist primarily of the Late Jurassic Heather Formation, Kimmeridge Claystone Formation and the Fulmar Sandstone. The post rift sedimentation in the area is a result of thermal subsidence that continues to the present day. This subsidence has resulted in the deposition of over 5000m of sediments in the centre of the Graben (Holm, 1998). The Early Cretaceous mudstones and marls of the Cromer Knoll Group are overlain by the Late Cretaceous-Danian Chalk Group. Reactivation of the Caledonides in the Palaeocene resulted in the deposition of the Rogaland Group turbidites (Lovell, 1990). These were derived from the north to north-west and flowed southwards into the Central Graben. The lithology of the Palaeocene strata becomes more distal in nature and hence more mudstone-prone further south and on the edges of the basins. These Palaeocene sand-mudstone sequences are overlain by the Eocene to recent Nordland and Hordaland Group mudstones and siltstones which are over 3300m thick in the Graben area (Holm, 1998).

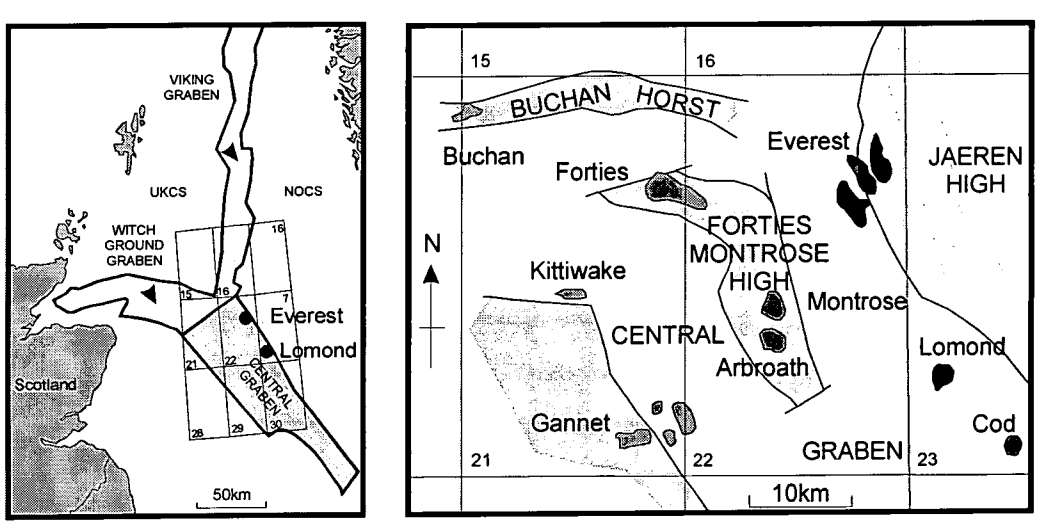

Figure 6.1 - Map showing the regional setting and location of the Everest Complex and Lomond Field. Redrawn after Holm (1998) and Thompson & Butcher (1991).

There are four major post-Danian periods of sedmentation (Liu & Galloway, 1997): in the late Palaeocene, Eocene (described in detail by Mudge and Bujak, 1994), Oligocene and Neogene which continues to the present day. Provenance areas are different for each of these major depositional periods. Palaeocene sediments were sourced

from the Atlantic Margin and from the west, Eocene sediments from the uplifted northern North Sea, Oligocene and Neogene sediments from Southern Norway (Jordt *et al*, 1995).

6.1.4 General pressure profile of the Tertiary section of the Central Graben

Very few direct pressure measurements exist in the Tertiary of the Central Graben apart from the Palaeocene sandstones and Danian chalk (Holm, 1998). Leonard (1993) compiled data from the Norwegian Sector of the Central Graben, using drill-stem tests and porosity logs. He concluded that there was an overpressured compartment in the Tertiary. The onset of overpressure occurred at a variable depth of 1500-2000m within different formations ranging from Oligocene to Miocene in age. The inferred transition zone associated with the onset of pressure is typically narrow, sustaining a pressure increase of up to 20.5MPa over an interval of up to 300m. Further north, Holm (1998) suggests that overpressure has developed in the lower Tertiary mudstones, basing his argument on mudweight required to prevent shales from spalling into the borehole while drilling. However, Palaeocene pressures are near hydrostatic where the sands are well developed.

6.1.5 Geological setting of the Everest Complex

The Everest complex is located on the eastern flank of the Eastern Central Graben in the UK sector of the Central North Sea (Figure 6.1). The major structural elements of the field are summarised in Figure 6.2. The stratigraphy above the Eocene Horda Formation comprises a drape of mudstone and silts (Thompson & Butcher, 1991). The Palaeocene sands onlap on the Chalk towards the northeast over the structural high provided by the Jaeren High.

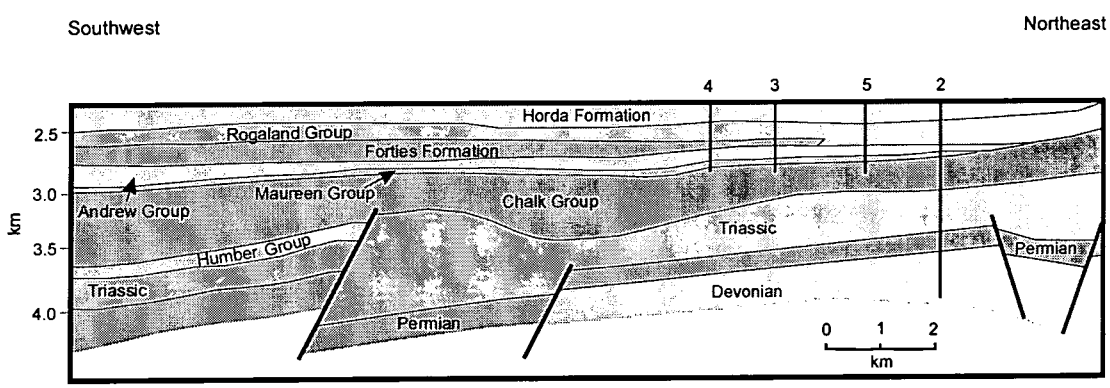

Figure 6.2 - Pre-Oligocene cross-section of the Everest Complex showing wells studied in 22/10a.

6.1.6 Geological setting of the Lomond Field

The Lomond field is situated 25km south of the Everest Complex, closer to the graben centre than Everest. The pre-Cretaceous rocks have not been penetrated by wells in the area, so Figure 6.3, summarising the structure of the area, is fully based on seismic interpretation. There is a salt diapir under the anticline that forms the Lomond Structure. This diapir has not penetrated the Jurassic, but has significantly influenced pre-Oligocene deposition, with many beds being thinned over the structure. The Palaeocene sediments are in a more distal setting than in the Everest Complex, so the sand to shale ratio is lower in Lomond. Again, the post-Palaeocene mudstone and silt sediments form a drape over the area. The post-Palaeocene sediments above the field are affected by a gas cloud (Probert *et al.*, 2000).

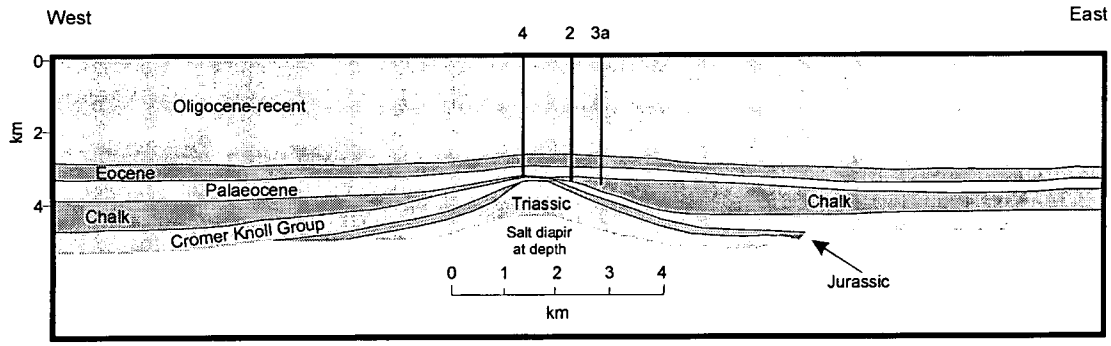

Figure 6.3 -Cross-section of the Lomond Field.

6.2 Mudstone characterisation

6.2.1 Introduction

Twenty-six mudstone samples were obtained from a variety of depths in well 23/21-2. The samples were analysed in the laboratory as described in Section 2.3 and the results were compared to the dataset produced by Hansen (1996a).

6.2.2 Results

The full results of the analysis are shown in Appendix G. Measured mudstone matrix density ranged from 2.64g cm^{-3} to 2.92g cm^{-3} (average 2.80g cm^{-3}) and clay fractions ranged from 40% to 65% (average 50%). The values of matrix density and clay fraction are in broadly the same range as that shown by Hansen (1996a) in his characterisation of mudstones from three wells drilled into the Norwegian Shelf.

6.3 Conclusions

The majority of the work performed in this case study was reliant upon wireline data. The quality of this data is suspect due to the influence of a gas cloud on the sonic log data taken from the post-Palaeocene sediments in the Lomond area. Thus the original aims of the case study have not been met, and no conclusions can be made about the nature of the pressure profile in the Tertiary section of the area.

Twenty-six mudstone samples from well 23/21-2 were characterised, yielding a range of matrix density values from 2.64g cm^{-3} to 2.92g cm^{-3} (average 2.80g cm^{-3}) and a range of clay fraction measurements from 40% to 65% (average 50%).

7 DISCUSSION, CONCLUSIONS AND SUGGESTED FUTURE WORK

7.1 Introduction

This chapter is subdivided into three sections - a general discussion, a summary of the major findings from the error analysis work and case studies and some suggestions for future work. The discussion comprises three broad categories:

- geological comments on the use of local and generic compaction curves in pressure estimation;
- a discussion of standard wireline techniques in the appraisal of mudstone characteristics; and
- comments on the use of artificial neural networks in wireline log data analysis.

7.2 Discussion

7.2.1 Pressure estimation and mudstone compaction

A full understanding of the sedimentary system being modelled is essential for accurate pressure estimation. This includes the lithology, compressibility, porosity-permeability behaviour, temperature history and age of all sediments. Knowledge of the tectonic history of the basin is also required to assess whether a consideration of one-dimensional compaction is sufficient to trace the geological history of the basin. Most of the parameters mentioned above are poorly constrained in most basins.

Selection of the correct compaction model is critical for successful pressure estimation. This selection may be a simple task in the case where a thick, monolithological mudstone unit of known hydrostatic pressure with good wireline coverage is present so that standard pressure estimation techniques can be calibrated and used. Such sedimentary sequences, however, are rare. Mudstone sequences are commonly highly heterogeneous. The onset of overpressure at shallow depths may also cause difficulty since there will be little or no wireline coverage in the normally pressured section. In these cases, one may be tempted to use a regional curve, but there may be problems with this approach. For example, using the compaction trends of proximal wells in a deltaic environment to define the compaction characteristics of wells in distal areas may cause trouble, since the grain size of distal sediments is smaller than those of proximal areas and the compactional behaviour and loading histories of the two wells may be completely different.

The models used in this thesis relating mudstone compactional behaviour to grain size are a first step to producing objective compaction and fluid flow models since they have their basis in laboratory measurements. They take into account difference in lithology due to grain size, so careful use of these compaction relationships may be the only way to define normal compaction, especially in deep water frontier environments. However, if the generic compaction curves produced by Aplin *et al.* (1995) or Yang & Aplin (2000) are to be used without lithological calibration from laboratory measurements on samples, a range of possible compaction curves should be used in order to create an envelope of potential pressure estimates.

The error and sensitivity analysis performed on the generic compaction curves of Yang & Aplin (2000) showed that accurate pressure estimation using soil mechanics based methods is reliant upon accurate measurement of porosity and the controls on compressibility, such as lithology. The sensitivity of the models to errors in the input parameters varies with respect to effective stress. At low effective stress, the rate of change of void ratio with respect to vertical effective stress is high, so small errors in porosity measurements yield small errors in estimates of vertical effective stress. At high effective stress the rate of change of void ratio with respect to effective stress is low, so small errors in porosity measurement will yield sizable errors in effective stress estimate. The inaccuracy associated with clay fraction measurement errors depends upon the relative geometry of the compaction curves. The curves defined by Yang & Aplin (2000) are convergent up to effective stresses of 35-40MPa and so the error in effective stress estimate associated with errors in clay fraction measurement for a given porosity decreases as the load on the sediment increases up to 35MPa. The model is poorly calibrated at effective stresses above 35MPa, hence its use at exceedingly high effective stress is unadvisable.

The Monte Carlo simulation provided a useful basis for the quick assessment of how errors in all constituent parameters combine during the estimation of effective stress. This has been extended to provide a measurement of uncertainty in the pressure estimates. Yang (pers com, 1999) suggested that the generic compaction curves should not be used to define absolute values for pressure; rather the techniques should be used to produce an overall trend in pressure within mudstone packages.

There are a significant number of potential systematic errors involved in the estimation of pore pressure using soil mechanics-based approaches. The following assumptions must be made:

- disequilibrium compaction is the principal mechanism for the development of overpressure;
- the sediments are currently at their maximum burial depth;
- the sediments have not undergone non-mechanical compaction; and
- the overburden gradient is known over the entire drilled interval.

Soil mechanics models are commonly based on vertical effective stress methods - this may be a cause of serious error as the primary control on compaction is likely to be mean effective stress.

Sensible application of generic compaction curves will highlight situations where normal compaction is impossible, which may be due to overpressure, but also due to the failure of the mechanical compaction relationships. This may lead to more detailed studies in which the possibilities of exhumation and /or non mechanical compaction are investigated.

7.2.2 Mudstone petrophysics and wireline log data visualisation

The three quantities used to describe mudstone lithology in this work, namely (1) normalised gamma ray, (2) clay content from neutron/density matrix inversion and (3) clay fraction estimated using *ShaleQuant* (Yang, 1999), are fundamentally different. Gamma ray normalisation and the neutron/density matrix inversion provide descriptions of

lithology that are based on simple sand-mudstone mixing models. Both models assume that sands and mudstones have unique wireline properties. This is not the case: facies vary downhole, the provenance of sediment can change and clay mineralogy can change. By contrast, *ShaleQuant* is an objective, data driven tool for lithological description, limited only by the amount of calibration data it is supplied with.

The transformation of logs in an attempt to remove the effects of compaction is a useful process, since very often compaction is the most significant contributor to the variation of wireline response with respect to depth. Fundamental questions arise, however, about the suitability of wireline transforms for mudstones, since the majority of transforms derived for the resistivity and sonic logs were created for sandstones. Some of the more empirical transforms used may be masking the true underlying physics of acoustic or electrical transmission through a clay mineral-rich porous medium.

7.2.3 Use of artificial neural networks

Neural networks are excellent tools for the analysis of complicated, noisy data such as wireline log data. Their main advantage is objectivity. Since they do not need an *a priori* mathematical model, no bias is applied by choosing the wrong underlying model right at the start of the analysis.

Since ANNs are data driven mathematical processes, one way of adding bias to the learning network is providing the network with only a limited subset of values of input and output parameters compared to the entire range during training; however, this can be stopped by the judicious choice of training examples. As with any data driven numerical method, if the training data or feed-forward data quality is poor, then the quality of the network output will be correspondingly poor.

If several ANNs are trained using the same training examples, all the outputs of the trained networks will be different to a lesser or greater extent depending upon the quality of the training examples. This is due to the initial randomisation of weights during training. The width of the distribution of the network outputs provides an indication of the uncertainty in the network output, which is a form of network precision. If the networks were trained using poor quality data, the network output distribution will be wide.

One common criticism of the neural network methodology is that it is a 'black box' technique. The same criticsm, however, may be raised when considering standard regression techniques. The results of any ANN analysis should be sense-checked with the same rigour with which the results of any regression analysis are checked. Artificial neural networks are commonly used in situations where many parameters are thought to have an influence, hence it is difficult to visualise the nature of any model's response to its input parameters. This is true for regression analysis, especially when non-linear methods are used, and probably more true for ANN analysis. The way a network responds to its inputs can be visualised quite easily in the form of two- or three-dimensional contour plots when there are only two or three inputs. If more inputs are used, linear compounds of inputs produced by, for example, the use of principal component analysis could be used to reduce the dimensionality of the inputs for visualisation.

7.3 Key conclusions

7.3.1 Error analysis

- The generic compaction model used in the thesis can provide estimates of pressure direct from wireline bulk density measurements within a required tolerance of up to an equivalent pressure gradient of ±0.5 pounds per US gallon (up to ±1.77MPa at a depth of 3km).

- Significant errors are likely to occur if an unsuitable compaction or overburden model is employed during pressure analysis.

7.3.2 Wireline log data visualisation

- *ColourLog*, an original software package for Microsoft Windows was created. This software enables the visualisation of three sets of log data by combining them into a single strip of colour, the ColourLog. Each set of data is associated to the intensities of one of the three primary colours at each point. The red, green and blue components are then mixed together using the same additive scheme that a computer monitor uses to produce a colour dependent upon the three input datasets.

- The software is useful for analysis of wireline as rocks with similar wireline characteristics show on the ColourLog as regions of similar colour.

- The wireline data can be manipulated mathematically within the software using techniques such as principal component analysis and cluster analysis; and the data can be visualised using three dimensional plots and triangular plots as well as the depth plots shown throughout this thesis.

7.3.3 Gulf of Thailand case study

- The origin of overpressure in the area is disequilibrium compaction.

- Artificial neural networks outperformed multiple linear regression techniques in the estimation of bulk density from sonic, resistivity and gamma ray wireline data.

- A set of 25 mudstone samples was fully characterised. Measured matrix densities range from 2.58g cm^{-3} to 2.93g cm^{-3} and clay fractions range from 53% to 74%.

- The sediments below the Mid Miocene Unconformity of both wells examined were overconsolidated.

- This overconsolidation suggests that the unconformity surface has undergone up to 1,300m of uplift and it has been reburied by up to 900m.

7.3.4 Gulf of Mexico case study

- Locally derived, resistivity-based pressure evaluation failed to produce a reliable pressure estimate below 3,000m TVDSS in all three study wells.

- Pressure estimates in mudstones could be made to match those measured in associated sandstones reasonably well by using a single generic compaction curve.

- The pressure estimates were improved when lithological information was provided from wireline data using an artificial neural network technique to select the correct generic compaction model at each depth point.

- One of the pressure transition zones observed was associated with high clay fraction in mudstones. This fine-grained sequence acts as a permeability barrier to vertical flow of fluid and hence pressure has built up beneath it. The second transition zone requires a two-dimensional explanation.

- The clay fraction estimates provided by the ShaleQuant technique were heavily influenced by gamma ray readings at each depth point.

7.3.5 Central North Sea case study

- The quality of the wireline data is suspect due to the influence of a gas cloud on the sonic log data taken from the post-Palaeocene sediments in the Lomond area. Thus the original aims of the case study have not been met, and no conclusions can be made about the nature of the pressure profile in the Tertiary section of the area.

- Twenty-six mudstone samples from well 23/21-2 were characterised, yielding a range of matrix density values from 2.64g cm^{-3} to 2.92 g cm^{-3} (average 2.80g cm^{-3}) and a range of clay fraction measurements from 40% to 65% (average 50%).

7.4 Suggestions for further work

7.4.1 Mudstone compaction

The soil mechanics based relationships should be recalibrated in terms of mean effective stress as opposed to vertical effective stress. This is not an easy task, but a first attempt would assume a constant ratio between minimum horizontal stress and vertical stress throughout the crust. This is not correct, but would be a useful first attempt. A second method would be to use one of Breckels & van Eekelen's (1982) relationships between pore pressure, depth and minimum horizontal stress. A third way would be to derive a minimum horizontal stress relationship locally or globally.

Other compaction and overpressure generation mechanisms need to be investigated with respect to their wireline signatures.

7.4.2 Mudstone petrophysics

The petrophysics of mudstones is poorly understood. The variability of sandstones is difficult to handle within a petrophysical framework, and the variability of mudstones is even greater, hence any global petrophysical framework created to describe mudstones will have to be very general in nature.

The underlying physics of wireline responses in mudstones needs to be understood far more clearly, so that petrophysical models are derived using physical first principles rather than empirical relationships.

7.4.3 Future work in the case study areas

Gulf of Thailand: The suggestion that the sediments have undergone chemical compaction needs to be investigated fully. This could be done by performing textural analyses on samples such as XRD crystal alignment studies or illite crystallinity studies. The physical structure of the rock could be investigated by examining SEM or TEM photomicrographs of samples.

More than two wells from the area need to be studied to see whether what has been observed in wells A and B is a real phenomenon and to try to find a regional pattern for the exhumation.

Gulf Mexico: The *ShaleQuant* clay fraction logs could be used to calibrate a full scale forward basin model by employing an upscaling technique to grid mudstone properties as accurately as possible, so that it can be confirmed whether the slight increase in clay fraction observed at each of the pressure transition zones allows the development of a sufficient permeability barrier. The effect of using the generic clay fraction dependent compaction curves in two and three dimensions could then be examined in detail.

Appendix A - BACKPROPAGATION OF ERRORS

A.1 Training algorithm

The method to determine the optimum values of each weight in a network is not trivial. The task is to minimise the network error function, E, when training an ANN with p training data sets. In vector notation:

$$E = \frac{1}{p}\sum_{k=1}^{p}(\underline{z}_k - \underline{\hat{z}}_k)^{\mathrm{T}}(\underline{z}_k - \underline{\hat{z}}_k) \tag{A.1}$$

where $\underline{z}_k$ is the k^{th} target output vector and $\underline{\hat{z}}_k$ is the k^{th} network output vector of the p training examples.

Johanssen *et al.* (1992) use an iterative weight update algorithm:

$$w_k \leftarrow w_k - \mu\frac{\partial E}{\partial w_k} \tag{A.2}$$

where μ is a small constant. They envisage a multi layer perceptron with N layers, each with M nodes. This is for simplicity of notation, in reality each layer can have any number of nodes. Figure A.1 shows the notation used for the network.

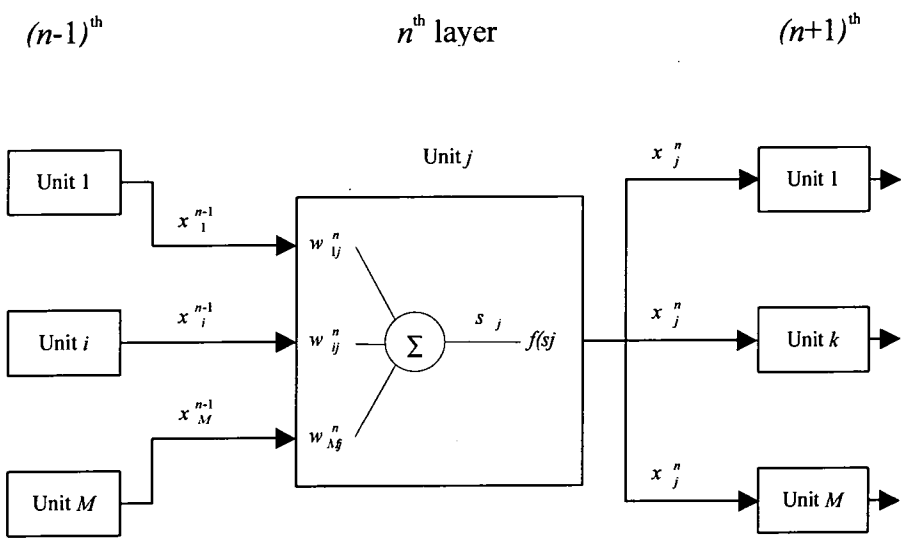

Figure A.1 - Structure of the backpropagation learning algorithm (after Dowla & Rogers, 1995).

Provided that the sigmoid is used as the transfer function, it can be shown that (Johanssen *et al.*, 1992) for the weight connecting the i^{th} node of the $(n\text{-}1)^{th}$ layer to the j^{th} node of the n^{th} layer, the iterative weight update rule is given by:

$$w_{ij}^{n} \leftarrow w_{ij}^{n} - \mu\delta_j^{n} x_i^{n-1} \tag{A.3}$$

where if $n = N$, i.e. in the output layer,

$$\delta_k^N = 2\sqrt{E}\,\frac{\exp\left(-s_k^N\right)}{\left[1+\exp\left(-s_k^N\right)\right]^2} \tag{A.4}$$

and for the hidden nodes in the n^{th} layer:

$$\delta_j^n = \sum_{k=1}^{M} w_{jk}^{n+1}\delta_k^{n+1} \tag{A.5}$$

where the sum is over all the nodes in the $(n+1)^{th}$ layer.

After repeated presentation of each set of input and desired output data to the network and adjusting the weights by using Equations 1.48 to 1.50, the network error will gradually converge to a minimum.

Appendix B - THE *BACKPROP* SUITE OF PROGRAMS

B.1 Description

The *BackProp* suite of programs is broadly based upon the program *bp* written by Dowla and Rogers (1995). This program is a basic exposition of the pure back propagation algorithm, discussed in Chapter 1. The program *bp* presented in this work is a refinement of Dowla and Rogers' program enabling a more automated approach to creating back propagation artificial neural networks. The rest of the programs allow the conversion of a numeric, tab or space delimited data set in tabular form into the data format required by *bp*.

The Borland C source code for each program is provided in the directory **\backprop\src** in the accompanying disk. The programs are also provided as MSDOS executables in the directory **\backprop\bin** in the accompanying disk. There are five separate programs in the *BackProp* suite, four of which, *decim*, *rdecim*, *prep* and *bp*, can be used interactively or with provision of command line arguments. The program *colcomb* can only be used with command line arguments. A brief description of the programs, together with their command line arguments is presented in Table A1.1. Note that the programs cannot handle header lines in files. For help using the programs, type: `ProgramName ?`.

B.2 Example – the Exclusive OR problem

An example of how the programs are used is provided on the disk in the directory **\backprop\XOR** and is outlined in figure A1.1. It is a formulation of the exclusive OR problem described in Beale and Jackson (1991). The constituent data are saved as **XOR.mpb** shown Table A1.2. There are inputs, X_1 and X_2, and one output, Y. The outline for creating the network is as follows:

Create full training data file : `decim XOR 4 3 4`

The full training file, **XOR.tst**, has 3 columns and 4 rows, 2 of the columns, columns 1 & 2, are inputs and column 3 is a required output. The minimum required output is 0 and the maximum is 1.

Create input files for training: `prep 0 XOR 3 4 2 1 0.1 1.1 1 2 3`

(output range) (input columns)

The full file, **XOR.mpb**, has 3 columns and 4 rows, 2 of the columns, columns 1 & 2, are inputs and 1, column 3, is a required output. All three columns are to be provided as reference data.

Create input files for feedforward: `prep 1 XOR 3 4 2 1 3 1 2 3 1 2`

(reference columns) (input columns)

Train a network: `bp 0 XOR 1000 0 2`

Program	Command	Function
decim	`decim [file] [Nteach] [Ncol] [Nact]`	Takes file **file.mpb** with dimensions N_{act} and N_{col} and extracts N_{act} rows equally distributed through the dataset. Saves the new file as **file.tst**.
rdecim	`rdecim [file] [Nteach] [Ncol] [Nact]`	Takes file **file.mpb** with dimensions N_{act} and N_{col} and extracts N_{teach} rows randomly distributed through the dataset. Saves the new file as **file.tst**.
prep (Learning mode)	`prep 0 [file] [Ncol] [Nteach] [Nin] [Nout] {output ranges} {input columns} {output columns}`	Takes file **file.tst** with dimensions N_{teach} and N_{col}. Extracts input columns and saves them as **file.tra**. Extracts output columns, normalises them and saves as **file.exp**.
bp (Learning mode)	`bp 0 [file] [Nit] 0 [Nneu]`	Trains a back propagation neural network with a single layer of N_{neu} neurons using **file.tra** as the inputs and **file.exp** as the required outputs. Creates **file.wei** which defines the network size and weights
prep (Feedforward mode)	`prep 1 [file] [Ncol] [Nact] [Nin] [Nout] [Nref] {reference columns} {input columns}`	Takes file **file.mpb** with dimensions N_{act} and N_{col}. Extracts input columns and saves them as **file.run**. Extracts reference columns and saves as **file.dum**.
bp (Feedforward mode)	`bp 1 [file]`	Runs the ANN defined by **file.wei** using **file.run** as the inputs to the network. **file.dum** contains reference data that are combined with the network outputs in **file.neu**.
colcomb	`colcomb [Nrows] [file1] [Ncol1] [file2] [Ncol2]`	Combines N_{row} rows of files **file1** and **file2** with N_{col1} and N_{col2} columns repectively,

Table B.1 - The commands used in the *BackProp* suite of programs.

X_1	X_2	Y
0	0	0
0	1	1
1	0	1
1	1	0

Table B.2 - The XOR problem raw data.

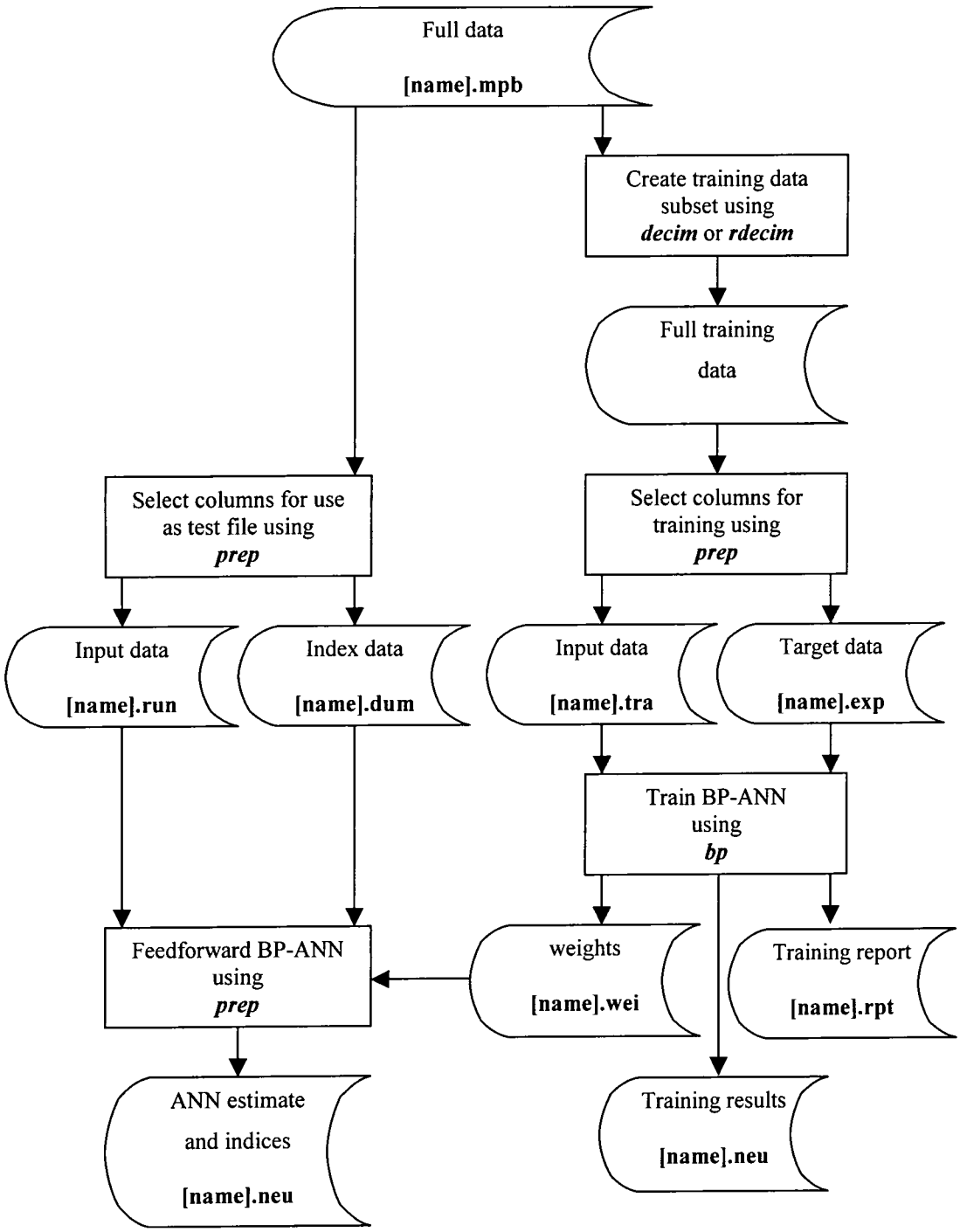

Figure B.1 - A schematic of a workflow used in training and testing a single neural nework using the backprop suite of programs.

Run the network: `bp 1 XOR`

The results of the ANN analysis are stored in `XOR.neu` in a tab-delimited format that can be read by any spreadsheet program.

B.3 Multiple artificial neural networks

The *BackProp* suite of programs can be used, with a little coaxing, to train and run multiple sets of neural networks. Example MSDOS batch files used to create a set of weights files for a particular set of data are shown in Listings A1.1 and A1.2. An example MSDOS batch file used to run the feedforward networks is shown in Listing A1.3.

Batch file *trainBP.bat* creates four separate neural network weights files called **[filename]01.wei** to **[filename]04.wei** by calling *randBP.bat* four times. This batch file creates a random subset of the main data file for training each time it is run, and trains an ANN with five hidden layer neurons using 5000 training iterations. *trainBP.bat* takes the weights file created by *randBP.bat* and renames it in numerical order. The training output is saved to a file named **training.txt**.

```
REM Batchfile trainBP
REM Usage trainBP [filesuite name (no extension)] ...
REM     ... [No of training examples required] ...
REM     ... [No of data vectors available]
REM Written by Paul Brown 1999

call randBP %1 %2 %3
copy %1.wei %101.wei
copy %1.neu training.txt

call randBP %1 %2 %3
copy %1.wei %102.wei
type %1.neu >> training.txt

call randBP %1 %2 %3
copy %1.wei %103.wei
type %1.neu >> training.txt

call randBP %1 %2 %3
copy %1.wei %104.wei
type %1.neu >> training.txt
```

Listing B.1 - Batch file trainBP.bat.

```
REM Batchfile randBP
REM Usage randBP [filesuite name (no extension)] ...
REM     ... [No of training examples required] ...
REM     ... [No of data vectors available]
REM Written by Paul Brown 1999

rdecim %1 %2 8 %3
prep 0 %1 8 %2 3 1 1.5 3 5 6 7 3
bp 0 %1 5000 0 5
```

Listing B.2 - Batch file randBP.bat.

Batch file *runBP.bat* takes the weights files created by *trainBP.bat* and runs the data in **[filename].mpb** through the resultant neural networks. The results of all the feedforward neural network runs are combined using the program *colcomb* into the file **results.txt**.

```
REM Batch file runBP
REM Usage run [weights root filename] ...
REM     ... [feedforward data filename] ...
REM     ... [No of data vectors to be used]
REM Written by Paul Brown 1999

REM prepare feedforward file with depth reference

prep 1 %2 8 %3 3 1 2 2 3 5 6 7

copy %101.wei %2.wei
bp 1 %2
copy %2.neu temp.jun
copy %2.neu %11.neu

REM prepare feedforward file without depth reference

prep 1 %2 8 %3 3 1 0 5 6 7

copy %102.wei %2.wei
bp 1 %2
colcomb %3 temp.jun 3 %2.neu 1 > results.txt
copy results.txt temp.jun
copy %2.neu %12.neu

copy %103.wei %2.wei
bp 1 %2
colcomb %3 temp.jun 4 %2.neu 1 > results.txt
copy results.txt temp.jun
copy %2.neu %13.neu

copy %104.wei %2.wei
bp 1 %2
colcomb %3 temp.jun 5 %2.neu 1 > results.txt
copy results.txt temp.jun
copy %2.neu %14.neu
```

Listing B.3 - Training batchfile.

Appendix C - DATA FROM THE GULF OF THAILAND

C.1 Pressure data

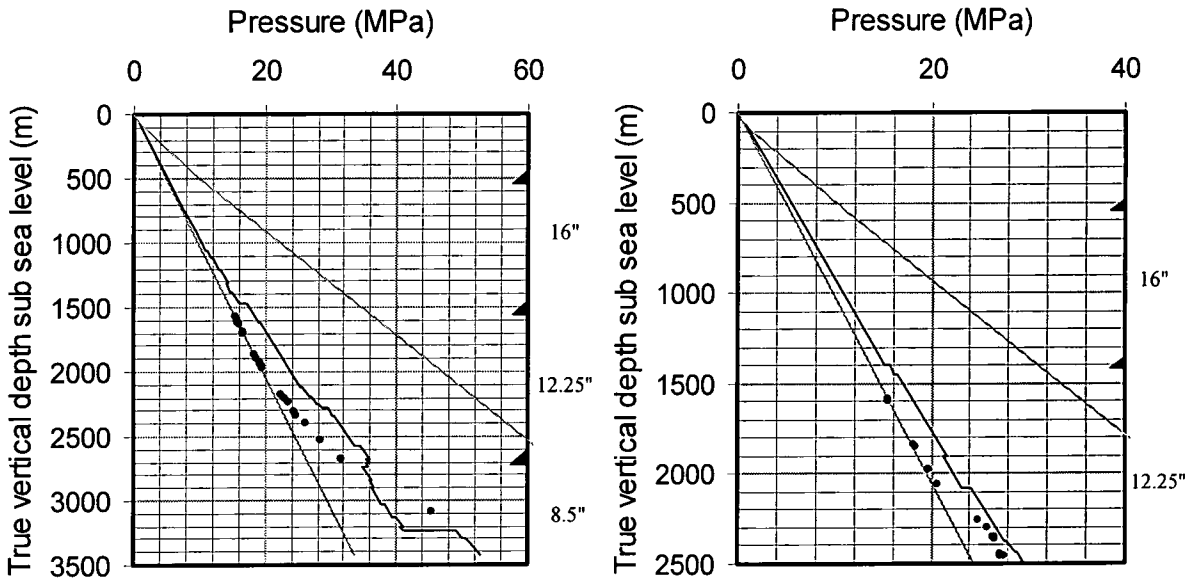

Figure C.1 - Pressure data from Well A (left) and Well B (right). Grey lines represent hydrostatic and lithostatic pressure. Black circles are MDT measurements of pressure in sand. The black curve is the drilling mud pressure and the triangles represent the casing points.

C.2 Wireline data

Bit Size	MD range (m)	TVDSS range (m)	Logs taken
Well A			
16"	560-1631	547-1550	Array induction imager, Array sonic, Gamma ray, Litho-density log, Compensated neutron log and Spectral gamma ray
12.25"	1631-3075	1550-2720	
8.5"	3075-3923	2720-3438	
Well B			
16"	555-1604	542-1405	As well A
12.25"	1604-3045	1405-2520	

Table C.1 - Wireline tools run and data obtained during the drilling of wells A and B.

C.3 Quality control of wireline data

Hole	16" above unconformity	Rest of 16"	12¼"	8½"
Well A				
Total number	3291	3896	9474	5451
>4"	554	3	35	127
>3"	1259	39	44	185
>2.5"	1860	83	70	262
>2"	2381	171	406	481
>1.5"	2870	438	1843	1125
>1"	3204	1114	4218	3373
>0.5"	3283	2287	7864	5215
Well B				
Total number	1635	5199	9526	-
>2.5"	22	7	229	-
>2"	120	27	637	-
>1.5"	338	108	1410	-
>1"	768	593	2435	-
>0.5"	1248	2141	6020	-

Table C.2 - Number of out of gauge data points in for different depth ranges in each well.

Hole size (inches)	SGR multipliers			CGR multipliers	
	Thorium	Potassium	Uranium	Thorium	Potassium
Well A					
16	2.736	11.498	5.177	2.734	11.501
12¼ & 8½	3.054 (1.116)	12.689 (1.104)	5.822 (1.125)	3.054 (1.117)	12.688 (1.104)
Well B					
16	2.789 (1.019)	11.702 (1.018)	5.285 (1.020)	2.788 (1.020)	11.702 (1.018)
12¼	3.303 (1.207)	13.688 (1.191)	6.317 (1.219)	3.303 (1.208)	13.688 (1.190)

Table C.3 - Multipliers used to calculate SGR and CGR from constituent elemental proportions. Figures in parentheses are proportion of Well A 16" hole.

C.4 Mudstone sample laboratory analysis

Depth (m TVDSS)	Matrix density			Clay fraction		
	Number of analyses	Value ($g\ cm^{-3}$)	Standard deviation ($g\ cm^{-3}$)	Number of analyses	Value (%)	Standard deviation (%)
598	3	2.93	0.010	3	53%	4%
751	3	2.63	0.024	3	62%	4%
877	3	2.58	0.008	2	52%	2%
1117	3	2.67	0.030	3	63%	3%
1187	2	2.71	0.015	2	58%	3%
1263	2	2.66	0.022	2	68%	5%
1839	3	2.63	0.032	3	69%	2%
1982	2	2.63	0.022	2	74%	5%
2062	3	2.79	0.023	2	60%	4%
2077	2	2.79	0.039	2	55%	2%
2077.5	3	2.8	0.002	3	55%	3%
2078.5	3	2.76	0.022	3	61%	1%
2082	3	2.77	0.010	2	71%	3%
2380	3	2.76	0.007	2	72%	2%
2546	3	2.69	0.005	3	69%	3%
2547	3	2.69	0.032	3	67%	1%
2548	3	2.82	0.014	3	62%	1%
2565	3	2.8	0.028	3	74%	4%
2835	3	2.59	0.010	3	49%	1%
2934	3	2.75	0.006	3	59%	4%
3267	2	2.55	0.028	2	72%	2%
3390	3	2.76	0.019	3	61%	3%

Table C.4 - Experimental measurements of clay fraction and matrix density on samples taken from Well A.

C.5 Synthetic density log creation

Training set \ Test set		Well A			Well B		
		Whole	Mud	Sand	Whole	Mud	Sand
Well A	Average uncertainty	0.054	0.031	0.073	0.052	0.048	0.056
	Percentage within $\pm 0.05 gcm^{-3}$	67.6	75.4	54.4	24.5	22.5	26.9
	Percentage within $\pm 0.10 gcm^{-3}$	87.9	94.2	82.7	52.3	52.1	52.6
Well B	Average uncertainty	0.056	0.042	0.065	0.047	0.041	0.054
	Percentage within $\pm 0.05 gcm^{-3}$	22.7	29.1	16.3	55.7	60.8	49.4
	Percentage within $\pm 0.10 gcm^{-3}$	56	70.8	41.6	85.7	90.6	79.7

Table C.5 - performance of the ANN models trained to estimate bulk density from sonic, resistivity and gamma ray data.

Training set \ Test set	Well A	Well B
Well A	***0.911***	0.845
Well B	0.893	***0.900***

Table C.6 - Correlation coefficients between actual measurements and ANN estimates of density. Bold, italic type indicates regions in which the ANN's were performing an interpolation.

Training set \ Test set		Well A	Well B
Well A	Correlation coefficient	0.835	0.801
	Percentage within ±0.05gcm^{-3}	45.4	32.5
	Percentage within ±0.10gcm^{-3}	76.6	56.8
Well B	Correlation coefficient	.791	0.864
	Percentage within ±0.05gcm^{-3}	26.3	54.1
	Percentage within ±0.10gcm^{-3}	61.3	81.0

Table C.7 - Descriptive statistics of the linear model estimates of density.

C.6 Pressure modelling using locally defined compaction curves

Well	Gamma ray range (API)	Compaction coefficients		R^2
		β	e_{100}	
Well A	100-110	0.26	1.56	0.81
	110-120	0.27	1.64	0.82
	120-130	0.25	1.52	0.76
	130-140	0.23	1.44	0.82
Well B	100-110	0.21	1.27	0.85
	110-120	0.22	1.33	0.91
	120-130	0.21	1.29	0.91
	130-140	0.21	1.35	0.86

Table C.8 - Soil mechanics based compaction trends calculated using void ratio derived from sonic log data measured below the Mid Miocene Unconformity.

Appendix D - UPLIFT CALCULATIONS

D.1 Uplift study - conversion of void ratio-effective stress to porosity-depth relationships

The following numerical process was used to convert Yang & Aplin's (2000) effective stress-based compaction trends to yield porosity-depth trends.

At any depth beneath the sediment surface, z, it was assumed that Terzaghi's (1923) effective stress relationship holds thus

$$\sigma_v(z) = s_v(z) - P_{fl}(z) \tag{D.1}$$

For any small increase in depth, Δz, there would be a corresponding increase in effective stress such that

$$\sigma_v(z+\Delta z) = \sigma_v(z) + \Delta s_v - \Delta P_{fl} \tag{D.2}$$

where

$$\Delta P_{fl} = \rho_{fl} g \Delta z \tag{D.3}$$

and the increment in depth is small enough so that the reduction in porosity of the sediment due to compaction is negligible so that the following simplification for the increase in vertical stress can be made

$$\Delta s_v = \{\phi(z)\rho_{fl} + (1-\phi(z))\rho_{ma}\} g \Delta z \tag{D.4}$$

substituting for ΔP_{fl} and Δs_v in D.2 and rearranging gives

$$\sigma_v(z+\Delta z) = \sigma_v + (\rho_{ma} - \rho_{fl})(1-\phi(z)) g \Delta z \tag{D.5}$$

void ratio at depth $z+\Delta z$ can be calculated using

$$e = e_{100} - \beta \ln\left(\frac{\sigma_v(z+\Delta z)}{100}\right) \tag{D.6}$$

where the compaction coefficients e_{100} and β are constrained by clay fraction using Yang & Aplin's (2000) relationships. The void ratio at depth $z+\Delta z$ is converted to porosity by

$$\phi = \frac{e}{1+e} \tag{D.7}$$

Thus if porosity is known at any depth, the remainder of the compaction curve can be estimated very quickly using a simple spreadsheet program such as that provided on the accompanying CD ROM. In the entirety of the study, a simplifying assumption is made that at a depth of 25m beneath the sediment surface, effective stress is equal to 100kPa and therefore $e = e_{100}$.

For analytic simplicity, a regression is performed to relate vertical hydrostatic effective stress, and hence vertical stress with depth. Typically this relation is shown throughout the work as a third order polynomial constrained so that effective stress is zero at the sediment surface. A sample of this analysis is included on the accompanying CD ROM entitled "Compaction - VRsig to phiZ.xls".

D.2 Uplift study - determination of clay fraction

At any depth, void ratio of the sediment is defined as a function of effective stress by

$$e = e_{100} - \beta \ln\left(\frac{\sigma_v}{100}\right) \tag{D.8}$$

provided the sediments are at their maximum burial depth. If the sediments are not that their maximum burial depth, the observed void ratio is then a function of maximum effective stress. This effective stress can be estimated using the integrated values of the density log, where available, and suitable effective stress -depth trends as derived in Section 4.5.3taking into consideration any apparent uplift.

Since the compaction coefficients e_{100} and β are constrained (Yang & Aplin, 2000) by

$$\beta = 0.0407 + 0.2479 v_{cf} + 0.3684 v_{cf}^2 \tag{D.9}$$

and

$$e_{100} = 0.3024 + 1.6867 v_{cf} + 1.9505 v_{cf}^2 \tag{D.10}$$

where v_{cf} is the clay fraction of the sediment. Thus at any depth

$$v_{cf}^2\left(1.9505 - 0.3684 \ln\left(\frac{\sigma_v}{100}\right)\right) + v_{cf}\left(1.6867 - 0.2479 \ln\left(\frac{\sigma_v}{100}\right)\right) + 0.3024 - 0.0407 \ln\left(\frac{\sigma_v}{100}\right) - e = 0 \tag{D.11}$$

which, provided real solutions exist, can be solved for v_{cf} by taking the positive root of the equation by using the quadratic formula.

Appendix E - REALISATION OF NEWTON-RAPHSON METHOD

E.1 Background theory

The roots of any continuous function can be found using the iterative Newton-Raphson method which is described below.

An estimate of a real root, r, of any continuous function $f(x)$ can be approximated by using the following iterative formula

$$x_{n+1} = x_n - \frac{f(x_n)}{f'(x_n)} \tag{E.1}$$

where x_n is an estimate of r, provided that the derivative of the function, $f'(x)$, is non zero at x_n.

E.2 Realisation of method for n^th order polynomials in MS Excel

The Newton-Raphson method for nth order polynomials was realised as a Visual Basic for Applications Function so that it could be used as an Excel Worksheet function.

```
Function PolyNewton(Coeff As Variant, Power As Variant, Estimate As
Double, Accuracy As Double, MaxIt As Double) As Variant
'This function performs the Newton-Raphson Method on an nth power
polynomial

    Dim i As Long, j As Long, NoCoeffCol As Long, NoCoeffRow As Long
    Dim Counter As Long, Converged As Boolean
    Dim Data() As Double, Coefficients As Variant, NoCoeff As Long
    Dim x1 As Double, x2 As Double, f As Double, fdash As Double


    Accuracy = 10 ^ (-Accuracy)
    Coefficients = Coeff

'Collate Data into useful format

    NoCoeffRow = UBound(Coefficients, 1)
    NoCoeffCol = UBound(Coefficients, 2)
    NoCoeff = NoCoeffCol * NoCoeffRow
    Counter = 1

    ReDim Data(NoCoeff, 4)

    For i = 1 To NoCoeffRow
        For j = 1 To NoCoeffCol
            'function data
            Data(Counter, 1) = Coefficients(i, j)
            Data(Counter, 2) = Power(i, j)
            'derivative data
            Data(Counter, 3) = Coefficients(i, j) * Data(Counter, 2)
            Data(Counter, 4) = Power(i, j) - 1
            Counter = Counter + 1
```

```
        Next
    Next


'main iterative loop
    Counter = 0
    Converged = False
    x1 = Estimate
    Do
        'calculate f and fdash
        f = 0
        fdash = 0
        For i = 1 To NoCoeff
            f = f + Data(i, 1) * x1 ^ Data(i, 2)
            fdash = fdash + Data(i, 3) * x1 ^ Data(i, 4)
        Next

        'calculate next estimate
        x2 = x1 - f / fdash

        'check tollerance
        If Abs(x1 - x2) < Accuracy Then Converged = True

        x1 = x2
        Counter = Counter + 1

    Loop While Counter < MaxIt And Converged = False

    If Converged Then
        PolyNewton = Array(x1, Counter)
    Else
        PolyNewton = Array("Did not converge", Counter)
    End If

End Function
```

Listing E.1 - Newton-Raphson method for polynomials.

The use of the function is outlined in the spreadsheet "Newtons Method.xls" on the accompanying CD ROM.

Appendix F - DATA FROM THE GULF OF MEXICO

F.1 Pressure data

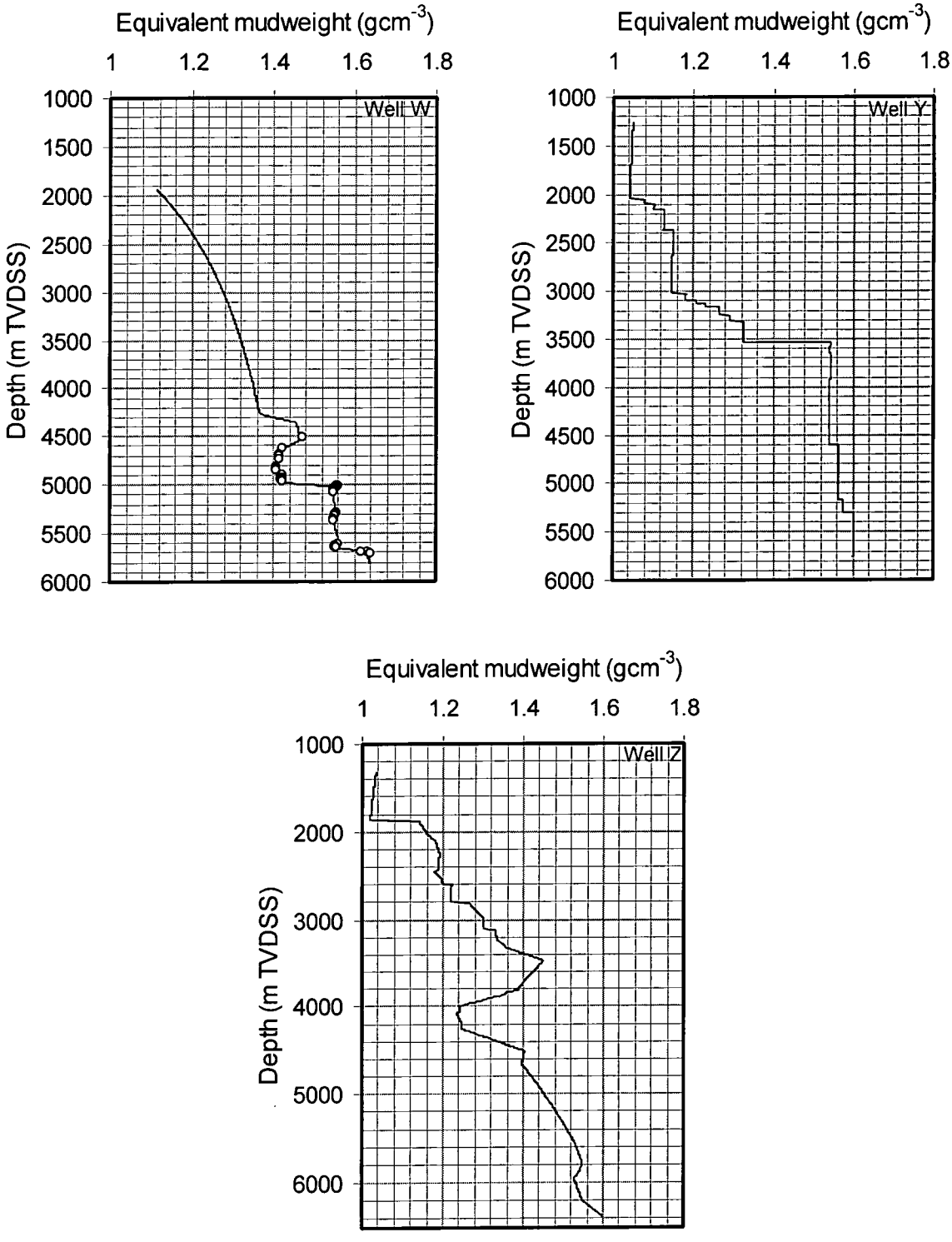

Figure F.1 - Mudweight pressure data from the study wells. The circles show MDT measurements.

F.2 Raw wireline data

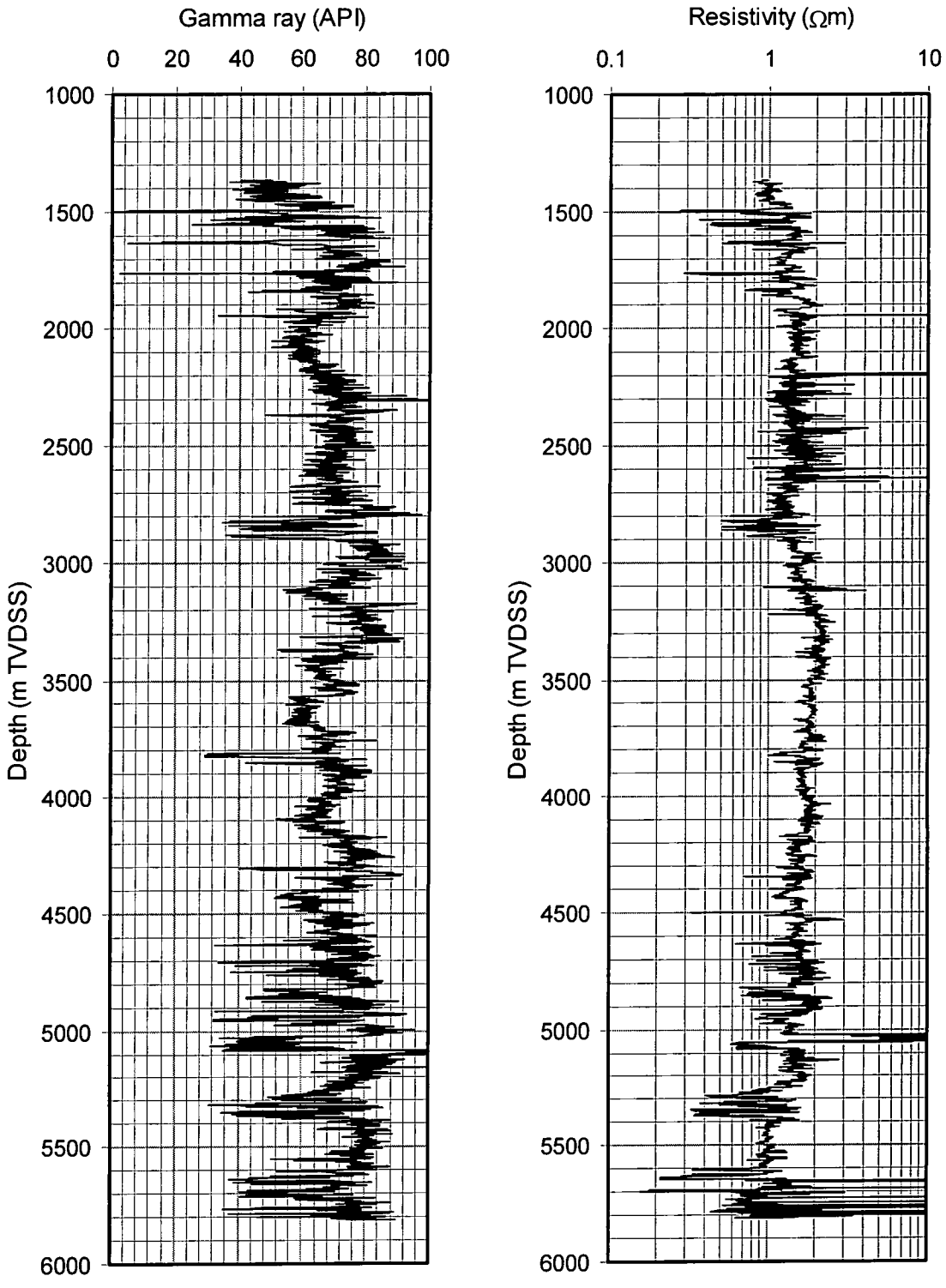

Figure F.2 - Well W gamma ray and resistivity data over the entire drilled interval.

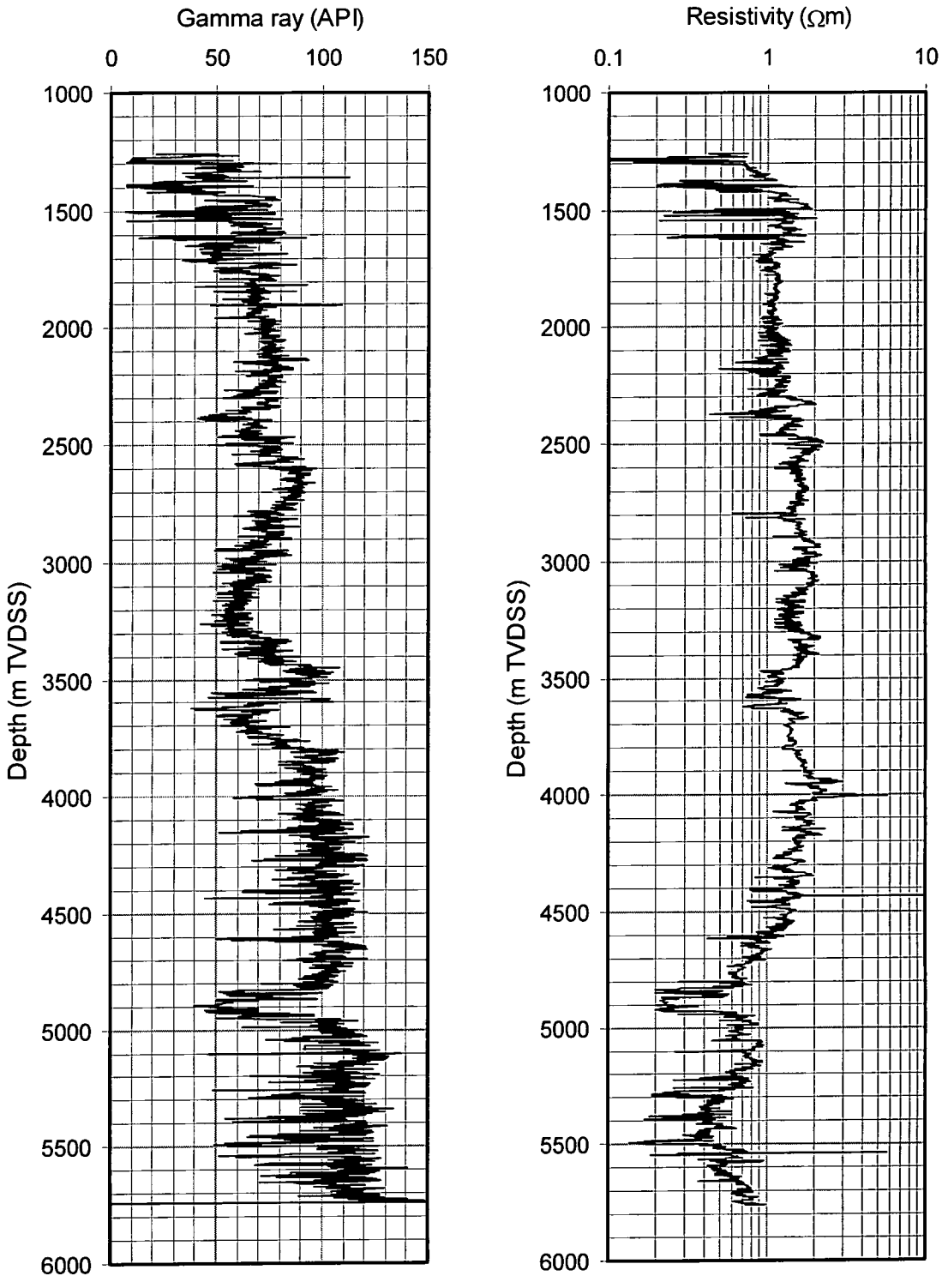

Figure F.3 - Well Y gamma ray and resistivity data over the entire drilled interval.

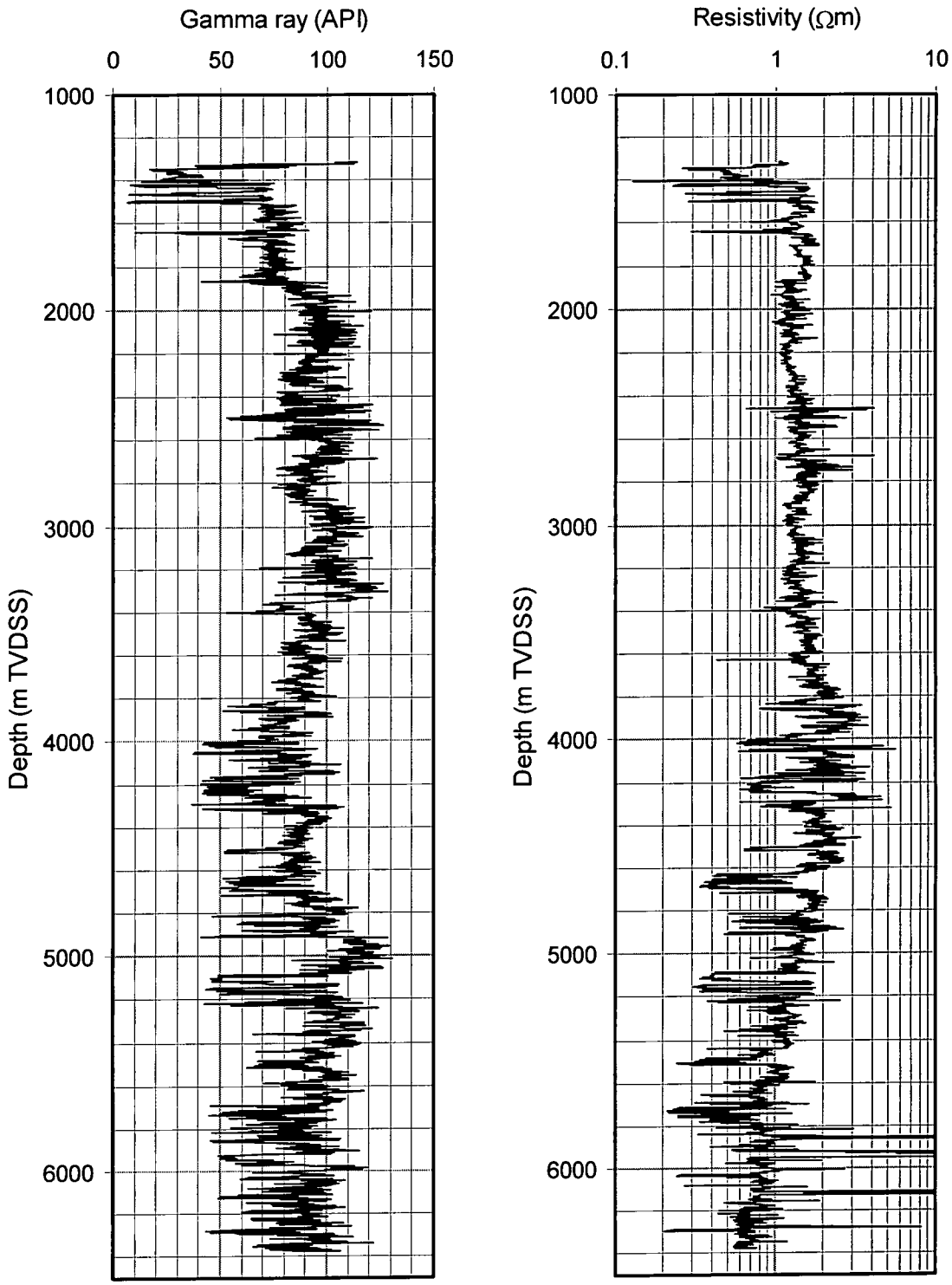

Figure F.4 - Well Z gamma ray and resistivity data over the entire drilled interval.

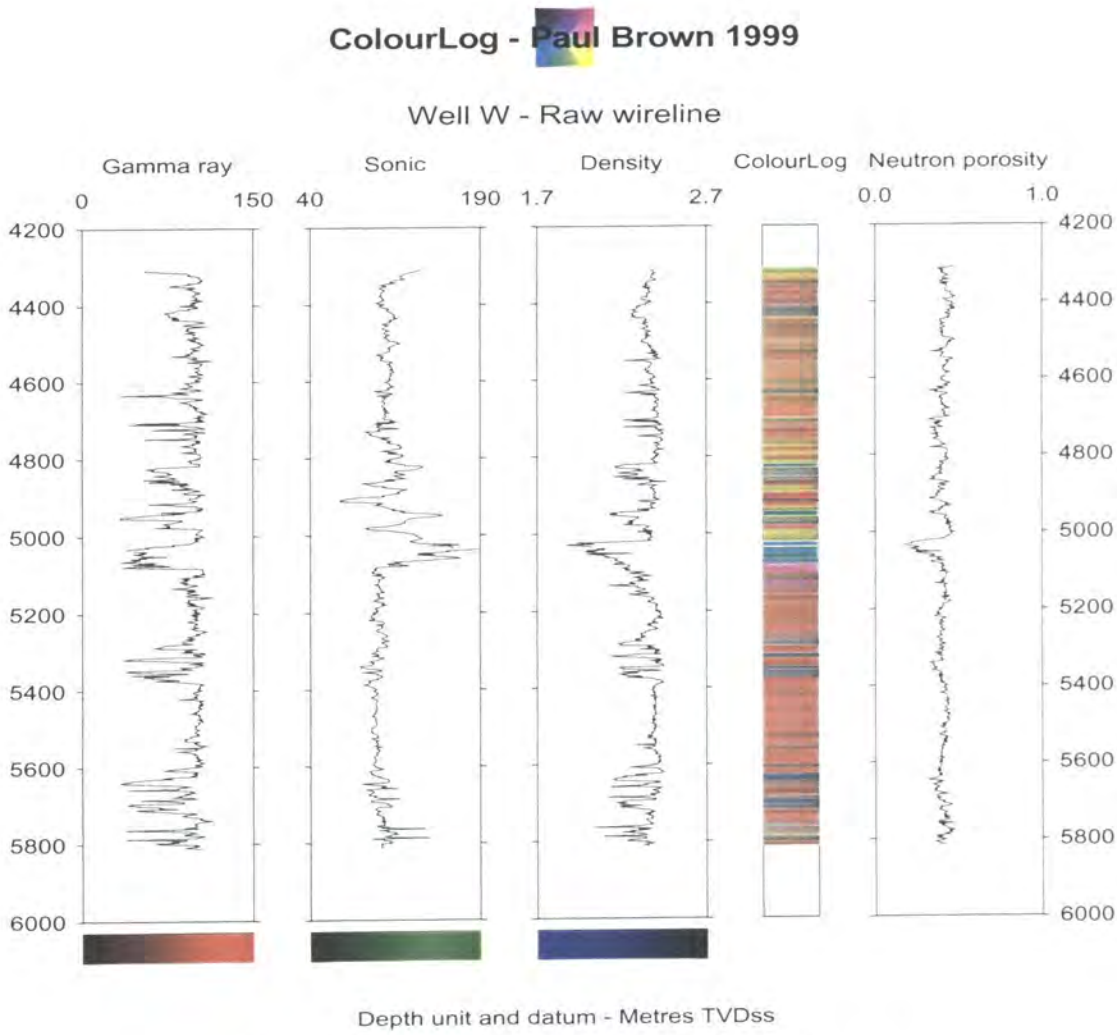

Figure F.5 - Well W wireline logs taken from 12¼" section.

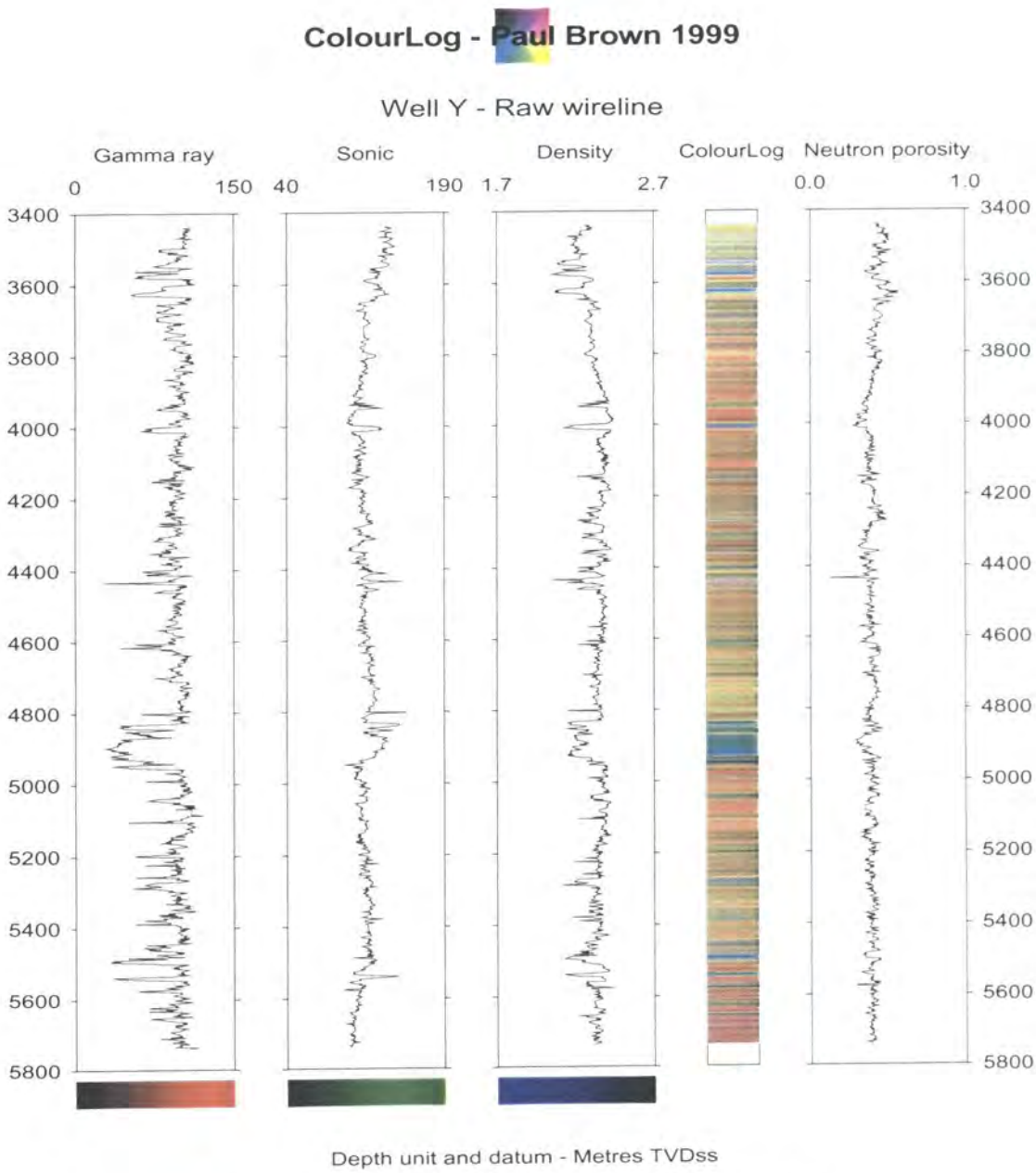

Figure F.6 - Well Y wireline logs taken from 12¼" section.

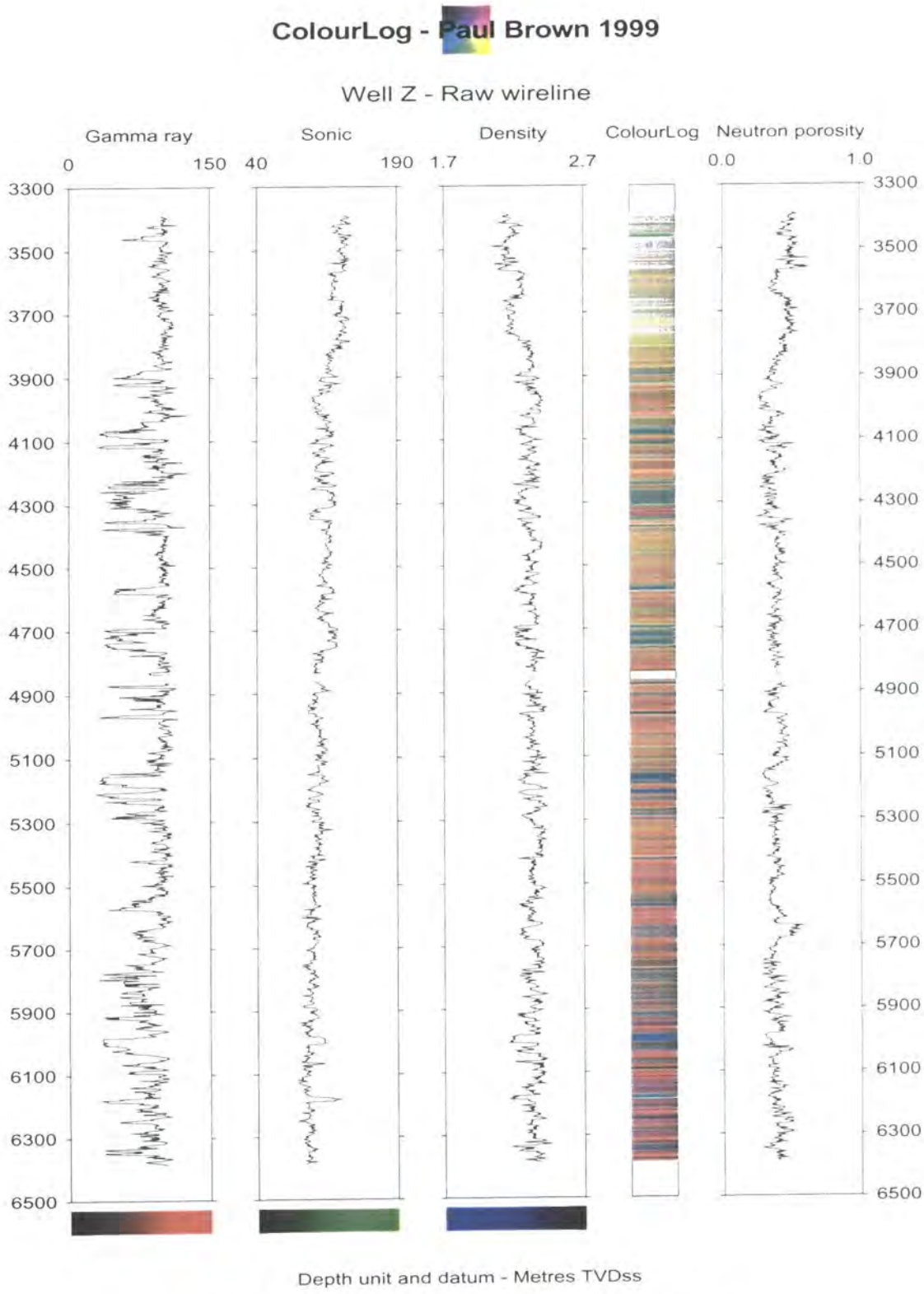

Figure F.7 - Well Z wireline logs taken from 12¼" section.

Appendix G - CENTRAL NORTH SEA DATA

G.1 Laboratory measurements of mudstone properties

Depth (m TVDSS)	Matrix density			Clay fraction		
	Number of analyses	Value ($g\ cm^{-3}$)	Standard deviation ($g\ cm^{-3}$)	Number of analyses	Value (%)	Standard deviation (%)
526	2	2.82	0.028	0	-	-
654	3	2.75	0.016	3	42%	2%
696	2	2.81	0.025	2	45%	3%
818	3	2.81	0.039	3	45%	1%
855	3	2.83	0.037	3	46%	4%
919	3	2.8	0.011	0	-	-
1020	3	2.85	0.023	3	46%	4%
1056	3	2.82	0.016	3	58%	3%
1303	3	2.79	0.014	3	64%	2%
1349	3	2.91	0.037	2	65%	4%
1376	3	2.79	0.044	2	54%	3%
1422	3	2.71	0.026	0	-	-
1486	3	2.92	0.017	0	-	-
1707	3	2.79	0.027	3	51%	4%
1768	2	2.7	0.019	2	53%	4%
1798	3	2.87	0.038	3	49%	5%
1847	3	2.75	0.037	3	42%	3%
1957	3	2.83	0.02	3	51%	2%
2066	2	2.83	0.042	2	44%	2%
2127	3	2.8	0.028	3	40%	5%
2158	3	2.83	0.031	3	46%	1%
2274	3	2.64	0.039	3	59%	3%
2365	3	2.77	0.029	3	48%	2%
2461	3	2.82	0.036	3	55%	4%
2534	3	2.88	0.034	2	52%	3%
2775	3	2.67	0.037	3	46%	2%

Table G.1 - Experimental measurements of clay fraction and matrix density on samples taken from well 23/21-2.

REFERENCES

Adams, J. A. & Weaver, C. E. (1958). Thorium-uranium ratios as indicators of sedimentary processes: example of concept of geochemical facies. *AAPG Bulletin*, **42**, 387-430.

Allen, C. R., Gillespie, A. R., Han, Y., Sieh, K. E., Zhang, B. & Zhu, C., (1984). Red river and associated faults, Yunnan Province, China: Quaternary geology, slip rates and seismic hazard. *Bulletin of the Geological Society of America*, **95**, 686-700.

Aplin, A.C., Yang, Y. & Hansen, S. (1995). Assessment of β, the compression coefficient of mudstones and its relationship with detailed lithology. *Marine and Petroleum Geology*, **12**, 955-963.

Aplin, A. C., Yang, Y. & Larter, S. R., (1999). Rapid, wireline log assessment of shale properties for basin modelling (Abstract). *Proceedings of the 1999 AAPG Annual Meeting, San Antonio, USA*, A6.

Archie, G., (1942). The electrical resistivity log as an aid in determining some reservoir characteristics. *Transactions of the AIME*, **146**, 54-62.

Asquith, G. E. & Gibson C., (1982). *Basic well log analysis for geologists.* AAPG Methods in Exploration. American Association of Petroleum Geologists, Tulsa, USA.

Atkinson, J., (1993). *An Introduction to the Mechanics of Soils and Foundations.* McGraw-Hill, London, UK.

Athy, L. F., (1930). Density, porosity and the compaction of sedimentary rocks. *AAPG Bulletin*, **14**, 1-24.

Audet, D. M., (1995). Mathematical modelling of gravitational compaction and clay dehydration in thick sediment layers. *Geophysical Journal International*, **122**, 283-298.

Audet, D. M. & McConnell, J.D.C., (1992). Forward modelling of porosity and pore pressure evolution in sedimentary basins. *Basin Research*, **4**, 147-162.

Baldwin, B. & Butler, C. O., (1985). Compaction curves. *AAPG Bulletin*, **69**, 622-626.

Barker, C., (1972). Aquathermal pressuring - role of temperature in development of abnormal pressure. *AAPG Bulletin*, **56**, 2068-2071.

Barker, C., (1990). Calculated volume and pressure changes during the thermal cracking of oil to gas in reservoirs. *AAPG Bulletin*, **74**, 1254-1261.

Beale, R. & Jackson, T., (1990). *Neural Computing: an Introduction.* Institute of Physics Publishing, Bristol, UK. 239pp.

Benouda, D., Wadge, G., Whitmarsh, R. B., Rothwell, R. G. & MacLeod, C., (1999). Inferring the lithology of borehole rocks by applying neural network classifiers to downhole logs: an example from the Ocean Drilling Program. *Geophysical Journal International*, **136**, 477-491.

Bethke, C. M. & Corbett, T. F., (1988). Linear and non-linear solutions for one-dimensional compaction flow in sedimentary basins. *Water Resources Research*, **24**, 461-467.

Biot, M. A., (1941). General theory of three-dimensional consolidation. *Journal of Applied Physics*, **12**, 155-164.

Bjørlykke, K., (1993). Fluid flow in sedimentary basins. *Sedimentary Geology*, **86**, 137-158.

Boas, M. L. (1983). *Mathematical Methods in the Physical Sciences 2nd edition.* John Wiley & Sons, New York, USA.

Boles, J. R. & Franks, S G., (1979). Clay diagenesis in the Wilcox Sandstones of Southwest Texas: Implications of smectite diagenesis on sandstone cementation. *Journal of Sedimentary Petrology*, **49**, 55-70.

Bowers, G., (1994). Pore pressure estimation from velocity data: accounting for overpressure mechanisms besides undercompaction. *SPE* **27488**, 515-529.

Breckels, I. M., & Van Eekelen H. A. M., (1982). Relationship between horizontal stress and depth in sedimentary basins. *Fall Technical Conference of the Society of Petroleum Engineers, San Antonio*, SPE 10336.

Bredehoeft, J. D., Djevanshir, R. D. & Belitz, K. R., (1988). Lateral fluid flow in a compacting sand-shale sequence, South Caspian Sea. *AAPG Bulletin*, **72**, 416-424.

Briggs, P. L., (1985). Color display of well logs. *Mathematical Geology*, **17**, 481.

Brigaud, F., Vasseur, G. & Caillet, G., (1992). Thermal state in the north Viking Graben (North Sea) determined from oil exploration well data. *Geophysics*, **57**, 69-88.

British Standard 1377 (1990). *Method of test for soils for civil engineering purpose.* British Standards Institution, London, UK.

Brown, M. P., Swarbrick, R. E. & Aplin, A. C., (1999). Estimation of pore pressure in shales: how useful are shale compaction curves? (abstract). *AAPG Bulletin*, **83**, 1302.

Bruce, C. H., (1984). Smectite dehydration-its relation to structural development and hydrocarbon accumulation in northern Gulf of Mexico. *AAPG Bulletin*, **68**, 673-683.

Bulat, J. & Stoker, S. J., (1987). Uplift determination from interval velocity studies, UK southern North Sea. In Brooks, J. & Glennie, K. (eds) *Petroleum Geology of Northwest Europe.* Graham and Trotman, London. 293-305.

Bunopas, S., (1981). Paleogeographic history of western thailand and adjacent parts of Southeast Asia: A plate tectonics interpretation. PhD thesis, Victoria University of Wellington, Wellington, New Zealand. 810pp.

Burland, J. B., (1990). On the compressibility and shear strength of natural clays. *Geotechnique*, **40**, 329-378.

Burley, S. D., Mullis, J. & Matter, A. (1989). Timing diagenesis in the Tartan reservoir (UK North Sea) - constraints from cathodoluminescence microscopy and fluid inclusion studies. *Marine and Petroleum Geology*, **6**, 98-120.

Burrus, J., Brosse, E., Choppin de Janvry, G., Grosjean, Y. & Oudin, J. L., (1992). Basin modelling in the Mahakam Delta based on the integrated 2D model TEMISPACK. *Proceedings of the 21st Meeting of the Indonesian Petroleum Association.* IPA paper 92-11-04, 23-44.

Burrus, J., (1998). Overpressure models for clastic rocks, their relation to hydrocarbon expulsion: a critical reevaluation. In Law, B. E., Ulmishek, G. F. & Slavin, V. I. (eds). *Abnormal Pressures in Hydrocarbon Environments*. AAPG Memoir, **70**, 35-63.

Buryakovskiy, L. A., Djevanshir, P. D. Alyarov, P. Y., (1983). Problem of studying anomalously high geopressures in relation to exploration and exploitation of oil and gas deposits. *Izvestiya Akademii Nauk USSR, Seryiya Sci Ear*, **1**, 119-127.

Byerlee, J., (1993). Model for episodic flow of high pressure water in fault zones before earthquakes. *Geology*, **10**, 42-50.

Cayley, G. T., (1987). Hydrocarbon migration in the Central North Sea. In Books J. & Glennie, K., (eds), *Petroleum Geology of North West Europe*. Graham & Trotman. 549-555.

Carpenter, G. A. & Grossberg, S. (1988). The ART of adaptive pattern recognition. *Computer*, **21**, 77-88.

Chapman, R. E., (1981). *Geology and Water: An Introduction to Fluid Mechanisms for Geologists*. Nijhoff, Den Haag, Netherlands.

Chonchawalit, A. & Bustin, R. M., (1994). Basin analysis of Tertiary strata in the Pattani Basin, Gulf of Thailand (Abstract). AAPG international conference and exhibition, Kuala Lumpur, Malaysia. *AAPG Bulletin*, **78**, 1138.

Collins, D. R. & Doveton, J. H., (1986). Color images of Kansas subsurface geology from well logs. *Computers and Geosciences*, **12**, 519-526.

Collins, D. R., Doveton J. H., & Macfarlane, P. A., (1992). Regional gamma ray gray tone intensity images of the Permian-Cretaceous sequence of western Kansas. *Abstracts of the SEPM 1992 Theme Meeting, Fort Collins, CO*, 19.

Colton-Bradley, V. A. C., (1987). Role of pressure in smectite dehydration - effects on geopressure and smectite-illite transistion. *AAPG Bulletin*, **71**, 1414-1427.

Cornford, C., (1994). Mandal-Ekofisk petroleum system in the Central Graben of the North Sea. In Magoon, L. B. & Dow, W. G. (eds), *The Petroleum System – from Trap to Source*. AAPG memoir, **60**, 537-571.

Daly, M. C., Cooper, M. A., Wilson, I., Smith, D. G. & Hooper, B. G. D., (1991). Cenozoic plate tectonics and basin evolution in Indonesia. *Marine and Petroleum Geology*, **8**, 2-21.

Darby, D., Hazeldine, R. S. & Couples, G. D. (1998). Central North Sea overpressures: insights into fluid flow from one- and two-dimensional basin modelling. In Düppenbecker, S. J. & Iliffe, J. E. (eds), *Basin modelling: Practice and progress*. Geological Society, London, Special Publications, **141**, 95-107.

Dewan, J. T., (1983). *Essentials of Modern Open-Hole Log Interpretation*. PennWell Books, Tulsa, USA. 361pp.

Dickinson, G., (1953), Geological aspects of abnormal reservoir pressures in Gulf Coast, Louisianna. *AAPG Bulletin*, **37**, 410-432.

Djéran-Maigre, I., Tessier, D., Grunberger, D, Velde, B. & Vasseur, G., (1998). Evolution of microstructures and of macroscopic properties of some clays during experimental compaction. *Marine and Petroleum Geology*, **15**, 109-128.

Doveton, J. H., (1992). *Geologic log analysis using computer methods*. AAPG computer applications in geology, number 2. American Association of Petroleum Geologists, Tulsa, USA.

Dowla, F. U. & Rogers, L. L., (1995). Solving problems in environmental engineering and geosciences with artificial neural networks. The MIT press, Cambridge, USA. 239pp.

Dzevanshir, R. D., Buryakovskiy, L. A. & Chilingarian, G. V., (1986). Simple quantitative evaluation of porosity of argillaceous sediments at various depths of burial. *Sedimentary Geology*, **46**, 169-175.

Eaton, B., (1972). Graphical method predicts geopressures worldwide. *World Oil*, **182** (6), 51-56.

Eaton, B., (1975). The equation for geopressure prediction from well logs. Society of Petroleum Engineers, paper 5544.

Eberhardt-Phillips, D., Han, D. H. & Zoback, M. D., (1989). Empirical relationships among seismic velocity, effective pressure, porosity and clay content in sandstone. *Geophysics*, **54**, 82-89.

Ellis, D, Howard, J., Flaum, C, McKeon, D, Scott, H., Serra, O. & Simmons, G., (1988). Mineral logging parameters: nuclear and acoustic. *The Technical Review*, **36**, 38-52.

Fertl, W. H., (1976). *Abnormal Formation Pressures: Dvevelopments in Petroleum Science 2*. Elsevier, Holland, 382pp.

Fertl, W. H. & Timko, D. J., (1972). How downhole temperatures and pressures affect drilling. *World Oil*, **73-82** (10 parts).

Fisher , M.J. & Mudge, D. C., (1990). The Triassic. In Glennie, K. W. (ed), *An Introduction to the Petroleum Geology of the North Sea.* Blackwell Scientific Publications, UK. 191-218.

FitzGerald, E. M., Bean, C. J. & Reilly, R., (1999). Fracture-frequency prediction from borehole wireline logs using artificial neural networks. *Geophysical Prospecting*, **47**, 1031-1044.

Gaarenstroom, L., Tromp, R. A. J., de Jong, M. C. & Brandenburg, A. M., (1993). Overpressures in the Central North Sea: implications for trap integrity and drilling safety. In Parker, J. R. (ed), *Petroleum Geology of Northwest Europe: Proceedings of the 4th Conference*, Geological Society, London. 1305-1313.

Giles, M. R., Indrelid, S. L., & James D. M. D., (1998). Compaction: the great unknown in basin modelling. In Düppenbecker, S. J. & Iliffe J. E. (eds) *Basin Modelling: Practice and Progress.* Geological Society, London , Special Publications, **141**, 15-43.

Glennie, K. W. (ed), (1990). *An Introduction to the Petroleum Geology of the North Sea.* Blackwell Scientific Publications, UK. 402pp.

Goulty, N. R., (1998). Relationship between porosity and effective stress in shales. *First Break*, **16**, 413-419.

Grauls, D. J. & Cassignol, C., (1993). Identification of a zone of fluid pressure induced fractures form log and seismic data - a case history. *First Break*, **11**, 59-68.

Hall, P. R., (1993). Mechanisms of overpressuring - an overview. In Manning, D. A. C., Hall, P. L. & Hughes, C. R. (eds) *Geochemistry of Clay Pore Fluid interactions.* Chapman and Hall, London, 265-315.

Hall, R., (1996). Reconstructing Cenozoic SE Asia. In Hall, R. & Blundell, D. (eds). *Tectonic Evolution of Southeast Asia.* Geological Society Special Publication, **106**, 153-184.

Hansen, S., (1996a). A compaction trend for Cretaceous and Tertiary shales on the Norwegian Shelf based on sonic transit times. *Petroleum Geoscience*, **2**, 159-166.

Hansen, S., (1996b). Quantification of net uplift and erosion on the Norwegian Shelf south of 66°N from sonic transit times of shale. *Norsk Geologisk Tidsskrift*, **76**, 245-252.

Harder, S. H., (1991). Extensional tectonics in the Gulf of Thailand South China Sea (Abstract). Seventh regional conference on geology, mineral and hydrocarbon resources of Southeast Asia (GEOSEA VII), Bangkok, Thailand, November 1991. *Journal of Southeast Asian Earth Sciences*, 7, 261.

Harder, S., McCabe, R. & Flower, M., (1994). A rotating stress field and the evolution of basins in the Gulf of Thailand (Abstract). AAPG international conference and exhibition, Kuala Lumpur, Malaysia. *AAPG Bulletin*, **78**, 1144.

Harrold, T. W. D., (2000). Porosity and Effective Stress Relationships in Mudrocks. PhD thesis. University of Durham, Durham, UK. 221pp.

Harrold, T. W. D., Swarbrick, R. E. & Goulty, N. R., (1999). Pore pressure estimation from mudrock porosities in Tertiary basins, Southeast Asia. *AAPG Bulletin*, **83**, 1057-1067.

Heppard, P. D., Cander, H. S. & Eggertson, E. B., (1998). Abnormal pressure and the occurrence of hydrocarbons in offshore eastern Trinidad, West Indies. In Law, B. E., Ulmishek, G. F. & Slavin, V. I. (eds). *Abnormal Pressures in Hydrocarbon Environments*. AAPG memoir, **70**, 215-246.

Hermanrud, C., (1993). Basin modelling techniques - an overview. In Doré *et al.* (eds). Basin Modelling: Advances and Applications. NPF Special Publication, **3**, 1-34.

Hermanrud C., Wensaas, L., Teige, G. M. G., Vik, E., Nordgård Bolås, H. M. & Hansen, S., (1998). Shale porosities from well logs on Haltenbanken (offshore Mid-Norway) show no influence of overpressuring. In Law, B. E., Ulmishek, G. F. & Slavin, V. I. (eds). *Abnormal Pressures in Hydrocarbon Environments*. AAPG memoir, **70**, 65-85.

Hillis, R. R., (1993). Quanitfying erosion in sedimentary basins from sonic velocities in shales and sandstones. *Exploration Geophysics*, **24**, 561-566.

Hillis, R. R., (1995). Quantification of Tertiary exhumation in the United Kingdom Southern North Sea using sonic velocity data. *AAPG Bulletin*, **79**, 130-152.

Holm, G. M., (1998). Distribution and origin of overpressure in the Central Graben of the North Sea. In Law, B. E., Ulmishek, G. F. & Slavin, V. I. (eds). *Abnormal Pressures in Hydrocarbon Environments*. AAPG Memoir, **70**, 123-144.

Hornby, B. E., Johnson, C. D., Cook, J. M. & Coyner, K. S., (1997). Experimental determination of the elastic properties of a compacting sediment. *Proceedings of the 67th International Meeting Society of Exploration Geophysicists*, 1035-1038.

Hottmann, C. E., & Johnson, R. K., (1965). Estimation of formation pressures from log-derived shale properties. *Journal of Petroleum Technology*, **17**, 717-722.

Hower, J., Eslinger, E. V., Hower, M. E. & Perry, (1976). Mechanism of burial metamorphism of argillaceous sediment: mineral and chemical evidence. *Bulletin of the Geological Society of America*, **87**, 725-737.

Huang, Z. & Williamson, M., (1996). Artificial neural network modelling as an aid to source rock characterization. *Marine and Petroleum Geology*, **13**, 277-290.

Huang, Z., Shimeld J., Williamson, M. & Katsube, J., (1996). Permeability prediction with artificial neural network modelling in the Venture gas field, offshore eastern Canada. *Geophysics*, **61**, 422-436.

Hubbert, K. M. & Rubey, W. W., (1959). Role of fluid pressure in mechanics of overthrust faulting. I. Mechanics of fluid-filled porous solids and its application to overthrust faulting. *Bulletin of the Geological Society of America*, **70**, 115-166.

Hunt, J. M., (1990). Generation and migration of petroleum from abnormally pressured fluid compartments. *AAPG Bulletin*, **74**, 1-12.

Hutchinson, C. S., (1989). *Geological evolution of SE Asia.* Oxford Monographs on Geology and Geophysics, **13**, Clarendon Press, Oxford, UK. 368pp.

Iliffe, J., (1999). Basin dynamics, plumbing, pressures and hydrocarbon charge of Tertiary reservoirs of the UKCS (abstract). *AAPG Bulletin*, **83**, 1318.

Issler, D. R., (1992). A new approach to shale compaction and stratigraphic restoration, Beaufort-MacKenzie Basin and MacKenzie Corridor, Northern Canada. *AAPG Bulletin*, **76**, 1170-1189.

James, W., (1890). *The Principles of Psychology (Vol 2).* Henry Holt, New York, USA. 714pp.

Johanssen, E. M., Dowla, F. U. & Goodman, D. M., (1992). Backpropagation learning for multi-layer feed-forward neural using the conjugate gradient method. *International Journal of Neural Systems*, **2**, 291-301.

Jordt, H., Faleide, J. I., Bjørlykke, K. & Ibrahim, M. T., (1995). Cenozoic sequence stratigraphy of the central and northern North Sea Basin: tectonic development, sediment distribution and provenance areas. *Marine and Petroleum Geology*, **12**, 845-879.

Karig, D. E. & Hou, G., (1992). High stress consolidation experiments and their geologic implications. *Journal of Geophysical Research - Solid Earth*, **97**, 289-300.

Katahara, K. & Corrigan, J., (1998). Effect of gas on poroelastic response to burial or erosion. *American Association of Drilling Engineers Forum 'Pressure Regimes in Sedimentary Basins and their Prediction.' Lake Conroe, Texas.*

Kohonen, T., (1988). An introduction to neural computing. *Neural Networks*, **1**, 3-16.

Kohonen, T., (1990). *Self organization and associative memory.* 3rd edition. Springer Verlag, Berlin, Germany.

Lacassin, R., Maluski, H., Leloup, P.H., Tapponnier, P., Hinthong, C., Siribhakdi, K., Chuaviroj, S. & Charoenravat, A., (1997). Tertiary diachronic extrusion and deformation of western Indochina: structural and $^{40}Ar/^{39}Ar$ evidence from NW Thailand. *Journal of Geophysical Research – Solid Earth*, **102**, B5, 10013-10037.

Lahann, R., (2000). Impact of diagenesis on compaction modelling and compaction equilibrium. *Proceedings of the Overpressure 2000 Workshop, Croydon, UK.*

Law, B. E., (1984). Relationships of source-rock, thermal maturity and overpressuring to gas generation and occurrence in low-permeability Upper Cretaceous and Lower Tertiary rocks, Greater Green river Basin,

Wyoming, Colorado and Utah. In Woodward, J., Meissner, F. F. & Clayton, J. L. (eds) *Hydrocarbon source rocks of the greater Rocky Mountain region.* Rocky Mountain Association of Geologists, 469-490.

La Vigne, J., Herron, M. & Hertzog, R., (1994). Density -neutron interpretation in shaly sands. *Proceedings of the SPWLA 35th Annual Logging Symposium*, paper EEE.

Le Dain, A. V., Taponnier, P. & Molnar, P., (1984). Active faulting and tectonics of Burma and surrounding region. *Journal of Geophysical Research*, **B89**, 453-472.

Lee, T. Y. & Lawver, L.A., (1994). Cenozoic plate reconstruction of the South China Sea region. *Tectonophysics*, **235**, 149-180.

Leo, C. T. A. M., (1997). Exploration in the Gulf of Thailand reservoirs related to the Bongkot Field. In Fraser, A. J., Matthews, S. J. & Murphy R. W. (eds). *Petroleum Geology of Southeast Asia.* Geological Society Special Publication, **126**, 77-87.

Leonard, R. C., (1993). Distribution of sub-surface pressure in the Norwegian Central Graben and applications for exploration. In Parker, J. R. (ed), *Petroleum Geology of Northwest Europe: Proceedings of the 4th Conference*, Geological Society, London. 1295-1303.

Lian, N. G. & Bradley, K., (1986). Exploration and development of natural gas, Pattani Basin, Gulf of Thailand. *Transactions of the Fourth Circum-Pacific Energy and Mineral Resources Conference, Singapore*, 171-181.

Liu, X. & Galloway, W. E., (1997). Quantitative determination of Tertiary sediment supply to the North Sea Basin. *AAPG Bulletin*, **81**, 1482-1509.

Lopatin, N. V., (1971). Temperature and geologic time as factors in coalification (in Russian). *Izvestiya Akademii Nauk USSR, Seriya Geologicheskaya*, **3**, 95-106.

Lovell, J. P. B., (1990). The Cenozoic. In Glennie, K. W. (ed), *An Introduction to the Petroleum Geology of the North Sea.* Blackwell Scientific Publications, UK. 255-272.

Luo, M., Baker, M. R. & Lemone, D. V., (1994). Distribution and generation of the overpressure system, eastern Delaware Basin, western Texas and southern New Mexico. *AAPG Bulletin*, **78**, 1386-1405.

Luo, X. R. & Vasseur, G., (1992). Contributions of compaction and aquathermal pressuring to geopressure and the influence of environmental conditions. *AAPG Bulletin*, **76**, 1550-1559.

Luo, X. R. & Vasseur, G., (1995). Modelling of pore pressure evolution associated with sedimentation and uplift in sedimentary basins. *Basin Research*, **7**, 35-52.

Luthi, S. M. & Bryant, I. D., (1997). Well log correlation using a backpropagation neural network. *Mathematical Geology*, **29**, 413-425.

McBride, B. C., (1998). The evolution of allochthonous salt along a megaregional profile across the Northern Gulf of Mexico Basin. *AAPG Bulletin*, **82**, 1037-1054.

McClelland, J. L., & Rumelhart, D. E., (1986). *Parallel Distributed Processing*. MIT Bradford Press, USA.

MacGregor, J. R., (1965). Quantitative determination of reservoir pressures from conductivity log. *Bulletin AAPG*, **49**,1502-1511.

MacKenzie, A.S. & Quigley, T. M., (1988). Principles of geochemical prospect appraisal. *AAPG Bulletin*, **72**, 399-415.

Magara, K., (1976). Thickness of removed sedimentary rocks paleopore pressure and paleotemperature, south western part of the Western Canada Basin. *AAPG Bulletin*, **60**, 554-565.

Mann, D. M. & MacKenzie, A. S., (1990). Prediction of pore fluid pressures in sedimentary basins. *Marine and Petroleum Geology*, **7**, 55-65.

Maranate, S. & Vella, P., (1986). Paleomagnetism of the Khorat Group, Mesozoic, Northeastern Thailand. *Journal of Southeast Asian Earth Sciences*, **1**, 23-31.

Marine, I. W. & Fritz, S. J., (1981). Osmotic model to explain anomalous hydraulic heads. *Water Resources Research*, **17**, 73-82.

Mazzoni, R., Wahdan, T., Bassem, A. & Ward, C. D., (1997). Real time pore and fracture pressure prediction with FEWD in the Nile Delta. *Society of Petroleum Engineers,* paper 37669.

Meissner, F. F., (1978a). Patterns of source rock maturity in non-marine source rocks of some typical Western interior basins. In *Non-Marine Tertiary and Upper Cretaceous Source Rocks and the Occurrence of Oil and Gas in West-Central US.* Rocky Mountain Association of Geologists Continuing Education Lecture Series, 1-37.

Meissner, F. F., (1978b). Petroleum geology of the Bakken Formation, Williston Basin, North Dakota and Montana. In *Proceedings of the 24th Annual Conference, Williston Basin Symposium.* Montana Geological Society, 207-227.

Mello, U. T., Karner, G. D. & Anderson, N., (1994). A physical explanation for the positioning of the top of overpressure in shale-dominated sequences in Gulf Coast basin, United States. *Journal of Geophysical Research*, **B99**, 2775-2789.

Meyer, B. L. & Nederlof, M. H., (1984). Identification of source rocks on wireline logs by density/resistivity and sonic transit time/resistivity crossplots. *AAPG Bulletin*, **68**, 121-129.

Micromeritics (1982). Sedigraph 5000ET instruction manual. Micromeritics, Norcross GA, USA.

Morley, C. K., Woganan, N., Sankumarn, N., Hoon, T. B., Alief, A. & Simmons, M., (2001). Late Oligocene-Recent stress evolution in rift basins of northern and central Thailand: implications for escape tectonics. *Tectonophysics*, **334**, 115-150.

Moss, B. & Seheult, A. (1987). Does principal component analysis have a role to play in the interpretation of petrophysical data? *Transactions of the SPWLA 28th Annual Logging Symposium,* Paper TT.

Mouchet, J. P. & Mitchell, A., (1989). *Abnormal Pressures While Drilling.* Elf Aquitaine Edition, Boussens, France. 264pp.

Mudge, D. C. & Bujak, J. P., (1994). Eocene stratigraphy of the North Sea Basin. *Marine and Petroleum Geology*, **11**, 166-181.

Myers, K. J. & Wignall, P. B. (1987). Understanding Jurassic organic rich mudrocks – new concepts using gamma ray spectrometry and palaeoecology. In Leggett, J. K. (ed). *Marine and clastic sedimentology: new developments and concepts.* Graham and Trotman, London, UK.

Nashaat, M., (1998). Abnormally high formation pressure and seal impacts on hydrocarbon accumulations in the Nile Delta and North Sinai Basins, Egypt. In Law, B. E., Ulmishek, G. F. & Slavin, V. I. (eds). *Abnormal pressures in hydrocarbon environments.* AAPG Memoir, **70**, 161-180.

Neuzil , C. J., (1995). Abnormal pressures as hydrodynamic phenomena. *American Journal of Science*, **295**, 742-786.

O'Connor, S. J. & Walker, D., (1993). Palaeocene reservoirs of the Everest trend. In Parker, J. R. (ed), *Petroleum Geology of Northwest Europe: Proceedings of the 4th Conference*, Geological Society, London. 145-160.

Okui, A., Siebert, R. M. & Matsubayashi, H., (1998) Simulation of oil expulsion by 1-D and 2-D basin modelling - saturation threshold and relative permeabilities of source rocks. In Düppenbecker, S. J. & Iliffe J. E. (eds) *Basin Modelling: Practice and Progress.* Geological Society, London , Special Publications, **141**, 45-72.

Osborne, M. J. & Swarbrick, R. E., (1997). Mechanisms for generating overpressure in sedimentary basins - a re-evaluation. *AAPG Bulletin*, **81**, 1023-1041.

Packham. G. H., (1993). Plate tectonics and the development of sedimentary basins of the dextral regime in western Southeast Asia. *Journal of Southeast Asian Earth Sciences*, **8**, 497-511.

Parasnis, D. S., (1960). The compaction of sediments and its bearing on some geophysical problems. *Geophysics Journal of the Royal Astronomical Society*, **3**, 1-28.

Pigott, J. D. & Sattayarak, N., (1991). Tectonic subsidence of the northern Gulf of Thailand. (Abstract). Seventh regional conference on geology, mineral and hydrocarbon resources of Southeast Asia (GEOSEA VII), Bangkok, Thailand, November 1991. *Journal of Southeast Asian Earth Sciences*, 7, 259.

Polachan, S., Pradidtan, S., Tongtaow, C., Janmaha, S. Intarawijitr, K. & Sangsuwan, C., (1991). Development of Cenozoic basins in Thailand. *Marine and Petroleum Geology*, **8**, 84-97.

Powers, M. C., (1967). Fluid release mechanisms in compacting marine mudrocks and their importance in oil exploration. *AAPG Bulletin*, **51**, 1240-1254.

Pradidtan, S. & Dook, R. (1982). Petroleum geology of the northern part of the Gulf of Thailand. *Proceedings of the National Conference on the Geologic Resources of Thailand: Potential for Future Development*, Bangkok, Thailand, 235-246.

Probert, T., Robinson, J. P., Ronen, S., Hoare, R., Pope, D., Kommedal, J., Crook, H. & Law, A., (2000). Imaging through gas using 4-component, 3D seismic data; a case study from the Lomond Field. *32nd Annual Offshore Technology Conference; 2000 Proceedings; Volume 1, Geology, Earth Sciences, and Environmental Factors*, 157-163.

Quirein, J. A., Garden, J. S. & Watson, J.T., (1982). Combined natural gamma ray spectral/litho-density measurements applied to complex lithologies. *SPE* **11143**, 1-14.

Raiga-Clemenceau, J., Martin, J. P. & Nicoletis, S., (1988). The concept of acoustic formation factor for more accurate porosity determination from sonic transit time data. *The Log Analyst*. Jan-Feb 1988, 54-60.

Rangin, C., Jolivet, L. & Pubellier, M. (1990). A simple model for the tectonic evolution of the Southeast Asia and Indonesia region for the past 43 million years. *Bulletin de la Société Géologique de France*, **8**, 889-905.

Raymer L. L., Hunt, E. R. & Gardner, J. S., (1980). An improved sonic transit time-to-porosity transform. *Transactions of the SPWLA 21st Annual Logging Symposium*, Paper P.

Rider, M., (1996). *The Geological Interpretation of Well Logs, (2nd ed.)*. Whittles Publishing, Caithness, UK. 280pp.

Rieke, H. H. & Chilingarian, G. V., (1974). *Compaction of Argillaceous Sediments*. Elsevier, Holland, 424pp.

Rogers, S., Fang, J. H., Karr, J. L. & Stanley D. A., (1992). Determination of lithology from well logs using a neural network. *AAPG Bulletin*, **76**, 731-739.

Rubey, W. W. & Hubbert, M. K., (1959). Role of fluid pressure in mechanics of overthrust faulting. *Geological Society of America Bulletin*, **70**, 167-206.

Rumelhart, D. E., Hinton, G. E. & Williams, R. J., (1986). Learning representation by back propagating errors. *Nature*, **323**, 533-536.

Rutter, E. H., (1983). Pressure solution in nature, theory and experiment. *Journal of the Geological Society, London*, **140**, 725-740.

Salvador, A. (ed), (1991). *The Gulf of Mexico Basin.* Geology of North America. Geological Society of America, USA. 568pp.

Sclater, J. G. & Christie, P. A. F., (1980). Continental stretching: an explanation of the post Mid Cretaceous subsidence of the Central North Sea Basin. *Journal of Geophysical Research - Solid Earth*, **85**, 3711-3739.

Schärer, U., Tapponnier, P., Lacassin, R., Leloup, P. H., Zhong, D. & Ji, S., (1990). Intraplate tectonics in Southeast Asia: a precise age for large scale Miocene movement along the Ailao Shan-Red River shear zone, China. *Earth and Planetary Science Letters*, **97**, 65-77.

Schneider, F., Burrus, J. & Wolf, S., (1993). Modelling overpressures by effective stress/porosity relationships in low permeability rocks: empirical artifice or physical reality? In Doré, A. G., Auguston, J. H., Hermannrud, C., Stewart, D. J. & Sylta, O. (eds) *Basin Modelling, Advances and Applications.* Norwegian Petroleum Special Publication, **3**, 333-341.

Schneider, F., Potdevin, J. L., Wolf, S. & Faille, I., (1994). Modèle de compaction élastoplastique et visocoplastique pour simulateur des basins sédimentaires. *Revue de l'Institut Français du Pétrole*, **49**, 141-148.

Schneider, F., Potdevin, J. L., Wolf, S. & Faille, I., (1996). Mechanical and chemical compaction model for sedimentary basin simulators. *Tectonophysics*, **263**, 307-317.

Schlumberger, (1989). *Log Interpretation Charts.* 151pp.

Schmoker, J. W. & Gautier, D. L., (1989). Compaction of basin sediments: modeling based on time-temperature history. *Journal of Geophysical Research - Solid Earth*, **94**, 7379-7386.

Shi, Y. & Wang, C. Y., (1986). Pore pressure generation in sedimentary basins, overloading versus aquathermal. *Journal of Geophysical Research - Solid Earth*, **91**, 2153-2162.

Skempton A. W., (1944). Notes on the compressibility of clays. *Journal of the Geological Society, London*, **100**, 119-135.

Skempton, A. W., (1970). The consolidation of clays by gravitational compaction. *Journal of the Geological Society, London*, **125**, 373-411.

Sladen, C., (1997). Exploring the lake basins of east and southeast Asia. In Fraser, A. J., Matthews, S. J. & Murphy R. W. (eds). *Petroleum Geology of Southeast Asia.* Geological Society Special Publication, **126**, 49-76.

Smith, J. E., (1971). The dynamics of shale compaction and the evolution of pore fluid pressure. *Mathematical Geology*, **3**, 239-263.

Spencer, C. W., (1987). Hydrocarbon generation as a mechanism for overpressuring in the Rocky Mountain Region. *AAPG Bulletin*, **71**, 368-388.

Swan, A. R. H., & Sandilands, M., (1995). *Introduction to Geological Data Analysis.* Blackwell Science, Oxford, UK, 446pp.

Swarbrick, R. E. & Osborne, M. J., (1996). The nature and diversity of pressure transition zones. *Marine and Petroleum Geology*, **2**, 111-116.

Swarbrick, R. E. & Osborne, M. J., (1998). Mechanisms that generate abnormal pressures: an overview. In Law, B. E., Ulmishek, G. F. & Slavin, V. I. (eds). *Abnormal Pressures in Hydrocarbon Environments.* AAPG Memoir, **70**, 13-34.

Sweeney, J. J., Braun, R. L., Burnham, A. K., Talukdar, S. & Vallejos, C., (1995). Chemical kinetic model of hydrocarbon generation, expulsion and destruction applied to the Maracaibo Basin, Venezuela. *AAPG Bulletin*, **79**, 1515-1532.

Tada. R., Maliva, R. & Siever, R., (1987). A new mechanism for pressure solution in porous quartzose sandstone. *Geochimica et Cosmochimica Acta*, 51, 2295-2301.

Tang, J. & Lerche, I., (1993). Geopressure evolution, hydrocarbon generation and migration in the Beaufort-Mackenzie Basin, Canada: results from two-dimensional quantitative modelling. *Marine and Petroleum Geology*, **10**, 373-393.

Tapponnier, P., Peltzer, G. & Armijo, R., (1986). On the mechanics of the collision between India and Asia. In Coward, M. P. & Ries, A. C., (eds) *Collision Tectonics.* Geological Society Special Publication, **19**, 115-157.

Tapponnier, P., Peltzer, G., Le Dain, A. Y., Armijo, R. & Cobbold, P., (1982). Propagating extrusion tectonics in Asia: new insights from simple experiments with plasticine. *Geology*, **10**, 611-616.

Terzaghi, K. (1923). *Die Berchnung der Durchlässigkeitsziffer des Tones aus dem Verlanf der Hydrodynamishcen Spannungserscheinungen.* Sitzungbrichte Akademie Wissenschaft, Vienna, **132**, 125-138.

Thompson, P. J. & Butcher, P. D., (1991). The geology and geophysics of the Everest complex. In Spencer A. M. (ed), *Generation, Accumulation and Production of Europe's Hydrocarbons.* Special Publication of the European Association of Petroleum Geoscientists, **1**. Oxford University Press, 89-98.

Todd, S. P., Dunn, M. E. & Barwise, A. J. G., (1997). Characterising petroleum charge systems in the Tertiary of SE Asia. In Fraser, A. J., Matthews, S. J. & Murphy R. W. (eds). *Petroleum Geology of Southeast Asia.* Geological Society Special Publication, **126**, 25-47.

Traugott, M., (2000). Use of model defined compaction trend lines in pore pressure prediction methods. *Proceedings of the Overpressure 2000 Workshop, Croydon, UK.*

Traugott, M., Heppard, P. & Dodd, T., (1999). Pressure prediction for shallow water evaluation. *Proceedings of the 1999 International Forum on Shallow Water Flows, League City, Texas.*

Upton, D., Hurford, A., Bristow, C. & Carter, A., (1999). Constructing Tertiary thermal histories in Thailand (Abstract). European Union of Geosciences conference, Strasbourg, France. *Terra Abstracts*, **11**, 58.

Vasseur, G., Djéran-Maigre, I., Grunberger, D., Rousset, G., Tessier, D. & Velde, B., (1995). Evolution of structural and physical parameters of clays during experimental compaction. *Marine and Petroleum Geology*, **12**, 941-954.

Vernik, L., (1994). Predicting lithology and transport properties from acoustic velocities based on petrophysical classification of siliciclastics. *Geophysics*, **59**, 420-427.

Vernik, L. & Liu, X., (1997). Velocity anisotropy in shales: a petrophysical study. *Geophysics*, **62**, 521-532.

Villamil, T., Arango, C., Weimer, P., Waterman, A., Rowan, M. G., Varnai, P., Pulham, A. J. & Crews, J. R., (1998). Biostratigraphic techniques for analysing benthic biofacies, stratigraphic condensation and key surface identification, Pliocene and Pleistocene sediments, Northern Green Canyon and Ewing Bank (Offshore Louisiana), Northern Gulf of Mexico. *AAPG Bulletin*, **82**, 961-985.

Vysotsky, V. I., Rodnikova, R. D. & Li, M .N., (1994). The petroleum geology of Cambodia. *Journal of Petroleum Geology*, **17**, 195-210.

Waples, D., (1998). Basin modelling: how well have we done? In Düppenbecker, S. J. & Iliffe, J. E. (eds), *Basin Modelling: Practice and Progress.* Geological Society, London, Special Publications, **141**, 15-44.

Weimer, P., Rowan, M. G., McBride, B. C. & Kligfield, R., (1998a). Evaluating the petroleum systems of the Northern Deep Gulf of Mexico through integrated basin analysis: an overview. *AAPG Bulletin*, **82**, 865-877.

Weimer, P., Varnai, P., Budhijanto, F. M., Acosta, Z. M., Martinez, R. E., Navarro, A. F., Rowan, M. G., McBride, B. C., Villamil, T., Arango, C., Crews, J. R. & Pulham, A. J., (1998b). Sequence stratigraphy of Pliocene and Pleistocene turbidite systems, Northern Green Canyon and Ewing Bank (Offshore Louisiana), Northern Gulf of Mexico. *AAPG Bulletin*, **82**, 918-960.

Wolff, M. & Pelissier-Combescure, J., (1992). FACIOLOG – automatic electrofacies determination. *Transactions of the SPWLA 23rd Annual Logging Symposium,* Paper FF.

Wollands, M. A. & Haw, D., (1976). Tertiary stratigraphy and sedimentation in the Gulf of Thailand. *Proceedings of the SEAPPEX Offshore SE Asia Conference, Singapore,* 1-22.

Wyllie, M. R. J., Gregory, A. R. & Gardiner, L. W., (1956). Elastic wave velocities in heterogeneous and porous media. *Geophysics*, **21**, 41-70.

Yang, Y. (1999). *ShaleQuant.* Proprietary software, University of Newcastle upon Tyne, UK.

Yang, Y. & Aplin, A. C., (1997). A method for the disaggregation of mudstones. *Sedimentology*, **44**, 559-562.

Yang, Y. & Aplin, A. C., (1998). Influence of lithology and compaction on the pore size distribution and modelled permeability of some mudstones from the Norwegian Margin. *Marine and Petroleum Geology*, **15**, 163-175.

Yang, Y. & Aplin, A. C. (2000). The definition of porosity-effective stress relationships in fine-grained sediments. *Proceedings of the Overpressure 2000 Workshop, Croydon, UK.*

Yardley, G. S. & Swarbrick, R. E., (2000). Lateral transfer: a source of additional overpressure? *Marine and Petroleum Geology*, **17**, 523-537.

Yassir, N. A. & Bell, J. S., (1994). Relationships between pore pressures, stresses and present-day geodynamics in the Scotian Shelf, offshore Eastern Canada. *AAPG Bulletin*, **78**, 1863-1880.

Yusof, W. I. & Swarbrick, R. E., (1994). Thermal and pressure histories of the Malay Basin, offshore Malaysia (Abs): *AAPG Bulletin*, **78**, 1171.